Title
Scalable Nanomanufacturing Techniques and Their Applications in Biomedicine: From Chemical Patterning to Implantable Neuroprobes

Author
Zhao, Chuanzhen

Publication Date
2020

Peer reviewed|Thesis/dissertation

UNIVERSITY OF CALIFORNIA

Los Angeles

Scalable Nanomanufacturing Techniques and Their Applications in Biomedicine: From Chemical Patterning to Implantable Neuroprobes

A dissertation submitted in partial satisfaction of the

requirements for the degree of Doctor of Philosophy

in Chemistry

by

Chuanzhen Zhao

2020

ABSTRACT OF THE DISSERTATION

Scalable Nanomanufacturing Techniques and Their Applications in Biomedicine:

From Chemical Patterning to Implantable Neuroprobes

by

Chuanzhen Zhao

Doctor of Philosophy in Chemistry

University of California, Los Angeles, 2020

Professor Anne M. Andrews, Co-Chair

Professor Paul S. Weiss, Co-Chair

Biomarkers from the human body can provide dynamic and powerful insight into a broad spectrum of health conditions. Monitoring biomarkers in body fluids will improve and advance prediction, screening, diagnosis, and treatment of disease. At present, however, the ability to study and to track the ever changing mixtures of chemicals inside and on the human body is limited. For example, chemical communication between neurons plays central roles in information processing in the brain, yet technologies for neurochemical recordings with high chemical, spatial, and temporal resolution are limited, and for some neurotransmitters, nonexistent. For the past five years, I have focused on developing transformative biosensors towards *in vivo* neurotransmitter monitoring to advance our understanding of brain activity and how behavior arises from this activity.

To achieve this goal, we developed ultrathin (~3-nm) In_2O_3 field-effect transistor (FET) biosensors, where DNA sequences (aptamers) covalently functionalized to the device surfaces enable specific, high-sensitivity molecular recognition. Building on the capabilities of these aptamer-FET biosensors, we developed multiplexed sensors that simultaneously target several important biomarkers, including dopamine, serotonin, glucose, phenylalanine, and cortisol.

A high-throughput, wafer-scale, and low-cost nanolithographic approach (chemical lift-off lithography, CLL) was developed and applied for the fabrication of nanoscale FETs, which are the functional core of these sensors. We have advanced CLL by using the self-collapsing nature of polymeric stamps to achieve small features (~15 nm). The capabilities of CLL have been expanded to pattern synthetic molecules, biomolecules, metallic nanostructures, and semiconductor nanostructures. We were able to fabricate different types of sensors, including plasmonic sensors and FET biosensors, with micro- and nanostructured patterning using CLL.

We designed and fabricated implantable neurochemical probes and wearable bioelectronics using micro-electro-mechanical-system technologies. We performed *ex vivo* and *in vivo* experiments with implanted neural probes to monitor neurotransmitters, *e.g.*, serotonin, in living, conscious animals. The technologies we are developing will advance our understanding of healthy brain function in relation to complex behavior, as well as corresponding dysfunction in psychiatric and neurodegenerative disorders.

The dissertation of Chuanzhen Zhao is approved.

Richard B. Kaner

Aydogan Ozcan

Alexander Michael Spokoyny

Anne M. Andrews, Committee Co-Chair

Paul S. Weiss, Committee Co-Chair

University of California, Los Angeles

2020

To my parents Zhidong Zhao and Jing Zhao, and my wife Tianxing Man

Table of Contents

List of Figures and Tables

List of Abbreviations and Symbols

Field-effect transistor (FET)

Trimethoxy(propyl)silane (PTMS)

(3-Aminopropyl)trimethoxysilane (APTMS)

3-Maleimidobenzoic acid *N*-hydroxysuccinimide ester (MBS)

Micro-electro-mechanical-system (MEMS)

Microcontact printing (μCP)

Chemical lift-off lithography (CLL)

Self-assembled monolayer (SAM)

Self-collapse lithography (SCL)

Polymer-pen chemical lift-off lithography (PPCLL)

Polydimethylsiloxane (PDMS)

Scanning electron microscopy (SEM)

Two-dimensional (2D)

Surface plasmon resonance (SPR)

Localized surface plasmon resonances (LSPR)

Digital versatile discs (DVDs)

High-definition DVD (HD-DVD)

2-Dioleoyl-*sn*-glycero-3-phosphocholine (DOPC)

Bovine serum albumin (BSA)

Limits of detection (LOD)

Dynamic range (DR)

Si nanowires (SiNWs)

Carbon nanotubes (CNTs)

One-dimensional (1D)

Chemical vapor deposition (CVD)

Electron-beam lithography (EBL)

Ethylenediaminetetraacetic acid disodium salt dihydrate (EDTA)

Deionized (DI)

Scanning electron microscopy (SEM)

Energy-dispersive X-ray (EDX)

Ion-sensitive field-effect transistor (ISFET)

Artificial cerebrospinal fluid (aCSF)

Polyethylene terephthalate (PET)

Indium-gallium-zinc oxide (IGZO)

Phosphate-buffered saline (PBS)

High-performance liquid chromatography (HPLC)

Fast-scan cyclic voltammetry (FSCV)

Carbon-fiber microelectrodes (CFMs)

5-hydroxytryptophan (5-HTP)

5-hydroxyindoleacetic acid (5-HIAA)

Central nervous system (CNS)

Acknowledgments

I would like to say thank you to my advisors, colleagues, friends, and family for your support and help over the past five years. Those five years at UCLA have been an amazing journey for me. During the summer of 2014, I was honored to be selected as a scholar of UCLA's Cross-Disciplinary Scholars in Science and Technology (CSST) program and spent 10 weeks in Prof. Paul Weiss' laboratory as an undergraduate researcher. I was fascinated by the biosensor projects in Prof. Anne Andrews' and Prof. Paul Weiss' groups and decided to come back to UCLA to pursue my Ph. D. in 2015. During these five years of study at this world-class research institute, I have been fortunate to work with so many fantastic people and pursue big and important problems in the field of biosensors. Many people have contributed to my research career, and I would like to thank you all sincerely.

First, I would like to thank my advisors, Prof. Anne Andrews and Prof. Paul Weiss. They have given me tremendous support and guidance. None of the projects in my thesis would be possible without the support and mentorship from Anne and Paul. I am fortunate to have diverse research directions with many collaborative projects inside and outside of UCLA. Anne and Paul always supported me to explore new directions and provided any support I need along the way, to help build the connections, to find the resources I needed, and more importantly, to guide me and challenge me to think bigger and to ask more important questions.

Secondly, I would like to thank my excellent colleagues and friends in the Andrews and Weiss labs: Prof. Xiaobin Xu, Dr. Qing Yang, Dr. Nako Nakatsuka, Dr. Kevin M. Cheung,

Dr. Jeffrey J. Schwartz, Dr. John M Abendroth, Prof. Beth Anderson, Dr. Steven Jonas, Wenfei Liu, and all other members from our labs. Also, I want to acknowledge the efforts contributed from our collaborators at UCLA and around the world.

I would like to thank the staff in the Chemistry and Biochemistry Department, Semel Institute, California Nanosystems Institute (CNSI), and UCLA Nanolab. In addition, I want to thank the funding sources and agencies, including the National Science Foundation (No. CMMI-1636136), National Institutes of Health (No. DA045550), and Hatos Center for Neuropharmacology at UCLA, that make our research possible.

Lastly, I really want to say “thank you” from the bottom of my heart to all my family members. They have always been supportive of my adventure and have encouraged me to chase bigger and bigger dreams. During the toughest time in my graduate career, they were always with me and provided a free space for me to embrace all the challenges. None of my accomplishments would be possible without their support. I want to thank my parents, Zhidong Zhao and Jing Zhao, for their strong support and unconditional love to me. I also want to thank my wife, Dr. Tianxing Man, who is also a close friend, a great mentor, and a fantastic collaborator to me. I am very glad that we have published three papers together (so far)!

Biographical Sketch

Chuanzhen Zhao attended Beijing Institute of Technology (BIT) in China from 2011 to 2015 as an undergraduate in the Department of Materials Science and Engineering. While he was at BIT, he was awarded the National Scholarship from the Ministry of Education of the P. R. China, which is considered to be the highest honor for undergraduate students in China. Besides excellent performance in coursework, he joined Prof. Haizheng Zhong's group to work on the synthesis and applications of semiconductor nanocrystals. He developed an efficient ligand exchange strategy for aqueous phase transfer of hydrophobic $CuInS_2$/ZnS QDs with high quantum yields and stability. In collaboration with Sanford Burnham Prebys Medical Discovery Institute in San Diego, they demonstrated the application of cadmium-free QDs for tumor imaging with minimal toxicity and strong tumor-specific homing.

At the end of his third year at BIT, he was selected as a UCLA CSST scholar and spent 10 weeks in Prof. Paul S. Weiss' lab at UCLA. During his stay at UCLA, he started working on the development of highly-sensitive biosensors. He received several awards and honors during his undergraduate career, including an Outstanding Graduate in Beijing Award, an Outstanding Graduate at BIT Award, a UCLA CSST Fellowship, and an Outstanding Research and Presentation at UCLA CSST 2014 Summer Program. In 2015, he received his Bachelor of Science degree in Materials Science and Engineering.

In 2015, he returned to the University of California, Los Angeles to pursue his graduate research career. He joined Prof. Paul S. Weiss' and Prof. Anne M. Andrews' groups in the Department of Chemistry and Biochemistry. During his graduate career at UCLA, he:

(1) fabricated large-area, one-, two-, and three-dimensional metal and semiconductor nanostructures for biosensing, flexible electronics, and point-of-care devices; (2) advanced nanoscale chemical patterning using soft lithography for a variety of applications, including biomolecule patterning and nanoelectronics; (3) developed ultra-sensitive aptamer-based neurochemical biosensors for neurotransmitter detection in physiological environments; (4) designed and fabricated implantable silicon-based neuroprobes with arrays of aptamer-field-effect transistors for *in vivo* neurotransmitter monitoring with high spatial resolution and selectivity; (5) fabricated implantable and flexible neurochemical probes towards *in vivo* neurotransmitter monitoring; (6) designed and fabricated fully integrated field-effect transistor wearable biosensors for sweat metabolite monitoring towards clinical applications.

He has received numerous awards in recognition of his research achievements and professional activities, including the Dimitris N Chorafas Prize, a Dissertation Year Fellowship at UCLA, a Thomas and Ruth F. Jacobs Dissertation Award, a *Micromachines* Best Poster Award, a UCLA Research Showcase Fellowship, an Outstanding Reviewer Awards at IOP Publishing, and an Excellence in Second Year Academics and Research Award at UCLA. He will receive his Doctor of Philosophy degree in Chemistry (Materials and Nanoscience specialization) after submitting this thesis in December of 2020.

Chapter 1

Introduction

Part of the information in this chapter is in preparation for submission

and has been adapted here.

Authors: **Zhao, C.**; Huang, I. W.; Cheung, K. M.; Nakatsuka, N.; Yang, H.; Liu, W.; Cao, Y.; Man. T.; Weiss, P. S.; Monbouquette, H. G.; Andrews, A. M.

Authors: **Zhao, C.**; Xu, X.; Yang, Q.; Man, T.; Jonas, S. J.; Schwartz, J. J.; Andrews, A. M.; Weiss, P. S.

Recently, the field of bioelectronics has created new opportunities for advancing our understanding of the human body by leveraging the skills of an interdisciplinary community spanning biology, chemistry, electronics, engineering, and materials science.[1-8] Advances have been made in healthcare monitoring and medical therapies with potential for enhancing human well-being and performance yet to be realized.[9-14]

For example, understanding how information is encoded in brain function is at the heart of neuroscience. New discoveries in brain information processing have led to improvements in the treatment of neurological diseases, such as Parkinson's disease, Alzheimer's disease, and epilepsy.[15-17] Understanding neural function requires advanced technologies that approach the spatial and temporal resolution of neurotransmission. Implantable and genetically encoded neural recording strategies have emerged as powerful tools to monitor brain activity directly with high spatiotemporal resolution.[18-21] Efforts in implantable electrodes have focused on monitoring electrical signals, such as action potentials, which travel along axons and are one major form of information processing in the brain.[22] With recent innovations in micro- and nanofabrication, materials science, and electrical engineering, implantable neural devices have become more sophisticated with increased densities of recording elements having decreased sizes. Recently, up to 1,024 recording units have been integrated into a single neuroprobe of <100 μm width.[23-29]

In addition to electrical signaling, chemical neurotransmission plays an equal or more important role in brain information processing.[1,2,30,31] However, fewer tools are available for investigating neurochemical transmission directly by monitoring rapid changes in neurotransmitter concentration *in vivo*.[32] Recent development in genetically coded indicators for neurotransmitters provided tools for imaging neurotransmitters with limited dynamic resolution.[33,34] Therefore, it is important to continue to develop sensing platforms to monitor

chemical signaling. To measure and to understand complex neurochemical fluxes in the brain, recording strategies must be able to monitor neurotransmitters with high selectivity and sensitivity in the appropriate physiological ranges, the necessary spatial and temporal resolution, and the ability to measure and to discriminate multiple neurotransmitters concurrently.

Recently, we developed aptamer field-effect transistor (FET) biosensors for small-molecule detection under high ionic strength conditions.[35-39] We used nanoscale In_2O_3 semiconducting films (~3 nm thick) as an ultrasensitive platform for biosensing. Aptamers, previously selected for specific target binding, were functionalized onto the semiconductor surface.[38] Conformational changes of the charged aptamer backbone occurred upon target capture, and the subsequent surface charge redistribution was detected by these sensors.[38] This sensing mechanism was independent of the charge or electrochemical properties of the analytes, and thus presents a promising approach for universal neurotransmitter monitoring.

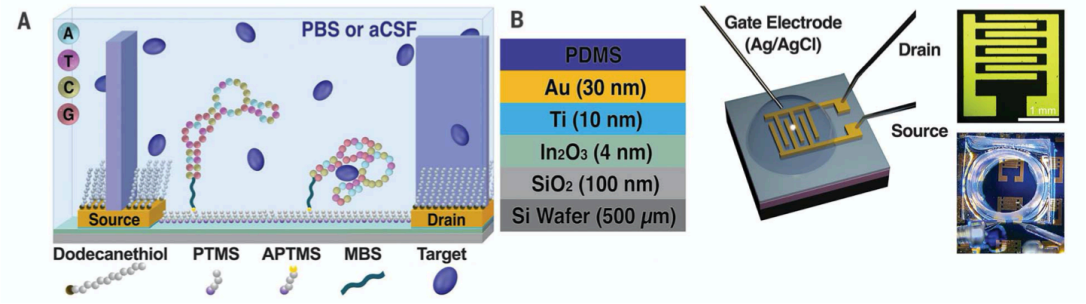

Figure 1.1. Aptamer field-effect transistor (FET) biosensors. (A) Schematic of FET surface chemistry. Trimethoxy(propyl)silane (PTMS); (3-aminopropyl)trimethoxysilane (APTMS); 3-maleimidobenzoic acid *N*-hydroxysuccinimide ester (MBS). (B) Layer-by-layer composition of FETs, FET microscope image, and photograph of experimental setup.

PDMS, polydimethylsiloxane. Reproduced with permission from *Science*. Copyright 2018, American Association for the Advancement of Science.

We demonstrated detection of a variety of biomarkers in complex physiological environments using aptamer-FETs, including serotonin, glucose, and phenylalanine.[35-38] Due to the high selectivity of the newly reported aptamers, aptamer-FET biosensors showed high selectivity against structurally similar molecules. We also reported the real-time and simultaneous detection of serotonin and dopamine using these aptamer-FET biosensors, which lays the foundation for multiplexed monitoring of neurotransmitters in the brain.[35] (Chapter 8)

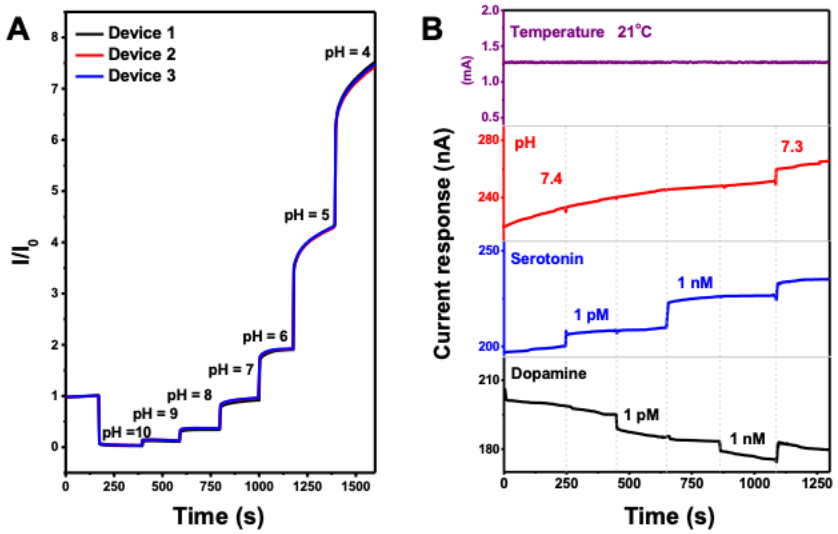

Figure 1.2. Multiplexed aptamer-field-effect transistors for biosensing. (A) Real-time pH sensing at unfunctionalized In_2O_3 nanoribbons in three different devices exposed to buffer solutions with pH values from 10 to 4. (B) Simultaneous sensing of temperature, pH, serotonin, and dopamine (pH = 7.4). Reproduced with permission from *iScience*. Copyright 2020, Elsevier.

To achieve *in vivo* neurotransmitter detection and neurotransmission monitoring, we focused on developing implantable FET neuroprobes. We designed, fabricated, and tested implantable aptamer FET neuroprobes to monitor small-molecule neurotransmitters (*i.e.*, serotonin) and validated device functionality *in vivo*. Micro-electro-mechanical-system (MEMS) technologies were used to produce neuroprobes in a high-throughput manner, where 150 probes were fabricated per Si wafer. These implantable neuroprobes showed high sensitivity to the neurotransmitter serotonin with fM to nM detection limits in physiological environments, making them promising candidates for other monoamine and amino acid neurotransmitter real-time monitoring in brain (Chapter 8).

To improve the interface between implanted devices and tissue, soft materials that yield readily to pressure and thus, more closely comply with the pliable nature of biological tissues were developed. Fabrication of electronic devices on substrates having low Young's moduli, *i.e.*, greater elasticity, compared with rigid substrates is hypothesized to reduce immunological responses after brain implantation.[40,41] Soft bioelectronics with capabilities to detect multiple neurotransmitters simultaneously and in real time are needed to investigate chemical information processing in brains,[30] particularly in the context of chronic neural recordings.[42] We have developed flexible multiplexed aptamer-field-effect transistor biosensors to monitor temperature, pH, serotonin, and dopamine simultaneously (Chapter 7).

In parallel with sensor development, I also advanced high-throughput, wafer-scale, and low-cost nanolithographic approaches to nanofabrication, which are at the core of these sensors. To meet demands for further advances, needs must be met for economical and high-throughput molecular patterning techniques to enable efficient nanofabrication. Conventional

photolithography methods cannot achieve robust nanoscale patterns as their resolutions are limited by optical and/or UV light sources and are prohibitively slow for large-area patterning. Additionally, current costs of state-of-the-art nanolithography tools, including parallel approaches (*e.g.,* extreme ultraviolet patterning,[43] and X-ray patterning[44]) and direct-write methods (*e.g.*, electron-beam lithography,[45,46] focused ion-beam milling,[47] and scanning probe lithography[48,49]), require highly specialized equipment and significant infrastructural investments that limit availability outside of large corporations, and academic and government research centers.

Several molecular patterning strategies have been developed as economical and accessible alternatives to conventional nanofabrication methods, including soft-lithographic microcontact printing (μCP),[50-53] replica molding,[54,55] nanoimprint lithography,[56] polymer pen lithography,[57-61] nanotransfer printing,[62] decal transfer printing,[63] and nanoskiving.[64] The most widely utilized of these methods, μCP, achieves micro- and nanoscale patterning of molecular "inks" (*e.g.,* alkanethiols[50-53] or biomolecules[65-67]) *via* stamps replica-molded from masters typically prepared by conventional photolithography. Some molecular inks (*e.g.,* alkanethiols) have been shown to serve as etch resists that enable the transfer of the desired patterns into the underlying substrates.[68,69]

The quality of the final patterns produced *via* μCP is limited by a variety of factors, including diffusion of molecular inks and/or the deformation of stamp features.[52,53,70] For example, lateral diffusion of ink molecules on surfaces results in enlarged features with lower contrast that can, in some cases, result in the complete loss of the transferred pattern.[52] This effect becomes even more significant when patterning sub-μm features, and often limits the resolution of μCP to ~100 nm. Several modified μCP approaches have been developed by our

groups to minimize or to eliminate lateral diffusion of ink molecules.[71-74] Microdisplacement printing[72,75] and microcontact insertion printing[71,76,77] were invented to print molecules on alkanethiol self-assembled monolayer (SAM)-modified substrates through displacement and insertion processes, respectively. The SAMs in the unpatterned regions prevent ink molecules from diffusing beyond the contact areas.[76,78] We also developed a subtractive molecular patterning method called chemical lift-off lithography (CLL) that effectively eliminates ink-molecule diffusion and is capable of high-fidelity patterning down to 20-nm linewidths.[69,74,79] Further refinements of CLL have achieved feature sizes down to ~15 nm.[73]

Inspired by the mechanical deformation of elastomers, I explored whether these methods could be leveraged further for nanoscale patterning. We developed (multiple) novel nanopatterning methods that utilize nanoscale deformation of elastomeric stamps, targeting ultrahigh resolution. In self-collapse lithography (SCL), nanoscale channels that form naturally at the edges of microscale relief features on elastomeric stamps were used to achieve large-scale nanoscale chemical patterns down to sub-30-nm scales (Chapter 2). This work also provided fundamental understanding of stamp collapse. In related work, we developed polymer-pen chemical lift-off lithography (PPCLL), where we utilized precisely controlled pyramidal and v-shaped polymer-pen arrays to enable large-scale patterning with resolution <50 nm.[80] Molecular patterns can serve as resists for nanostructure patterning. We used CLL to pattern Au micro- and nanostructures, including Au nanoribbon, disk, square, and circle arrays, and to pattern other metal and semiconductor surfaces.[37,81-83] (Chapter 3,4)

The unique optical and electronic properties and high surface-to-volume ratios of nanostructured materials form the basis for the development of next-generation sensors used in

environmental, biological, and chemical sensing applications. We designed a Au nanoplasmonic sensor platform fabricated using nanoribbon arrays, which demonstrated high plasmonic sensitivity (Chapter 3).[84] We adapted these materials for the detection of different classes of biomacromolecules, namely zwitterionic lipid vesicles and bovine serum albumin protein. The plasmonic properties of these two-dimensional Au nanostructures opened new opportunities for photothermal intracellular delivery, where our platform enabled the delivery of biomolecular cargo (*e.g.*, Calcein) through the plasma membrane into cells, with high delivery efficiencies and cell viabilities (Chapter 4).[85] We leveraged this patterning approach to produce wafer-scale one-dimensional semiconductor In_2O_3 nanoribbons for high-performance field-effect transistors (Chapter 5)[82] and highly sensitive biosensors (Chapter 6).[86]

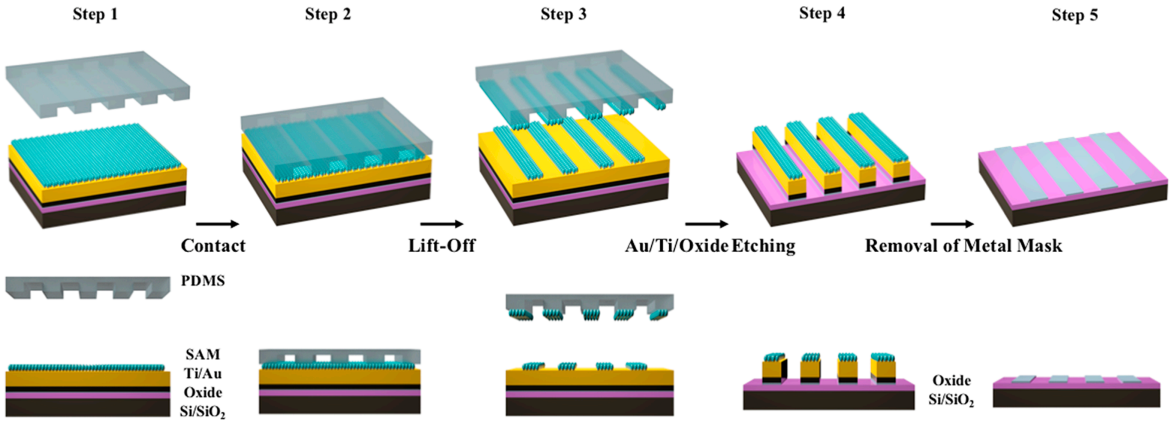

Figure 1.3. Fabrication scheme for producing In_2O_3 nanoribbons using chemical lift-off lithography. Step 1: A thin film of 3-nm In_2O_3 was deposited on a SiO_2/Si substrate *via* a sol-gel process followed by Au (30 nm)/Ti (10 nm) deposition and functionalization with a self-assembled monolayer (SAM). Step 2: A polydimethylsiloxane (PDMS) stamp, activated by an oxygen plasma, was brought into conformal contact with the substrate. Step 3: Upon lifting the stamp from the surface, SAM molecules in the contacted areas were removed, transferring the pattern (periodic lines and spaces) into the SAM. Step 4: Successive

selective etch processes removed Au/Ti and In_2O_3 layers from unprotected regions on the surface. Step 5: Remaining SAM, Au, and Ti were removed to produce In_2O_3 nanoribbon arrays. Reproduced with permission from *Nano Letters*. Copyright 2018, American Chemical Society.

Patterning of different materials other than Au, such as other coinage metal, transition metal, semiconductor, and metal oxide surfaces, represents unexplored areas of potential interest.[87-89] We demonstrated that CLL can be used as a technique to pattern a variety of substrates composed of coinage metals (Pt, Pd, Ag, Cu), transition metals (Ni, Ti, Al), and a semiconductor (Ge) using straightforward alkanethiolate self-assembly chemistry.[83]

In summary, I have developed scalable and low-cost nanofabrication techniques and multiple sensing platforms towards next-generation, ultrasensitive, nanoscale sensors enabled by these advanced nanofabrication techniques. I spent five years of my graduate career developing nanofabrication and nanoelectronics to advance our understanding of the brain. The biosensors developed by me and our groups foretell a revolution in the biomedicine community.

References

(1) Alivisatos, A. P.; Andrews, A. M.; Boyden, E. S.; Chun, M.; Church, G. M.; Deisseroth, K.; Donoghue, J. P.; Fraser, S. E.; Lippincott-Schwartz, J.; Looger, L. L.; Masmanidis, S.; McEuen, P. L.; Nurmikko, A. V.; Park, H.; Peterka, D. S.; Reid, C.; Roukes, M. L.; Scherer, A.; Schnitzer, M.; Sejnowski, T. J.; et al. Nanotools for Neuroscience and Brain Activity Mapping. *ACS Nano* **2013,** *7*, 1850–1866.

(2) Alivisatos, A. P.; Chun, M.; Church, G. M.; Deisseroth, K.; Donoghue, J. P.; Greenspan, R. J.; McEuen, P. L.; Roukes, M. L.; Sejnowski, T. J.; Weiss, P. S.; Yuste, R. The Brain Activity Map. *Science* **2013,** *339*, 1284–1285.

(3) Weiss, P. S. President Obama Announces the Brain Initiative. *ACS Nano* **2013,** *7*, 2873–2874.

(4) Liu, Z.; Qi, D.; Leow, W. R.; Yu, J.; Xiloyannnis, M.; Cappello, L.; Liu, Y.; Zhu, B.; Jiang, Y.; Chen, G.; Masia, L.; Liedberg, B.; Chen, X. 3D-Structured Stretchable Strain Sensors for out-of-Plane Force Detection. *Adv. Mater.* **2018,** *30*, e1707285.

(5) Gao, W.; Emaminejad, S.; Nyein, H. Y. Y.; Challa, S.; Chen, K.; Peck, A.; Fahad, H. M.; Ota, H.; Shiraki, H.; Kiriya, D.; Lien, D. H.; Brooks, G. A.; Davis, R. W.; Javey, A. Fully Integrated Wearable Sensor Arrays for Multiplexed *in Situ* Perspiration Analysis. *Nature* **2016,** *529*, 509–514.

(6) Kim, J.; Campbell, A. S.; de Avila, B. E.; Wang, J. Wearable Biosensors for Healthcare Monitoring. *Nat. Biotechnol.* **2019,** *37*, 389–406.

(7) Rogers, J.; Bao, Z.; Lee, T. W. Wearable Bioelectronics: Opportunities for Chemistry. *Acc. Chem. Res.* **2019,** *52*, 521–522.

(8) Biteen, J. S.; Blainey, P. C.; Cardon, Z. G.; Chun, M.; Church, G. M.; Dorrestein, P. C.; Fraser, S. E.; Gilbert, J. A.; Jansson, J. K.; Knight, R.; Miller, J. F.; Ozcan, A.; Prather, K. A.; Quake, S. R.; Ruby, E. G.; Silver, P. A.; Taha, S.; van den Engh, G.; Weiss, P. S.; Wong, G. C.; et al. Tools for the Microbiome: Nano and Beyond. *ACS Nano* **2016,** *10*, 6–37.

(9) Kim, D. H.; Viventi, J.; Amsden, J. J.; Xiao, J.; Vigeland, L.; Kim, Y. S.; Blanco, J. A.; Panilaitis, B.; Frechette, E. S.; Contreras, D.; Kaplan, D. L.; Omenetto, F. G.; Huang, Y.; Hwang, K. C.; Zakin, M. R.; Litt, B.; Rogers, J. A. Dissolvable Films of Silk Fibroin for Ultrathin Conformal Bio-Integrated Electronics. *Nat. Mater.* **2010,** *9*, 511–517.

(10) Minev, I. R.; Musienko, P.; Hirsch, A.; Barraud, Q.; Wenger, N.; Moraud, E. M.; Gandar, J.; Capogrosso, M.; Milekovic, T.; Asboth, L.; Torres, R. F.; Vachicouras, N.; Liu, Q.; Pavlova, N.; Duis, S.; Larmagnac, A.; Voros, J.; Micera, S.; Suo, Z.; Courtine, G.; et al. Electronic Dura Mater for Long-Term Multimodal Neural Interfaces. *Science* **2015,** *347*, 159–163.

(11) Wang, S.; Xu, J.; Wang, W.; Wang, G. N.; Rastak, R.; Molina-Lopez, F.; Chung, J. W.; Niu, S.; Feig, V. R.; Lopez, J.; Lei, T.; Kwon, S. K.; Kim, Y.; Foudeh, A. M.; Ehrlich, A.; Gasperini, A.; Yun, Y.; Murmann, B.; Tok, J. B.; Bao, Z. Skin Electronics from Scalable Fabrication of an Intrinsically Stretchable Transistor Array. *Nature* **2018,** *555*, 83–88.

(12) Rim, Y. S.; Bae, S. H.; Chen, H.; Yang, J. L.; Kim, J.; Andrews, A. M.; Weiss, P. S.; Yang, Y.; Tseng, H. R. Printable Ultrathin Metal Oxide Semiconductor-Based Conformal Biosensors. *ACS Nano* **2015,** *9*, 12174–12181.

(13) Luan, L.; Wei, X. L.; Zhao, Z. T.; Siegel, J. J.; Potnis, O.; Tuppen, C. A.; Lin, S. Q.; Kazmi, S.; Fowler, R. A.; Holloway, S.; Dunn, A. K.; Chitwood, R. A.; Xie, C. Ultraflexible Nanoelectronic Probes Form Reliable, Glial Scar-Free Neural Integration. *Sci. Adv.* **2017,** *3*, e1601966.

(14) Zhou, T.; Hong, G.; Fu, T. M.; Yang, X.; Schuhmann, T. G.; Viveros, R. D.; Lieber, C. M. Syringe-Injectable Mesh Electronics Integrate Seamlessly with Minimal Chronic Immune Response in the Brain. *Proc. Natl. Acad. Sci. U. S. A.* **2017,** *114*, 5894–5899.

(15) Rivnay, J.; Wang, H.; Fenno, L.; Deisseroth, K.; Malliaras, G. G. Next-Generation Probes, Particles, and Proteins for Neural Interfacing. *Sci. Adv.* **2017,** *3*, e1601649.

(16) Chen, R.; Canales, A.; Anikeeva, P. Neural Recording and Modulation Technologies. *Nat. Rev. Mater.* **2017,** *2*.

(17) Chapman, C. A. R.; Goshi, N.; Seker, E. Multifunctional Neural Interfaces for Closed-Loop Control of Neural Activity. *Adv. Funct. Mater.* **2018,** *28*, 1703523.

(18) Seymour, J. P.; Wu, F.; Wise, K. D.; Yoon, E. State-of-the-Art MEMS and Microsystem Tools for Brain Research. *Microsyst. Nanoeng.* **2017,** *3*, 16066.

(19) Won, S. M.; Song, E.; Zhao, J.; Li, J.; Rivnay, J.; Rogers, J. A. Recent Advances in Materials, Devices, and Systems for Neural Interfaces. *Adv. Mater.* **2018,** *30*, e1800534.

(20) Hochbaum, D. R.; Zhao, Y.; Farhi, S. L.; Klapoetke, N.; Werley, C. A.; Kapoor, V.; Zou, P.; Kralj, J. M.; Maclaurin, D.; Smedemark-Margulies, N.; Saulnier, J. L.; Boulting, G. L.; Straub, C.; Cho, Y. K.; Melkonian, M.; Wong, G. K.; Harrison, D. J.; Murthy, V. N.; Sabatini, B. L.; Boyden, E. S.; et al. All-Optical Electrophysiology in Mammalian Neurons Using Engineered Microbial Rhodopsins. *Nat. Methods* **2014,** *11*, 825–833.

(21) Vogt, N. Voltage Imaging in vivo. *Nat Methods* **2019,** *16*, 573.

(22) Scanziani, M.; Hausser, M. Electrophysiology in the Age of Light. *Nature* **2009,** *461*, 930–939.

(23) Du, J.; Blanche, T. J.; Harrison, R. R.; Lester, H. A.; Masmanidis, S. C. Multiplexed, High Density Electrophysiology with Nanofabricated Neural Probes. *PLoS One* **2011,** *6*, e26204.

(24) Rios, G.; Lubenov, E. V.; Chi, D.; Roukes, M. L.; Siapas, A. G. Nanofabricated Neural Probes for Dense 3-D Recordings of Brain Activity. *Nano Lett.* **2016,** *16*, 6857–6862.

(25) Jun, J. J.; Steinmetz, N. A.; Siegle, J. H.; Denman, D. J.; Bauza, M.; Barbarits, B.; Lee, A. K.; Anastassiou, C. A.; Andrei, A.; Aydin, C.; Barbic, M.; Blanche, T. J.; Bonin, V.; Couto, J.; Dutta, B.; Gratiy, S. L.; Gutnisky, D. A.; Hausser, M.; Karsh, B.; Ledochowitsch, P.; et al. Fully Integrated Silicon Probes for High-Density Recording of Neural Activity. *Nature* **2017,** *551*, 232–236.

(26) Driscoll, N.; Richardson, A. G.; Maleski, K.; Anasori, B.; Adewole, O.; Lelyukh, P.; Escobedo, L.; Cullen, D. K.; Lucas, T. H.; Gogotsi, Y.; Vitale, F. Two-Dimensional Ti_3C_2 Mxene for High-Resolution Neural Interfaces. *ACS Nano* **2018,** *12*, 10419–10429.

(27) Jiang, Y.; Li, X.; Liu, B.; Yi, J.; Fang, Y.; Shi, F.; Gao, X.; Sudzilovsky, E.; Parameswaran, R.; Koehler, K.; Nair, V.; Yue, J.; Guo, K.; Tsai, H.-M.; Freyermuth, G.; Wong, R. C. S.; Kao, C.-M.; Chen, C.-T.; Nicholls, A. W.; Wu, X.; et al. Rational Design of Silicon Structures for Optically Controlled Multiscale Biointerfaces. *Nat. Biomed. Eng.* **2018,** *2*, 508–521.

(28) Hong, G.; Fu, T. M.; Qiao, M.; Viveros, R. D.; Yang, X.; Zhou, T.; Lee, J. M.; Park, H. G.; Sanes, J. R.; Lieber, C. M. A Method for Single-Neuron Chronic Recording from the Retina in Awake Mice. *Science* **2018,** *360*, 1447–1451.

(29) Venton, B. J.; Cao, Q. Fundamentals of Fast-Scan Cyclic Voltammetry for Dopamine Detection. *Analyst* **2020,** *145*, 1158–1168.

(30) Andrews, A. M. The Brain Initiative: Toward a Chemical Connectome. *ACS Chem. Neurosci*. **2013,** *4*, 645.

(31) Andrews, A. M.; Schepartz, A.; Sweedler, J. V.; Weiss, P. S. Chemistry and the Brain Initiative. *J. Am. Chem. Soc*. **2014,** *136*, 1–2.

(32) Scida, K.; Plaxco, K. W.; Jamieson, B. G. High Frequency, Real-Time Neurochemical and Neuropharmacological Measurements in Situ in the Living Body. *Transl. Res*. **2019,** *213*, 50–66.

(33) Sabatini, B. L.; Tian, L. Imaging Neurotransmitter and Neuromodulator Dynamics in Vivo with Genetically Encoded Indicators. *Neuron* **2020,** *108*, 17-32.

(34) Sun, F.; Zeng, J.; Jing, M.; Zhou, J.; Feng, J.; Owen, S. F.; Luo, Y.; Li, F.; Wang, H.; Yamaguchi, T.; Yong, Z.; Gao, Y.; Peng, W.; Wang, L.; Zhang, S.; Du, J.; Lin, D.; Xu, M.; Kreitzer, A. C.; Cui, G.; et al. A Genetically Encoded Fluorescent Sensor Enables Rapid and Specific Detection of Dopamine in Flies, Fish, and Mice. *Cell* **2018,** *174*, 481-496 e419.

(35) Liu, Q.; Zhao, C.; Chen, M.; Liu, Y.; Zhao, Z.; Wu, F.; Li, Z.; Weiss, P. S.; Andrews, A. M.; Zhou, C. Flexible Multiplexed In_2O_3 Nanoribbon Aptamer-Field-Effect Transistors for Biosensing. *iScience* **2020,** *23*, 101469.

(36) Cheung, K. M.; Yang, K. A.; Nakatsuka, N.; Zhao, C.; Ye, M.; Jung, M. E.; Yang, H.; Weiss, P. S.; Stojanovic, M. N.; Andrews, A. M. Phenylalanine Monitoring *via* Aptamer-Field-Effect Transistor Sensors. *ACS Sens*. **2019,** *4*, 3308–3317.

(37) Kim, J.; Rim, Y. S.; Chen, H.; Cao, H. H.; Nakatsuka, N.; Hinton, H. L.; Zhao, C.; Andrews, A. M.; Yang, Y.; Weiss, P. S. Fabrication of High-Performance Ultrathin In_2O_3 Film Field-Effect Transistors and Biosensors Using Chemical Lift-Off Lithography. *ACS Nano* **2015,** *9*, 4572–4582.

(38) Nakatsuka, N.; Yang, K. A.; Abendroth, J. M.; Cheung, K. M.; Xu, X.; Yang, H.; Zhao, C.; Zhu, B.; Rim, Y. S.; Yang, Y.; Weiss, P. S.; Stojanovic, M. N.; Andrews, A. M. Aptamer-Field-Effect Transistors Overcome Debye Length Limitations for Small-Molecule Sensing. *Science* **2018,** *362*, 319–324.

(39) Cheung, K. M.; Abendroth, J. M.; Nakatsuka, N.; Zhu, B.; Yang, Y.; Andrews, A. M.; Weiss, P. S. Detecting DNA and RNA and Differentiating Single-Nucleotide Variations *via* Field-Effect Transistors. *Nano Lett*. **2020,** *20*, 5982–5990.

(40) Kozai, T. D.; Jaquins-Gerstl, A. S.; Vazquez, A. L.; Michael, A. C.; Cui, X. T. Brain Tissue Responses to Neural Implants Impact Signal Sensitivity and Intervention Strategies. *ACS Chem. Neurosci*. **2015,** *6*, 48–67.

(41) Gunasekera, B.; Saxena, T.; Bellamkonda, R.; Karumbaiah, L. Intracortical Recording Interfaces: Current Challenges to Chronic Recording Function. *ACS Chem. Neurosci*. **2015,** *6*, 68–83.

(42) Du, Z. J.; Kolarcik, C. L.; Kozai, T. D. Y.; Luebben, S. D.; Sapp, S. A.; Zheng, X. S.; Nabity, J. A.; Cui, X. T. Ultrasoft Microwire Neural Electrodes Improve Chronic Tissue Integration. *Acta Biomater*. **2017,** *53*, 46–58.

(43) Wagner, C.; Harned, N. EUV Lithography: Lithography Gets Extreme. *Nat. Photonics* **2010,** *4*, 24–26.

(44) Miszta, K.; Greullet, F.; Marras, S.; Prato, M.; Toma, A.; Arciniegas, M.; Manna, L.; Krahne, R. Nanocrystal Film Patterning by Inhibiting Cation Exchange *via* Electron-Beam or X-Ray Lithography. *Nano Lett*. **2014,** *14*, 2116–2122.

(45) Manfrinato, V. R.; Wen, J.; Zhang, L.; Yang, Y.; Hobbs, R. G.; Baker, B.; Su, D.; Zakharov, D.; Zaluzec, N. J.; Miller, D. J.; Stach, E. A.; Berggren, K. K. Determining the Resolution Limits of Electron-Beam Lithography: Direct Measurement of the Point-Spread Function. *Nano Lett*. **2014,** *14*, 4406–4412.

(46) Bat, E.; Lee, J.; Lau, U. Y.; Maynard, H. D. Trehalose Glycopolymer Resists Allow Direct Writing of Protein Patterns by Electron-Beam Lithography. *Nat. Commun*. **2015,** *6*, 6654.

(47) Volkert, C. A.; Minor, A. M. Focused Ion Beam Microscopy and Micromachining. *MRS Bull*. **2011,** *32*, 389–399.

(48) Xu, S.; Liu, G. Y. Nanometer-Scale Fabrication by Simultaneous Nanoshaving and Molecular Self-Assembly. *Langmuir* **1997,** *13*, 127–129.

(49) Piner, R. D.; Zhu, J.; Xu, F.; Hong, S. H.; Mirkin, C. A. "Dip-Pen" Nanolithography. *Science* **1999,** *283*, 661–663.

(50) Kumar, A.; Whitesides, G. M. Features of Gold Having Micrometer to Centimeter Dimensions Can Be Formed through a Combination of Stamping with an Elastomeric Stamp and an Alkanethiol ‘‘Ink’’ Followed by Chemical Etching. *Appl. Phys. Lett.* **1993,** *63*, 2002–2004.

(51) Xia, Y.; Whitesides, G. M. Soft Lithography. *Angew. Chem. Int. Ed.* **1998,** *37*, 550–575.

(52) Srinivasan, C.; Mullen, T. J.; Hohman, J. N.; Anderson, M. E.; Dameron, A. A.; Andrews, A. M.; Dickey, E. C.; Horn, M. W.; Weiss, P. S. Scanning Electron Microscopy of Nanoscale Chemical Patterns. *ACS Nano* **2007,** *1*, 191–201.

(53) Qin, D.; Xia, Y.; Whitesides, G. M. Soft Lithography for Micro- and Nanoscale Patterning. *Nat. Protoc.* **2010,** *5*, 491–502.

(54) Xia, Y. N.; McClelland, J. J.; Gupta, R.; Qin, D.; Zhao, X. M.; Sohn, L. L.; Celotta, R. J.; Whitesides, G. M. Replica Molding Using Polymeric Materials: A Practical Step toward Nanomanufacturing. *Adv. Mater.* **1997,** *9*, 147–149.

(55) Tian, C.; Kim, H.; Sun, W.; Kim, Y.; Yin, P.; Liu, H. DNA Nanostructures-Mediated Molecular Imprinting Lithography. *ACS Nano* **2017,** *11*, 227–238.

(56) Chou, S. Y.; Krauss, P. R.; Renstrom, P. J. Imprint Lithography with 25-Nanometer Resolution. *Science* **1996,** *272*, 85–87.

(57) Huo, F.; Zheng, Z.; Zheng, G.; Giam, L. R.; Zhang, H.; Mirkin, C. A. Polymer Pen Lithography. *Science* **2008,** *321*, 1658–1660.

(58) Shim, W.; Braunschweig, A. B.; Liao, X.; Chai, J.; Lim, J. K.; Zheng, G.; Mirkin, C. A. Hard-Tip, Soft-Spring Lithography. *Nature* **2011,** *469*, 516–520.

(59) Zhong, X.; Bailey, N. A.; Schesing, K. B.; Bian, S.; Campos, L. M.; Braunschweig, A. B. Materials for the Preparation of Polymer Pen Lithography Tip Arrays and a Comparison of Their Printing Properties. *J. Polym. Sci. A: Polym. Chem.* **2013,** *51*, 1533–1539.

(60) Liao, X.; Huang, Y.-K.; Mirkin, C. A.; Dravid, V. P. High Throughput Synthesis of Multifunctional Oxide Nanostructures within Nanoreactors Defined by Beam Pen Lithography. *ACS Nano* **2017,** *11*, 4439–4444.

(61) Xue, Y.; Kang, D.; Ma, Y.; Feng, X.; Rogers, J. A.; Huang, Y. Collapse of Microfluidic Channels/Reservoirs in Thin, Soft Epidermal Devices. *Extreme Mech. Lett.* **2017**, 18–23.

(62) Jeon, S.; Menard, E.; Park, J. U.; Maria, J.; Meitl, M.; Zaumseil, J.; Rogers, J. A. Three-Dimensional Nanofabrication with Rubber Stamps and Conformable Photomasks. *Adv. Mater.* **2004,** *16*, 1369–1373.

(63) Childs, W. R.; Nuzzo, R. G. Decal Transfer Microlithography: A New Soft-Lithographic Patterning Method. *J. Am. Chem. Soc.* **2002,** *124*, 13583–13596.

(64) Xu, Q. B.; Rioux, R. M.; Dickey, M. D.; Whitesides, G. M. Nanoskiving: A New Method to Produce Arrays of Nanostructures. *Acc. Chem. Res.* **2008,** *41*, 1566–1577.

(65) James, C. D.; Davis, R. C.; Kam, L.; Craighead, H. G.; Isaacson, M.; Turner, J. N.; Shain, W. Patterned Protein Layers on Solid Substrates by Thin Stamp Microcontact Printing. *Langmuir* **1998,** *14*, 741–744.

(66) Bernard, A.; Renault, J. P.; Michel, B.; Bosshard, H. R.; Delamarche, E. Microcontact Printing of Proteins. *Adv. Mater.* **2000,** *12*, 1067–1070.

(67) Vaish, A.; Shuster, M. J.; Cheunkar, S.; Weiss, P. S.; Andrews, A. M. Tuning Stamp Surface Energy for Soft Lithography of Polar Molecules to Fabricate Bioactive Small-Molecule Microarrays. *Small* **2011,** *7*, 1471–1479.

(68) Xia, Y.; Zhao, X.-M.; Kim, E.; Whitesides, G. M. A Selective Etching Solution for Use with Patterned Self-Assembled Monolayers of Alkanethiolates on Gold. *Chem. Mater.* **1995,** *7*, 2332–2337.

(69) Kim, J.; Rim, Y. S.; Chen, H.; Cao, H. H.; Nakatsuka, N.; Hinton, H. L.; Zhao, C.; Andrews, A. M.; Yang, Y.; Weiss, P. S. Fabrication of High-Performance Ultrathin In_2O_3 Film Field-Effect Transistors and Biosensors Using Chemical Lift-Off Lithography. *ACS Nano* **2015,** *9*, 4572–4582.

(70) Delamarche, E.; Schmid, H.; Bietsch, A.; Larsen, N. B.; Rothuizen, H.; Michel, B.; Biebuyck, H. Transport Mechanisms of Alkanethiols During Microcontact Printing on Gold. *J. Phys. Chem. B* **1998,** *102*, 3324–3334.

(71) Mullen, T. J.; Srinivasan, C.; Hohman, J. N.; Gillmor, S. D.; Shuster, M. J.; Horn, M. W.; Andrews, A. M.; Weiss, P. S. Microcontact Insertion Printing. *Appl. Phys. Lett.* **2007,** *90*, 063114.

(72) Dameron, A. A.; Hampton, J. R.; Smith, R. K.; Mullen, T. J.; Gillmor, S. D.; Weiss, P. S. Microdisplacement Printing. *Nano Lett.* **2005,** *5*, 1834–1837.

(73) Andrews, A. M.; Liao, W.-S.; Weiss, P. S. Double-Sided Opportunities Using Chemical Lift-Off Lithography. *Acc. Chem. Res.* **2016,** *49*, 1449–1457.

(74) Liao, W.-S.; Cheunkar, S.; Cao, H. H.; Bednar, H. R.; Weiss, P. S.; Andrews, A. M. Subtractive Patterning *via* Chemical Lift-Off Lithography. *Science* **2012,** *337*, 1517–1521.

(75) Saavedra, H. M.; Mullen, T. J.; Zhang, P. P.; Dewey, D. C.; Claridge, S. A.; Weiss, P. S. Hybrid Strategies in Nanolithography. *Rep. Prog. Phys.* **2010,** *73*, 036501.

(76) Srinivasan, C.; Mullen, T. J.; Hohman, J. N.; Anderson, M. E.; Dameron, A. A.; Andrews, A. M.; Dickey, E. C.; Horn, M. W.; Weiss, P. S. Scanning Electron Microscopy of Nanoscale Chemical Patterns. *ACS Nano* **2007,** *1*, 191-201.

(77) Shuster, M. J.; Vaish, A.; Cao, H. H.; Guttentag, A. I.; McManigle, J. E.; Gibb, A. L.; Martinez, M. M.; Nezarati, R. M.; Hinds, J. M.; Liao, W. S.; Weiss, P. S.; Andrews, A. M. Patterning Small-Molecule Biocapture Surfaces: Microcontact Insertion Printing *vs.* Photolithography. *Chem. Comm.* **2011,** *47*, 10641–10643.

(78) Claridge, S. A.; Liao, W. S.; Thomas, J. C.; Zhao, Y.; Cao, H. H.; Cheunkar, S.; Serino, A. C.; Andrews, A. M.; Weiss, P. S. From the Bottom Up: Dimensional Control and Characterization in Molecular Monolayers. *Chem. Soc. Rev.* **2013,** *42*, 2725–2745.

(79) Cao, H. H.; Nakatsuka, N.; Serino, A. C.; Liao, W.-S.; Cheunkar, S.; Yang, H.; Weiss, P. S.; Andrews, A. M. Controlled DNA Patterning by Chemical Lift-Off Lithography: Matrix Matters. *ACS Nano* **2015,** *9*, 11439–11454.

(80) Xu, X.; Yang, Q.; Cheung, K. M.; Zhao, C.; Wattanatorn, N.; Belling, J. N.; Abendroth, J. M.; Slaughter, L. S.; Mirkin, C. A.; Andrews, A. M.; Weiss, P. S. Polymer-Pen Chemical Lift-Off Lithography. *Nano Lett.* **2017,** *17*, 3302–3311.

(81) Zhao, C.; Xu, X.; Yang, Q.; Man, T.; Jonas, S. J.; Schwartz, J. J.; Andrews, A. M.; Weiss, P. S. Self-Collapse Lithography. *Nano Lett*. **2017,** *17*, 5035–5042.

(82) Zhao, C.; Xu, X.; Bae, S. H.; Yang, Q.; Liu, W.; Belling, J. N.; Cheung, K. M.; Rim, Y. S.; Yang, Y.; Andrews, A. M.; Weiss, P. S. Large-Area, Ultrathin Metal-Oxide Semiconductor Nanoribbon Arrays Fabricated by Chemical Lift-Off Lithography. *Nano Lett*. **2018,** *18*, 5590–5595.

(83) Cheung, K. M.; Stemer, D. M.; Zhao, C.; Young, T. D.; Belling, J. N.; Andrews, A. M.; Weiss, P. S. Chemical Lift-Off Lithography of Metal and Semiconductor Surfaces. *ACS Mater*. *Lett*. **2019,** *2*, 76–83.

(84) Zhao, C.; Xu, X.; Ferhan, A. R.; Chiang, N.; Jackman, J. A.; Yang, Q.; Liu, W.; Andrews, A. M.; Cho, N. J.; Weiss, P. S. Scalable Fabrication of Quasi-One-Dimensional Gold Nanoribbons for Plasmonic Sensing. *Nano Lett*. **2020,** *20*, 1747–1754.

(85) Zhao, C.; Man, T.; Xu, X.; Yang, Q.; Liu, W.; Jonas, S. J.; Teitell, M. A.; Chiou, P.-Y.; Weiss, P. S. Photothermal Intracellular Delivery Using Gold Nanodisk Arrays. *ACS Mater*. *Lett*. **2020,** *2*, 1475–1483.

(86) Zhao, C.; Liu, Q.; Cheung, K. M.; Liu, W.; Yang, Q.; Xu, X.; Weiss, P. S.; Zhou, C.; Andrews, A. M. Narrower Nanoribbon Biosensors Fabricated by Chemcial Lift-Off Lithography Show Higher Sensitivity. *ACS Nano* **2020**, in revision.

(87) Liao, W.-S.; Cheunkar, S.; Cao, H. H.; Bednar, H. R.; Weiss, P. S.; Andrews, A. M. Subtractive Patterning *via* Chemical Lift-Off Lithography. *Science* **2012,** *337*, 1517–1521.

(88) Kim, E.; Park, K.; Hwang, S. Electrochemical Investigation of Chemical Lift-Off Lithography on Au and ITO. *Electrochim. Acta* **2017,** *246*, 165–172.

(89) Nguyen, H. M.; Park, K.; Hwang, S. The Effect of an Antigalvanic Reduction of Silver on Gold for the Stability of a Self-Assembled Alkanethiol Monolayer and Chemical Lift-Off Lithography. *J. Phys. Chem. C* **2018,** *122*, 16070–16078.

Chapter 2

Self-Collapse Lithography

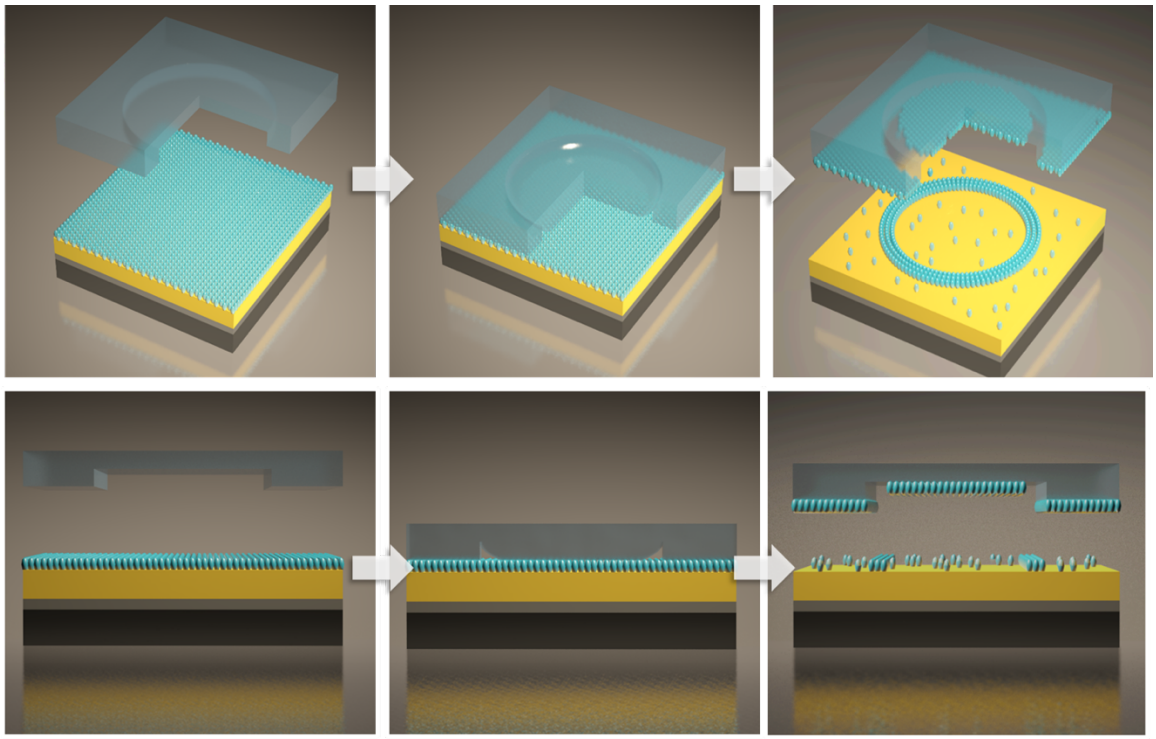

The information in this chapter is reprinted with permission from

Nano Lett. **2017**, *17*, 5035–5042. Copyright (2017) American Chemical Society

Authors: **Zhao, C.**; Xu, X.; Yang, Q.; Man, T.; Jonas, S. J.; Schwartz, J. J.;

Andrews, A. M.; Weiss, P. S.

2.1 Abstract

We report a facile, high-throughput soft lithography process that utilizes nanoscale channels formed naturally at the edges of microscale relief features on soft, elastomeric stamps. Upon contact with self-assembled monolayer (SAM) functionalized substrates, the roof of the stamp collapses, resulting in the selective removal of SAM molecules *via* a chemical lift-off process. With this technique, which we call self-collapse lithography (SCL), sub-30-nm patterns were achieved readily using masters with microscale features prepared by conventional photolithography. The feature sizes of the chemical patterns can be varied continuously from ~2 μm to below 30 nm by decreasing stamp relief heights from 1 μm to 50 nm. Likewise, for fixed relief heights, reducing the stamp Young's modulus from ~2.0 to ~0.8 MPa resulted in shrinking the features of resulting patterns from ~400 to ~100 nm. The self-collapse mechanism was studied using finite element simulation methods to model the competition between adhesion and restoring stresses during patterning. These results correlate well with the experimental data and reveal the relationship between the linewidths, channel heights, and Young's moduli of the stamps. In addition, SCL was applied to pattern two-dimensional arrays of circles and squares. These chemical patterns served as resists during etching processes to transfer patterns to the underlying materials (*e.g.,* gold nanostructures). This work provides new insights into the natural propensity of elastomeric stamps to self-collapse and demonstrates a means of exploiting this behavior to achieve patterning *via* nanoscale chemical lift-off lithography.

2.2 Introduction

The rapid development of new and more complex nanoscale technologies, including those in electronics,[1-4] displays and lighting,[5-8] nanofluidics,[9,10] wearable and flexible sensors,[3,11-13] ultrasensitive biosensors,[14-17] and medical devices[18-21] is transforming modern life. To meet demands for further advances in these areas, needs must be met for economical and high-throughput molecular patterning techniques to enable efficient nanofabrication. Conventional photolithography methods cannot achieve robust nanoscale patterns as their resolutions are limited by optical and/or UV light sources and are prohibitively slow for large-area patterning. Additionally, current costs of state-of-the-art nanolithography tools, including parallel approaches (*e.g.,* extreme ultraviolet patterning,[22] and X-ray patterning[23]) and direct-write methods (*e.g.*, electron-beam lithography,[24,25] focused ion-beam milling,[26] and scanning probe lithography[27,28]), require highly specialized equipment and significant infrastructural investments that limit availability outside of large corporations, and academic and government research centers.

Several molecular patterning strategies have been developed as economical and accessible alternatives to conventional nanofabrication methods, including soft lithographic microcontact printing (μCP),[29-32] replica molding,[33,34] nanoimprint lithography,[35] polymer pen lithography,[36-40] nanotransfer printing,[41] decal transfer printing,[42] and nanoskiving.[43] The most widely utilized of these methods, μCP, achieves micro- and nanoscale patterning of molecular "inks" (*e.g.,* alkanethiols[29-32] or biomolecules[44-46]) *via* stamps replica-molded from masters prepared by conventional photolithography. Some molecular inks (*e.g.,* alkanethiols) have been shown to serve as etch resists that enable the transfer of the desired patterns into the underlying substrates.[14,47]

The quality of the final patterns produced *via* μCP is limited by a variety of factors, including diffusion of molecular inks and/or the deformation of stamp features.[31,32,48] For example, lateral diffusion of ink molecules on surfaces results in enlarged features with lower contrast that can, in some cases, results in the complete loss of the transferred pattern.[31] This effect becomes even more significant when patterning sub-μm features, and often limits the resolution of μCP to ~100 nm. Several modified μCP approaches have been developed by our group to minimize or to eliminate lateral diffusion of ink molecules.[49-52] Microdisplacement printing[50,53] and microcontact insertion printing[49,54,55] were invented to print molecules on alkanethiol self-assembled monolayer (SAM) modified substrates through displacement or insertion processes, respectively. The SAMs in the unpatterned regions prevent ink molecules from diffusing beyond the contact areas.[54,56] We also developed a subtractive molecular patterning method called chemical lift-off lithography (CLL) that effectively eliminates ink-molecule diffusion and is capable of high-fidelity patterning down to 20-nm linewidths.[14,52,57] Further refinements of CLL have achieved feature sizes down to ~5 nm.[51]

In addition to lateral diffusion, the accuracy of transferred patterns can also be affected adversely by deformations of stamps upon physical contact with substrates during μCP (*e.g.,* mechanical sagging, sliding, and/or compression of stamp features).[32,58-60] For example, when an external load is applied to a polydimethylsiloxane (PDMS) stamp, the relief features sag causing the roof of the stamp to collapse and to contact the substrate. Recent studies demonstrated that this roof-collapse phenomenon could occur spontaneously even without the application of an external load when the aspect ratio of the stamp features was engineered to be sufficiently large.[58-60] This "self-collapsing" behavior occurs due to the adhesion force between the stamp and substrate. Several groups, including Rogers, Huang, and coworkers have

investigated stamp designs that minimize self-collapse, which include tailoring feature aspect ratios, adhesion energy, and Young's modulus.[40,61-63] While seen initially as a disadvantage for pattern reproduction, other groups, including Erickson and colleagues have harnessed self-collapse for the fabrication of 60-nm nanofluidic channels from microchannels under controlled loads.[64,65] We have also exploited this phenomenon for precise control of patterns using polymer-pen arrays and integral supporting structures.[40] However, to the best of our knowledge, self-collapse has not been specifically exploited for nanolithography.

Here, we report control of self-collapse behavior of PDMS stamps precisely at the nanoscale when integrated with CLL to establish a new nanolithography method—self-collapse lithography (SCL). Using SCL, we achieve sub-30 nm features by tailoring the dimensions of the stamp features, as well as the stiffness of the PDMS.

2.3 Materials and Methods

Materials. Prime quality 4″ Si(100) wafers (P/B, 1-10 Ω-cm) were purchased from University Wafer Inc. (Boston, MA, USA). Sylgard 184® silicone elastomer kits (lot # 0008823745) were purchased from Ellsworth Adhesives (Germantown, WI, USA). All other chemicals were purchased from Sigma-Aldrich (St. Louis, MO, USA) and used as received. The SPR 700-1.2 photoresist and MF-26A developer were obtained from the Integrated Systems Nanofabrication Cleanroom (ISNC) at UCLA.

Characterization. Scanning electron microscopy (SEM) images were obtained using a Zeiss Supra 40VP scanning electron microscope with an Inlens SE Detector (Inlens secondary electron detector). Optical images were taken with a Zeiss Axiotech optical microscope.

Growth of SiO_2 on Si (100). A 1-μm SiO_2 film was thermally grown on Si(100) wafers. If needed, SiO_2/Si wafers are also available for purchase elsewhere.

Photolithography. Photomasks were designed using the AutoCAD software suite (Autodesk, Inc.) with patterns consisting of two-dimensional (2D) arrays of lines, circles, or squares. The linewidths of the feature investigated here were >2 μm and thus, were fabricated by conventional photolithography. Positive photoresist SPR700-1.2 was spin-coated on SiO_2/Si wafer surfaces, followed by a 90-s soft bake at 90 °C on a hotplate. A Karl Suss contact aligner was used to expose the photoresist on the wafer with the pattern from a photomask with an optimal exposure time of 16.5 s (UV wavelength = 365 nm, intensity = 8.5 mW/cm^2). Each exposed wafer was post-exposure baked at 110 °C for 90 s, immersed in MF-26A developer for 1 min, rinsed with deionized water, and blown dry with N_2 gas.

Reactive ion etching (RIE) of SiO_2. After patterning by photolithography, the exposed SiO_2 was selectively etched by RIE (Oxford 80 Plus) with a gas mixture of CHF_3 (25 sccm) and Ar (25 sccm) at 35 mTorr. Channel heights were tuned by varying the etch times. A Dektak profilometer was used to confirm the heights of the etched features. Once the desired channel height was obtained, the remaining photoresist was removed from each surface using a Matrix Asher or dissolved using acetone. The molds were then coated with silane (trichloro(1H,1H,2H,2H-perfluorooctyl)silane) as a release layer.

Preparation of PDMS stamps. The Young's modulus of polydimethylsiloxane (PDMS) was tuned by varying the mass ratio of the Sylgard® 184 elastomer silicone elastomer base and curing agent at 5:1, 10:1, 15:1, or 20:1 ratios. Base and curing agent were thoroughly mixed. The mixture was poured into a petri dish containing the Si masters and then degassed in a vacuum

desiccator and cured overnight at 65 °C. Afterwards, PDMS stamps were carefully removed from the Si masters.

Surface functionalization of Au/Ti/Si substrate for self-collapse lithography. The 10-nm Ti and 30-nm Au films were deposited on clean silicon wafers with a CHA Solution E-Beam Evaporator at high vacuum (10^{-8} Torr) at an evaporation rate of 0.1 nm/s. The Au/Ti/Si wafers were annealed in a hydrogen flame for ~10 s to create Au(111) surfaces and then immersed into 1 mM 11-mercapto-1-undecanol ethanolic solution overnight for self-assembled monolayer formation on the Au surfaces.

Activation of PDMS stamps. Clean PDMS stamps were treated in oxygen plasma (Harrick Plasma, Ithaca, NY) for 40 s at a power of 18 W and a pressure of 10 psi to generate hydrophilic surfaces.

Contact and removal of stamps. A pair of tweezers was used to place each PDMS stamp on a substrate without applying a compression force. In the stamp removal process, one pair of tweezers was used to hold the substrate and another pair was used to lift off the stamp. In the future, more precise control can be achieved by coupling the stamp to a scanning stage system.

Estimate of the Young's modulus of PDMS stamps. The Young's modulus of PDMS stamps prepared using a 10:1 ratio (X:Y) of Sylgard 184 pre-polymer base (X) and curing agent (Y) is approximately 1.75 MPa (cured at 65 °C). The Young's moduli of PDMS cast from different ratios of X:Y were estimated based on previously reported values,[66,67] where stamps used in the present study were 2.0 MPa (5:1), 1.15 MPa (15:1), and 0.85 MPa (20:1).

Error analyses. The errors in linewidths were based on 10 measurements of the patterned molecules on three different PDMS stamps. The three PDMS stamps were prepared using one silicon master for a fixed height. The errors in the heights originate from the RIE process and were determined by five measurements at different locations on the same substrate. The errors in heights were determined to be 100 ± 15 nm, 200 ± 10 nm, 300 ± 20 nm, 400 ± 25 nm, 500 ± 10 nm for heights under 500 nm. The errors in widths were determined to be within 10%, measured over five lines on the same substrate, which is not critical for this study, as described in the manuscript.

Wet etching. After PDMS stamps were lifted-off from SAM-modified substrates, each substrate was immersed into an aqueous solution of 20 mM iron nitrate and 30 mM thiourea to etch Au films selectively.[14] The etching rate was ~1 nm/min and the samples were put into the etching solution for 30 min. After 30 min of etching, the substrates were rinsed with DI water and blown dry with a N_2 gun.

2.4. Results and Discussions

A typical SCL process is illustrated in **Figure 2.1**. Step 1, a Au (30 nm)/Ti (10 nm)/Si substrate is immersed into a hydroxyl-terminated alkanethiol solution (1 mM 11-mercapto-1-undecanol in ethanol) for ~12 h to form a self-assembled monolayer (SAM) on the Au surface. Next, a PDMS stamp with the desired pattern is "activated" by exposure to oxygen plasma for 40 s, which generates hydrophilic silanol (—Si-OH) groups on the stamp surface. Step 2, an activated stamp is placed in conformal contact with the SAM-functionalized Au surface without an externally applied load. The Au surface is flame annealed before functionalization. The surface roughness is ~1 nm, which is necessary for the subsequent high-resolution chemical patterning. Self-collapse of the stamp's recessed features occurs

spontaneously due to adhesion forces between the PDMS and the SAM on the Au surface. As the self-collapsing regions of the stamp, as well as the stamp protruding features contact the surface, covalent bonds form *via* condensation reactions between the -OH moieties of the SAM and the silanol groups of the activated PDMS stamp.[47] Upon lifting the PDMS stamp off the substrate (Step 3), alkanethiol molecules are removed selectively from the Au surface in the stamp-contact regions, leaving intact SAMs in the non-contacted areas. As observed in CLL, Au atoms are also removed during lift-off as the Au-S bonds between alkanethiol adsorbates and Au surface atoms are stronger than Au-Au bonds at the surface of the substrate.[51,52] Note that as discovered in our previous work and shown in **Figure 2.1c,f**, not all of the molecules in the contact regions are removed in the CCL process (and the remaining molecules can form a matrix for controlled chemical patterning).[57]

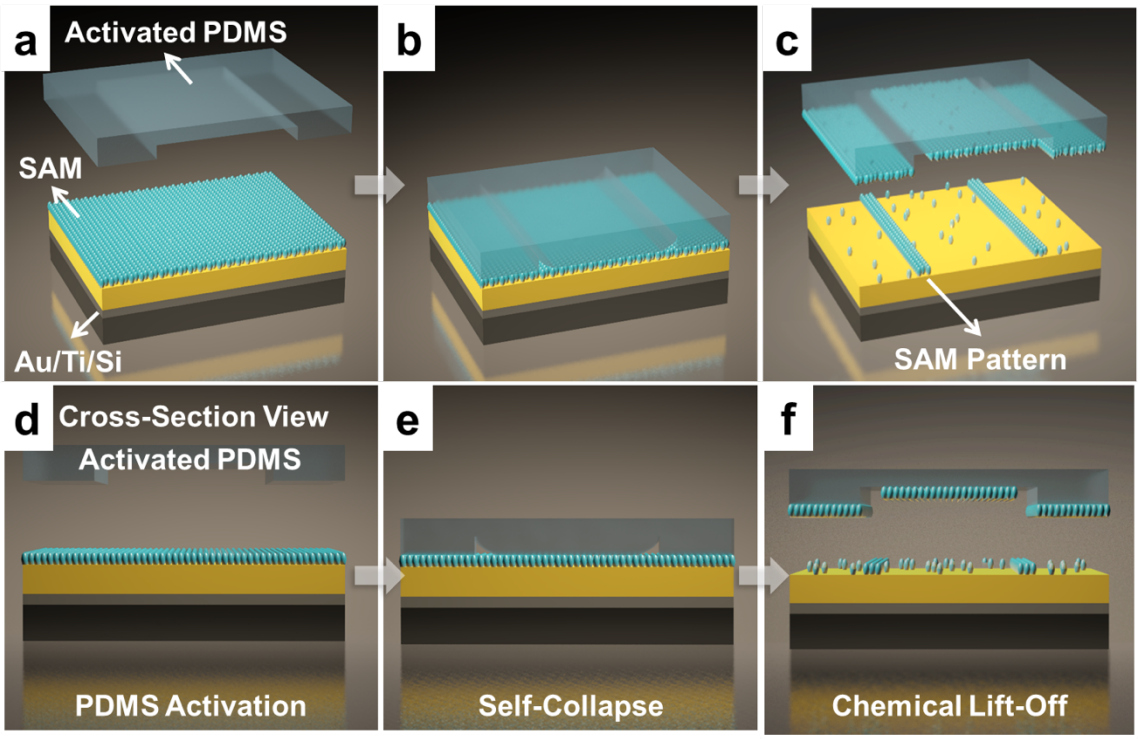

Figure 2.1. Schematic illustration of self-collapse lithography (SCL). (a,d) Hydroxyl-terminated alkanethiols form a self-assembled monolayer (SAM) on the surface of an Au/Ti-coated Si substrate. A polydimethylsiloxane (PDMS) stamp is activated by oxygen plasma treatment. (b,e) The activated stamp is brought into conformal contact with the SAM-coated Au surface without externally applied forces. (c,f) The chemical lift-off process removes the SAM from regions of the functionalized surface in direct contact with the stamp, thereby producing a pattern from molecules remaining in non-contacted regions.[57]

For self-collapse to occur, the aspect ratios (channel width/height) of stamp features and Young's modulus must satisfy specific criteria.[61] We assembled stamps with recessed channels having widths and heights configured to collapse at desired locations, resulting in controlled, reproducible patterns. Scanning electron microscope (SEM) images, as seen in **Figure 2.2**, demonstrate the removal of SAMs in regions that were in conformal contact with the stamps. Due to stamp self-collapse, narrow structures with linewidths much smaller than the original channel dimensions were observed on the SCL-patterned surface. In **Figures 2.2a**,**b**, arrays of lines ~170 nm wide were produced *via* SCL using PDMS stamps with 6 μm wide channels and 300 nm channel heights. The patterned lines were straight and continuous for tens of micrometers, corresponding to the edges of the original microscale channel. Despite one side of the line being determined by the edge of the stamp contact and the other side being determined by the collapsed polymer, no significant differences in the two sides of the patterned features were observed in these and other patterns.

Table 2.1. Gap linewidths (*L*) produced using stamps with different channel heights (*h*) and channel widths (*w*), with a fixed Young's modulus (*E* = 1.75 MPa).

h	***L***	***w***
50 nm	27 ± 5 nm	1 μm
100 nm	48 ± 6 nm	4 μm
200 nm	78 ± 6 nm	6 μm
300 nm	168 ± 12 nm	6 μm
400 nm	235 ± 17 nm	10 μm
400 nm	227 ± 19 nm	20 μm
500 nm	411 ± 9 nm	20 μm
700 nm	872 ± 82 nm	20 μm
1 μm	1710 ± 98 nm	80 μm

We identified a set of basic design rules that govern SCL to understand the effects of key parameters on the final patterns. It has previously been reported that for reproducible self-collapse to occur, the channel width needs to be larger than a threshold value fixed for each value of the Young's modulus of the stamps, where the potential energy for the collapse is employed to determine the threshold.[61] The aspect ratios (channel width/height) of the stamp features were engineered to be sufficiently large to enable self-collapse.[61] We denote stamp features as follows: channel width as ***w***, channel height as ***h***, and the non-collapsed gap linewidth as ***L*** (**Figure 2.2c**). We first examined the dependence of ***L*** on ***h***. Stamps with discrete values of ***h***, within the range of 50 (w = 1 μm) to 400 nm (w = 10 μm), produced patterned lines with ***L*** values of 27 ± 5, 48 ± 6, 78 ± 6, 168 ± 12, and 235 ± 17 nm, respectively, as shown in **Figure 2.2d** and reported in

Table 2.1. The channel width for each height is highlighted in the table. Note that when ***w*** is larger than this threshold value, at fixed ***h***, changes in ***w*** have little influence on ***L***,[61] in agreement with our experimental results. For example, we obtained similar values of ***L*** at 235 or 227 nm for different values ***w*** at 10 or 20 μm, respectively, with ***h*** fixed at 400 nm.[61,63] We kept the thickness of PDMS stamps the same (5 mm) in all experiments, and the influence of gravity was neglected in this study. Note that the applied external force and the thickness of the PDMS could also be used to control ***L***, *e.g.*, larger widths can be achieved by applying external stress, which is currently under investigation.

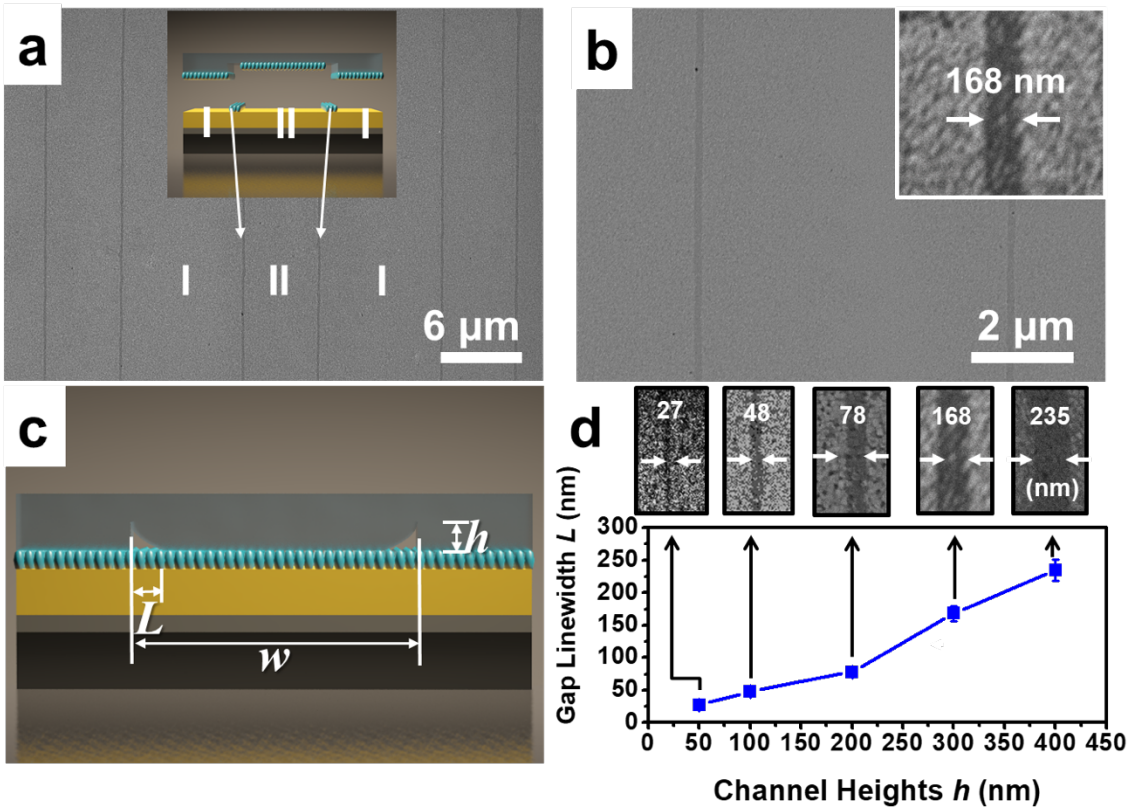

Figure 2.2. (a, b) Scanning electron microscope (SEM) images of linear arrays with sub-200 nm linewidths created by self-collapse lithography using a stamp with microchannel features (6 μm channel width, 300 nm channel height). (c) Schematic

illustration of a collapsed stamp (*L*: gap linewidth; *w*: channel width; and *h*: channel height). (d) Plot of gap linewidths *L* obtained using different channel heights *h* with a fixed Young's modulus of 1.75 MPa. The channel width for each data point is listed in Table 2.1. Insets correspond to a representative SEM image for each data point.

Next, we investigated the relationship between ***L*** and the Young's modulus (***E)*** of stamps. The PDMS stamps were prepared using different ratios (X:Y) of Sylgard 184 pre-polymer base (X) and curing agent (Y) to control the relationship with the patterned linewidths. Values of ***E*** were estimated based on previous reports with details included in the Supporting Information.[66-68] Stamps with ***E*** ranging from 0.85 to 2.0 MPa were molded from a master with relief channel heights fixed at 400 nm. When these stamps were utilized for SCL, ***L*** was found to decrease proportionally with decreasing ***E*** (**Table 2.2**). These results indicate that SCL patterns can be fine-tuned by varying stamp stiffness, *i.e.*, a smaller *L* can be achieved by using softer stamps.

Table 2.2. Gap linewidths (*L*) produced using stamps with different Young's moduli (*E*), and a fixed channel height (*h* = 400 nm) and width (*w* = 10 μm).

E	***L***
2.0 MPa	366 ± 12 nm
1.15 MPa	165 ± 16 nm
1.75 MPa	235 ± 17 nm
0.85 MPa	100 ± 17 nm

A key distinction between SCL and other soft lithographic strategies is that nanoscale patterns are generated from the deformation of micron-scale features on stamps molded from conventional photolithographically prepared masters. The self-collapse process transfers the two-dimensional pattern of the stamp features to the surface while avoiding scaling issues that limit conventional lithographic methods. In principle, the scale over which stamp patterns are reduced is limited only by the precision to which masters can be fabricated and the degree of control over stamp stiffness.

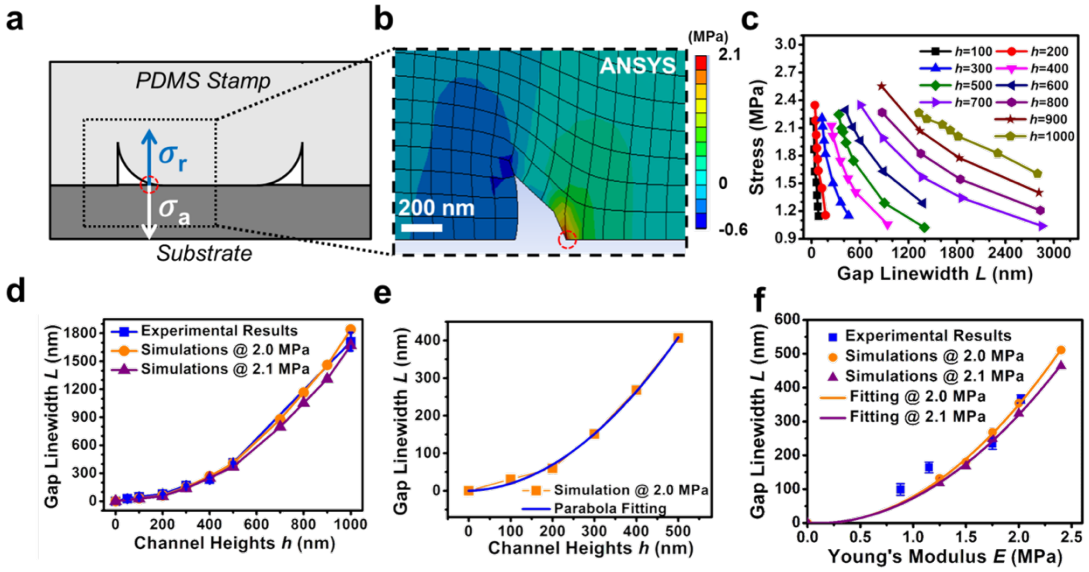

Figure 2.3. (a) Schematic illustration of the self-collapse model used in finite element analysis (FEA) simulations, where σ_r represents the restoring stress and σ_a denotes the adhesion stress between the PDMS stamp and the substrate. (b) A typical FEA simulation result illustrating the stress distribution on a self-collapse stamp (only the restoring stresses normal to the substrate are depicted). (c) Relationships between simulated stresses and gap sizes *L* at different channel heights *h*. (d) Experimentally measured gap widths and channel heights (squares) plotted with simulated values (circles, triangles) using Young's moduli

(*E*) of 2.0 and 2.1 MPa. (e) Simulated gap linewidths plotted as a function of channel height with a parabolic fit. (f) Plots of simulated and experimental results showing variations in gap linewidths at different values of *E*.

Adhesion forces between the stamp and the underlying substrate drive the self-collapse of recessed elastomer features. Previously, this process has been approximated using a classic crack growth model (*i.e.,* crack growth stops when the required work equals the adhesion energy) by Huang *et al*.[61,63] Here, we examined the self-collapse process more directly by modeling stress distributions along the gap (***L***) between collapsed regions and the edges of the original features. Two stresses compete at the edges of the gap: an elastic restoring force ($\boldsymbol{\sigma}_\mathbf{r}$) and an adhesion force ($\boldsymbol{\sigma}_\mathbf{a}$), both acting normal to the substrate. Interactions between $\boldsymbol{\sigma}_\mathbf{r}$ and $\boldsymbol{\sigma}_\mathbf{a}$ can be used to predict ***L*** during SCL (**Figure 2.3a**). The adhesion force acts to collapse the top of the channel, pulling it toward the substrate surface, while the restoring force acts to retain the shape of the channel, pulling it away from the substrate. At equilibrium ($\boldsymbol{\sigma}_\mathbf{r} = \boldsymbol{\sigma}_\mathbf{a}$), a stable gap (***L***) is formed between the collapsed top and edges of the channel.

Finite element analysis (FEA) simulations were carried out using the ANSYS software suite (Ansys Inc. Student version 16.0, Canonsburg, PA) to model the distributions of mechanical stress within a stamp with minimum mesh sizes fixed at 100 nm (**Figure 2.3b**). We employed an inverse method to simulate the mechanism of self-collapse, where the roofs of simulated channels of specified widths were displaced toward their corresponding substrates by an amount equal to the channel height, ***h***. By varying the widths of the simulated channel roof, we obtained a series of restoring stresses along the gap edges and their corresponding gap linewidths, ***L***. In this way, we simulated the collapse of stamps configured with different channel

heights to obtain an approximate relationship between the restoring stress and gap width at different channel heights.

As illustrated in **Figure 2.3c**, increases in stamp channel heights result in increases in the resulting gap linewidths as less of each channel's roof makes contact with the substrate surface at fixed stress. A comparison of the results from our FEA simulations at adhesion stresses of 2.0 and 2.1 MPa with those obtained from SCL experiments are shown in **Figure 2.3d.** There is excellent agreement between simulated responses and experimental data, indicating that our stress-balance model correlates well and is predictive of the self-collapse phenomenon. Moreover, the simulation results can be used to predict the line widths of patterns with smaller features. Fitting a parabolic function to the 2.0 MPa curve (**Figure 2.3e**):

$$L = f(h) = ah + bh^2 \qquad \textbf{Eq. (2.1)}$$

we determined the fitting constants a = 0.038 nm^{-1} and b = 0.00156 nm^{-2}. Using **Eq. (2.1)**, we can estimate the $\boldsymbol{L}$ of a pattern produced with any $\boldsymbol{h}$ at stable collapse regions, which enables the manipulation of SCL-generated patterns *via* strategic design of stamp features. For example, to achieve a linewidth of 100 nm, a stamp with channel heights of $\boldsymbol{h} \approx$ 242 nm is needed, according to **Eq. (2.1)**. With proper design and optimization, we estimate that SCL will be able to produce linewidths as small as 5 nm (corresponding to patterns about 10 molecules across).[40,51]

In addition to channel height, our studies demonstrate how the mechanical stiffness of PDMS affects linewidths of the final pattern. We modeled the behavior of stamps using different ratios (X:Y) of Sylgard 184 pre-polymer base (X) and curing agent (Y) to determine the relationship with the pattern linewidth. Simulation results of stress and $\boldsymbol{L}$, at a fixed channel

height of 400 nm, are shown in **Figure S2.1** using different values of ***E***: 2.0 MPa (5:1), 1.75 MPa (10:1), 1.15 MPa (15:1) and 0.85 MPa (20:1). Analyses of these data were used to visualize the relationship between ***E*** and ***L*** (**Figure 2.3f)**. A trend emerges showing that a decrease in ***E*** (*i.e.,* as the PDMS stamp becomes softer) results in smaller values of ***L*** when patterning using stamps with identical channel heights. Therefore, stamps derived from a single master may be used to generate a range of feature sizes by varying ***E.***

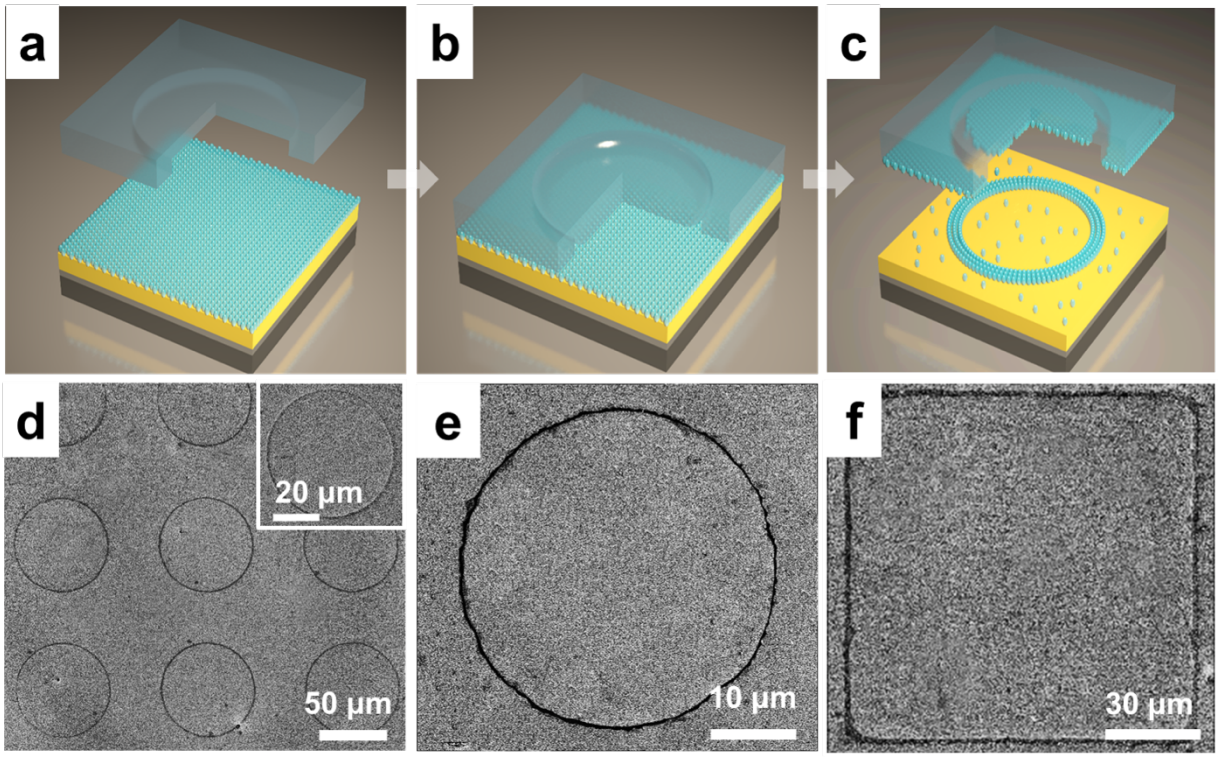

Figure 2.4. (a–c) Schematic illustrations of a ring chemical pattern fabricated *via* self-collapse lithography (SCL). (a) Hydroxyl-terminated alkanethiols form a self-assembled monolayer (SAM) on the surface of an Au/Ti-coated Si substrate. (b) A stamp with recessed circular features is activated by oxygen plasma and then placed into conformal contact with the functionalized Au surface, without an external force. The

central portions of the recessed features on the stamp contact the underlying SAM in smaller circular regions due to self-collapse. (c) The chemical lift-off process removes the SAM in direct contact with the polydimethlysiloxane (PDMS) surfaces from the Au substrate, leaving raised (dark), ring-like SAM patterns behind. (d–f) Contrast enhanced SEM images of (d) ring patterns (*L* ~1.71 μm), patterned by SCL with a stamp with recessed circles (50 μm in diameter and 1 μm in height), (e) a ring pattern (*L* ~235 nm) patterned using recessed circles (40 μm in diameter and 400 nm in height), and (f) raised (dark) squares (*L* ~1.71 μm) patterned with recessed square structures (100 μm on each edge and 1 μm in height).

To demonstrate the versatility of SCL, we produced a variety of patterns, including arrays of circle and square features from PDMS stamps comprised of micron-scale, recessed circular or square features, as illustrated in **Figures 2.4** and **2.5**. Nanoscale patterning of other shapes can be similarly achieved by careful design of the stamp mold. To date, we have produced robust arrays of ~250 nm linewidth circular rings *via* SCL from stamps comprised of circular holes with diameters ~40 μm and heights ~400 nm (**Figure 2.4e**). By deconstructing these patterns into component lines and angular elements, it is possible to extend SCL further to achieve more complex pattern configurations, such those needed for circuits for nanoelectronics.

The chemical patterns produced *via* SCL can be utilized as templates for selectively patterning a variety of materials, including metals and biomolecules. For example, the intact SAM that remains on a gold substrate following SCL can resist selective chemical etching, enabling the creation of Au nanostructures, including large-area arrays of Au micro-/nano-rings, wires, or square structures (**Figure 2.5)**. We used atomic force microscopy for depth analysis to

image the SAM patterns by CLL, and, in our previous work, wet etching processed samples.[52] Nanostructures of other materials such as silver and copper can be fabricated similarly. As demonstrated by our prior work in developing CLL, SCL may also be applied to pattern biomolecules at the nanoscale.[40,51,52,57,69]

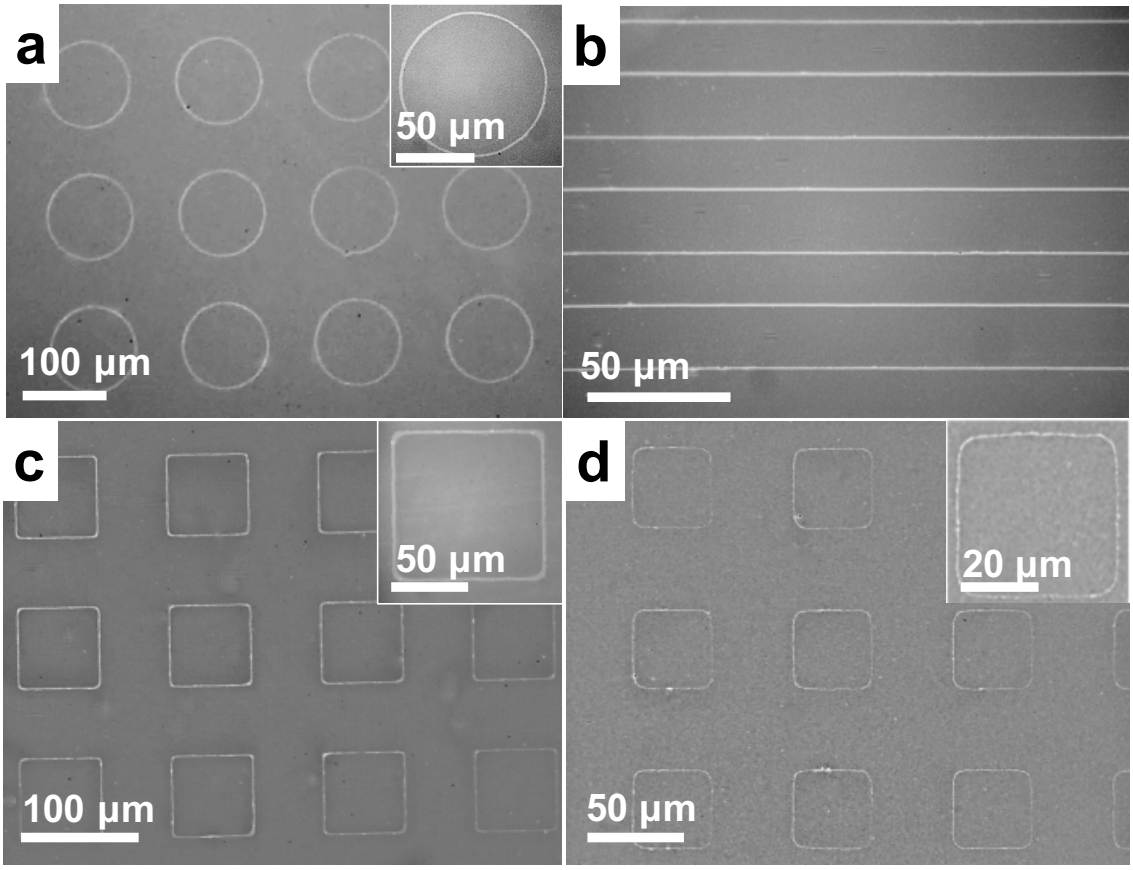

Figure 2.5. Optical microscope images of Au micro/nanostructures fabricated by self-collapse lithography (SCL) followed by selective etching. (a) The Au rings with linewidths of 1.71 µm were fabricated using stamps patterned with 100-µm-diameter circles recessed by 1 µm. (b) Here, Au lines 870 nm wide were fabricated using stamps possessing recessed linear features that were 40 µm wide and 700 nm deep. (c) Sub-2 µm Au squares fabricated using stamps patterned with recessed square features that were

100 μm on an edge and 1 μm in height. (d) Sub-250-nm Au squares fabricated using stamps with recessed squares that were 40 μm in width and 400 nm in height.

2.5 Conclusions and Prospects

In summary, SCL represents a facile and robust nanolithography technique to achieve sub-30-nm resolution by exploiting the elasticity of PDMS structures and natural stamp-substrate adhesion forces. A wide range of shapes and feature sizes can be patterned by strategically designing stamp feature dimensions (*e.g.,* height/width) and/or Young's modulus. Importantly, this soft-lithographic approach can be used as a complement or alternative to slow and expensive direct-writing processes (*e.g.*, electron-beam lithography). The SCL technique provides new insight into how a previously undesirable characteristic of soft lithography can be exploited, *via* CLL, to yield nanoscale patterns. Finite element model simulations suggest a straightforward mechanism for the self-collapse process through the competition between restoring and adhesion stresses along the gap edge produced between the protruding and collapsed stamp features. Results from these simulations correlate well with experimental data and elucidate design rules for using controlled self-collapse to generate complex patterns at the nanoscale that can be applied broadly to applications in nanoelectronics, biosensing, energy storage, and catalysis.

2.6 Supplementary Materials

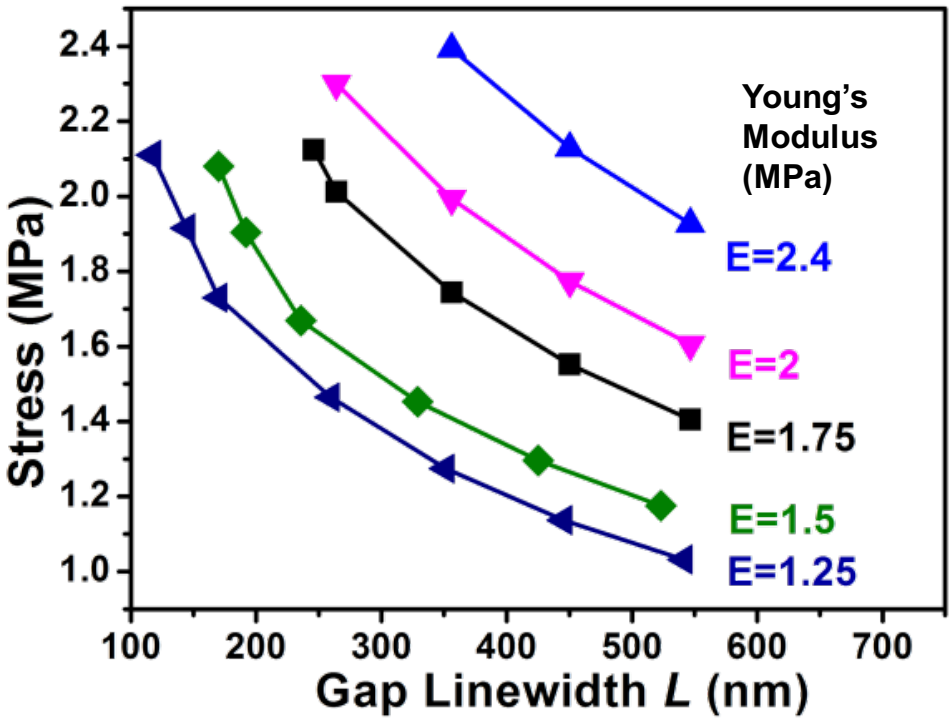

Figure S2.1. Plots of simulation results at different Young's moduli. The relationships between stress at the critical point and gap linewidths at a 400-nm channel height are shown.

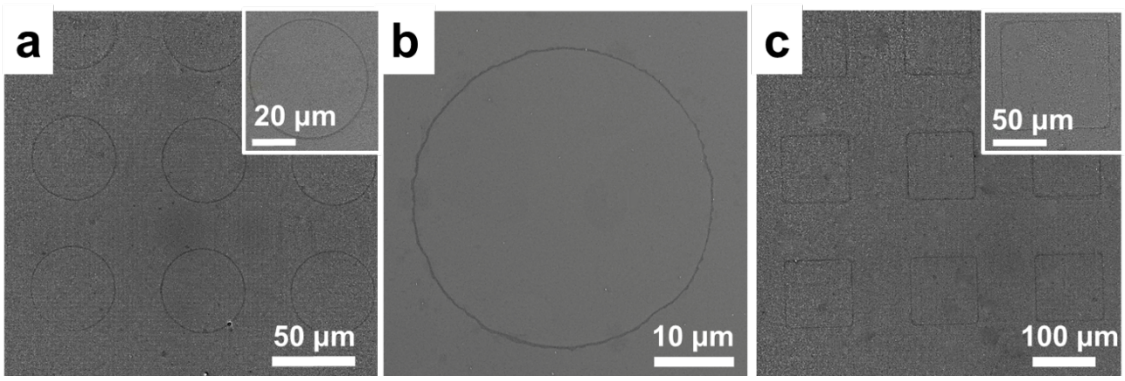

Figure S2.2. Scanning electron microscope (SEM) images of (a) ring patterns (L ~1.71 µm) patterned by a stamp with recessed circles (50 µm diameter and 1 µm height). (b) A ring pattern (L ~235 nm) by a stamp with recessed circles (40 µm diameter and 400 nm height), (c) hollow squares (L ~1.71 µm) by a stamp with recessed square structures (100 µm length and 1 µm height).

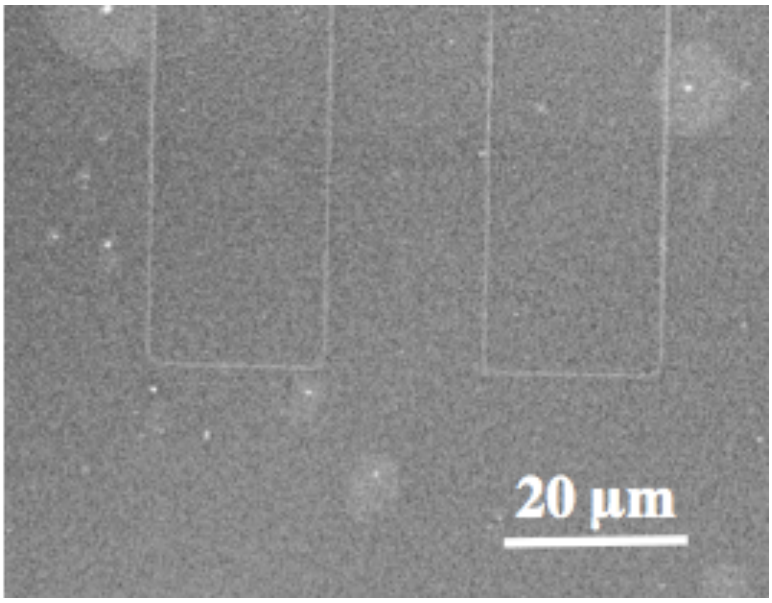

Figure S2.3. Scanning electron microscope (SEM) images of line patterns at the pattern corners formed with a stamp height of 500 nm.

2.7 References

(1) Yan, H.; Chen, Z.; Zheng, Y.; Newman, C.; Quinn, J. R.; Dotz, F.; Kastler, M.; Facchetti, A. A High-Mobility Electron-Transporting Polymer for Printed Transistors. *Nature* **2009,** *457*, 679–686.

(2) Jeon, H.-J.; Kim, K. H.; Baek, Y.-K.; Kim, D. W.; Jung, H.-T. New Top-Down Approach for Fabricating High-Aspect-Ratio Complex Nanostructures with 10 nm Scale Features. *Nano Lett*. **2010,** *10*, 3604–3610.

(3) Kim, D.-H.; Lu, N.; Ma, R.; Kim, Y.-S.; Kim, R.-H.; Wang, S.; Wu, J.; Won, S. M.; Tao, H.; Islam, A.; Yu, K. J.; Kim, T.-i.; Chowdhury, R.; Ying, M.; Xu, L.; Li, M.; Chung, H.-J.; Keum, H.; McCormick, M.; Liu, P.; et al. Epidermal Electronics. *Science* **2011,** *333*, 838–843.

(4) Tsai, H.; Pitera, J. W.; Miyazoe, H.; Bangsaruntip, S.; Engelmann, S. U.; Liu, C.-C.; Cheng, J. Y.; Bucchignano, J. J.; Klaus, D. P.; Joseph, E. A.; Sanders, D. P.; Colburn, M. E.; Guillorn, M. A. Two-Dimensional Pattern Formation Using Graphoepitaxy of Ps-B-Pmma Block Copolymers for Advanced Finfet Device and Circuit Fabrication. *ACS Nano* **2014,** *8*, 5227–5232.

(5) Kim, T.-H.; Cho, K.-S.; Lee, E. K.; Lee, S. J.; Chae, J.; Kim, J. W.; Kim, D. H.; Kwon, J.-Y.; Amaratunga, G.; Lee, S. Y.; Choi, B. L.; Kuk, Y.; Kim, J. M.; Kim, K. Full-Colour Quantum Dot Displays Fabricated by Transfer Printing. *Nat. Photonics* **2011,** *5*, 176–182.

(6) Kim, B. H.; Onses, M. S.; Lim, J. B.; Nam, S.; Oh, N.; Kim, H.; Yu, K. J.; Lee, J. W.; Kim, J.-H.; Kang, S.-K.; Lee, C. H.; Lee, J.; Shin, J. H.; Kim, N. H.; Leal, C.; Shim, M.; Rogers,

J. A. High-Resolution Patterns of Quantum Dots Formed by Electrohydrodynamic Jet Printing for Light-Emitting Diodes. *Nano Lett*. **2015,** *15*, 969–973.

(7) Kim, B. H.; Nam, S.; Oh, N.; Cho, S.-Y.; Yu, K. J.; Lee, C. H.; Zhang, J.; Deshpande, K.; Trefonas, P.; Kim, J.-H.; Lee, J.; Shin, J. H.; Yu, Y.; Lim, J. B.; Won, S. M.; Cho, Y. K.; Kim, N. H.; Seo, K. J.; Lee, H.; Kim, T.-i.; et al. Multilayer Transfer Printing for Pixelated, Multicolor Quantum Dot Light-Emitting Diodes. *ACS Nano* **2016,** *10*, 4920–4925.

(8) Park, J.-S.; Kyhm, J.; Kim, H. H.; Jeong, S.; Kang, J.; Lee, S.-e.; Lee, K.-T.; Park, K.; Barange, N.; Han, J.; Song, J. D.; Choi, W. K.; Han, I. K. Alternative Patterning Process for Realization of Large-Area, Full-Color, Active Quantum Dot Display. *Nano Lett*. **2016,** *16*, 6946–6953.

(9) Whitesides, G. M. The Origins and the Future of Microfluidics. *Nature* **2006,** *442*, 368–373.

(10) Liang, X.; Morton, K. J.; Austin, R. H.; Chou, S. Y. Single Sub-20 nm Wide, Centimeter-Long Nanofluidic Channel Fabricated by Novel Nanoimprint Mold Fabrication and Direct Imprinting. *Nano Lett*. **2007,** *7*, 3774–3780.

(11) Rogers, J. A.; Someya, T.; Huang, Y. Materials and Mechanics for Stretchable Electronics. *Science* **2010,** *327*, 1603–1607.

(12) Gao, W.; Emaminejad, S.; Nyein, H. Y. Y.; Challa, S.; Chen, K.; Peck, A.; Fahad, H. M.; Ota, H.; Shiraki, H.; Kiriya, D.; Lien, D.-H.; Brooks, G. A.; Davis, R. W.; Javey, A. Fully Integrated Wearable Sensor Arrays for Multiplexed *in Situ* Perspiration Analysis. *Nature* **2016,** *529*, 509–514.

(13) Xu, J.; Wang, S.; Wang, G.-J. N.; Zhu, C.; Luo, S.; Jin, L.; Gu, X.; Chen, S.; Feig, V. R.; To, J. W. F.; Rondeau-Gagné, S.; Park, J.; Schroeder, B. C.; Lu, C.; Oh, J. Y.; Wang, Y.; Kim, Y.-H.; Yan, H.; Sinclair, R.; Zhou, D.; et al. Highly Stretchable Polymer Semiconductor Films through the Nanoconfinement Effect. *Science* **2017,** *355*, 59–64.

(14) Kim, J.; Rim, Y. S.; Chen, H.; Cao, H. H.; Nakatsuka, N.; Hinton, H. L.; Zhao, C.; Andrews, A. M.; Yang, Y.; Weiss, P. S. Fabrication of High-Performance Ultrathin In_2O_3 Film Field-Effect Transistors and Biosensors Using Chemical Lift-Off Lithography. *ACS Nano* **2015,** *9*, 4572–4582.

(15) Rim, Y. S.; Bae, S.-H.; Chen, H.; Yang, J. L.; Kim, J.; Andrews, A. M.; Weiss, P. S.; Yang, Y.; Tseng, H.-R. Printable Ultrathin Metal Oxide Semiconductor-Based Conformal Biosensors. *ACS Nano* **2015,** *9*, 12174–12181.

(16) Limaj, O.; Etezadi, D.; Wittenberg, N. J.; Rodrigo, D.; Yoo, D.; Oh, S.-H.; Altug, H. Infrared Plasmonic Biosensor for Real-Time and Label-Free Monitoring of Lipid Membranes. *Nano Lett*. **2016,** *16*, 1502–1508.

(17) Liu, Q.; Aroonyadet, N.; Song, Y.; Wang, X.; Cao, X.; Liu, Y.; Cong, S.; Wu, F.; Thompson, M. E.; Zhou, C. Highly Sensitive and Quick Detection of Acute Myocardial Infarction Biomarkers Using In_2O_3 Nanoribbon Biosensors Fabricated Using Shadow Masks. *ACS Nano* **2016,** *10*, 10117–10125.

(18) Hochbaum, A. I.; Aizenberg, J. Bacteria Pattern Spontaneously on Periodic Nanostructure Arrays. *Nano Lett*. **2010,** *10*, 3717–3721.

(19) Ul-Haq, E.; Patole, S.; Moxey, M.; Amstad, E.; Vasilev, C.; Hunter, C. N.; Leggett, G. J.; Spencer, N. D.; Williams, N. H. Photocatalytic Nanolithography of Self-Assembled Monolayers and Proteins. *ACS Nano* **2013,** *7*, 7610–7618.

(20) Chiappini, C.; De Rosa, E.; Martinez, J. O.; Liu, X.; Steele, J.; Stevens, M. M.; Tasciotti, E. Biodegradable Silicon Nanoneedles Delivering Nucleic Acids Intracellularly Induce Localized *In vivo* neovascularization. *Nat. Mater.* **2015,** *14*, 532–539.

(21) Moxey, M.; Johnson, A.; El-Zubir, O.; Cartron, M.; Dinachali, S. S.; Hunter, C. N.; Saifullah, M. S. M.; Chong, K. S. L.; Leggett, G. J. Fabrication of Self-Cleaning, Reusable Titania Templates for Nanometer and Micrometer Scale Protein Patterning. *ACS Nano* **2015,** *9*, 6262–6270.

(22) Wagner, C.; Harned, N. EUV Lithography: Lithography Gets Extreme. *Nat. Photonics* **2010,** *4*, 24–26.

(23) Miszta, K.; Greullet, F.; Marras, S.; Prato, M.; Toma, A.; Arciniegas, M.; Manna, L.; Krahne, R. Nanocrystal Film Patterning by Inhibiting Cation Exchange *via* Electron-Beam or X-Ray Lithography. *Nano Lett.* **2014,** *14*, 2116–2122.

(24) Manfrinato, V. R.; Wen, J.; Zhang, L.; Yang, Y.; Hobbs, R. G.; Baker, B.; Su, D.; Zakharov, D.; Zaluzec, N. J.; Miller, D. J.; Stach, E. A.; Berggren, K. K. Determining the Resolution Limits of Electron-Beam Lithography: Direct Measurement of the Point-Spread Function. *Nano Lett.* **2014,** *14*, 4406–4412.

(25) Bat, E.; Lee, J.; Lau, U. Y.; Maynard, H. D. Trehalose Glycopolymer Resists Allow Direct Writing of Protein Patterns by Electron-Beam Lithography. *Nat. Commun.* **2015,** *6*, 6654.

(26) Volkert, C. A.; Minor, A. M. Focused Ion Beam Microscopy and Micromachining. *MRS Bull*. **2011,** *32*, 389–399.

(27) Xu, S.; Liu, G. Y. Nanometer-Scale Fabrication by Simultaneous Nanoshaving and Molecular Self-Assembly. *Langmuir* **1997,** *13*, 127–129.

(28) Piner, R. D.; Zhu, J.; Xu, F.; Hong, S. H.; Mirkin, C. A. "Dip-Pen" Nanolithography. *Science* **1999,** *283*, 661–663.

(29) Kumar, A.; Whitesides, G. M. Features of Gold Having Micrometer to Centimeter Dimensions Can Be Formed through a Combination of Stamping with an Elastomeric Stamp and an Alkanethiol ‘‘Ink’’ Followed by Chemical Etching. *Appl*. *Phys*. *Lett*. **1993,** *63*, 2002–2004.

(30) Xia, Y.; Whitesides, G. M. Soft Lithography. *Angew*. *Chem*. *Int*. *Ed*. **1998,** *37*, 550–575.

(31) Srinivasan, C.; Mullen, T. J.; Hohman, J. N.; Anderson, M. E.; Dameron, A. A.; Andrews, A. M.; Dickey, E. C.; Horn, M. W.; Weiss, P. S. Scanning Electron Microscopy of Nanoscale Chemical Patterns. *ACS Nano* **2007,** *1*, 191–201.

(32) Qin, D.; Xia, Y.; Whitesides, G. M. Soft Lithography for Micro- and Nanoscale Patterning. *Nat*. *Protoc*. **2010,** *5*, 491–502.

(33) Xia, Y. N.; McClelland, J. J.; Gupta, R.; Qin, D.; Zhao, X. M.; Sohn, L. L.; Celotta, R. J.; Whitesides, G. M. Replica Molding Using Polymeric Materials: A Practical Step toward Nanomanufacturing. *Adv*. *Mater*. **1997,** *9*, 147–149.

(34) Tian, C.; Kim, H.; Sun, W.; Kim, Y.; Yin, P.; Liu, H. DNA Nanostructures-Mediated Molecular Imprinting Lithography. *ACS Nano* **2017,** *11*, 227–238.

(35) Chou, S. Y.; Krauss, P. R.; Renstrom, P. J. Imprint Lithography with 25-Nanometer Resolution. *Science* **1996,** *272*, 85–87.

(36) Huo, F.; Zheng, Z.; Zheng, G.; Giam, L. R.; Zhang, H.; Mirkin, C. A. Polymer Pen Lithography. *Science* **2008,** *321*, 1658–1660.

(37) Shim, W.; Braunschweig, A. B.; Liao, X.; Chai, J.; Lim, J. K.; Zheng, G.; Mirkin, C. A. Hard-Tip, Soft-Spring Lithography. *Nature* **2011,** *469*, 516–520.

(38) Zhong, X.; Bailey, N. A.; Schesing, K. B.; Bian, S.; Campos, L. M.; Braunschweig, A. B. Materials for the Preparation of Polymer Pen Lithography Tip Arrays and a Comparison of Their Printing Properties. *J. Polym. Sci. A: Polym. Chem.* **2013,** *51*, 1533–1539.

(39) Liao, X.; Huang, Y.-K.; Mirkin, C. A.; Dravid, V. P. High Throughput Synthesis of Multifunctional Oxide Nanostructures within Nanoreactors Defined by Beam Pen Lithography. *ACS Nano* **2017,** *11*, 4439–4444.

(40) Xue, Y.; Kang, D.; Ma, Y.; Feng, X.; Rogers, J. A.; Huang, Y. Collapse of Microfluidic Channels/Reservoirs in Thin, Soft Epidermal Devices. *Extreme Mech. Lett.* **2017**, 18–23.

(41) Jeon, S.; Menard, E.; Park, J. U.; Maria, J.; Meitl, M.; Zaumseil, J.; Rogers, J. A. Three-Dimensional Nanofabrication with Rubber Stamps and Conformable Photomasks. *Adv. Mater.* **2004,** *16*, 1369–1373.

(42) Childs, W. R.; Nuzzo, R. G. Decal Transfer Microlithography: A New Soft-Lithographic Patterning Method. *J. Am. Chem. Soc.* **2002,** *124*, 13583–13596.

(43) Xu, Q. B.; Rioux, R. M.; Dickey, M. D.; Whitesides, G. M. Nanoskiving: A New Method to Produce Arrays of Nanostructures. *Acc. Chem. Res.* **2008,** *41*, 1566–1577.

(44) James, C. D.; Davis, R. C.; Kam, L.; Craighead, H. G.; Isaacson, M.; Turner, J. N.; Shain, W. Patterned Protein Layers on Solid Substrates by Thin Stamp Microcontact Printing. *Langmuir* **1998,** *14*, 741–744.

(45) Bernard, A.; Renault, J. P.; Michel, B.; Bosshard, H. R.; Delamarche, E. Microcontact Printing of Proteins. *Adv. Mater.* **2000,** *12*, 1067–1070.

(46) Vaish, A.; Shuster, M. J.; Cheunkar, S.; Weiss, P. S.; Andrews, A. M. Tuning Stamp Surface Energy for Soft Lithography of Polar Molecules to Fabricate Bioactive Small-Molecule Microarrays. *Small* **2011,** *7*, 1471–1479.

(47) Xia, Y.; Zhao, X.-M.; Kim, E.; Whitesides, G. M. A Selective Etching Solution for Use with Patterned Self-Assembled Monolayers of Alkanethiolates on Gold. *Chem. Mater.* **1995,** *7*, 2332–2337.

(48) Delamarche, E.; Schmid, H.; Bietsch, A.; Larsen, N. B.; Rothuizen, H.; Michel, B.; Biebuyck, H. Transport Mechanisms of Alkanethiols During Microcontact Printing on Gold. *J. Phys. Chem. B* **1998,** *102*, 3324–3334.

(49) Mullen, T. J.; Srinivasan, C.; Hohman, J. N.; Gillmor, S. D.; Shuster, M. J.; Horn, M. W.; Andrews, A. M.; Weiss, P. S. Microcontact Insertion Printing. *Appl. Phys. Lett.* **2007,** *90*, 063114.

(50) Dameron, A. A.; Hampton, J. R.; Smith, R. K.; Mullen, T. J.; Gillmor, S. D.; Weiss, P. S. Microdisplacement Printing. *Nano Lett.* **2005,** *5*, 1834–1837.

(51) Andrews, A. M.; Liao, W.-S.; Weiss, P. S. Double-Sided Opportunities Using Chemical Lift-Off Lithography. *Acc. Chem. Res.* **2016,** *49*, 1449–1457.

(52) Liao, W.-S.; Cheunkar, S.; Cao, H. H.; Bednar, H. R.; Weiss, P. S.; Andrews, A. M. Subtractive Patterning *via* Chemical Lift-Off Lithography. *Science* **2012,** *337*, 1517–1521.

(53) Saavedra, H. M.; Mullen, T. J.; Zhang, P. P.; Dewey, D. C.; Claridge, S. A.; Weiss, P. S. Hybrid Strategies in Nanolithography. *Rep. Prog. Phys.* **2010,** *73*, 036501.

(54) Srinivasan, C.; Mullen, T. J.; Hohman, J. N.; Anderson, M. E.; Dameron, A. A.; Andrews, A. M.; Dickey, E. C.; Horn, M. W.; Weiss, P. S. Scanning Electron Microscopy of Nanoscale Chemical Patterns. *ACS Nano* **2007,** *1*, 191-201.

(55) Shuster, M. J.; Vaish, A.; Cao, H. H.; Guttentag, A. I.; McManigle, J. E.; Gibb, A. L.; Martinez, M. M.; Nezarati, R. M.; Hinds, J. M.; Liao, W. S.; Weiss, P. S.; Andrews, A. M. Patterning Small-Molecule Biocapture Surfaces: Microcontact Insertion Printing *vs.* Photolithography. *Chem. Comm.* **2011,** *47*, 10641–10643.

(56) Claridge, S. A.; Liao, W. S.; Thomas, J. C.; Zhao, Y.; Cao, H. H.; Cheunkar, S.; Serino, A. C.; Andrews, A. M.; Weiss, P. S. From the Bottom Up: Dimensional Control and Characterization in Molecular Monolayers. *Chem. Soc. Rev.* **2013,** *42*, 2725–2745.

(57) Cao, H. H.; Nakatsuka, N.; Serino, A. C.; Liao, W.-S.; Cheunkar, S.; Yang, H.; Weiss, P. S.; Andrews, A. M. Controlled DNA Patterning by Chemical Lift-Off Lithography: Matrix Matters. *ACS Nano* **2015,** *9*, 11439–11454.

(58) Hui, C. Y.; Jagota, A.; Lin, Y. Y.; Kramer, E. J. Constraints on Microcontact Printing Imposed by Stamp Deformation. *Langmuir* **2002,** *18*, 1394–1407.

(59) Sharp, K. G.; Blackman, G. S.; Glassmaker, N. J.; Jagota, A.; Hui, C. Y. Effect of Stamp Deformation on the Quality of Microcontact Printing: Theory and Experiment. *Langmuir* **2004,** *20*, 6430–6438.

(60) Hsia, K. J.; Huang, Y.; Menard, E.; Park, J. U.; Zhou, W.; Rogers, J.; Fulton, J. M. Collapse of Stamps for Soft Lithography Due to Interfacial Adhesion. *Appl. Phys. Lett.* **2005,** *86*, 154106.

(61) Huang, Y. G. Y.; Zhou, W. X.; Hsia, K. J.; Menard, E.; Park, J. U.; Rogers, J. A.; Alleyne, A. G. Stamp Collapse in Soft Lithography. *Langmuir* **2005,** *21*, 8058–8068.

(62) Zhou, W.; Huang, Y.; Menard, E.; Aluru, N. R.; Rogers, J. A.; Alleyne, A. G. Mechanism for Stamp Collapse in Soft Lithography. *Appl. Phys. Lett.* **2005,** *87*, 251925.

(63) Xue, Y.; Zhang, Y.; Feng, X.; Kim, S.; Rogers, J. A.; Huang, Y. A Theoretical Model of Reversible Adhesion in Shape Memory Surface Relief Structures and Its Application in Transfer Printing. *J. Mech. Phys. Solids* **2015,** *77*, 27–42.

(64) Huh, D.; Mills, K. L.; Zhu, X.; Burns, M. A.; Thouless, M. D.; Takayama, S. Tuneable Elastomeric Nanochannels for Nanofluidic Manipulation. *Nat. Mater.* **2007,** *6*, 424-428.

(65) Park, S. M.; Huh, Y. S.; Craighead, H. G.; Erickson, D. A Method for Nanofluidic Device Prototyping Using Elastomeric Collapse. *Proc. Natl. Acad. Sci.* **2009,** *106*, 15549–15554.

(66) Armani, D.; Liu, C.; Aluru, N. Re-Configurable Fluid Circuits by Pdms Elastomer Micromachining. *Proc. IEEE MEMS99* **1999**, 222–227.

(67) Carrillo, F.; Gupta, S.; Balooch, M.; Marshall, S. J.; Marshall, G. W.; Pruitt, L.; Puttlitz, C. M. Nanoindentation of Polydimethylsiloxane Elastomers: Effect of Crosslinking, Work of Adhesion, and Fluid Environment on Elastic Modulus. *J. Mater. Res.* **2011,** *20*, 2820–2830.

(68) Johnston, I. D.; McCluskey, D. K.; Tan, C. K. L.; Tracey, M. C. Mechanical Characterization of Bulk Sylgard 184 for Microfluidics and Microengineering. *J. Micromech. Microeng.* **2014,** *24*, 035017.

(69) Cao, H. H.; Nakatsuka, N.; Liao, W.-S.; Serino, A. C.; Cheunkar, S.; Yang, H.; Weiss, P. S.; Andrews, A. M. Advancing Biocapture Substrates *via* Chemical Lift-Off Lithography. *Chem. Mater.* **2017,** *29*, 6829–6839.

Chapter 3

Scalable Fabrication of Quasi-One-Dimensional Au Nanoribbons for Plasmonic Sensing

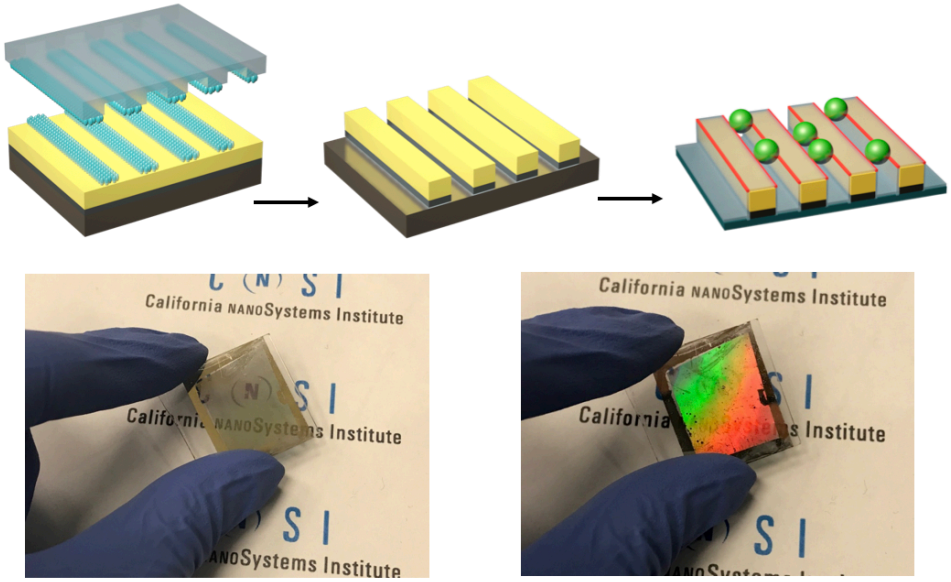

The information in this chapter is reprinted with permission from

Nano Lett. **2020**, *20*, 1747–1754. Copyright (2020) American Chemical Society

Authors: **Zhao, C.**; Xu, X.; Ferhan, A. R.; Chiang, N.; Jackman, J. A.; Yang, Q.; Liu, W.; Andrews, A. M.; Cho, N. J.; Weiss, P. S.

3.1 Abstract

Plasmonic nanostructures have a wide range of applications including chemical and biological sensing. However, the development of techniques to fabricate sub-micron plasmonic structures over large scales remains challenging. We demonstrate a high-throughput, cost-effective approach to fabricate Au nanoribbons *via* chemical lift-off lithography (CLL). Commercial HD-DVDs were used as large-area templates for CLL. Transparent glass slides were coated with Au/Ti films and functionalized with self-assembled alkanethiolate monolayers. Monolayers were patterned with lines *via* CLL. The lifted-off, exposed regions of underlying Au were selectively etched into large-area grating-like patterns (200-nm linewidth; 400-nm pitch; 60-nm height). After removal of the remaining monolayers, a thin In_2O_3 layer was deposited and the resulting gratings were used as plasmonic sensors. Distinct features in the extinction spectra varied in their responses to refractive index changes in the solution environment with a maximum bulk sensitivity of ~510 nm/refractive index unit. Sensitivity to local refractive index changes in the near-field was also achieved, as evidenced by real-time tracking of lipid vesicle or protein adsorption. These findings show how CLL provides a simple and economical means to pattern large-area plasmonic nanostructures for applications in optoelectronics and sensing.

3.2 Introduction

One of the most common measurement principles behind nanoplasmonic sensors is based on localized surface plasmon resonances (LSPRs), which result from interactions between light and noble metal nanostructures and lead to amplified electromagnetic fields in the vicinity of sensor surfaces.[1,2] Typical analytes for nanoplasmonic sensors include ions, proteins, nucleic acids, viruses, exosomes, and liposomes.[3-11] Depending on sensor design, nonspecific adsorption or specific analyte recognition *via* surface receptors can occur on sensor surfaces, leading to changes in the local refractive index within the amplified electromagnetic field near nanostructure surfaces. Such changes affect the plasmonic properties of the nanostructures and thereby give rise to changes in distinct features in the corresponding extinction spectra, including shifts in the LSPR resonance frequency (expressed as the peak shift wavelength).[12] Nanoplasmonic sensors enable label-free and sensitive sensing capabilities for chemical and biological targets making these platforms attractive for applications related to food safety, defense, environmental protection, and biomedical devices.[10,13-22]

Fabrication of plasmonic substrates with nanometer-scale features is critical for practical applications. Producing sub-micron features often relies on state-of-the-art nanolithography tools, such as electron-beam or focused ion-beam lithographies. However, low throughput, high cost, and limited availability constrain scalable manufacturing of plasmonic nanostructures using the aforementioned methods. Soft lithographies, which utilize soft materials, *e.g.*, polydimethylsiloxane (PDMS), to print or to replicate micro-/nanostructures, have emerged as alternatives to conventional photolithography for patterning at low cost and with high throughput.[23-25] Nonetheless, it remains challenging to realize high-fidelity, sub-micron patterning using soft lithographies.

We have shown through chemical lift-off lithography (CLL) that we can produce large-area patterns having features with dimensions as small as tens of nanometers.[26-31] The CLL process uses activated polymeric stamps to remove self-assembled monolayer (SAM) molecules from Au substrates selectively within (stamp-) contact areas. Sub-100 nm features are straightforwardly patterned using CLL, with features as small as 15 nm having been achieved.[29,30,32] In addition, CLL can be used to pattern functional biomolecules for applications involving target recognition.[28,29,33,34] Moreover, the chemical patterns produced by CLL serve as wet etching resists for transferring patterns to underlying materials, such as Au and In_2O_3.[24,30]

Herein, we report a scalable strategy for fabricating plasmonic nanostructures *via* CLL and the application of these substrates as nanoplasmonic sensors. Commercially available optical storage discs, which are inexpensive and ubiquitous, were used as nanostructured templates for making stamps for CLL.[35] The CLL-patterned features functioned as etch resists to pattern underlying Au into plasmonic nanoribbons. Seminconductor-coated Au nanoribbons showed sensing capabilities with high sensitivity to refractive index changes relative to media composition or adsorption of biomolecules.

3.3 Materials and Methods

Materials. Sylgard 184® silicone elastomer kits (lot #0008823745) were purchased from Ellsworth Adhesives (Germantown, WI). Vinylmethylsiloxane-dimethylsiloxane copolymer (7-8%), platinum divinyltetramethyl-disiloxane complex in xylene, and methylhydrosiloxane-dimethylsiloxane copolymer (25-30%) were purchased from Gelest Inc. (Morrisville, PA) and used as received. 2,4,6,8-Tetramethyl-2,4,6,8-tetravinylcyclotetrasiloxane, iron nitrate, thiourea, ammonium hydroxide, hydrogen peroxide, ethylenediaminetetraacetic acid disodium salt

dihydrate (EDTA), sodium chloride, bovine serum albumin (#A8806), and Tris buffer (#648315) were purchased from Sigma-Aldrich (St. Louis, MO) and used as received. 1,2-Dioleoyl-*sn*-glycero-3-phosphocholine (DOPC) was purchased from Avanti Polar Lipids (Alabaster, AL). Commercially available DVD-R recordable 16× speed 4.7 GB blank discs were Memorex brand (Digital Products International, Inc. St. Louis, MO). Water was deionized before use (with resistivity of 18.2 MΩ cm) using a Milli-Q system (Millipore, Billerica, MA).

Au nanoribbon fabrication. Commercially available DVD-R recordable blank discs were used to produce masters for patterning by chemical lift-off lithography. Steps for DVD master preparation were reported previously. Stamps made of *h*-PDMS were prepared by mixing vinylmethylsiloxane-dimethylsiloxane copolymer, platinum divinyltetramethyl-disiloxane complex in xylene, 2,4,6,8-tetramethyl-2,4,6,8-tetravinylcyclotetrasiloxane, and methylhydrosiloxane-dimethylsiloxane with Sylgard® 184 elastomer. A detailed procedure can be found in our previous report.[S1] A 10-nm layer of Ti followed by a 50-nm layer of Au were deposited onto glass slides (VWR, #16004-430, Radnor, PA) using a CHA solution electron-beam evaporator at high vacuum (10^{-8} Torr) with an evaporation rate of 0.1 nm/s.

To form alkanethiol self-assembled monolayers (SAMs), substrates were immersed into an ethanolic 1 mM 11-mercapto-1-undecanol solution overnight before performing the chemical lift-off lithography process described in main text **Figure 3.1**. Substrates were then rinsed with ethanol and dried under N_2 gas. An aqueous solution of 20 mM iron nitrate and 30 mM thiourea was used to etch the Au films for ~30 min in the exposed areas to produce Au nanoribbon features. The Ti etchant was composed of 0.42 g EDTA, 1 mL hydrogen peroxide, and 0.42 mL

ammonia hydrate dissoloved in 10 mL deionized water. This etching steop was performed for ~3 min.

DOPC vesicle preparation. Lipid vesicles composed of DOPC were prepared by an extrusion method. After extrusion, vesicle solutions were stored at 4 °C until each experiment and used within 48 h. Dilution with deionized water to the experimental lipid concentration occurred immediately before use.

Plasmonic measurements and sensitivity calculations. Optical measurements were conducted using an XNano instrument (Insplorion AB, Gothenburg, Sweden), operated in transmission mode. Bulk plasmonic sensitivities were calculated using shifts in key features of the extinction spectra divided by the solution reflective index (nm/RIU). For glycerol with different mass proportions, reflective indices were from 1.33 for 0% to 1.37 for 30% in Tris buffer. Plasmonic feature shifts upon biomolecule addition were normalized based bulk refractive index sensitivities. The methods can be found in our previous report.

Since the LSPR wavelength shift is not only a function of RI change in the near vicinity of the nanoplasmonic transducer, but also a function of the RI sensitivity of the spectral feature associated with the transducer (which, in turn, is dependent on the transducer material, geometry, arrangement, and dielectric coating, if any), a normalization procedure is needed to compare measurement responses directly across different transducers and spectral features. To do so, the bulk RI sensitivity corresponding to each spectral feature of a particular transducer is experimentally determined *via* titration of glycerol-water mixtures (0-30% glycerol) and plotted to determine the linear dependence of the wavelength shifts on refractive index. The slopes of the linear regressions yield the bulk RI sensitivities. The normalization of a particular wavelength

shift measurement response is then calculated by dividing the absolute value of the specific response by the bulk RI sensitivity of the spectral feature that produces that response.

$$Normalized\ reponse\ (in\ RIU) = \frac{Absolute\ reponses\ (in\ nm)}{Bulk\ RI\ sensitivity\ (in\ nm/RIU)}$$

3.4. Results and Discussions

Optical storage media such as digital versatile discs (DVDs) and high-definition DVD (HD-DVD) versions contain sub-micron periodic grating-like structures that can be used as templates for soft-lithography. As in our prior work, HD-DVDs were mechanically split into two layers to expose the layer of each disc having a nanotextured surface containing large-area concentric nanochannels.[35] These nanostructured DVD layers were then used as masters for PDMS stamps. For high-quality stamp replication of the small features on DVDs, hard PDMS (*h*-PDMS) was used as the stamp material.

The fabrication process for Au nanoribbon arrays using *h*-PDMS stamps templated from HD-DVD masters *via* CLL was similar to our previously reported procedure,[35] with some modification. The current process is described in **Figure 3.1** and the supplemental information.

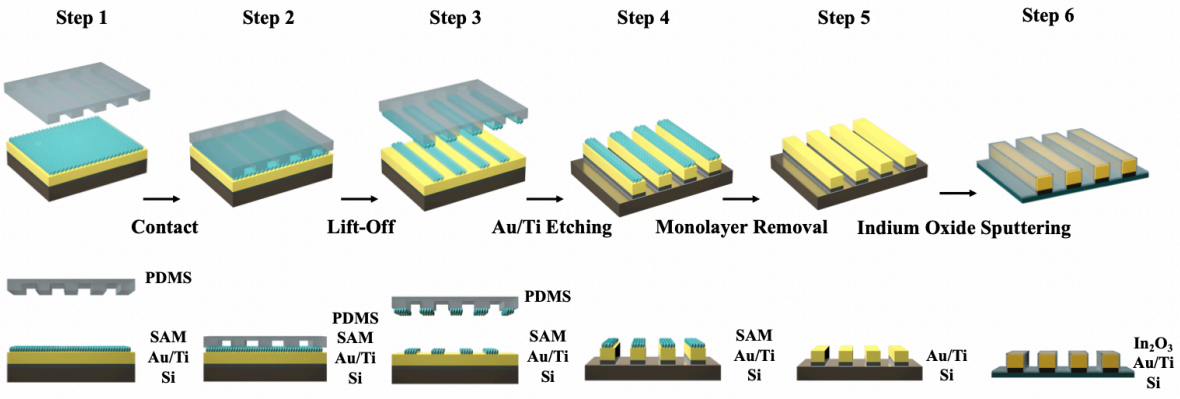

Figure 3.1. Schematic of Au nanoscale grating fabrication. *Step 1:* The Au (50 nM) and Ti (10 nm) layers deposited using electron-beam evaporation onto glass substrates were functionalized with self-assembled monolayers (SAMs) of 11-mercapto-1-undecanol. *Step 2*: Patterned hard polydimethylsiloxane (*h*-PDMS) stamps activated by oxygen plasma were brought into conformal contact with functionalized substrates. *Step 3*: Molecules in the contacted areas were removed from each surface to form nanoribbon patterns. *Step 4*: Selective etching of the exposed Au regions. *Step 5*: Remaining SAM molecules were removed to obtain bare Au nanoscale gratings. *Step 6*: A layer of In_2O_3 (10 nm) was sputtered to cover the sensor surface.

A DVD template is shown in **Figure 3.2a**. Atomic force microscopy (AFM) images of HD-DVDs masters (**Figure 3.2b,c**) show large-area parallel nanoline features (~200-nm linewidth and 400-nm periodicity). Hard PDMS stamps produced from the HD-DVD template are shown in **Figure 3.2d**. Corresponding AFM images of representative stamps confirm high-quality feature replication (**Figure 3.2e**,**f**). After CLL, large-area SAM patterns were formed and characterized *via* scanning electron microscopy (SEM) (**Figure 3.2g**).

Selective Au etching produced sharp, uniform Au nanoribbon arrays that were continuous over large areas (tens of microns) (**Figure 3.2h**). The depth of etching was determined by measuring nanoribbon heights *via* AFM. (**Figure 3.2i**). Sputtering was used to coat In_2O_3 conformally on patterned Au nanoribbon surfaces. The Au nanoribbon patterns following monolayer removal (**Figure S3.1**) remained after In_2O_3 surface deposition (**Figure 3.2j**, **3.2k**, **3.2l**, and **Figure S3.2**).

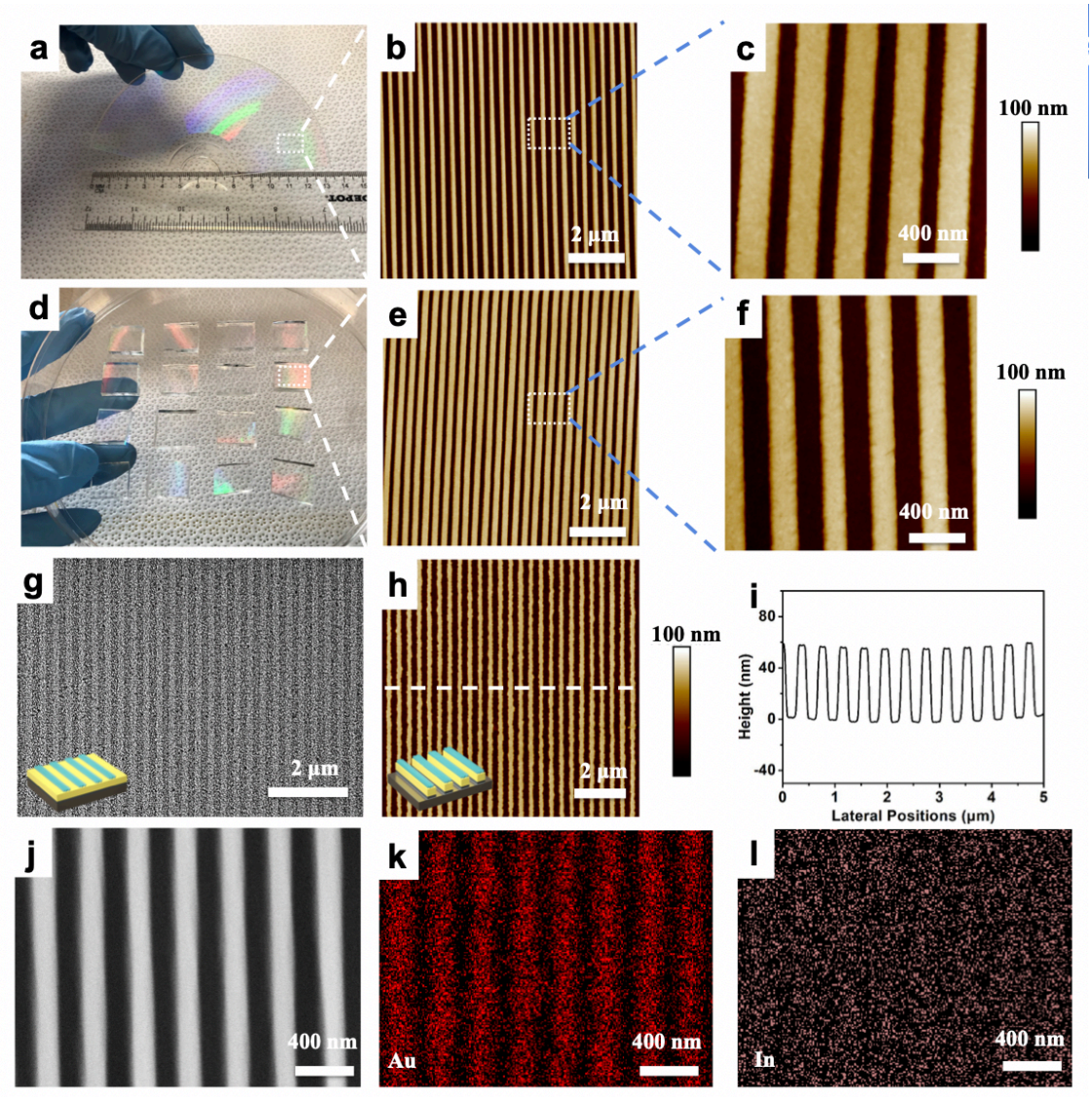

Figure 3.2. (a) Photograph of a HD-DVD master after separation from a commercial disk. (b, c) Atomic force microscope images of HD-DVD master. (d) Photograph of hard polydimethylsiloxane (*h*-PDMS) stamps prepared using a single HD-DVD master, each measuring approximately 1.5 cm × 1.5 cm. (e, f) Atomic force microscope images of patterned *h*-PDMS. (g) A scanning electron microscope (SEM) image of a self-assembled-monolayer nanoribbon pattern, where the darker lines represent regions where molecules

were removed to expose the underlying Au surface. (h) Atomic force microscope image of Au nanoribbons with 200-nm widths and a 400-nm pitch. (i) Profile of Au nanoribbons indicating heights of ~60 nm. (j) An SEM image of Au nanoribbons after In_2O_3 deposition. (k, l) Energy-dispersive X-ray mapping of Au and In, respectively, after conformal sputtering of In_2O_3 at the same spot shown in j.

The In_2O_3-coated Au nanoribbon arrays were investigated for use as nanoplasmonic sensors. Apart from increasing platform stability, dielectric coatings, *e.g.*, In_2O_3, enable indirect nanoplasmonic sensing and thus, characterization of interactions of biomolecules with a variety of materials beyond Au.[36,37] This approach has paved the way for studies involving biomolecule interactions with silicon and TiO_2 surfaces (using other nanostructures as optical transducers).[38-43] Here, arrays were fabricated on clear glass substrates to enable optical measurements in transmission mode. (The measurement setup is shown in **Figure S3.3**.) Arrays on opaque substrates, *e.g.*, Si, could be investigated using reflective mode.

Unlike flat substrates composed of thin Au films, which are typically used in surface plasmon resonance (SPR) sensors, nanostructured substrates lead to a unique interplay of plasmon modes involving localized and propagating surface plasmons. As such, nanoplasmonic sensors enable spectral features related to LSPR to be used to advantage in sensing applications. For example, nanoplasmonic sensors are more surface sensitive compared to conventional SPR sensors and are capable of tracking biomacromolecular interactions with high spatiotemporal resolution.[15,44,45] In addition, measurements can be performed with a simple instrument setup consisting of a white light source and a spectrometer.

Although nanoplasmonic arrays on glass were translucent when viewed at an angle normal to the surface, they were reflective when tilted (**Figure 3.3a**). The latter is due to the high

periodicity of the Au nanoribbons, which produces a diffraction grating. The UV-vis extinction spectra obtained in transmission mode exhibited five distinct features labelled peak 0, dip 1, peak 1, dip 2, and peak 2 at wavelengths of *ca.* 415, 503, 559, 581, and 649 nm in air, respectively (**Figure 3.3b**). With the exception of peak 0, which is due to blue light absorption by Au and is non-plasmonic, the other peaks and dips underwent varying degrees of wavelength shift upon exposure to buffer solution due to the change in refractive index *vs.* air, ranging from *ca.* 30 nm (dip 1) to *ca.* 1 nm (peak 2) (**Figure S3.4**).

By considering the Au nanoribbons as analogous to high-aspect-ratio Au nanorods, peaks 1 and 2 were attributed to the transverse and longitudinal LSPR modes, respectively.[46-48] However, contrary to discreet Au nanorod structures, where larger spectral shifts are typically observed at longer wavelengths,[49,50] peak 2 and dip 2, *i.e.*, spectral features at longer wavelengths of the Au nanoribbon arrays, were less sensitive to bulk refractive-index changes compared to peak 1 and dip 1, *i.e.*, spectral features at shorter wavelengths, as shown in **Figure 3.3b**. This result may be due to nanoribbons having ultra-high aspect ratios, *i.e.*, the length of each ribbon was much larger than its width. Large-aspect-ratio geometries greatly diminish spectral contributions from the longitudinal LSPR mode.[51-53]

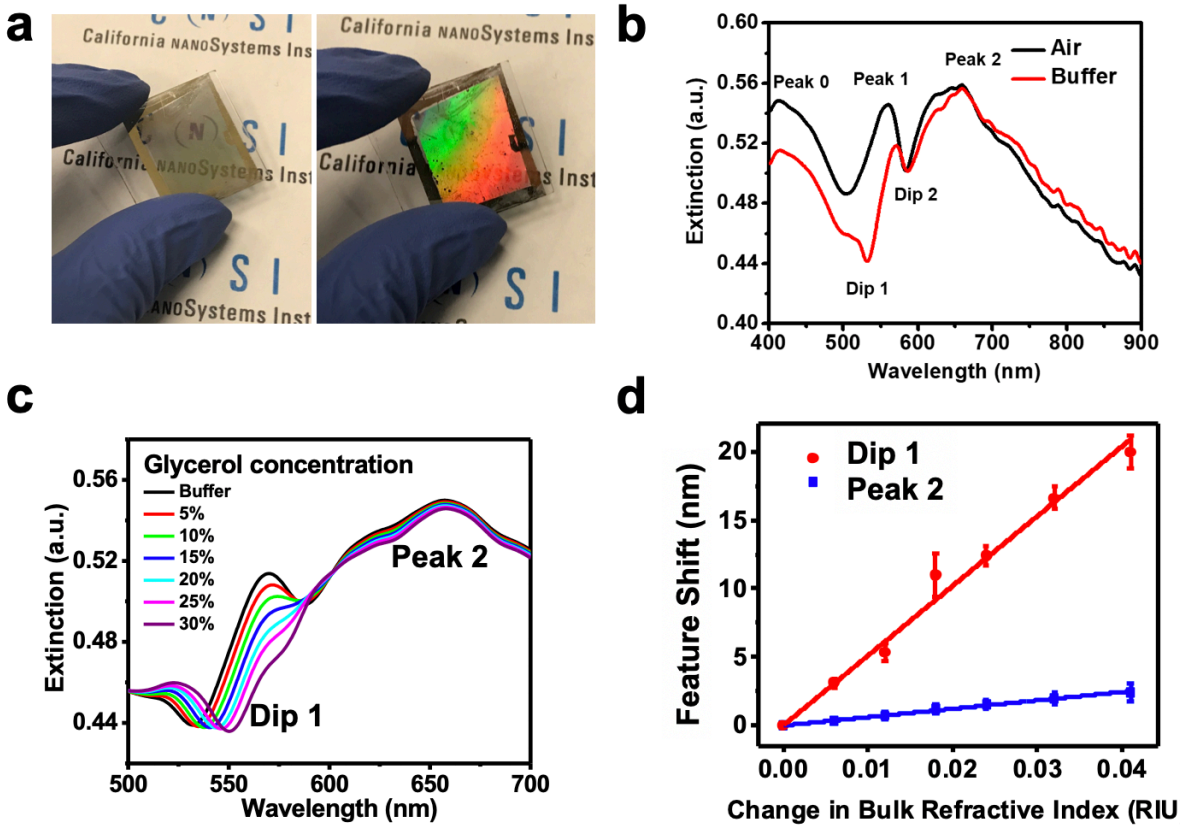

Figure 3.3. (a) Photograph of Au nanoribbons fabricated on glass slides (~3 cm × 3 cm) viewed from different perspectives showing transparency *vs.* reflectivity depending on the viewing angle. (b) Extinction spectra of a representative Au nanoribbon array in air (black trace) *vs.* buffer (10 mM tris(hydroxymethyl)aminomethane, pH 7.5, with 150 mM NaCl) (red trace). (c) Representative extinction spectra of a Au nanoribbon array exposed to buffer solutions with increasing glycerol concentrations (0-30 wt%) during bulk refractive index sensitivity characterization. (d) Bulk refractive index sensitivities of the dip 1 and peak 2 features from spectra obtained at each of the glycerol concentrations. Sensitivities were determined from the slopes of the curves. Data are from *N*=3 substrates produced from different fabrication runs. Error bars are standard errors of the means and too small to be visualized in some cases.

To characterize the sensitivity of the nanoribbon arrays to bulk refractive index (RI), we quantified extinction spectra feature shifts associated with different glycerol-water mixtures (0-30 wt% glycerol), each of which has a well-defined refractive index.[54] From the evolution of the spectra, it was evident that dip 1 was the most sensitive feature, while peak 2 was the least sensitive to bulk RI changes (**Figure 3.3c**, full spectra in **Figure S3.5**). The bulk RI sensitivities for dip 1 and peak 2 were determined to be *ca.* 510 nm/RIU (refractive index unit) and 60 nm/RIU, respectively (**Figure 3.3d**). The bulk RI sensitivity of dip 1 was significantly greater than other reported Au nanostructure arrays[5,39,55-57] suggesting that our Au nanoribbon arrays might be particularly sensitive in chemical and biological sensing applications.

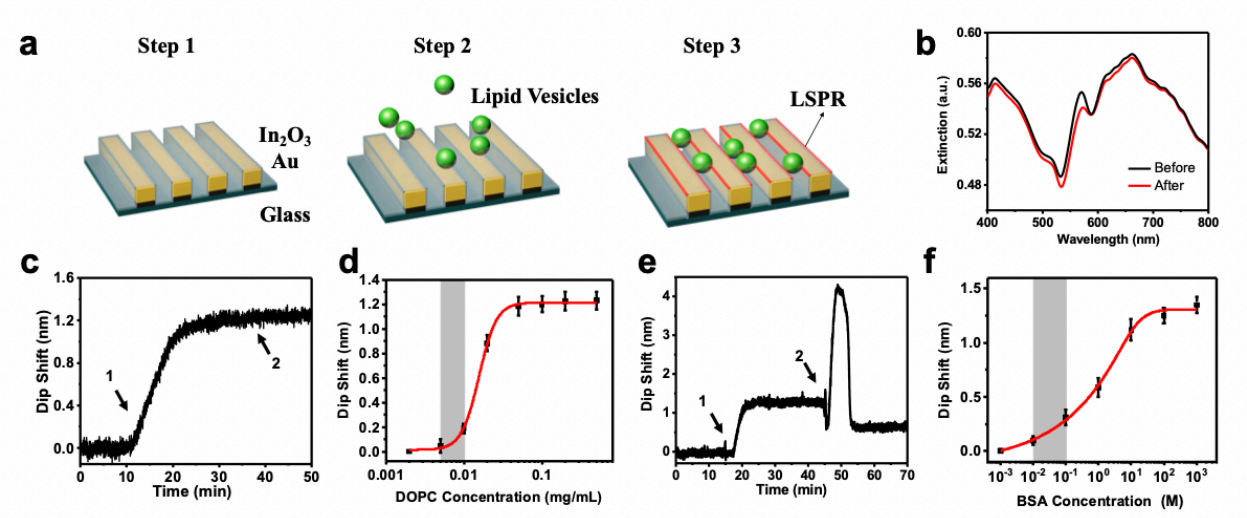

Figure 3.4 (a) Schematic illustration of lipid vesicle detection using a Au plasmonic sensor. A solution containing 1,2-dioleoyl-*sn*-glycero-3-phosphocholine (DOPC) vesicles was continuously flowed across a nanoribbon array (step 2). Some liposomes adsorbed noncovalently to the oxide surface, where red lines indicate the localized surface plasmon resonance (step 3). (b) Extinction spectra showing spectral shifts before and after vesicle adsorption. Time-resolved shifts in the positions of dip 1 during the adsorption of (c)

DOPC lipid vesicles or (e) bovine serum albumin (BSA). Arrows indicate the time points where (1) flow was switched from Tris buffer to buffer containing DOPC lipid vesicles or BSA and (2) flow was switched back to buffer. Concentration dependence of the net wavelength shift (before washing) upon addition of (d) DOPC lipid vesicles or (f) BSA protein. The respective limits of detection (LOD) in grey are included and represent the lowest detectable concentration that would produce a wavelength shift corresponding to 3σ, where σ is the standard deviation of the background signal in the presence of blank buffer. Data are from *N*=3 runs on the same substrate and error bars represent standard deviations.

We investigated the nanoplasmonic characteristics of lipid vesicle interactions with In_2O_3-coated Au-nanoribbon arrays (**Figure 3.4a**). We first determined the spectral noise by calculating the standard deviations of dip 1 and peak 2 wavelength positions over 3 min for arrays immersed in blank buffer.[19] The spectral noise for dip 1 and peak 2 were 4.2 x 10^{-2} nm and 1.0 x 10^{-1} nm, respectively. Based on the corresponding bulk refractive index sensitivity of the features, the spectral noise values of these two spectral features translate to a minimum practical resolution of 8.2 x 10^{-5} RIU and 1.7 x 10^{-3} RIU, respectively.[58] Of note, despite relatively high spectral noise, the practical resolution of dip 1 is comparable to that obtained from commercially available oxide-coated nanoplasmonic substrates used in previous work, highlighting the advantage of high bulk refractive index sensitivity.[19,59]

Since dip 1 was the most responsive spectral feature to environmental changes based on bulk RI measurements, we characterized lipid vesicle adsorption *via* wavelength shifts for dip 1 (**Figure 3.4b**). Baseline spectra were obtained in buffer (10 mM tris(hydroxymethyl)aminomethane (Tris), pH 7.5, with 150 mM NaCl) (**Figure 3.4c**). Next, 1,2-dioleoyl-*sn*-glycero-3-phosphocholine (DOPC) lipid vesicles (0.2 mg/mL) were introduced in Tris buffer at a continuous flow rate of 100 µL/min. The time-resolved wavelength shifts indicated that the peak position of dip 1 increased linearly for ~10 min before reaching a plateau. The time-dependent signal did not change upon subsequent buffer rinsing.

This result suggests a slow accumulation of DOPC lipid vesicles on nanoribbon surfaces. The mean absolute wavelength shift obtained from three different substrates was 1.2 ± 0.1 nm. This shift is near the range observed in our previous work involving the adsorption of lipid vesicles on titanium oxide-coated Au nanodisk arrays, *i.e.*, peak shift of ~2.5-3.0 nm.[9,40,43] However, the wavelength shift normalized to the bulk RI sensitivity of dip 1 was significantly lower

considering the higher bulk RI sensitivity value, *i.e.*, 510 nm/RIU, compared to the bulk RI sensitivity of the analogous spectral dip associated with Au nanodisk arrays. *i.e.*, 140 nm/RIU. The mean absolute wavelength shift for peak 2 from the Au nanoribbon arrays revealed a final value of 2.0 ± 0.2 nm (**Figure S3.6a**). The slope (*i.e.*, from baseline to plateau) can provide a series of quantitative information (**Figure S3.7**), such as initial rate and the number of intermediate steps, in any, involved in the biomolecular interaction, as we reported previously.[29,36,39] Plasmonic features showed different responses to lipid vesicle adsorption with respect to their bulk sensitivities, suggesting a mismatch between bulk and surface sensitivities of the dips and peaks of the Au nanoribbon arrays.

To investigate this mismatch further, we characterized adsorption of a protein biomolecule, BSA, which is widely employed in a variety of applications, often as a blocking agent to prevent nonspecific adsorption on sensor surfaces.[60-63] Recent efforts have relied on nanoplasmonic sensing strategies to quantify the adsorption of serum albumin on various surfaces for understanding adsorptive processes,[38,42,59] as well as for investigating protein corona formation.[64-67]

After obtaining baseline signals in Tris buffer, 100 μM BSA in Tris buffer was introduced at a flow rate of 100 μL/min and adsorption was monitored as a function of time on three different substrates. The time-resolved wavelength shift in the position of dip 1 revealed a steady initial increase, which plateaued at 1.2 ± 0.2 nm (**Figure 3.4d**). Upon switching the flow back to Tris buffer, a sharp spike was reproducibly observed across different substrates prior to stabilization of the wavelength shift of dip 1 at 0.7 ± 0.1 nm. The net decrease in wavelength shift from ~1.2 nm to ~0.7 nm was likely due to the removal of weakly bound BSA molecules by washing, resulting in a decrease in local refractive index near the nanoplasmonic transducer surfaces.

The sharp, transient spike in the LSPR signal from ~1.2 nm to ~4.0 nm suggested a brief increase in local refractive index upon washing. As no additional protein was introduced into the system during this rinse step, the transient positive wavelength shift may have resulted from a redistribution of protein mass closer to the surfaces of the nanoplasmonic sensors into a region of higher electric field enhancement. In other words, the BSA molecules that remained strongly bound to the surface might have undergone post-adsorption redistribution, specifically protein spreading, wherein strongly adsorbed BSA molecules shifted nearer to the surface, on average.[68] Weakly bound protein molecules were displaced leading to eventual net decreases in wavelength shifts.

The final wavelength shift of the dip 1 position is in good agreement with absolute values observed in our previous work, whereby the adsorption of bovine or human serum albumin onto Si or TiO_2 surfaces led to LSPR peak shifts in the range 0.50-1.5 nm.[42,59] However, similar to DOPC lipid vesicle adsorption, the shift in the position of dip 1 resulting from BSA adsorption was relatively low when normalized to the bulk RI sensitivity. To determine whether this smaller shift was due to lower amounts of BSA adsorbed on indium oxide or to differences in surface sensitivity, we extracted the time-resolved wavelength shifts for peak 2 during BSA adsorption (**Figure S3.6b**). The absolute peak 2 shift saturated close to 1.0 nm, which is rather high considering the bulk RI sensitivity of this peak is only ~60 nm/RIU, ruling out sparse BSA adsorption.

We further investigated the dependence of the signal responses on DOPC lipid vesicle and BSA protein concentrations. The DOPC lipid vesicle concentration dependency curve extracted from dip 1 revealed a limit of detection (LOD) of 8.7 μg/mL and a dynamic range (DR) of 0.01–0.05 mg/mL (**Figure 3.4d**). In comparison, the LOD and DR for BSA protein adsorption based

on the same spectral feature were 24 nM (1.58 μg/mL) and 0.1–100 uM (6.6–6.6×10^4 μg/mL), respectively (**Figure 3.4f**). On the other hand, the LOD and DR based on peak 2 for DOPC lipid vesicles were 16 μg/mL and 0.02–0.2 mg/mL (**Figure S3.6c**), and for BSA protein were 540 nM (1.58 μg/mL) and 0.1–100 μM (6.6–6.6×10^4 μg/mL), respectively (**Figure S3.6d**). Overall, dip 1 represents a more sensitive spectral feature than peak 2 for quantification of DOPC lipid vesicle and BSA protein adsorption at lower concentrations. However, peak 2 offers better quantification than dip 1 for resolving DOPC lipid vesicle concentration differences over a wider range, while the opposite is true for BSA protein. This distinction likely arises from different plasmon modes and probing volumes attributed to each spectral feature and highlights the merits of using this type of Au nanoribbon array.

The variations in the final shifts in the positions of dip 1 *vs.* peak 2 during DOPC vesicle and BSA adsorption, which did not scale proportionally with their respective bulk RI sensitivities confirm a mismatch between surface and bulk sensitivities of the dip 1 and peak 2 spectral features (**Table S3.1**). Thus, while dip 1 exhibited higher bulk RI sensitivity than peak 2, *surface* sensitivities were *lower* for dip 1. This difference might arise from an enhanced electric field in the dip-sensitive region that extends over larger sensing volumes compared to the electric field of the peak-sensitive region, which is focused at the Au-solution interface and covers smaller sensing volumes. For nanoplasmonic sensors, the correlation between bulk and surface sensitivities is complex, as there are several interacting factors of importance, including nanoplasmonic transducer geometry, orientation, and dielectric coating.[69,70]

Particularly in the context of sensing applications, it is important to distinguish between bulk and surface sensitivities since changes in local refractive indices close to sensor surfaces are specific to molecular adsorption events. A more pronounced spike was observed in the shift of

the position of dip 1 (**Figure 3.4d**) compared to the peak 2 shift (**Figure S3.6b**) during buffer rinsing after BSA adsorption. This result suggests that the post-adsorption protein spreading on the In_2O_3-coated Au nanoribbon surfaces is significant and extends beyond the sensing volume of the peak-sensitive region. By contrast, the overall profiles of the shifts in the positions of the principal dips and peaks for DOPC vesicle adsorption indicated no significant lipid redistribution after rinsing.

Taken together, we have demonstrated the capability of Au nanoribbon arrays with a thin indium oxide coating prepared *via* a simple fabrication approach to detect the adsorption of biomolecules in real time. These arrays enabled post-adsorption changes in protein distribution to be monitored, providing new information on the interactions between serum albumin and oxide surfaces. While the importance of distinguishing bulk and surface sensitivities has been discussed,[71] our work highlights mismatches in the respective sensitivities of two plasmonic spectral features from the same sensor array, which were used to compare qualitatively the extent of adsorption of two different biomolecules.

3.5 Conclusions and Prospects

In summary, we report a high-throughput, large-scale, and low-cost nanofabrication approach to produce Au plasmonic sensors. Commercially available HD-DVDs were employed as large-area templates for soft lithography. Stamps patterned using HD-DVD templates possessed large-area nanoline features (200-nm linewidths with 400-nm pitch) and were used to fabricate subwavelength Au plasmonic sensors.

Optical characterization of indium oxide-coated Au nanoarrays revealed plasmon-active spectral features with varying bulk refractive index sensitivities (~60-500 nm/RIU). We utilized Au nanoribbon arrays for real-time sensing of DOPC vesicle or BSA adsorption, and exploited

the mismatch in bulk and surface sensitivities between key dip- and peak-sensitive regions to distinguish adsorptive properties of these two types of biomolecules. Together, these results demonstrate that scalable patterning by chemical lift-off lithography provides a straightforward approach for large-area plasmonic nanostructure fabrication with applications in optoelectronics and biointerfacial science. In this proof-of-concept work, we studied the interactions between biomolecules and nonfunctionalized nanostructure surfaces. Selective sensing could be achieved on functionalized nanoplasmonic surfaces, *e.g.*, with antibodies or DNA, towards antigen or complementary DNA detection, respectively.[10,58,72-74] Further work using the platform will use target-specific biomolecules, including DNA and antigens, to build a universal biosensor platform for broad applications.

3.6 Supplementary Materials

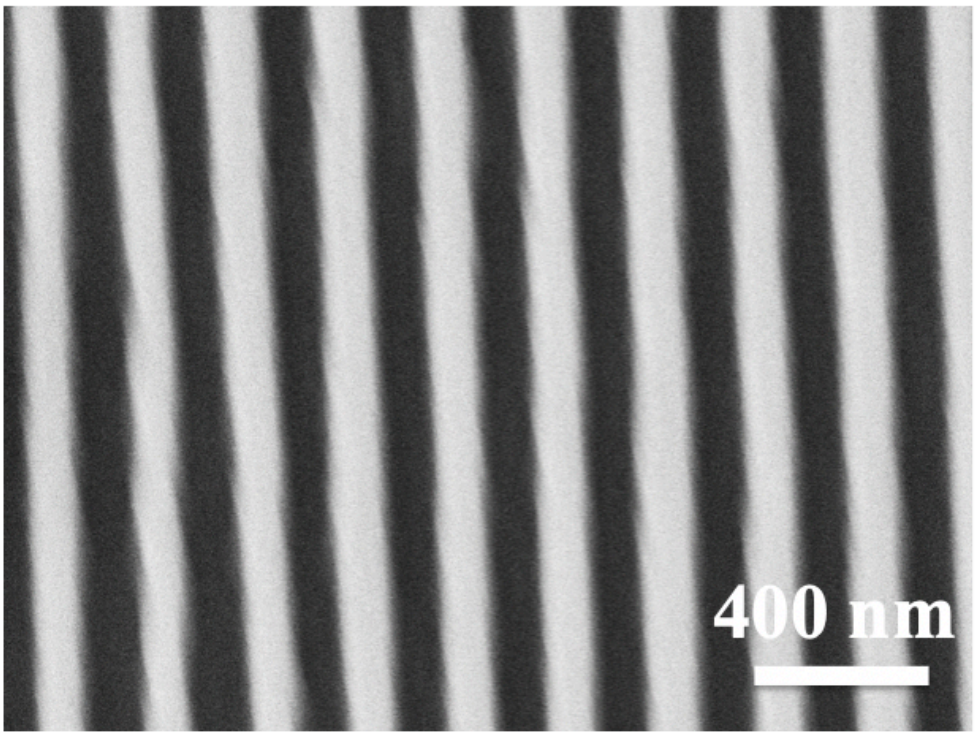

Figure S3.1. Scanning electron microscope image of Au nanoribbons after monolayer removal and before In_2O_3 deposition. This nanoribbon pattern was similar to the pattern observed after In_2O_3 deposition (main text Figure 3.3j).

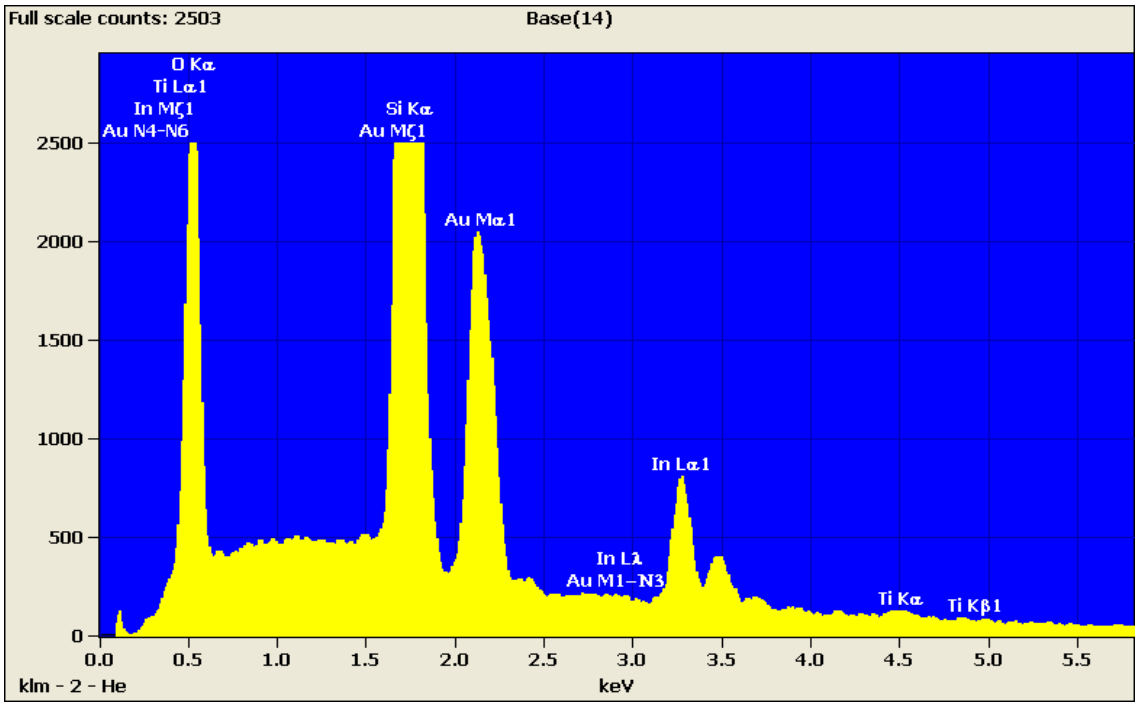

Figure S3.2. Energy-dispersive X-ray spectrum of an In_2O_3-coated Au nanoribbon substrate confirming the elemental presence of Au, Ti, In, and Si.

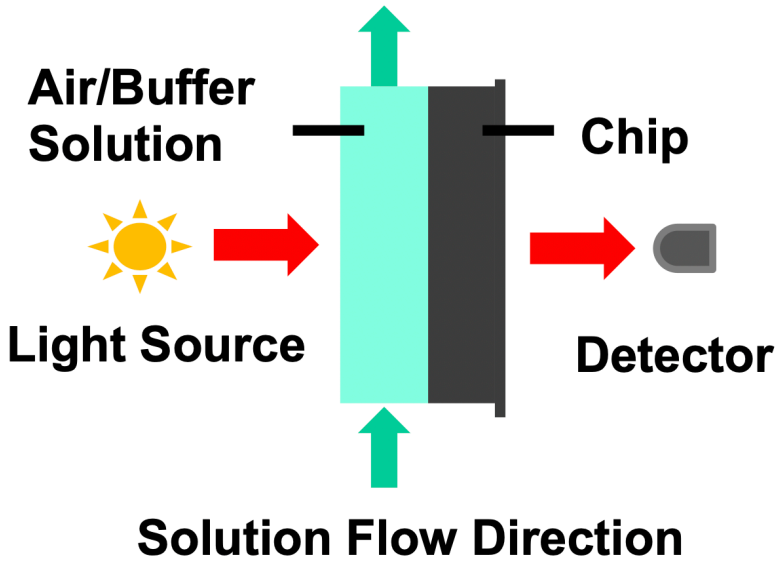

Figure S3.3. Flow-cell transmission spectra measurement set-up. Buffer and target solutions were interrogated during continuous flow.

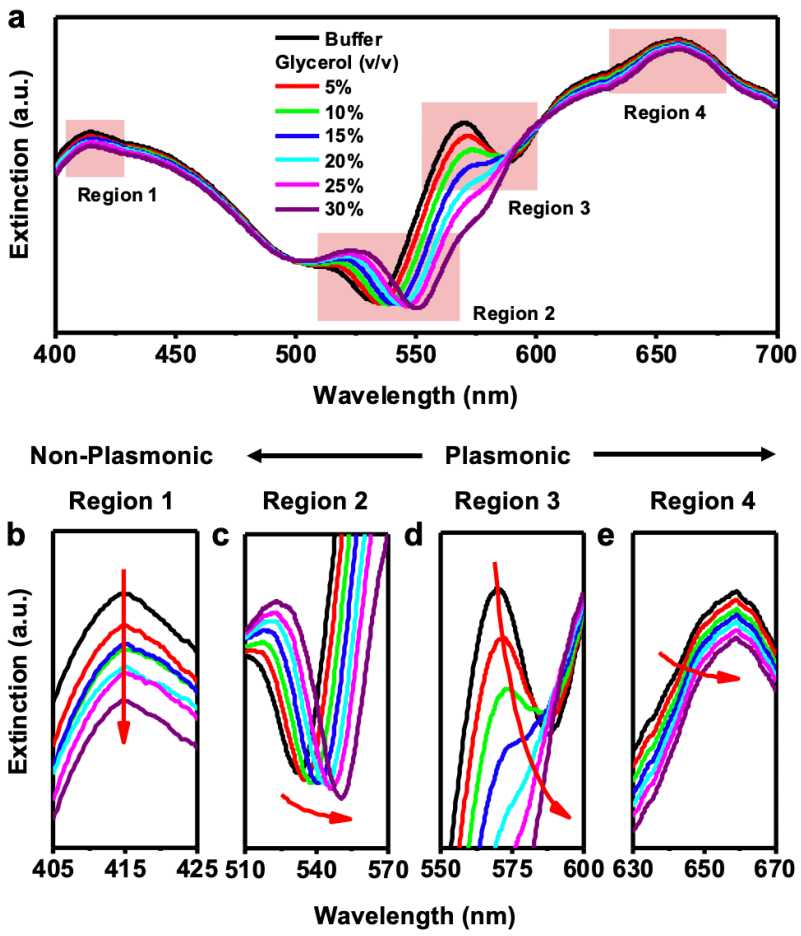

Figure S3.4. (a) Optical extinction spectra of a Au nanoribbon substrate in buffer and in glycerol-buffer mixtures with increasing glycerol fraction, highlighting distinct transformations to the features associated with different regions of the spectra under different bulk refractive indices of the solution. Over the course of the refractive index variation, the enlarged view in (b) of region 1 shows a peak with decreasing extinction intensity at the same wavelength position, indicating that it is a non-plasmonic feature relating to the blue light absorption of the Au film. By contrast, the features in (c) for region 2, (d) for region 3, and in (e) for region 4 show changes to both extinction intensity

and wavelength, indicating that these features arise from localized surface plasmon resonances attributed to the nanostructure geometry.

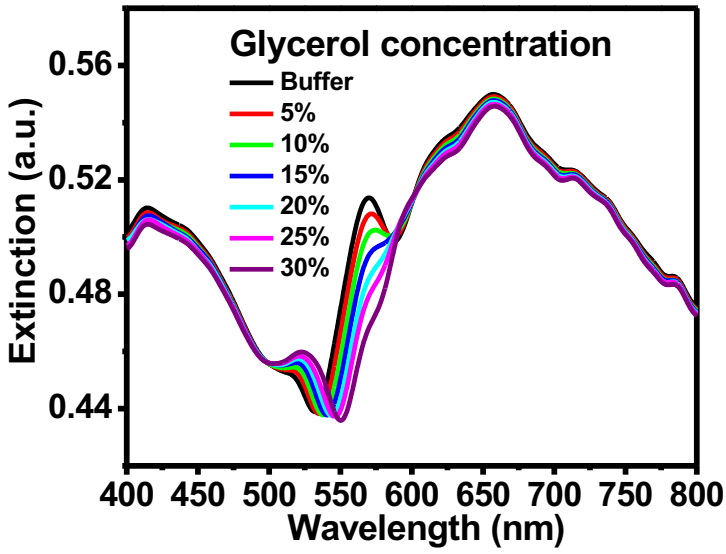

Figure S3.5. Full extinction spectra corresponding to main text Figure 3.3c for a Au nanoribbon array exposed to different concentrations of glycerol.

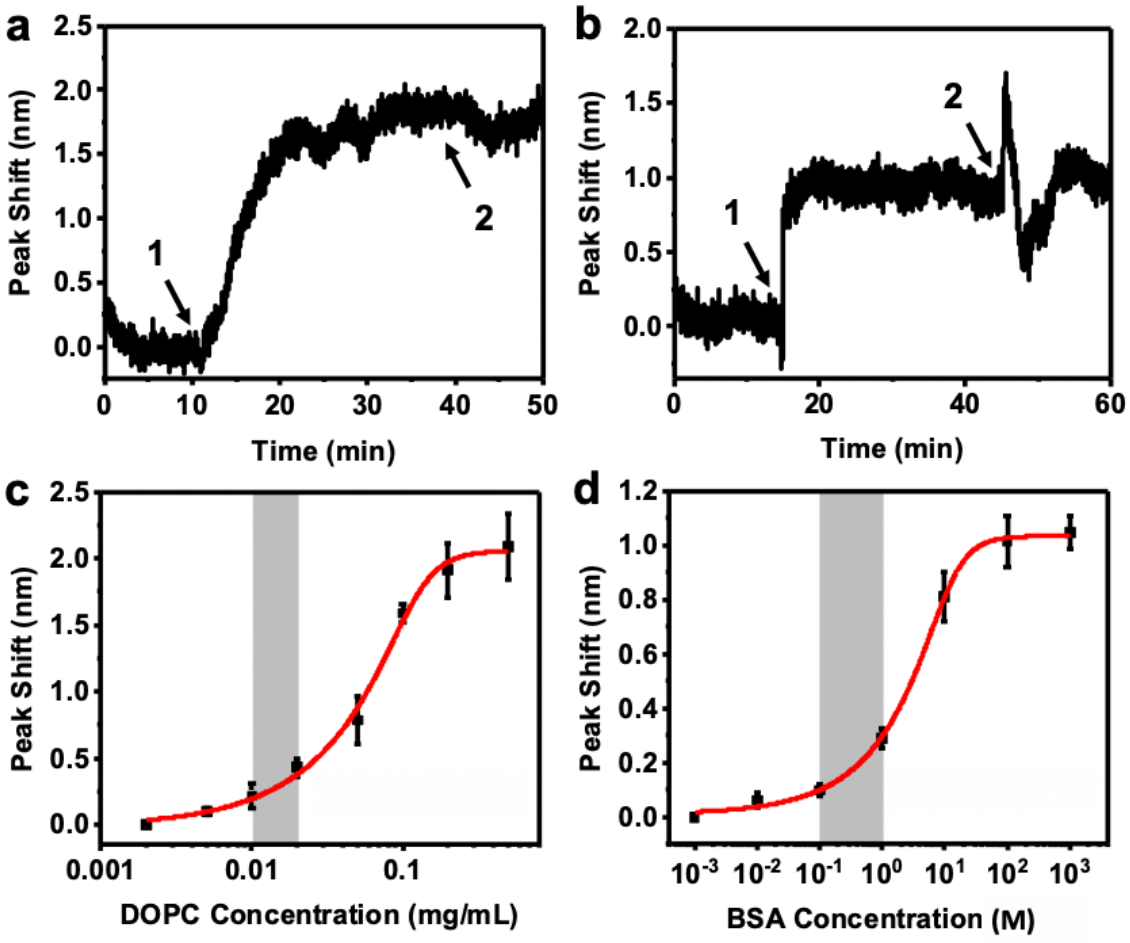

Figure S3.6. Time-resolved wavelength shifts of peak 2 during the adsorption of (a) DOPC lipid vesicles or (b) BSA protein. Arrows indicate the time points where (1) flow was switched from Tris buffer to buffer containing DOPC vesicles or BSA and (2) flow was switched back to buffer. Concentration dependence of the net wavelength shift (before washing) upon addition of (c) DOPC lipid vesicles or (d) BSA protein. Data are from *N*=3 runs repeated on the same substrate. Error bars represent standard deviations.

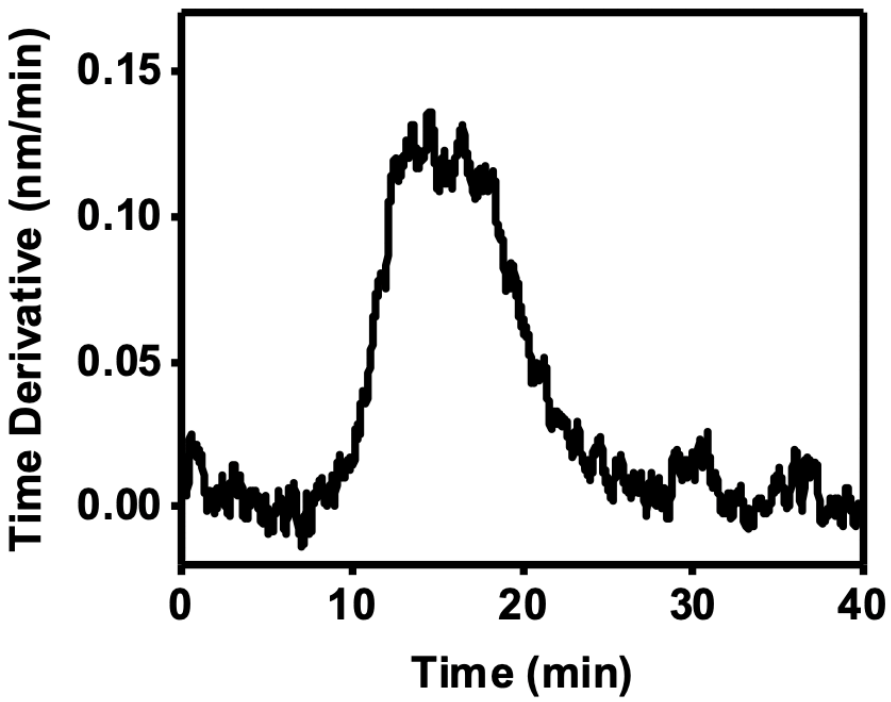

Figure S3.7. Time derivative of the shift of the dip, from Figure 3.4c.

Table S3.1. Summary of plasmonic responses.

	Calculated bulk RI sensitivity (nm/RIU)	Absolute wavelength shift for lipid vesicles (nm)	Normalized shift for lipid vesicle (RIU)	Absolute wavelength shift for BSA (nm)	Normalized shift for BSA (RIU)
Dip 1	510	1.2	0.002	1.2	0.002
Peak 2	60	2.0	0.033	1.0	0.16

3.7 References

(1) Anker, J. N.; Hall, W. P.; Lyandres, O.; Shah, N. C.; Zhao, J.; Van Duyne, R. P. Biosensing with Plasmonic Nanosensors. *Nat. Mater.* **2008,** *7*, 442–453.

(2) Dahlin, A. B.; Wittenberg, N. J.; Hook, F.; Oh, S. H. Promises and Challenges of Nanoplasmonic Devices for Refractometric Biosensing. *Nanophotonics* **2013,** *2*, 83–101.

(3) Sharpe, J. C.; Mitchell, J. S.; Lin, L.; Sedoglavich, N.; Blaikie, R. J. Gold Nanohole Array Substrates as Immunobiosensors. *Anal. Chem.* **2008,** *80*, 2244–2249.

(4) Yang, J. C.; Ji, J.; Hogle, J. M.; Larson, D. N. Metallic Nanohole Arrays on Fluoropolymer Substrates as Small Label-Free Real-Time Bioprobes. *Nano Lett.* **2008,** *8*, 2718–2724.

(5) Lee, S.-W.; Lee, K.-S.; Ahn, J.; Lee, J.-J.; Kim, M.-G.; Shin, Y.-B. Highly Sensitive Biosensing Using Arrays of Plasmonic Au Nanodisks Realized by Nanoimprint Lithography. *ACS Nano* **2011,** *5*, 897–904.

(6) Zheng, Y. B.; Payton, J. L.; Chung, C. H.; Liu, R.; Cheunkar, S.; Pathem, B. K.; Yang, Y.; Jensen, L.; Weiss, P. S. Surface-Enhanced Raman Spectroscopy to Probe Reversibly Photoswitchable Azobenzene in Controlled Nanoscale Environments. *Nano Lett.* **2011,** *11*, 3447–3452.

(7) Kumar, K.; Dahlin, A. B.; Sannomiya, T.; Kaufmann, S.; Isa, L.; Reimhult, E. Embedded Plasmonic Nanomenhirs as Location-Specific Biosensors. *Nano Lett.* **2013,** *13*, 6122–6129.

(8) Valsecchi, C.; Brolo, A. G. Periodic Metallic Nanostructures as Plasmonic Chemical Sensors. *Langmuir* **2013,** *29*, 5638–5649.

(9) Jackman, J. A.; Yorulmaz Avsar, S.; Ferhan, A. R.; Li, D.; Park, J. H.; Zhdanov, V. P.; Cho, N.-J. Quantitative Profiling of Nanoscale Liposome Deformation by a Localized Surface Plasmon Resonance Sensor. *Anal. Chem.* **2017,** *89*, 1102–1109.

(10) Oliverio, M.; Perotto, S.; Messina, G. C.; Lovato, L.; De Angelis, F. Chemical Functionalization of Plasmonic Surface Biosensors: A Tutorial Review on Issues, Strategies, and Costs. *ACS Appl. Mater. Inter.* **2017,** *9*, 29394–29411.

(11) Cetin, A. E.; Iyidogan, P.; Hayashi, Y.; Wallen, M.; Vijayan, K.; Tu, E.; Nguyen, M.; Oliphant, A. Plasmonic Sensor Could Enable Label-Free DNA Sequencing. *ACS Sensors* **2018,** *3*, 561–568.

(12) Willets, K. A.; Van Duyne, R. P. Localized Surface Plasmon Resonance Spectroscopy and Sensing. *Annu. Rev. Phys. Chem.* **2007,** *58*, 267–297.

(13) Anker, J. N.; Hall, W. P.; Lyandres, O.; Shah, N. C.; Zhao, J.; Van Duyne, R. P. Biosensing with Plasmonic Nanosensors. *Nat. Mater.* **2008,** *7*, 442–453.

(14) Spackova, B.; Wrobel, P.; Bockova, M.; Homola, J. Optical Biosensors Based on Plasmonic Nanostructures: A Review. *Proc. IEEE* **2016,** *104*, 2380–2408.

(15) Jackman, J. A.; Rahim Ferhan, A.; Cho, N.-J. Nanoplasmonic Sensors for Biointerfacial Science. *Chem. Soc. Rev.* **2017,** *46*, 3615–3660.

(16) Escobedo, C.; Brolo, A. G.; Gordon, R.; Sinton, D. Optofluidic Concentration: Plasmonic Nanostructure as Concentrator and Sensor. *Nano Lett*. **2012,** *12*, 1592–1596.

(17) Tokel, O.; Inci, F.; Demirci, U. Advances in Plasmonic Technologies for Point of Care Applications. *Chem. Rev*. **2014,** *114*, 5728–5752.

(18) Jeong, J. W.; Yang, S. R.; Hur, Y. H.; Kim, S. W.; Baek, K. M.; Yim, S.; Jang, H. I.; Park, J. H.; Lee, S. Y.; Park, C. O.; Jung, Y. S. High-Resolution Nanotransfer Printing Applicable to Diverse Surfaces *via* Interface-Targeted Adhesion Switching. *Nat. Commun*. **2014,** *5*, 5387.

(19) Wang, X.; Chang, T. W.; Lin, G.; Gartia, M. R.; Liu, G. L. Self-Referenced Smartphone-Based Nanoplasmonic Imaging Platform for Colorimetric Biochemical Sensing. *Anal. Chem*. **2017,** *89*, 611–615.

(20) Ballard, Z. S.; Shir, D.; Bhardwaj, A.; Bazargan, S.; Sathianathan, S.; Ozcan, A. Computational Sensing Using Low-Cost and Mobile Plasmonic Readers Designed by Machine Learning. *ACS Nano* **2017,** *11*, 2266–2274.

(21) Belushkin, A.; Yesilkoy, F.; Altug, H. Nanoparticle-Enhanced Plasmonic Biosensor for Digital Biomarker Detection in a Microarray. *ACS Nano* **2018,** *12*, 4453–4461.

(22) Narasimhan, V.; Siddique, R. H.; Lee, J. O.; Kumar, S.; Ndjamen, B.; Du, J.; Hong, N.; Sretavan, D.; Choo, H. Multifunctional Biophotonic Nanostructures Inspired by the Longtail Glasswing Butterfly for Medical Devices. *Nat. Nanotechnol*. **2018,** *13*, 512–519.

(23) Qin, D.; Xia, Y.; Whitesides, G. M. Soft Lithography for Micro- and Nanoscale Patterning. *Nat. Protocols* **2010,** *5*, 491–502.

(24) Saavedra, H. M.; Mullen, T. J.; Zhang, P.; Dewey, D. C.; Claridge, S. A.; Weiss, P. S. Hybrid Strategies in Nanolithography. *Rep. Prog. Phys.* **2010,** *73*, 036501.

(25) Shuster, M. J.; Vaish, A.; Cao, H. H.; Guttentag, A. I.; McManigle, J. E.; Gibb, A. L.; Martinez-Rivera, M.; Nezarati, R. M.; Hinds, J. M.; Liao, W. S.; Weiss, P. S.; Andrews, A. M. Patterning Small-Molecule Biocapture Surfaces: Microcontact Insertion Printing vs. Photolithography. *Chem. Comm.* **2011,** *47*, 10641–10643.

(26) Liao, W. S.; Cheunkar, S.; Cao, H. H.; Bednar, H. R.; Weiss, P. S.; Andrews, A. M. Subtractive Patterning via Chemical Lift-Off Lithography. *Science* **2012,** *337*, 1517–1521.

(27) Kim, J.; Rim, Y. S.; Chen, H.; Cao, H. H.; Nakatsuka, N.; Hinton, H. L.; Zhao, C.; Andrews, A. M.; Yang, Y.; Weiss, P. S. Fabrication of High-Performance Ultrathin In_2O_3 Film Field-Effect Transistors and Biosensors Using Chemical Lift-Off Lithography. *ACS Nano* **2015,** *9*, 4572–4582.

(28) Abendroth, J. M.; Nakatsuka, N.; Ye, M.; Kim, D.; Fullerton, E. E.; Andrews, A. M.; Weiss, P. S. Analyzing Spin Selectivity in DNA-Mediated Charge Transfer *via* Fluorescence Microscopy. *ACS Nano* **2017,** *11*, 7516–7526.

(29) Xu, X.; Yang, Q.; Cheung, K. M.; Zhao, C.; Wattanatorn, N.; Belling, J. N.; Abendroth, J. M.; Slaughter, L. S.; Mirkin, C. A.; Andrews, A. M.; Weiss, P. S. Polymer-Pen Chemical Lift-Off Lithography. *Nano Lett.* **2017,** *17*, 3302–3311.

(30) Zhao, C.; Xu, X.; Yang, Q.; Man, T.; Jonas, S. J.; Schwartz, J. J.; Andrews, A. M.; Weiss, P. S. Self-Collapse Lithography. *Nano Lett.* **2017,** *17*, 5035–5042.

(31) Cheung, K. M.; Stemer, D. M.; Zhao, C.; Young, T. D.; Belling, J. N.; Andrews, A. M.; Weiss, P. S. Chemical Lift-Off Lithography of Metal and Semiconductor Surfaces. *ACS Mater. Lett*. **2019,** *2*, 76–83.

(32) Andrews, A. M.; Liao, W. S.; Weiss, P. S. Double-Sided Opportunities Using Chemical Lift-Off Lithography. *Acct. Chem. Res*. **2016,** *49*, 1449–1457.

(33) Cao, H. H.; Nakatsuka, N.; Liao, W.-S.; Serino, A. C.; Cheunkar, S.; Yang, H.; Weiss, P. S.; Andrews, A. M. Advancing Biocapture Substrates *via* Chemical Lift-Off Lithography. *Chem. Mater*. **2017,** *29*, 6829–6839.

(34) Cao, H. H.; Nakatsuka, N.; Serino, A. C.; Liao, W. S.; Cheunkar, S.; Yang, H.; Weiss, P. S.; Andrews, A. M. Controlled DNA Patterning by Chemical Lift-Off Lithography: Matrix Matters. *ACS Nano* **2015,** *9*, 11439–11454.

(35) Zhao, C.; Xu, X.; Bae, S. H.; Yang, Q.; Liu, W.; Belling, J. N.; Cheung, K. M.; Rim, Y. S.; Yang, Y.; Andrews, A. M.; Weiss, P. S. Large-Area, Ultrathin Metal-Oxide Semiconductor Nanoribbon Arrays Fabricated by Chemical Lift-Off Lithography. *Nano Lett*. **2018,** *18*, 5590–5595.

(36) Langhammer, C.; Larsson, E. M.; Kasemo, B.; Zoric, I. Indirect Nanoplasmonic Sensing: Ultrasensitive Experimental Platform for Nanomaterials Science and Optical Nanocalorimetry. *Nano Lett*. **2010,** *10*, 3529–3538.

(37) Li, J. Q.; Ye, J.; Chen, C.; Li, Y.; Verellen, N.; Moshchalkov, V. V.; Lagae, L.; Van Dorpe, P. Revisiting the Surface Sensitivity of Nanoplasmonic Biosensors. *ACS Photonics* **2015,** *2*, 425–431.

(38) Zen, F.; Karanikolas, V. D.; Behan, J. A.; Andersson, J.; Ciapetti, G.; Bradley, A. L.; Colavita, P. E. Nanoplasmonic Sensing at the Carbon-Bio Interface: Study of Protein Adsorption at Graphitic and Hydrogenated Carbon Surfaces. *Langmuir* **2017,** *33*, 4198–4206.

(39) Zan, G. H.; Jackman, J. A.; Kim, S. O.; Cho, N. J. Controlling Lipid Membrane Architecture for Tunable Nanoplasmonic Biosensing. *Small* **2014,** *10*, 4828–4832.

(40) Jackman, J. A.; Zhdanov, V. P.; Cho, N.-J. Nanoplasmonic Biosensing for Soft Matter Adsorption: Kinetics of Lipid Vesicle Attachment and Shape Deformation. *Langmuir* **2014,** *30*, 9494–9503.

(41) Jackman, J. A.; Spackova, B.; Linardy, E.; Kim, M. C.; Yoon, B. K.; Homola, J.; Cho, N.-J. Nanoplasmonic Ruler to Measure Lipid Vesicle Deformation. *Chem. Comm.* **2016,** *52*, 76–79.

(42) Jackman, J. A.; Ferhan, A. R.; Yoon, B. K.; Park, J. H.; Zhdanov, V. P.; Cho, N. J. Indirect Nanoplasmonic Sensing Platform for Monitoring Temperature-Dependent Protein Adsorption. *Anal. Chem.* **2017,** *89*, 12976–12983.

(43) Ferhan, A. R.; Jackman, J. A.; Cho, N.-J. Investigating How Vesicle Size Influences Vesicle Adsorption on Titanium Oxide: A Competition between Steric Packing and Shape Deformation. *Phys. Chem. Chem. Phys.* **2017,** *19*, 2131–2139.

(44) Junesch, J.; Emilsson, G.; Xiong, K.; Kumar, S.; Sannomiya, T.; Pace, H.; Voros, J.; Oh, S. H.; Bally, M.; Dahlin, A. B. Location-Specific Nanoplasmonic Sensing of Biomolecular Binding to Lipid Membranes with Negative Curvature. *Nanoscale* **2015,** *7*, 15080–15085.

(45) Ferhan, A. R.; Jackman, J. A.; Malekian, B.; Xiong, K.; Emilsson, G.; Park, S.; Dahlin, A. B.; Cho, N. J. Nanoplasmonic Sensing Architectures for Decoding Membrane Curvature-Dependent Biomacromolecular Interactions. *Anal. Chem.* **2018,** *90*, 7458–7466.

(46) Wu, H.-Y.; Chu, H.-C.; Kuo, T.-J.; Kuo, C.-L.; Huang, M. H. Seed-Mediated Synthesis of High Aspect Ratio Gold Nanorods with Nitric Acid. *Chem. Mater.* **2005,** *17*, 6447–6451.

(47) Yasukuni, R.; Ouhenia-Ouadahi, K.; Boubekeur-Lecaque, L.; Félidj, N.; Maurel, F.; Métivier, R.; Nakatani, K.; Aubard, J.; Grand, J. Silica-Coated Gold Nanorod Arrays for Nanoplasmonics Devices. *Langmuir* **2013,** *29*, 12633–12637.

(48) Wang, Y.-N.; Wei, W.-T.; Yang, C.-W.; Huang, M. H. Seed-Mediated Growth of Ultralong Gold Nanorods and Nanowires with a Wide Range of Length Tunability. *Langmuir* **2013,** *29*, 10491–10497.

(49) Miller, M. M.; Lazarides, A. A. Sensitivity of Metal Nanoparticle Surface Plasmon Resonance to the Dielectric Environment. *J. Phys. Chem. B* **2005,** *109*, 21556–21565.

(50) Lee, K.-S.; El-Sayed, M. A. Gold and Silver Nanoparticles in Sensing and Imaging: Sensitivity of Plasmon Response to Size, Shape, and Metal Composition. *J. Phys. Chem. B* **2006,** *110*, 19220–19225.

(51) Link, S.; El-Sayed, M. A. Spectral Properties and Relaxation Dynamics of Surface Plasmon Electronic Oscillations in Gold and Silver Nanodots and Nanorods. *J. Phys. Chem. B* **1999,** *103*, 8410–8426.

(52) Schmucker, A. L.; Harris, N.; Banholzer, M. J.; Blaber, M. G.; Osberg, K. D.; Schatz, G. C.; Mirkin, C. A. Correlating Nanorod Structure with Experimentally Measured and Theoretically Predicted Surface Plasmon Resonance. *ACS Nano* **2010,** *4*, 5453–5463.

(53) Zhang, S.; Chen, L.; Huang, Y.; Xu, H. Reduced Linewidth Multipolar Plasmon Resonances in Metal Nanorods and Related Applications. *Nanoscale* **2013,** *5*, 6985–6991.

(54) Lide, D. R. Crc Handbook of Chemistry and Physics. *CRC Press, Boca Raton, USA* **2001,** *76*, 1995–1996.

(55) Xiong, K.; Emilsson, G.; Dahlin, A. B. Biosensing Using Plasmonic Nanohole Arrays with Small, Homogenous and Tunable Aperture Diameters. *Analyst* **2016,** *141*, 3803–3810.

(56) Ode, K.; Honjo, M.; Takashima, Y.; Tsuruoka, T.; Akamatsu, K. Highly Sensitive Plasmonic Optical Sensors Based on Gold Core–Satellite Nanostructures Immobilized on Glass Substrates. *ACS Appl. Mater. Inter.* **2016,** *8*, 20522–20526.

(57) Malekian, B.; Xiong, K.; Emilsson, G.; Andersson, J.; Fager, C.; Olsson, E.; Larsson-Langhammer, E.; Dahlin, A. Fabrication and Characterization of Plasmonic Nanopores with Cavities in the Solid Support. *Sensors* **2017,** *17*, 1444.

(58) Homola, J. Surface Plasmon Resonance Sensors for Detection of Chemical and Biological Species. *Chem. Rev.* **2008,** *108*, 462–493.

(59) Ferhan, A. R.; Jackman, J. A.; Sut, T. N.; Cho, N. J. Quantitative Comparison of Protein Adsorption and Conformational Changes on Dielectric-Coated Nanoplasmonic Sensing Arrays. *Sensors (Basel)* **2018,** *18*, 1283.

(60) Sweryda-Krawiec, B.; Devaraj, H.; Jacob, G.; Hickman, J. J. A New Interpretation of Serum Albumin Surface Passivation. *Langmuir* **2004,** *20*, 2054–2056.

(61) Reimhult, K.; Petersson, K.; Krozer, A. Qcm-D Analysis of the Performance of Blocking Agents on Gold and Polystyrene Surfaces. *Langmuir* **2008,** *24*, 8695–8700.

(62) Jeyachandran, Y. L.; Mielczarski, J. A.; Mielczarski, E.; Rai, B. Efficiency of Blocking of Non-Specific Interaction of Different Proteins by BSA Adsorbed on Hydrophobic and Hydrophilic Surfaces. *J. Colloid Interface Sci.* **2010,** *341*, 136–142.

(63) Park, J. H.; Sut, T. N.; Jackman, J. A.; Ferhan, A. R.; Yoon, B. K.; Cho, N.-J. Controlling Adsorption and Passivation Properties of Bovine Serum Albumin on Silica Surfaces by Ionic Strength Modulation and Cross-Linking. *Phys. Chem. Chem. Phys.* **2017,** *19*, 8854–8865.

(64) Frost, R.; Wadell, C.; Hellman, A.; Molander, S.; Svedhem, S.; Persson, M.; Langhammer, C. Core-Shell Nanoplasmonic Sensing for Characterization of Biocorona Formation and Nanoparticle Surface Interactions. *ACS Sensors* **2016,** *1*, 798–806.

(65) Frost, R.; Langhammer, C.; Cedervall, T. Real-Time in Situ Analysis of Biocorona Formation and Evolution on Silica Nanoparticles in Defined and Complex Biological Environments. *Nanoscale* **2017,** *9*, 3620–3628.

(66) Ke, P. C.; Lin, S.; Parak, W. J.; Davis, T. P.; Caruso, F. A Decade of the Protein Corona. *ACS Nano* **2017,** *11*, 11773–11776.

(67) Xu, M.; Soliman, M. G.; Sun, X.; Pelaz, B.; Feliu, N.; Parak, W. J.; Liu, S. J. How Entanglement of Different Physicochemical Properties Complicates the Prediction of in Vitro and in Vivo Interactions of Gold Nanoparticles. *ACS Nano* **2018,** *12*, 10104–10113.

(68) Park, J. H.; Jackman, J. A.; Ferhan, A. R.; Ma, G. J.; Yoon, B. K.; Cho, N. J. Temperature-Induced Denaturation of BSA Protein Molecules for Improved Surface Passivation Coatings. *ACS Appl. Mater. Inter.* **2018,** *10*, 32047–32057.

(69) Li, J.; Ye, J.; Chen, C.; Li, Y.; Verellen, N.; Moshchalkov, V. V.; Lagae, L.; Van Dorpe, P. Revisiting the Surface Sensitivity of Nanoplasmonic Biosensors. *ACS Photonics* **2015,** *2*, 425–431.

(70) Li, J.; Chen, C.; Lagae, L.; Van Dorpe, P. Nanoplasmonic Sensors with Various Photonic Coupling Effects for Detecting Different Targets. *J. Phys. Chem. C* **2015,** *119*, 29116–29122.

(71) Szunerits, S.; Boukherroub, R. Sensing Using Localised Surface Plasmon Resonance Sensors. *Chem. Comm.* **2012,** *48*, 8999–9010.

(72) Belushkin, A.; Yesilkoy, F.; Gonzalez-Lopez, J. J.; Ruiz-Rodriguez, J. C.; Ferrer, R.; Fabrega, A.; Altug, H. Rapid and Digital Detection of Inflammatory Biomarkers Enabled by a Novel Portable Nanoplasmonic Imager. *Small* **2019**, e1906108.

(73) Špačková, B.; Lynn, N. S.; Slabý, J.; Šípová, H.; Homola, J. A Route to Superior Performance of a Nanoplasmonic Biosensor: Consideration of Both Photonic and Mass Transport Aspects. *ACS Photonics* **2018,** *5*, 1019–1025.

(74) Yoo, S. Y.; Kim, D. K.; Park, T. J.; Kim, E. K.; Tamiya, E.; Lee, S. Y. Detection of the Most Common Corneal Dystrophies Caused by Bigh3 Gene Point Mutations Using a Multispot Gold-Capped Nanoparticle Array Chip. *Anal. Chem.* **2010,** *82*, 1349–1357.

Chapter 4

Photothermal Intracellular Delivery Using Gold Nanodisk Arrays

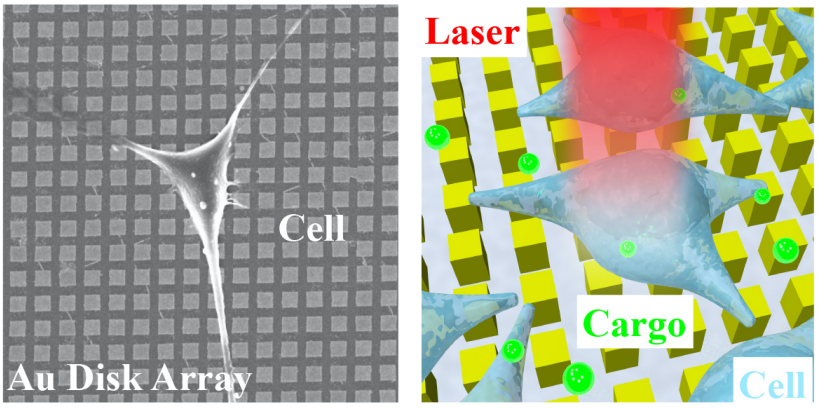

The information in this chapter is reprinted with permission from

ACS Mater. Lett. **2020**, *2*, 1475–1483 Copyright (2020) American Chemical Society

Authors: **Zhao, C.**; Man, T.; Xu, X.; Yang, Q.; Liu, W.; Jonas, S. J.; Teitell, M. A.; Chiou, P. Y.; Weiss, P. S.

4.1 Abstract

Local heating using pulsed laser-induced photothermal effects on plasmonic nanostructured substrates can be used for intracellular delivery applications. However, the fabrication of plasmonic nanostructured interfaces is hampered by complex nanomanufacturing schemes. Here, we demonstrate the fabrication of large-area plasmonic gold (Au) nanodisk arrays that enable photothermal intracellular delivery of biomolecular cargo at high efficiency. The Au nanodisks (350 nm in diameter) were fabricated using chemical lift-off lithography (CLL). Nanosecond laser pulses were used to excite the plasmonic nanostructures, thereby generating transient pores at the outer membranes of targeted cells that enable the delivery of biomolecules *via* diffusion. Delivery efficiencies of >98% were achieved using the cell impermeable dye calcein (0.6 kDa) as a model payload, while maintaining cell viabilities at >98%. The highly efficient intracellular delivery approach demonstrated in this work will facilitate translational studies targeting molecular screening and drug testing that bridge laboratory and clinical investigations.

4.2 Introduction

Intracellular delivery of exogenous cargo, such as nucleic acids,[1-4] proteins,[5,6] and membrane-impermeable drugs,[6-8] is of great importance across a spectrum of biomedical and therapeutic applications, including precision gene modification,[9-12] immunotherapy,[13-15] intracellular imaging/sensing,[16,17] drug delivery,[6,8,18,19] and regenerative medicine.[20,21] To date, efforts towards intracellular delivery have been advanced by carrier-based and membrane-disruption-based approaches.[22-24] Viral-vector-based methods remain the most clinically advanced carrier-based strategies, achieving nucleic acid delivery with high efficiencies and specificities.[25,26] However, challenges associated with their potential immunogenicity, safety concerns from off-target effects, complexity, and high costs have limited their broader application.[25] Moreover, viral-based carrier systems suffer from intrinsic limitations in their cargo-carrying capacity, which preclude effective complex biomolecules or mixtures of components. Membrane-disruption-based approaches,[23,27,28] where transient pores are created in cell membranes *via* mechanical,[24,29-35] electrical,[36,37] or photothermal methods,[38-44] are less dependent on cargo and cell type.[45] Electroporation-based methods yield appropriate efficiencies but suffer from low viability and require specialized equipment and reagents.[22,46-49] Strategies using nanostructures, such as nanowires,[50,51] nanostraws,[52-54] and nanoneedles[30,55-58] to create pores in cell membranes, have also been shown to have suitable efficiencies and viabilities for intracellular delivery, but are limited by poor reproducibility, slow processing throughputs, and complicated fabrication processes.

Photothermal strategies that utilize the generation of cavitation bubbles induced by laser irradiation of noble metal nanoparticles or metal plasmonic structures represent another promising membrane-disruption method.[59,60] Upon laser irradiation, metallic nanostructures

absorb incident photon energy through electron oscillations, which results in abrupt temperature increases in the surrounding aqueous medium.[61,62] Explosive cavitation bubbles nucleate when the temperature exceeds the critical temperature of the aqueous medium.[43] Large fluid shear stress induced by the rapid expansion and collapse of cavitation generates transient and localized pores an adjacent cell membrane.[63] The size of cavitation bubbles dependents on the laser fluences radiated, which has been previously studied to be in the range of 100 nm to 1 μm.[64] Previous studies have demonstrated that noble metal nanoparticles, such as Au nanoparticles, are well suited to serve as high-efficiency delivery agents.[38-44,65,66] However, the cytotoxicity of Au nanoparticles is still under investigation, and this method also suffers from limitations in reproducibility. For example, it has been shown that the number and the location of pores created on each cell is not well controlled due to the random distribution of nanoparticles. Moreover, high delivery efficiencies achieved with increased nanoparticle concentration typically resulted in compromised cell viability.[67] Alternatively, substrate-supported plasmonic structures, fabricated using micro- and nanolithography techniques, serve as promising platforms for high-efficiency and high-viability intracellular delivery.[6,8,19,68] In addition, because of the physical separation of the nanostructures, the stoichiometry of the interactions with the cells can be controlled precisely (as compared to the case for plasmonic nanoparticles). Current methods of producing plasmonic architectures for photothermal delivery applications are limited by time consuming and costly conventional nanolithographic fabrication processes (*e.g.*, electron-beam lithography) used to pattern metal layers, which hinder the scalability of these techniques and represent a critical barrier to applying these technologies to clinical targets. Alternatively, nanofabrication approaches that yield repeatable, scalable, and economical processing of plasmonic nanostructures could facilitate consideration of this approach for wide-scale clinical

applications. Recent advances have been made in producing plasmonic structures using template-stripping processes. For example, nanopyramid structures have been fabricated in an economical and high-throughput manner.[8] However, challenges remain for a facile fabrication process as the template stripping process requires the fabrication on a polymer layer and an extra transfer process.

Soft lithography uses soft polymeric stamps to fabricate a range of micro- and nanoscale features in a high-throughput, large-scale, and cost-effective manner.[69,70] Microcontact printing (μCP), as a representative soft lithography method, transfers molecular inks, such as alkanethiols, from stamp to target surfaces.[70,71] A complementary, subtractive soft lithography process chemical lift-off lithography (CLL), uses oxygen plasma-activated polydimethylsiloxane (PDMS) stamps to remove self-assembled monolayer (SAM) molecules selectively from contacted areas on surfaces to create patterns over large areas, and may be used to achieve high-fidelity chemical patterns with line widths approaching 5 nm (corresponding to patterns ~10 molecules across).[72-79] The remaining SAM molecules in the non-lifted-off regions can act as resists to enable selective etching of exposed Au to produce Au nanostructures, such as Au nanolines, nanocircles, and nanosquares.[74,79-81]

In this work, we apply CLL to achieve fabrication of Au plasmonic nanostructures over large areas for photothermal intracellular delivery. Large-area two-dimensional (2D) Au nanodisk arrays are fabricated across centimeter length scales on a variety of substrates, such as silicon wafers, glass slices, and plastic petri dishes, which provides a significant advantage for versatile intracellular delivery environments and creates opportunities for integration with medical devices. Nanodisk arrays of different sizes have been fabricated in this study to measure delivery efficiencies and cell viabilities as a function of nanostructure surface density per cell.

Upon excitation of the nanodisks with a nanosecond laser, delivery efficiencies of >98% and cell viabilities of >98% were achieved using 0.6 kDa cell membrane-impermeable calcein as a model cargo molecule, which is comparable with current photothermal intracellular delivery platforms. This work demonstrates a promising economical and reproducible intracellular delivery approach, with widespread applicability for drug delivery, nanoparticle delivery, and regenerative medicine.

4.3 Materials and Methods

Materials. Prime quality 4″ silicon (Si) wafers (P/B, 0.001-0.005 Ω·cm, thickness 500 μm) were purchased from Silicon Valley Microelectronics, Inc. (Santa Clara, CA, USA). Sylgard 184® silicone elastomer kits were purchased from Ellsworth Adhesives (Germantown, WI, USA). Iron nitrate, and thiourea were purchased from Sigma-Aldrich (St. Louis, MO, USA) and used as received. Deionized water (18.2 MΩ·cm) from a Milli-Q system (Millipore, Billerica, MA) was used in all experiments.

Chemical lift-off lithography. Gold nanodisk substrates were prepared *via* chemical lift-off lithography (CLL).[79] Briefly**,** a CHA solution electron-beam evaporator was used to first deposit a 10-nm-thick titanium (Ti) adhesion layer followed by a 30-nm gold (Au) film onto desired substrates. The substrates were then annealed in a hydrogen flame for ~10 s before immersion into 1 mM 11-mercapto-1-undecanol solution for over 12 h. Polydimethylsiloxane (PDMS) stamps[S1] were exposed to oxygen plasma (Harrick Plasma, Ithaca, NY) for 40 s at a power of 18 W and a pressure of 10 psi for activation before contact with the substrate for over 12 h. After the PDMS stamps were lifted-off, the substrate was then immersed into an aqueous solution of 20 mM iron nitrate and 30 mM thiourea for 30 min to etch the Au film selectively within the exposed area. The etch rate was ~1 nm/min. Substrates were then rinsed with

deionized water, dried under a stream of N_2 before use, and sterilized *via* ultraviolet (UV) irradiation overnight.

Characterization. Scanning electron microscope (SEM) images were obtained using a Zeiss Supra 40VP scanning electron microscope with an Inlens SE Detector (Inlens secondary electron detector). Atomic force microscope (AFM) imaging was performed on a Bruker FastScan system using peak force tapping mode with ScanAsyst-Air tips. Optical images were taken with a Zeiss Axiotech optical microscope. Fluorescence images were taken with an upright fluorescence microscope (Axio Scope.A1, Carl Zeiss) equipped with a 10× objective lens.

Cell Seeding and Culture on Substrate. HeLa cells (ATCC) were maintained in Dulbecco's modified essential medium (DMEM, Corning) supplemented with 10% (vol/vol) fetal bovine serum (FBS, Thermo Scientific), 1% penicillin/streptomycin (Mediatech), and 1% sodium pyruvate (Corning). Chips were coated with fibronectin (Sigma, 40 μg/mL in phosphate-buffered saline, PBS) to promote cell adhesion. HeLa cells were seeded on to the chip and kept in an incubator at 37 °C and 5% CO_2 for 24 h. Cells were stained with 1 μg/mL Calcein AM (Invitrogen) to show cell seeding results.

Cell Fixation. Chips with HeLa cells were rinsed with PBS three times and soaked in 4% paraformaldehyde in PBS for 20 min at room temperature. The chips were then removed from the paraformaldehyde solution and were then rinsed with PBS three times prior to immersion in ethanol of graded concentrations (50%, 70%, 90%, and 100%) for 5 min each. And then hexamethyldisilazane (HMDS) three times for 7 min each. Samples were then air dried overnight prior to analysis.

Laser-Scanning and Delivery Setup. A Q-switched Nd:YAG laser (Minilite I, Continuum) with wavelength of 532 nm, beam diameter of 3 mm, and pulse duration of 6 ns was used to scan each sample. A half-wave polarizer and polarizing beam splitter designed for a 532 nm laser was used to adjust the power splitting ratio of the two beams. Laser energy was checked prior to each experiment using a laser energy meter (Nova II, Ophir). Sample were placed on an automated X-Y translation stage to expose their entire 1 cm^2 area to the laser beam (Figure S1). As shown in the schematic, the laser beam was directed from the top of the sample. We used 35-mm petri dishes to hold the sample in the center during the laser pulsing, which mitigates the effect of the meniscus. The laser beam is 3 mm in diameter, while the HeLa cell sizes are in the range of tens of microns. In our experiments, cells were treated with single laser pulses to obtain the current results.

Fluorescence Microscopy and Cell Counting. Scanning Cells were incubated in 37 °C and 5% CO_2 for 90 min before checking delivery efficiency and viability. The cell permeable nuclear dye Hoechst 33342 was used to label all processed cells for ease of quantifying the total number of cells present on each chip. HeLa cells that retained the cell-impermeable calcein molecules represented successful delivery. Cell viability was determined using propidium iodide (5 μg/mL), which is permeable to dead cells. Cell number was determined using both the automatic counting algorithm of the Fiji image processing software package and manual counting to double check. Each data point in **Figure 4.5e-g** represents the mean value of at least 3 randomly selected fields of view with at least 200 cells; error bars represent standard deviation.

Numerical Simulations. Temperature distributions from the plasmonic structures were modeled using a finite element method (COMSOL, Multiphysics 5.3) to calculate substrate-light

interactions. The geometry was constructed based on the dimensions of the actual nanodisk chips. Electromagnetic wave with linear polarization in diagonal direction was applied, which is consistent with experimental configurations. Electromagnetic interaction was calculated using a scattered field formulation method in the z direction (wavelength = 532 nm, fluence = 11 mJ/cm^2) and the resistive loss was used as the heat source for transient heat transfer. Perfectly matched layers were applied to truncate the modeling domain.

4.4. Results and Discussions

We exploit the plasmonic properties of the gold nanodisks whereby exposure to nanosecond laser pulses generates cavitation bubbles with energies sufficient to puncture cellular membranes, forming pores that facilitate intracellular delivery of desired cargo (**Figure 4.1**). HeLa cells, used as a model cell line, were cultured onto CLL-patterned nanodisk substrates and placed in a growth medium containing calcein. By scanning the laser across the wafer-scale Au plasmonic substrate, plasmonic hotspots formed upon illumination. Cavitation bubbles generated at these local regions in contacting the plasma membranes of the target HeLa cells serve as projectiles that render the cells transiently permeable. Cargo molecules within the surrounding medium are able to enter the cytoplasm *via* diffusion.[6] Precision control of the pulsed-laser spot position across the substrate is maintained with a pair of X-Y scanning mirrors. It takes 10 s to scan across the entire 25-mm^2 chip, with over 10^4 cells per chip.

The fabrication of periodic metal nanostructures with micron-scale features can be achieved readily *via* conventional photolithography, while producing sub-micron features often requires specialized tools such as electron beam lithography (EBL) and focused ion beam lithography (FIB). However, these serial writing processes systems are time consuming and costly to operate, leading to extremely limited production yields and output. Transfer printing

techniques, such as nanotransfer printing, provide an alternative solution for nanofabrication over large areas while achieving higher processing throughputs.[82] Existing nanoscale printing approaches are limited to certain substrates based on surface energy constraints that are critical for successful and reproducible pattern transfer. In this study, we extend the applications of CLL for biomedical applications. Double-patterning CLL has been recently reported as a means of fabricating Au plasmonic nanodisk arrays (**Figure 4.2a**).[81] Polydimethylsiloxane stamps, textured with lines of different widths and pitches are activated by exposure to oxygen plasma to generate hydrophilic silanol groups at the stamp surface. Substrates for CLL (*e.g.*, silicon wafers) are coated with a thin layer of Au (30 nm) that is functionalized with a hydroxyl-terminated alkanethiol (11-mercapto-1-undecanol) SAM. Conformal contact between the stamp and the substrate leads to condensation reactions between OH-groups of SAM and the silanol groups of activated PDMS, leading to the formation of covalent bonds (Si–O–SAM). Lifting the stamp from the substrate results in selective removal of the SAM corresponding to the stamp's pattern, leaving SAM molecules within the non-contacted regions that establish a series of nanoscale lines. A second CLL step was then carried out using a re-activated stamp that is rotated 90° and registered to the initial pattern. After the second patterning step, arrays comprised of SAM nanosquares are produced, which serve as molecular resists during the subsequent wet etching to generate 2D Au nanodisk substrates.

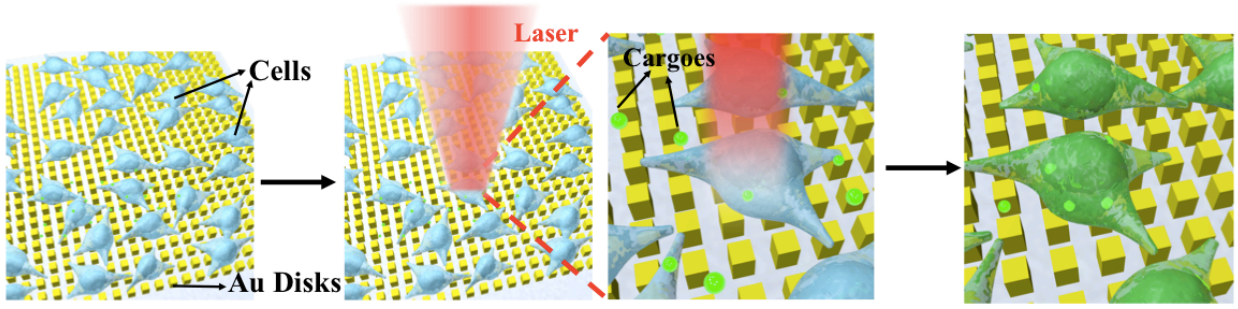

Figure 4.1. (a) Illustration of photothermal intracellular delivery enabled by localized surface plasmon resonance (LSPR) of gold nanodisks excited by a nanosecond laser. After cell seeding, the laser was rastered over cells seeded onto the nanostructures and cultured in a medium containing membrane impermeable biomolecules. Upon irradiation, the gold plasmonic structures heat up rapidly and generate cavitation bubbles, which facilitate the delivery of the biomolecular cargo into targeted cells by creating transient pores along nearby their outer membranes.

A representative image of a Au nanodisk array on a petri dish is shown in **Figure 4.2b**, where the central area contains uniformly patterned plasmonic nanostructures over cm scales. We extend the capabilities of this technique by demonstrating fabrication on multiple materials (*e.g.*, plastic petri dishes) that are easily coated with Au thin films and then modified *via* CLL patterning (**Figure 4.2c**). The ease of integration with commercially available cell culture products demonstrates the potential of our platform to add new functionality to existing medical devices, enabling opportunities for controlled *in situ* drug delivery and molecular screening. Stamps with periodic lines of different feature sizes were used in this study, with widths ranging from 350 nm to 10 μm and pitches ranging from 700 nm to 20 μm. To create sub-micron features, we used commercial optical storage products, such as DVDs (~ $1 each), as masters that contain

large-area, periodic gratings with 350 nm wide at 700 nm pitch to circumvent the need for expensive and slow lithographic techniques such as EBL. Atomic force microscope (AFM) images show the morphology of the fabricated Au nanodisks, with widths of 350 nm (**Figure 4.2d**), 1 μm (**Figure 4.2e**), and 2 μm (**Figure 4.2f**). The nanostructures maintain uniform shape with sharp edges, as seen in the AFM images. Corresponding optical microscope images that demonstrate the capability to tune the microscale widths of the patterned structures at 350 nm (**Figure S4.1**), 1 μm (**Figure 4.2g**), 2 μm (**Figure 4.2h**), and 10 μm (**Figure 4.2i**).

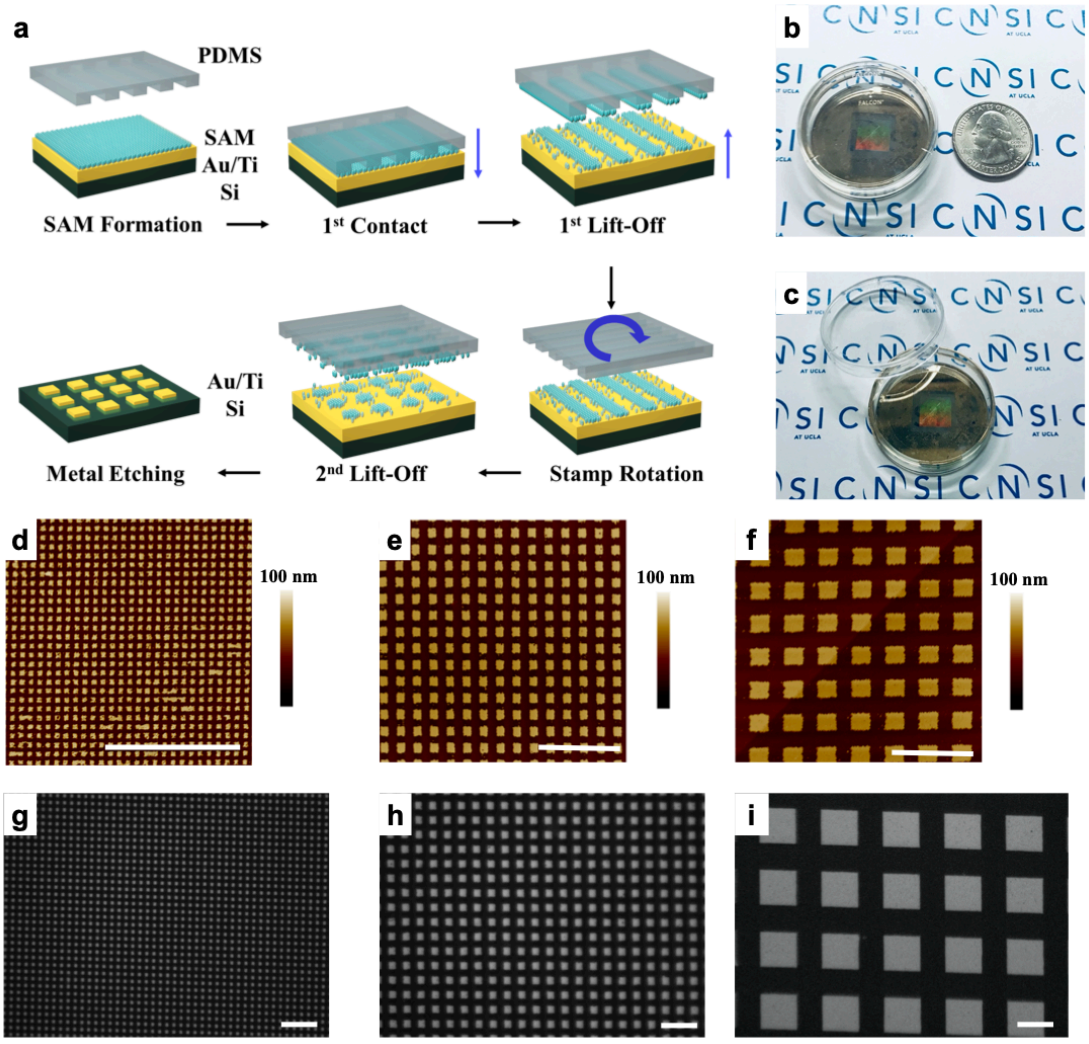

Figure 4.2. Gold plasmonic disk arrays fabricated by double-patterning chemical lift-off lithography (CLL). (a) Schematic of the patterning process. Substrates were coated with gold (Au) before being functionalized with self-assembled monolayers (SAMs). Polydimethylsiloxane (PDMS) stamps with line patterns were "activated" by exposure to an oxygen plasma to generate hydrophilic silanol groups on their surfaces. The stamps were then placed in conformal contact with the substrate. Molecules were selectively removed in the contact region upon lifting the stamp. A second patterning step was then performed by rotating the stamp 90° to generate two dimensional (2D) nanosquare

chemical patterns. Exposed metal was removed *via* wet etching to generate Au 2D nanodisk arrays. (b,c) Representative images of large-area 350-nm-wide Au nanodisk arrays on a plastic petri dish. (d-f) Atomic force microscope images of Au nanodisk arrays comprised of (d) 350-nm wide, (e) 1-µm wide, and (f) 2-µm wide features. (g-i) Optical microscope images of gold nanodisk arrays with feature widths (g) 1 µm, (h) 2 µm, and (i) 10 µm. Scale bars: 10 µm. CNSI at UCLA logo used with permission.

Plasmonic nanodisk arrays fabricated in this manner are promising candidates for substrates for surface plasmonic resonance (SPR) measurements.[81] Surface plasmon resonance properties of Au nanodisks are studied in separate work.[81] Therefore, we hypothesized that these plasmonic structures could be applied for photothermal delivery, where sharp edges concentrate effectively laser energy to generate cavitation bubbles in the cell culture medium.[68] Explosive boiling of water will occur when the temperature reaches 80–90% of its critical temperature (~650 K) that enables the bubbles formed in close proximity to a cell to puncture its outer membrane discretely.[6,8] Finite element analysis simulations (COMSOL, Multiphysics 4.4) were conducted that estimate that the aqueous cell culture medium reaches above 640 K (~360 °C) locally at laser irradiances of 11 mJ/cm^2 (**Figure 4.3h,i**), which is sufficient to initiate cavitation bubble formation. We have performed the simulations on different dimensions of Au nanodisk arrays, which show temperature increases between 636 and 644 K upon laser radiation across different nanodisk array sizes (**Figure S4.2**). Calcein AM (AM = acetoxymethyl), a cell membrane permeable variant of calcein, was used for short-term labeling of HeLa cells, as shown in **Figure 4.3a**, prior to fixation on a 1-µm wide nanodisk array. A scanning electron microscope (SEM) image of same region after cell fixation (**Figure 4.3b)** illustrates that cells are able to adhere to the Au nanodisk arrays substrates. An overlay of the optical and SEM images,

within the green box (**Figure 4.3b**), is presented in **Figure 4.3c** with matching cell distribution and morphology. Results of florescence image of calcein, cell fixation, and an image overlay on 2-μm wide nanodisk arrays are shown in **Figure 4.3d-3f**, respectively. Single cell morphology on a 2-μm wide nanodisk array was shown in **Figure 4.3g** with diameters of *ca*. 20 μm.

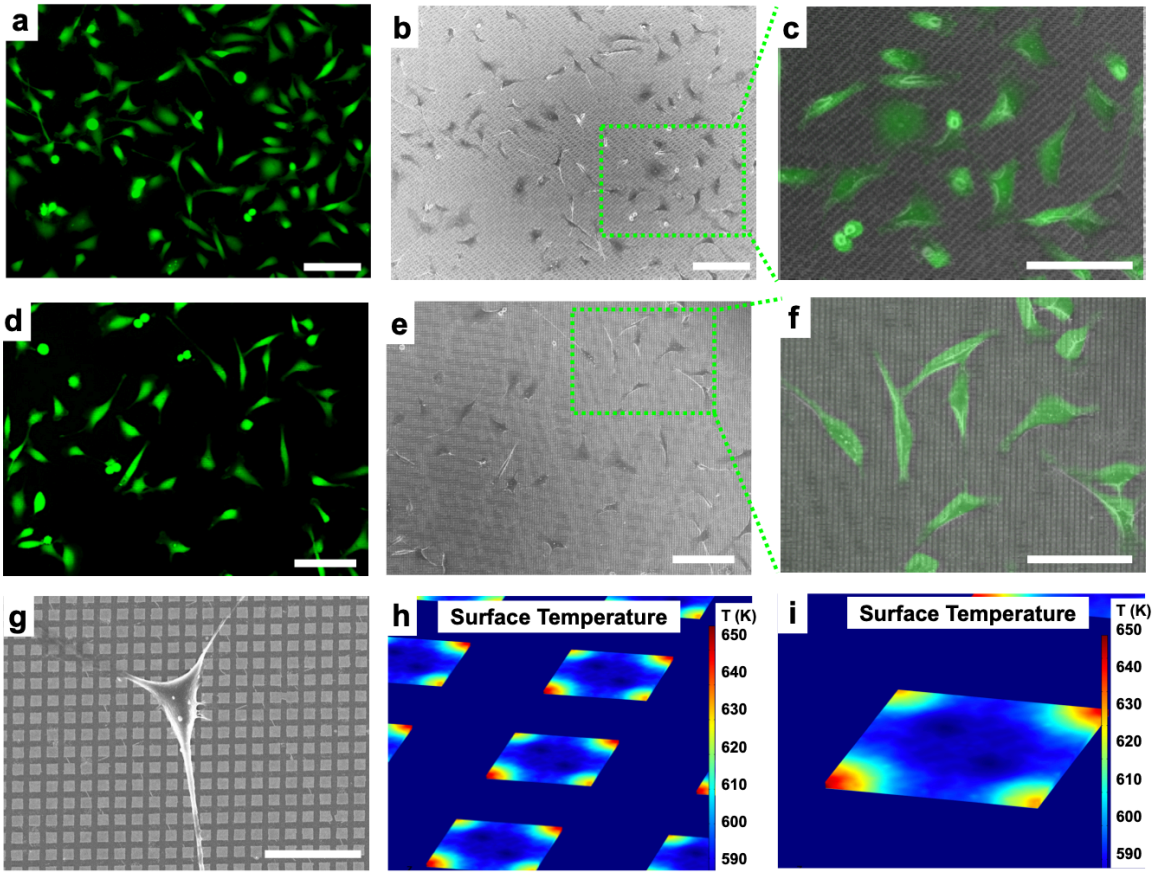

Figure 4.3. (a) Fluorescence microscope images of HeLa cells on 1-µm-wide gold (Au) nanodisk arrays labeled with a cell membrane-impermeable dye (Calcein AM). (b) Scanning electron microscope images of fixed cells on a substrate. (c) Overlay of the green-box-designated region seen in (b) with (a). (d) Fluorescence microscope images of HeLa cells on 2-µm-wide gold (Au) nanodisk arrays labeled with a cell membrane impermeable dye (Calcein AM). (e) Scanning electron microscope images of fixed cells on a substrate. (f) Overlay of the green box-designated region seen in (b) with (a). (g) Scanning electron microscope image of single Hela cell on 2-µm-wide Au nanodisk array substrate. (h,i) Simulation results of surface temperature at the gold nanodisk array (1-µm wide) interface in water. Scale bars: (a-f) 100 µm, (g) 20 µm.

We next demonstrated delivery of Calcein green (0.6 kDa membrane impermeable cargo) with high efficiency and high viability. A schematic of optical setup is shown in **Figure S4.3**. Calcein delivery using Au nanodisks (1 μm radius, 2 μm pitch, 30 nm thick) under 11 mJ/cm^2 laser irradiation can be seen in **Figure 4.4a**. Hoechst 33342, a cell-permeable nucleus fluorescence dye that emits at 497 nm, was used to label cell nuclei to quantify the total number of cells (**Figure 4.4b**). Propidium iodide (PI), which is not permeable to live cells, was used to detect dead cells (**Figure 4.4c**). Overlaid images of Calcein green fluorescence, Hoechst 33342 nucleus staining, and PI staining were taken 90 min after laser pulsing and are shown in **Figure 4.4d**. Efficiency was determined to be 98 ± 1%, with a viability of 99 ± 1% under the condition described above, with three independent experiments of ~740 cells in total. Control experiments were performed on uniformly flat gold films (30 nm thick) under the same conditions show negligible delivery efficiency, which verifies the critical role of the Au nanostructure in the intracellular delivery of Calcein green under laser irradiation. It has been shown previously for similar systems that the cells will have minimal Au residue after laser radiation.[8]

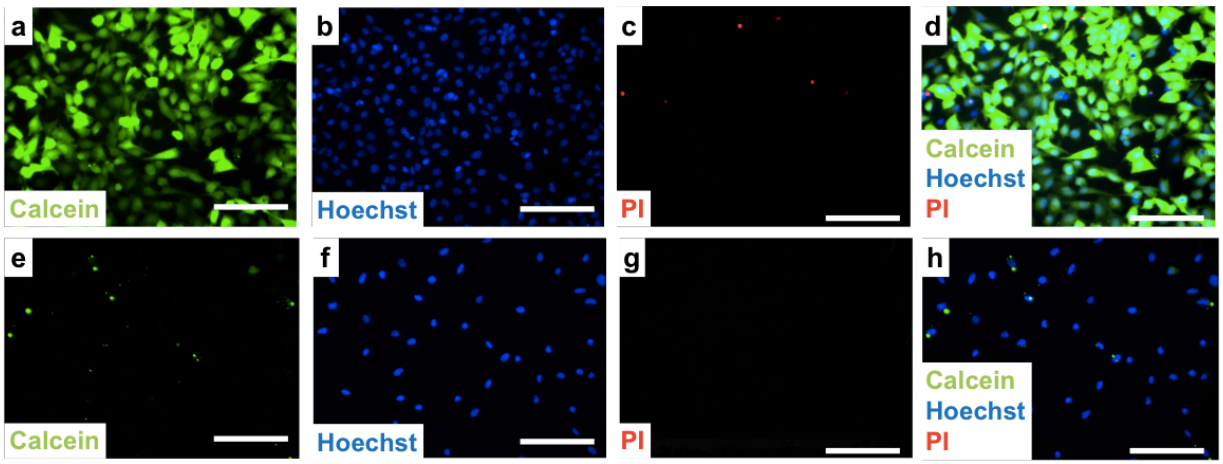

Figure 4.4. (a) Delivery efficiency and cell viability testing. (a-d) Delivery of calcein to HeLa cells using gold nanodisk arrays (1 µm wide, 2 µm pitch, 30 nm thickness) under laser irradiation with 11 mJ/cm^2 fluence. (a) Representative image of delivery of calcein (green) to targeted cells. (b) Cell nuclei are stained with Hoechst 33342 to label both live and dead cells (blue). (c) Propidium iodide (PI) assay to identify dead cells (red). (d) Overlaid image of calcein, Hoechst 33342, and PI dyes. Efficiency was found to be 98 ± 1%, and viability to be 99 ± 1%. (e–h) Control experiment using flat gold thin film under the same laser irradiation of 11 mJ/cm^2 fluence, where (e) corresponds to the calcein channel, (f) is the Hoechst dye, (g) is the PI dye, and (h) is the overlaid image of (e–g). Scale bars: 100 µm.

Different laser fluences, ranging from 7 to 21 mJ/cm^2, were studied to optimize delivery performance (**Figure 4.5a,b)**. We observed that the number of cells receiving the calcein cargo (green) decreased while cytotoxicity (red) increased with increasing laser fluence. Additional experiments studying the effect of different laser fluences were performed with results plotted in **Figure 4.5e**. Over 2,500 cells were counted for each sample tested. Delivery efficiencies increased when the laser fluence was increased from the minimum laser intensity up to

11 mJ/cm^2, reaching 98 ± 1% efficiency. At higher laser fluences, both cell viability and efficiency decreased significantly (with viability decreasing to 16 ± 2% and 6 ± 1% efficiency at 21 mJ/cm^2). We attribute this cytotoxicity to irrecoverable membrane disruption occurring at the higher laser intensities.[6,8,19,83] The delivery efficiency decrease with cell viability is expected, as calcein will only remain in live cells with intact plasma membranes.

We also studied the effects of width and pitch of the periodic nanodisk arrays on delivery performance. Fewer calcein-delivered cells were observed as the sizes of Au nanodisks were increased from 2 μm to 10 μm (**Figure 4.5c,d**) while the numbers of dead cells (red) remained the same relative to the total number of cells (blue). This phenomenon can be explained by the density of cavitation bubbles induced by the gold plasmonic structures per cell.[6] Results from our simulations of photothermal response (**Figure 4.3f**) indicate that hotspots occur at the corner of each nanodisk where the pitch of nanodisk array is twice the width of an individual disk. Disk arrays with larger disk widths have fewer hotspots and thus form fewer cavitation bubbles. Delivery efficiency therefore decreases on these substrates, due to the smaller numbers of cavitation bubbles. Our data indicate that the delivery efficiency is maximized for disks with widths smaller than 2 μm. Delivery efficiency and cell viability results on nanodisk arrays with different feature widths are shown in **Figure 4.5f**. Cargoes with different sizes were also studied, including 0.6 kDa calcein, 4 kDa calcein, and a 150 kDa dextran (**Figure 4.5g**). Delivery efficiencies of 98 ± 1% and 94 ± 1% were achieved for 0.6 kDa and 4 kDa calcein, respectively. Decreased efficiency of 36 ± 5% was observed for the dextran, which we infer is related to its lower diffusion coefficient. Note that the gold nanodisk substrates have the added benefit of being reusable as we did not notice any drop in performance after five experiments **(Figure S4.4).**

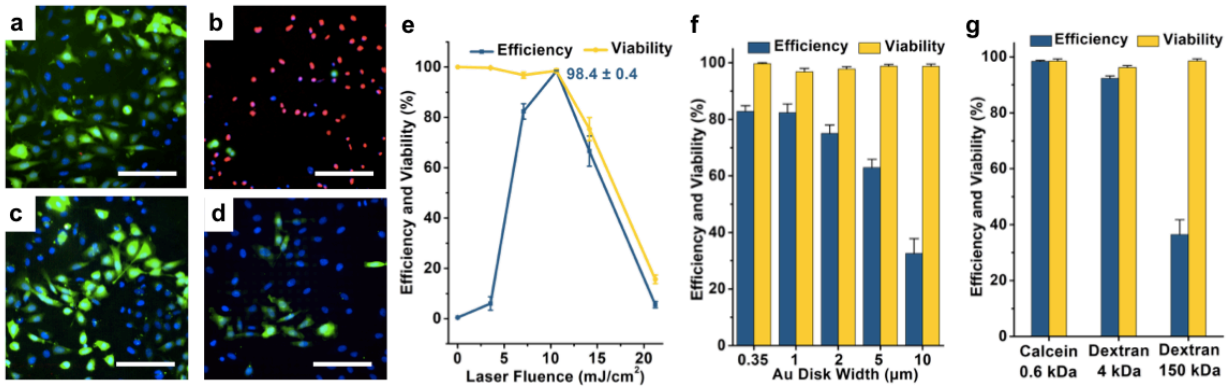

Figure 4.5. (a) Delivery efficiency and cell viability at different laser fluences and gold disk sizes are shown in overlaid images (a-d) of 0.6 kDa calcein delivery (green), Hoechst dye (blue), and PI dye (red). Delivery results under different laser fluence at (a) 7 mJ/cm^2, and (b) 21.2 mJ/cm^2, respectively, both on 1-μm wide nanodisk arrays. Delivery results using different sizes of gold nanodisk arrays of (c) 2 μm and (d) 10 μm widths, respectively, both under laser fluence of 7 mJ/cm^2. (e) Delivery efficiencies and viabilities after 90 min as a function of laser fluence on 1-μm wide nanodisk arrays. Error bars represented standard error mean (s.e.m.) (n = ~2,500 cells for all tests). (f) Delivery efficiencies and viabilities with different sizes of gold nanodisk arrays at 7 mJ/cm^2. Error bars, s.e.m. (n = ~1,900 cells for all tests). (g) Delivery efficiencies and viabilities with different cargoes at 11 mJ/cm^2 on 1-μm-wide nanodisk arrays. Error bars, s.e.m. (n = ~2,000 cells for all tests). Scale bars: 100 μm.

4.5 Conclusions and Prospects

In summary, effective and safe delivery of biomolecular cargos intracellularly was achieved by exposing large-area gold plasmonic substrates fabricated using double-patterning CLL to nanosecond-laser pulses. Gold surfaces patterned with 2D SAM nanosquare arrays were

used to create sub-micron nanostructures. Illuminating the gold nanostructures with nanosecond laser pulses induced cavitation bubbles at the plasmonic hotspots through a photothermal effect. Cells seeded on the nanostructures were rendered transiently porous upon contact with the bubbles, enabling delivery of exogenous biomolecular cargo. Laser fluences and nanodisk sizes were optimized to achieve delivery efficiencies of over 98% for 0.6 kDa calcein with cell viability maintained at over 98%. Note that we attribute the photothermal delivery predominantly to the sheer force generated by the formation and collapse of the cavitation bubble, but we do not exclude the effects of local thermal heating of the plasma membrane.

Desirable features of this CLL-based strategy include: (1) cost-effective and high-throughput fabrication of uniform nanostructures over large (square centimeter) areas, (2) versatile substrate selection, (3) scalability and reproducibility, and (4) economical setup that does not require specialized instrumentation. Efficient delivery of membrane impermeant small molecules to HeLa cells with minimal cell death was achieved, which opens new opportunities for testing and manipulating in disease-relevant cellular targets and potential integration with medical devices. Both the PDMS stamps and the fabricated plasmonic substrates are reusable, enabling scale-up to larger formats. Compared with femtosecond lasers sometimes used in laboratory studies, the nanosecond pulsed laser used here is economical and straightforward to operate. This study demonstrates a promising method for high-efficiency intracellular delivery for cellular therapeutic and drug-discovery applications. In this work, we focused on delivery of small molecules into HeLa cells. Previously, we have shown that our photothermal delivery platform can be applied to deliver large functional cargoes, such as live bacteria, proteins, and plasmids, into a variety of cell types, including primary normal human dermal fibroblasts and human B lymphocyte cells.[22,68] Future optimization and investigations of the Au nanodisk arrays

will focus on advancing this technique so as to enable clinical applications, such as gene therapy and cancer immunotherapy.

4.6 Supplementary Materials

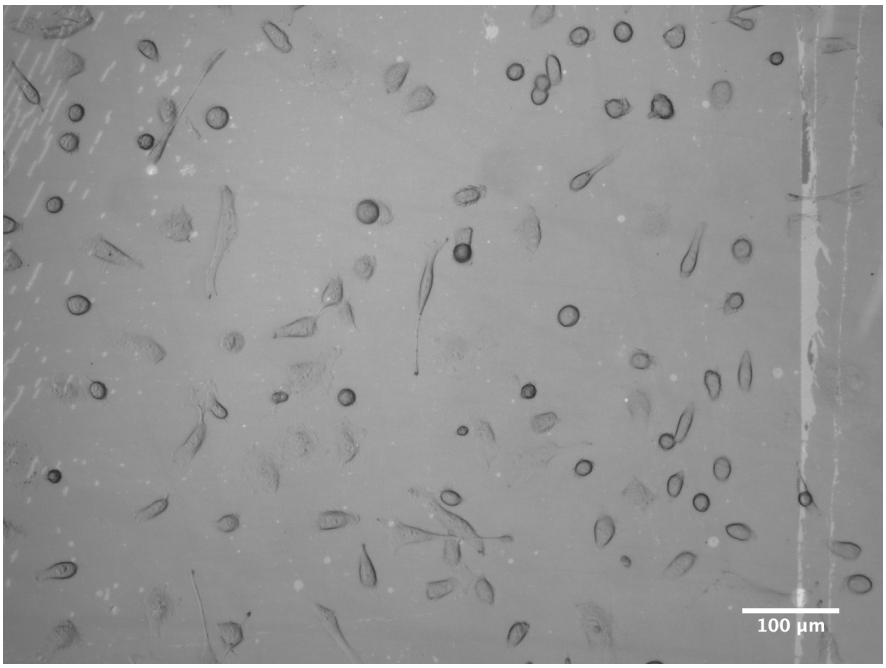

Figure S4.1. Optical microscope image of cells on 350-nm Au nanodisk arrays. The Au nanodisks are not visible in the optical microscope due to their sub-micron features.

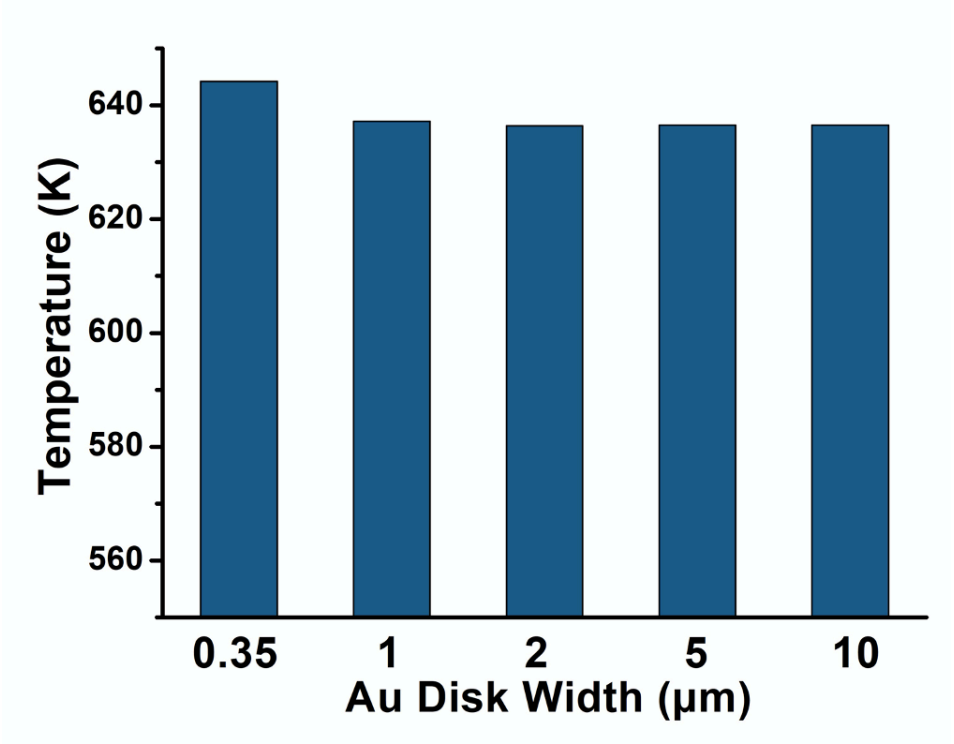

Figure S4.2. Simulation results for tip temperature on different dimensions of Au nanodisk arrays upon laser radiation of 11 mJ/cm^2.

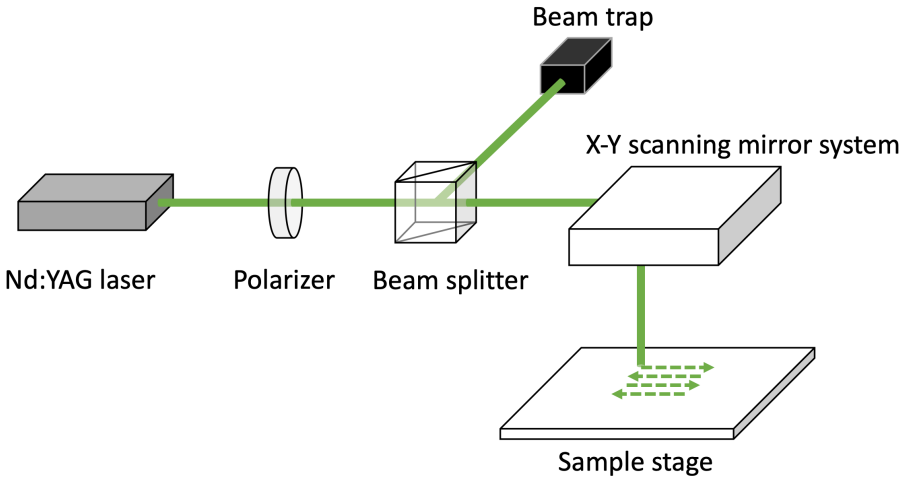

Figure S4.3. Schematic diagram of the optical setup.

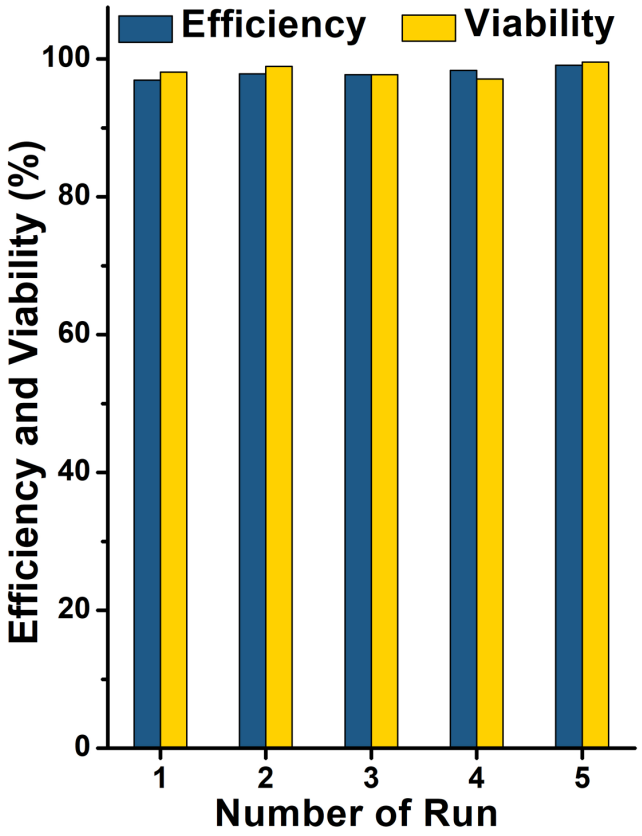

Figure S4.4. Delivery efficiency and cell viability results of 0.6 kDa calcein AM using a 1-μm-wide gold (Au) nanodisk arrays chip after five runs under 11 mJ/cm^2 laser fluence.

4.7 References

(1) Esteban-Fernández de Ávila, B.; Angell, C.; Soto, F.; Lopez-Ramirez, M. A.; Báez, D. F.; Xie, S.; Wang, J.; Chen, Y. Acoustically Propelled Nanomotors for Intracellular siRNA Delivery. *ACS Nano* **2016,** *10*, 4997–5005.

(2) Ding, X.; Stewart, M.; Sharei, A.; Weaver, J. C.; Langer, R. S.; Jensen, K. F. High-Throughput Nuclear Delivery and Rapid Expression of DNA *via* Mechanical and Electrical Cell-Membrane Disruption. *Nat. Biomed. Eng.* **2017,** *1*, 0039.

(3) Xu, X.; Hou, S.; Wattanatorn, N.; Wang, F.; Yang, Q.; Zhao, C.; Yu, X.; Tseng, H. R.; Jonas, S. J.; Weiss, P. S. Precision-Guided Nanospears for Targeted and High-Throughput Intracellular Gene Delivery. *ACS Nano* **2018,** *12*, 4503–4511.

(4) Ball, R. L.; Hajj, K. A.; Vizelman, J.; Bajaj, P.; Whitehead, K. A. Lipid Nanoparticle Formulations for Enhanced Co-Delivery of siRNA and mRNA. *Nano Lett.* **2018,** *18*, 3814–3822.

(5) Yan, M.; Du, J.; Gu, Z.; Liang, M.; Hu, Y.; Zhang, W.; Priceman, S.; Wu, L.; Zhou, Z. H.; Liu, Z.; Segura, T.; Tang, Y.; Lu, Y. A Novel Intracellular Protein Delivery Platform Based on Single-Protein Nanocapsules. *Nat. Nanotechnol.* **2010,** *5*, 48–53.

(6) Wu, Y. C.; Wu, T. H.; Clemens, D. L.; Lee, B. Y.; Wen, X.; Horwitz, M. A.; Teitell, M. A.; Chiou, P. Y. Massively Parallel Delivery of Large Cargo into Mammalian Cells with Light Pulses. *Nat. Methods* **2015,** *12*, 439–444.

(7) Chou, L. Y.; Ming, K.; Chan, W. C. Strategies for the Intracellular Delivery of Nanoparticles. *Chem. Soc. Rev.* **2011,** *40*, 233–245.

(8) Saklayen, N.; Huber, M.; Madrid, M.; Nuzzo, V.; Vulis, D. I.; Shen, W.; Nelson, J.; McClelland, A. A.; Heisterkamp, A.; Mazur, E. Intracellular Delivery Using Nanosecond-Laser Excitation of Large-Area Plasmonic Substrates. *ACS Nano* **2017,** *11*, 3671–3680.

(9) Yin, H.; Kanasty, R. L.; Eltoukhy, A. A.; Vegas, A. J.; Dorkin, J. R.; Anderson, D. G. Non-Viral Vectors for Gene-Based Therapy. *Nat. Rev. Genet.* **2014,** *15*, 541–555.

(10) Wang, H. X.; Li, M.; Lee, C. M.; Chakraborty, S.; Kim, H. W.; Bao, G.; Leong, K. W. CRISPR/Cas9-Based Genome Editing for Disease Modeling and Therapy: Challenges and Opportunities for Nonviral Delivery. *Chem. Rev.* **2017,** *117*, 9874–9906.

(11) Zhu, H.; Zhang, L.; Tong, S.; Lee, C. M.; Deshmukh, H.; Bao, G. Spatial Control of *in vivo* CRISPR-Cas9 Genome Editing *via* Nanomagnets. *Nat. Biomed. Eng.* **2019,** *3*, 126–136.

(12) Fang, J.; Hsueh, Y. Y.; Soto, J.; Sun, W.; Wang, J.; Gu, Z.; Khademhosseini, A.; Li, S. Engineering Biomaterials with Micro/Nanotechnologies for Cell Reprogramming. *ACS Nano* **2020,** *14*, 1296–1318.

(13) Qin, X.-F.; An, D. S.; Chen, I. S. Y.; Baltimore, D. Inhibiting HIV-1 Infection in Human T Cells by Lentiviral-Mediated Delivery of Small Interfering RNA against CCR5. *Proc. Natl. Acad. Sci. U. S. A.* **2003,** *100*, 183–188.

(14) Tebas, P.; Stein, D.; Tang, W. W.; Frank, I.; Wang, S. Q.; Lee, G.; Spratt, S. K.; Surosky, R. T.; Giedlin, M. A.; Nichol, G.; Holmes, M. C.; Gregory, P. D.; Ando, D. G.; Kalos, M.; Collman, R. G.; Binder-Scholl, G.; Plesa, G.; Hwang, W. T.; Levine, B. L.; June, C. H. Gene Editing of CCR5 in Autologous CD4 T Cells of Persons Infected with HIV. *N. Engl. J. Med.* **2014,** *370*, 901–910.

(15) Rosenberg, S. A.; Restifo, N. P. Adoptive Cell Transfer as Personalized Immunotherapy for Human Cancer. *Science* **2015,** *348*, 62–68.

(16) Zhao, C.; Bai, Z.; Liu, X.; Zhang, Y.; Zou, B.; Zhong, H. Small GSH-Capped $CuInS_2$ Quantum Dots: MPA-Assisted Aqueous Phase Transfer and Bioimaging Applications. *ACS Appl. Mater. Inter.* **2015,** *7*, 17623–17629.

(17) Syed, A. M.; Sindhwani, S.; Wilhelm, S.; Kingston, B. R.; Lee, D. S. W.; Gommerman, J. L.; Chan, W. C. W. Three-Dimensional Imaging of Transparent Tissues *via* Metal Nanoparticle Labeling. *J. Am. Chem. Soc.* **2017,** *139*, 9961–9971.

(18) Fox, C. B.; Cao, Y.; Nemeth, C. L.; Chirra, H. D.; Chevalier, R. W.; Xu, A. M.; Melosh, N. A.; Desai, T. A. Fabrication of Sealed Nanostraw Microdevices for Oral Drug Delivery. *ACS Nano* **2016,** *10*, 5873–5881.

(19) Madrid, M.; Saklayen, N.; Shen, W.; Huber, M.; Vogel, N.; Mazur, E. Laser-Activated Self-Assembled Thermoplasmonic Nanocavity Substrates for Intracellular Delivery. *ACS Appl. Bio. Mater.* **2018,** *1*, 1793–1799.

(20) Naldini, L. *Ex vivo* Gene Transfer and Correction for Cell-Based Therapies. *Nat. Rev. Genet.* **2011,** *12*, 301–315.

(21) Cavazzana-Calvo, M.; Payen, E.; Negre, O.; Wang, G.; Hehir, K.; Fusil, F.; Down, J.; Denaro, M.; Brady, T.; Westerman, K.; Cavallesco, R.; Gillet-Legrand, B.; Caccavelli, L.; Sgarra, R.; Maouche-Chrétien, L.; Bernaudin, F.; Girot, R.; Dorazio, R.; Mulder, G.-J.; Polack, A.; Bank, A.; Soulier, J.; Larghero, J.; Kabbara, N.; Dalle, B.; Gourmel, B.; Socie, G.; Chrétien, S.; Cartier, N.; Aubourg, P.; Fischer, A.; Cornetta, K.; Galacteros, F.; Beuzard, Y.; Gluckman, E.; Bushman, F.; Hacein-Bey-Abina, S.; Leboulch, P. Transfusion Independence and HMGA2 Activation after Gene Therapy of Human β-Thalassaemia. *Nature* **2010,** *467*, 318–322.

(22) Stewart, M. P.; Sharei, A.; Ding, X.; Sahay, G.; Langer, R.; Jensen, K. F. *In Vitro* and *Ex vivo* Strategies for Intracellular Delivery. *Nature* **2016,** *538*, 183–192.

(23) Stewart, M. P.; Langer, R.; Jensen, K. F. Intracellular Delivery by Membrane Disruption: Mechanisms, Strategies, and Concepts. *Chem. Rev.* **2018,** *118*, 7409–7531.

(24) Belling, J. N.; Heidenreich, L. K.; Tian, Z.; Mendoza, A. M.; Chiou, T. T.; Gong, Y.; Chen, N. Y.; Young, T. D.; Wattanatorn, N.; Park, J. H.; Scarabelli, L.; Chiang, N.; Takahashi, J.; Young, S. G.; Stieg, A. Z.; De Oliveira, S.; Huang, T. J.; Weiss, P. S.; Jonas, S. J. Acoustofluidic Sonoporation for Gene Delivery to Human Hematopoietic Stem and Progenitor Cells. *Proc. Natl. Acad. Sci. U. S. A.* **2020,** *117*, 10976–10982.

(25) Thomas, C. E.; Ehrhardt, A.; Kay, M. A. Progress and Problems with the Use of Viral Vectors for Gene Therapy. *Nat. Rev. Genet.* **2003,** *4*, 346–358.

(26) Kotterman, M. A.; Chalberg, T. W.; Schaffer, D. V. Viral Vectors for Gene Therapy: Translational and Clinical Outlook. *Annu. Rev. Biomed. Eng.* **2015,** *17*, 63–89.

(27) Qu, Y.; Zhang, Y.; Yu, Q.; Chen, H. Surface-Mediated Intracellular Delivery by Physical Membrane Disruption. *ACS Appl. Mater. Inter.* **2020,** *12*, 31054–31078.

(28) Tay, A. The Benefits of Going Small: Nanostructures for Mammalian Cell Transfection. *ACS Nano* **2020**, Article ASAP.

(29) Sharei, A.; Zoldan, J.; Adamo, A.; Sim, W. Y.; Cho, N.; Jackson, E.; Mao, S.; Schneider, S.; Han, M.-J.; Lytton-Jean, A.; Basto, P. A.; Jhunjhunwala, S.; Lee, J.; Heller, D. A.; Kang, J. W.; Hartoularos, G. C.; Kim, K.-S.; Anderson, D. G.; Langer, R.; Jensen, K. F. A Vector-Free Microfluidic Platform for Intracellular Delivery. *Proc. Natl. Acad. Sci. U. S. A.* **2013,** *110*, 2082–2087.

(30) Chiappini, C.; Campagnolo, P.; Almeida, C. S.; Abbassi-Ghadi, N.; Chow, L. W.; Hanna, G. B.; Stevens, M. M. Mapping Local Cytosolic Enzymatic Activity in Human Esophageal Mucosa with Porous Silicon Nanoneedles. *Adv. Mater.* **2015,** *27*, 5147–5152.

(31) Seong, H.; Higgins, S. G.; Penders, J.; Armstrong, J. P. K.; Crowder, S. W.; Moore, A. C.; Sero, J. E.; Becce, M.; Stevens, M. M. Size-Tunable Nanoneedle Arrays for Influencing Stem Cell Morphology, Gene Expression, and Nuclear Membrane Curvature. *ACS Nano* **2020,** *14*, 5371–5381.

(32) Kang, G.; Carlson, D. W.; Kang, T. H.; Lee, S.; Haward, S. J.; Choi, I.; Shen, A. Q.; Chung, A. J. Intracellular Nanomaterial Delivery *via* Spiral Hydroporation. *ACS Nano* **2020,** *14*, 3048–3058.

(33) Tay, A.; Melosh, N. Nanostructured Materials for Intracellular Cargo Delivery. *Acc. Chem. Res.* **2019,** *52*, 2462–2471.

(34) Dixit, H. G.; Starr, R.; Dundon, M. L.; Pairs, P. I.; Yang, X.; Zhang, Y.; Nampe, D.; Ballas, C. B.; Tsutsui, H.; Forman, S. J.; Brown, C. E.; Rao, M. P. Massively-Parallelized, Deterministic Mechanoporation for Intracellular Delivery. *Nano Lett.* **2020,** *20*, 860–867.

(35) Deng, Y.; Kizer, M.; Rada, M.; Sage, J.; Wang, X.; Cheon, D. J.; Chung, A. J. Intracellular Delivery of Nanomaterials *via* an Inertial Microfluidic Cell Hydroporator. *Nano Lett.* **2018,** *18*, 2705–2710.

(36) Chopra, A.; Krishnan, S.; Simmel, F. C. Electrotransfection of Polyamine Folded DNA Origami Structures. *Nano Lett.* **2016,** *16*, 6683–6690.

(37) Geng, T.; Zhan, Y. H.; Wang, J.; Lu, C. Transfection of Cells Using Flow-through Electroporation Based on Constant Voltage. *Nat. Protoc.* **2011,** *6*, 1192–1208.

(38) Lukianova-Hleb, E. Y.; Mutonga, M. B. G.; Lapotko, D. O. Cell-Specific Multifunctional Processing of Heterogeneous Cell Systems in a Single Laser Pulse Treatment. *ACS Nano* **2012,** *6*, 10973–10981.

(39) Xiong, R. H.; Raemdonck, K.; Peynshaert, K.; Lentacker, I.; De Cock, I.; Demeester, J.; De Smedt, S. C.; Skirtach, A. G.; Braeckmans, K. Comparison of Gold Nanoparticle Mediated Photoporation: Vapor Nanobubbles Outperform Direct Heating for Delivering Macromolecules in Live Cells. *ACS Nano* **2014,** *8*, 6288–6296.

(40) Sengupta, A.; Kelly, S. C.; Dwivedi, N.; Thadhani, N.; Prausnitz, M. R. Efficient Intracellular Delivery of Molecules with High Cell Viability Using Nanosecond-Pulsed Laser-Activated Carbon Nanoparticles. *ACS Nano* **2014,** *8*, 2889–2899.

(41) Kalies, S.; Heinemann, D.; Schomaker, M.; Gentemann, L.; Meyer, H.; Ripken, T. Immobilization of Gold Nanoparticles on Cell Culture Surfaces for Safe and Enhanced Gold Nanoparticle-Mediated Laser Transfection. *J. Biomed. Opt.* **2014,** *19*.

(42) Li, M.; Lohmuller, T.; Feldmann, J. Optical Injection of Gold Nanoparticles into Living Cells. *Nano Lett.* **2015,** *15*, 770–775.

(43) Lukianova-Hleb, E.; Hu, Y.; Latterini, L.; Tarpani, L.; Lee, S.; Drezek, R. A.; Hafner, J. H.; Lapotko, D. O. Plasmonic Nanobubbles as Transient Vapor Nanobubbles Generated around Plasmonic Nanoparticles. *ACS Nano* **2010,** *4*, 2109–2123.

(44) Lyu, Z. L.; Zhou, F.; Liu, Q.; Xue, H.; Yu, Q.; Chen, H. A Universal Platform for Macromolecular Delivery into Cells Using Gold Nanoparticle Layers *via* the Photoporation Effect. *Adv. Funct. Mater.* **2016,** *26*, 5787–5795.

(45) Tong, S.; Moyo, B.; Lee, C. M.; Leong, K.; Bao, G. Engineered Materials for *in vivo* Delivery of Genome-Editing Machinery. *Nat. Rev. Mater.* **2019,** *4*, 726–737.

(46) Lee, W. G.; Demirci, U.; Khademhosseini, A. Microscale Electroporation: Challenges and Perspectives for Clinical Applications. *Integr. Biol.* **2009,** *1*, 242–251.

(47) Priceman, S. J.; Tilakawardane, D.; Jeang, B.; Aguilar, B.; Murad, J. P.; Park, A. K.; Chang, W. C.; Ostberg, J. R.; Neman, J.; Jandial, R.; Portnow, J.; Forman, S. J.; Brown, C. E. Regional Delivery of Chimeric Antigen Receptor-Engineered T Cells Effectively Targets HER2(+) Breast Cancer Metastasis to the Brain. *Clin. Cancer Res.* **2018,** *24*, 95–105.

(48) Shi, J.; Ma, Y.; Zhu, J.; Chen, Y.; Sun, Y.; Yao, Y.; Yang, Z.; Xie, J. A Review on Electroporation-Based Intracellular Delivery. *Molecules* **2018,** *23*, 3044.

(49) Stewart, M. P.; Langer, R.; Jensen, K. F. Intracellular Delivery by Membrane Disruption: Mechanisms, Strategies, and Concepts. *Chem. Rev.* **2018,** *118*, 7409–7531.

(50) Xu, X. B.; Liu, C.; Kim, K.; Fan, D. L. Electric-Driven Rotation of Silicon Nanowires and Silicon Nanowire Motors. *Adv. Funct. Mater.* **2014,** *24*, 4843–4850.

(51) Kim, W.; Ng, J. K.; Kunitake, M. E.; Conklin, B. R.; Yang, P. Interfacing Silicon Nanowires with Mammalian Cells. *J. Am. Chem. Soc.* **2007,** *129*, 7228–7229.

(52) Xie, X.; Xu, A. M.; Leal-Ortiz, S.; Cao, Y.; Garner, C. C.; Melosh, N. A. Nanostraw–Electroporation System for Highly Efficient Intracellular Delivery and Transfection. *ACS Nano* **2013,** *7*, 4351–4358.

(53) VanDersarl, J. J.; Xu, A. M.; Melosh, N. A. Nanostraws for Direct Fluidic Intracellular Access. *Nano Lett.* **2012,** *12*, 3881–3886.

(54) He, G.; Feng, J.; Zhang, A.; Zhou, L.; Wen, R.; Wu, J.; Yang, C.; Yang, J.; Li, C.; Chen, D.; Wang, J.; Hu, N.; Xie, X. Multifunctional Branched Nanostraw-Electroporation Platform for Intracellular Regulation and Monitoring of Circulating Tumor Cells. *Nano Lett.* **2019,** *19*, 7201–7209.

(55) Chiappini, C.; De Rosa, E.; Martinez, J. O.; Liu, X.; Steele, J.; Stevens, M. M.; Tasciotti, E. Biodegradable Silicon Nanoneedles Delivering Nucleic Acids Intracellularly Induce Localized *in Vivo* Neovascularization. *Nat. Mater.* **2015,** *14*, 532–539.

(56) Peer, E.; Artzy-Schnirman, A.; Gepstein, L.; Sivan, U. Hollow Nanoneedle Array and Its Utilization for Repeated Administration of Biomolecules to the Same Cells. *ACS Nano* **2012,** *6*, 4940–4946.

(57) Xie, X.; Xu, A. M.; Angle, M. R.; Tayebi, N.; Verma, P.; Melosh, N. A. Mechanical Model of Vertical Nanowire Cell Penetration. *Nano Lett.* **2013,** *13*, 6002–6008.

(58) Wang, Y.; Yang, Y.; Yan, L.; Kwok, S. Y.; Li, W.; Wang, Z.; Zhu, X.; Zhu, G.; Zhang, W.; Chen, X.; Shi, P. Poking Cells for Efficient Vector-Free Intracellular Delivery. *Nat. Commun.* **2014,** *5*, 4466.

(59) Lee, S. E.; Sasaki, D. Y.; Park, Y.; Xu, R.; Brennan, J. S.; Bissell, M. J.; Lee, L. P. Photonic Gene Circuits by Optically Addressable siRNA-Au Nanoantennas. *ACS Nano* **2012,** *6*, 7770–7780.

(60) Xin, H.; Namgung, B.; Lee, L. P. Nanoplasmonic Optical Antennas For life Sciences and Medicine. *Nat. Rev. Mater.* **2018,** *3*, 228–243.

(61) Boulais, E.; Lachaine, R.; Meunier, M. Plasma Mediated Off-Resonance Plasmonic Enhanced Ultrafast Laser-Induced Nanocavitation. *Nano Lett.* **2012,** *12*, 4763–4769.

(62) Furlani, E. P.; Karampelas, I. H.; Xie, Q. Analysis of Pulsed Laser Plasmon-Assisted Photothermal Heating and Bubble Generation at the Nanoscale. *Lab Chip* **2012,** *12*, 3707–3719.

(63) Prentice, P.; Cuschieri, A.; Dholakia, K.; Prausnitz, M.; Campbell, P. Membrane Disruption by Optically Controlled Microbubble Cavitation. *Nat. Phys.* **2005,** *1*, 107–110.

(64) Wu, T. H.; Teslaa, T.; Kalim, S.; French, C. T.; Moghadam, S.; Wall, R.; Miller, J. F.; Witte, O. N.; Teitell, M. A.; Chiou, P. Y. Photothermal Nanoblade for Large Cargo Delivery into Mammalian Cells. *Anal. Chem.* **2011,** *83*, 1321–1327.

(65) Ghosh, P.; Han, G.; De, M.; Kim, C. K.; Rotello, V. M. Gold Nanoparticles in Delivery Applications. *Adv. Drug. Deliver. Rev.* **2008,** *60*, 1307–1315.

(66) Peng, T.; Li, X.; Li, K.; Nie, Z.; Tan, W. DNA-Modulated Plasmon Resonance: Methods and Optical Applications. *ACS Appl. Mater. Inter.* **2020,** *12*, 14741–14760.

(67) Pitsillides, C. M.; Joe, E. K.; Wei, X.; Anderson, R. R.; Lin, C. P. Selective Cell Targeting with Light-Absorbing Microparticles and Nanoparticles. *Biophys. J.* **2003,** *84*, 4023–4032.

(68) Man, T.; Zhu, X.; Chow, Y. T.; Dawson, E. R.; Wen, X.; Patananan, A. N.; Liu, T. L.; Zhao, C.; Wu, C.; Hong, J. S.; Chung, P. S.; Clemens, D. L.; Lee, B. Y.; Weiss, P. S.; Teitell, M. A.; Chiou, P. Y. Intracellular Photothermal Delivery for Suspension Cells Using Sharp Nanoscale Tips in Microwells. *ACS Nano* **2019,** *13*, 10835–10844.

(69) Odom, T. W.; Love, J. C.; Wolfe, D. B.; Paul, K. E.; Whitesides, G. M. Improved Pattern Transfer in Soft Lithography Using Composite Stamps. *Langmuir* **2002,** *18*, 5314–5320.

(70) Qin, D.; Xia, Y.; Whitesides, G. M. Soft Lithography for Micro- and Nanoscale Patterning. *Nat. Protocols* **2010,** *5*, 491–502.

(71) Kumar, A.; Whitesides, G. M. Features of Gold Having Micrometer to Centimeter Dimensions Can Be Formed through a Combination of Stamping with an Elastomeric Stamp and an Alkanethiol ‘‘Ink’’ Followed by Chemical Etching. *Appl. Phys. Lett.* **1993,** *63*, 2002–2004.

(72) Andrews, A. M.; Liao, W. S.; Weiss, P. S. Double-Sided Opportunities Using Chemical Lift-Off Lithography. *Acc. Chem. Res.* **2016,** *49*, 1449-1457.

(73) Cao, H. H.; Nakatsuka, N.; Serino, A. C.; Liao, W.-S.; Cheunkar, S.; Yang, H.; Weiss, P. S.; Andrews, A. M. Controlled DNA Patterning by Chemical Lift-Off Lithography: Matrix Matters. *ACS Nano* **2015,** *9*, 11439–11454.

(74) Kim, J.; Rim, Y. S.; Chen, H.; Cao, H. H.; Nakatsuka, N.; Hinton, H. L.; Zhao, C.; Andrews, A. M.; Yang, Y.; Weiss, P. S. Fabrication of High-Performance Ultrathin In_2O_3 Film Field-Effect Transistors and Biosensors Using Chemical Lift-Off Lithography. *ACS Nano* **2015,** *9*, 4572–4582.

(75) Srinivasan, C.; Mullen, T. J.; Hohman, J. N.; Anderson, M. E.; Dameron, A. A.; Andrews, A. M.; Dickey, E. C.; Horn, M. W.; Weiss, P. S. Scanning Electron Microscopy of Nanoscale Chemical Patterns. *ACS Nano* **2007,** *1*, 191–201.

(76) Smith, R. K.; Lewis, P. A.; Weiss, P. S. Patterning Self-Assembled Monolayers. *Prog. Surf. Sci.* **2004,** *75*, 1–68.

(77) Liao, W.-S.; Cheunkar, S.; Cao, H. H.; Bednar, H. R.; Weiss, P. S.; Andrews, A. M. Subtractive Patterning *via* Chemical Lift-Off Lithography. *Science* **2012,** *337*, 1517–1521.

(78) Vaish, A.; Shuster, M. J.; Cheunkar, S.; Weiss, P. S.; Andrews, A. M. Tuning Stamp Surface Energy for Soft Lithography of Polar Molecules to Fabricate Bioactive Small-Molecule Microarrays. *Small* **2011,** *7*, 1471–1479.

(79) Zhao, C.; Xu, X.; Bae, S. H.; Yang, Q.; Liu, W.; Belling, J. N.; Cheung, K. M.; Rim, Y. S.; Yang, Y.; Andrews, A. M.; Weiss, P. S. Large-Area, Ultrathin Metal-Oxide Semiconductor Nanoribbon Arrays Fabricated by Chemical Lift-Off Lithography. *Nano Lett.* **2018,** *18*, 5590–5595.

(80) Zhao, C.; Xu, X.; Yang, Q.; Man, T.; Jonas, S. J.; Schwartz, J. J.; Andrews, A. M.; Weiss, P. S. Self-Collapse Lithography. *Nano Lett.* **2017,** *17*, 5035–5042.

(81) Zhao, C.; Xu, X.; Chiang, N.; Yang, Q.; Liu, W.; Schwartz, J. J.; Andrews, A. M.; Weiss, P. S. Two-Dimensional Plasmonic Nanostructure Arrays Fabricated by Double-Patterning Chemical Lift-Off Lithography. **2020,** *In prep.*

(82) Carlson, A.; Bowen, A. M.; Huang, Y.; Nuzzo, R. G.; Rogers, J. A. Transfer Printing Techniques for Materials Assembly and Micro/Nanodevice Fabrication. *Adv. Mater.* **2012,** *24*, 5284–5318.

(83) Raun, A.; Saklayen, N.; Zgrabik, C.; Shen, W.; Madrid, M.; Huber, M.; Hu, E.; Mazur, E. A Comparison of Inverted and Upright Laser-Activated Titanium Nitride Micropyramids for Intracellular Delivery. *Sci. Rep.* **2018,** *8*, 15595.

Chapter 5

Large-Area, Ultrathin Metal-Oxide Semiconductor Nanoribbon Arrays Fabricated by Chemical Lift-Off Lithography

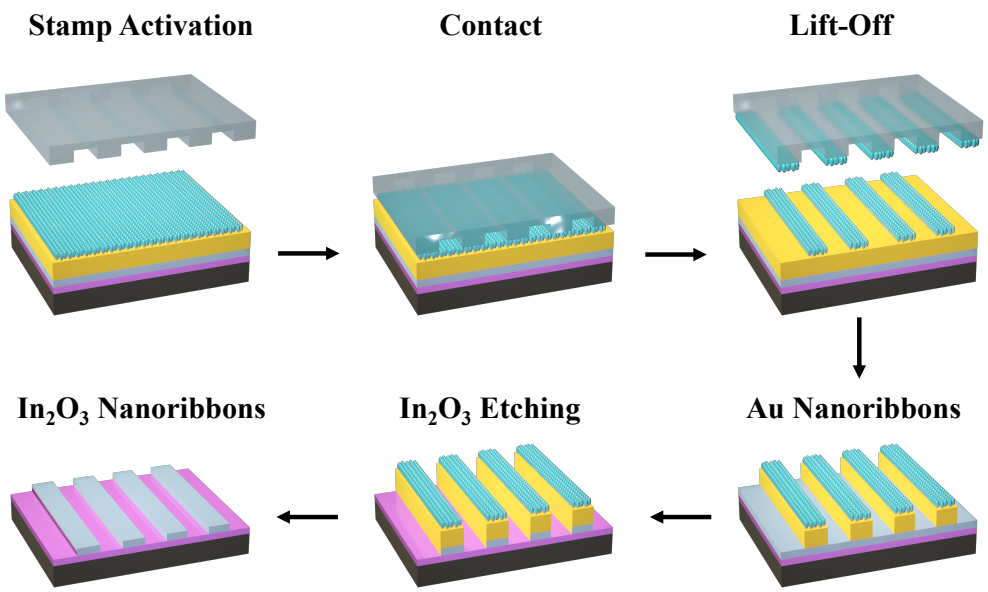

The information in this chapter is reprinted with permission from

Nano Lett. **2018**, *18*, 5590–55954 Copyright (2020) American Chemical Society

Authors: **Zhao, C.**; Xu, X.; Bae, S.H.; Yang, Q.; Liu, W.; Belling, J.N.; Cheung, K.M.; Rim, Y.S.; Yang, Y.; Andrews, A. M.; Weiss, P. S.

5.1 Abstract

Nanoribbon- and nanowire-based field-effect transistors (FETs) have attracted significant attention due to their high surface-to-volume ratios, which make them effective as chemical and biological sensors. However, conventional nanofabrication of these devices is challenging and costly, posing a major barrier to widespread use. We report a high-throughput approach for producing arrays of ultrathin (~3 nm) In_2O_3 nanoribbon FETs at the wafer scale. Uniform films of semiconducting In_2O_3 were prepared on Si/SiO_2 surfaces *via* a sol-gel process, prior to depositing Au/Ti metal layers. Commercially available HD-DVDs were employed as low-cost, large-area templates to prepare polymeric stamps for chemical lift-off lithography, which selectively removed molecules from self-assembled monolayers functionalizing the outermost Au surfaces. Nanoscale chemical patterns, consisting of one-dimensional lines (200 nm wide, 400 nm pitch) extending over centimeter length scales, were etched into the metal layers using the remaining monolayer regions as resists. Subsequent etch processes transferred the patterns into the underlying In_2O_3 films before removing the protective organic and metal coatings, revealing large-area nanoribbon arrays. We employed nanoribbons in semiconducting FET channels, achieving current on/off ratios over 10^7 and carrier mobilities up to 13.7 $cm^2 V^{-1} s^{-1}$. Nanofabricated structures, such as In_2O_3 nanoribbons and others, will be useful in nanoelectronics and biosensors. The technique demonstrated here will enable these applications and expand low-cost, large-area patterning strategies to enable a variety of materials and design geometries in nanoelectronics.

5.2 Introduction

One-dimensional (1D) nanomaterials, such as nanowires, nanotubes, and nanoribbons, possess large surface-to-volume ratios and tunable physical properties. These characteristics can be leveraged to achieve superior performance over bulk materials in a variety of applications, including electronics,[1-5] optics and photonics,[6-10] energy-storage and conversion devices,[11,12] biological and chemical sensors,[13-19] intracellular delivery of bioactive molecules,[20] and medical devices.[21,22] For example, Si nanowires (SiNWs) and carbon nanotubes (CNTs) have been employed as channel components in field-effect transistors (FETs) for highly effective sensing of proteins,[23,24] DNA,[25,26] viruses,[27] and neurotransmitters.[28] However, significant problems remain to be solved before 1D nanomaterials find widespread use.

Bottom-up techniques, such as chemical vapor deposition (CVD) and solution processes,[29-33] dominate 1D-nanomaterial fabrication. However, these strategies have poor control over the orientations of as-grown nanostructures, often on substrates other than the final devices. Bottom-up methods require additional steps to transfer nanostructures and then to control their positions and orientations in devices.[34,35] For example, SiNWs and CNTs, typically synthesized by CVD, require precise control over specific growth parameters to produce high-quality 1D nanomaterials suitable for electronic devices.[29,36] Moreover, nanowires synthesized by CVD are randomly orientated greatly increasing the complexity of device fabrication.[37] Performance is limited by poor control over the numbers of functional nanowires present in devices.[38,39]

Top-down approaches, including photolithography and electron-beam lithography (EBL), are widely used in the semiconductor industry to fabricate 1D nanomaterials. Top-down methods

enable precise control over final shapes, sizes, positions, and orientations of the as-fabricated structures,[40,41] providing ready integration with devices and high reproducibility.[42,43] Nonetheless, top-down techniques suffer from substantial equipment and usage costs. Patterns produced *via* photolithography are limited by the costs of masks and photon sources. By contrast, EBL achieves nanometer-resolution patterning but at the expense of time-consuming serial writing processes. These drawbacks represent significant barriers for many users, hence the need for alternative high-throughput, economical nanoscale patterning strategies.

Recently, we reported a straightforward, high-fidelity nanopatterning technique called chemical lift-off lithography (CLL),[44-49] wherein oxygen plasma-activated polydimethylsiloxane (PDMS) stamps selectively remove portions of a self-assembled monolayer (SAM) in contacted areas without observable lateral diffusion at feature edges. The remaining SAM molecules in the non-contacted regions act as molecular resists during subsequent etching of the freshly exposed underlying substrate. We previously demonstrated that CLL can be used to simplify device fabrication, as well as to enable biomolecule patterning to investigate DNA hybridization and spin-selective electron transport.[50-54] High-fidelity chemical patterns with line widths as narrow as 40 ± 2 nm were achieved using CLL, with the possibility of features as narrow as 5 nm (corresponding to ~10 molecules).[46] As with other top-down patterning approaches, however, CLL relies on expensive nanofabricated masters to create PDMS stamps to produce nanoscale structures. Masters for CLL have been produced using low-throughput EBL methods, limiting impact.[47,48]

Many top-down nanofabrication processes, including CLL, have focused on patterning metals and group IV and III-V semiconductors (*e.g.*, Au and Si).[55] Metal oxides represent an

increasingly important material class in numerous applications due to their electronic, mechanical, and optical properties.[45,56-58] To date, top-down approaches for fabricating metal-oxide nanomaterials are under developed compared to patterning methods for other types of materials, yet patterned semiconductors are of interest for applications including electronics, displays and lighting, ultra-sensitive biosensors, and wearable, flexible sensors.[59-61]

We report on the fabrication of large-area In_2O_3 nanoribbon arrays using CLL, but without using masters generated *via* EBL. We utilize metal oxide nanoribbons as semiconducting channels in FET architectures. Through this demonstration, we extend the range and applicability of CLL patterning to nanoscale features on semiconducting metal oxides for functional electronic devices, achieving current on/off ratios of ~10^7 and a peak mobility of 13.7 $cm^2\ V^{-1}\ s^{-1}$, in a low-cost, high-throughput manner.

5.3 Materials and Methods

Materials. Prime quality 4″ Si{100} wafers (P/B, 0.001-0.005 Ω-cm, thickness 500 μm) were purchased from Silicon Valley Microelectronics, Inc. (Santa Clara, CA, USA). Sylgard 184® silicone elastomer kits (lot #0008823745) were purchased from Ellsworth Adhesives (Germantown, WI, USA). (7–8% Vinylmethylsiloxane)–(dimethylsiloxane) copolymer, platinum divinyltetramethyl-disiloxane complex in xylene, and (25–30% methylhydrosiloxane)–(dimethylsiloxane) copolymer were all purchased from Gelest Inc. (Morrisville, PA, USA) and used as received. 2,4,6,8-Tetramethyl-2,4,6,8-tetravinylcyclotetrasiloxane, indium(III) nitrate hydrate (99.999%), iron nitrate, thiourea, ammonium hydroxide, hydrogen peroxide, ethylenediaminetetraacetic acid disodium salt dihydrate (EDTA), and acetic acid were purchased

from Sigma-Aldrich (St. Louis, MO, USA) and used as received. Commercially available HD-DVD-R recordable 1× speed 15 GB blank discs and DVD-R recordable 16× speed 4.7 GB blank discs (Memorex) were purchased and used as received. The SPR 700-1.2 photoresist and MF-26A developer were obtained from the Integrated Systems Nanofabrication Cleanroom (ISNC) at UCLA. Water was deionized before use (18.2 MΩ cm) using a Milli-Q system (Millipore, Billerica, MA).

Substrate fabrication. A 100 nm SiO_2 film was thermally grown on Si{100} wafers. If needed, SiO_2/Si wafers are also available for purchase at Silicon Valley Microelectronics, Inc. (Santa Clara, CA, USA). Next, 10 nm Ti and 30 nm Au films were deposited onto In_2O_3 films using a CHA solution electron-beam evaporator at high vacuum (10^{-8} Torr) with an evaporation rate of 0.1 nm/s. The Au/Ti/In_2O_3/Si substrates were then annealed in a hydrogen flame for ~10 s to remove adsorbed organic contaminants on the Au surfaces. Substrates were then immersed into an ethanolic 1 mM 11-mercapto-1-undecanol solution overnight for self-assembled monolayer formation on Au surfaces.

Preparation of HD-DVD and DVD masters. Commercially available HD-DVD-R recordable 1× speed 15 GB blank discs and DVD-R recordable 16× speed 4.7 GB blank discs were used to produce masters for patterning. Both HD-DVD and DVD discs have similar structures and therefore the preparation processes are the same. The HD-DVD discs were cut into wedge-shaped pieces. A razor blade was used to separate the discs at the edges between Layer II and Layer III in **Figure 5.1a**, and jagged edges were removed. The transparent part of the discs with the dye (Layer III in **Figure 5.1a**) were then rinsed with ethanol to remove the dye

from the surfaces. The slices were then put into a beaker of ethanol for 1-2 min. After that, they were blow dried under a N_2 flow.

Hard PDMS (h-PDMS) stamps. For soft PDMS, which should be prepared before starting the *h*-PDMS preparation process, a mixture of Sylgard® 184 elastomer base and curing agent (10:1) was thoroughly mixed and degassed in a vacuum desiccator. For *h*-PDMS, 3.4 g (7–8% vinylmethylsiloxane)–(dimethylsiloxane) copolymer, 18 μL of platinum divinyltetramethyl-disiloxane complex in xylene, and 50 μL of 2,4,6,8-tetramethyl-2,4,6,8-tetravinylcyclotetrasiloxane were mixed and degassed for <5 min. Then 1 g of (25–30% methylhydrosiloxane)–(dimethylsiloxane) copolymer was added and mixed gently. The mixture was poured onto HD-DVD masters and spin-coated at 1000 rpm for 40 s. Stamps were annealed at 65 °C for 15 min. Soft PDMS was then poured onto the backsides of the *h*-PDMS stamps and annealed at 65 °C overnight.

After the final curing step, stamps were slowly peeled away from masters and stored in clean petri dishes. Stamps were rinsed with ethanol and dried under N_2 flow before use. Clean PDMS stamps were treated in oxygen plasma (Harrick Plasma, Ithaca, NY, USA) for 40 s at a power of 18 W and a pressure of 10 psi to generate activated surfaces. A pair of tweezers was used to place PDMS stamps onto substrates without applying a vertical compression force. In the stamp removal process, one pair of tweezers was used to hold the substrates and another pair was used to lift off the stamps.

Wet etching. After PDMS stamp removal from SAM-functionalized substrates, each substrate was immersed into an aqueous solution of 20 mM iron nitrate and 30 mM thiourea to etch the Au films selectively. The etching rate was ~1 nm/min and the samples were put into the

etching solution for 30 min. Substrates were then rinsed with deionized (DI) water and dried under N_2. Substrates were immersed into a solution containing 0.42 g EDTA, 1 mL hydrogen peroxide, and 0.42 mL ammonia hydrate in 10 mL deionized water for ~3 min to etch through the 10 nm Ti layer. The In_2O_3 was then removed from the exposed areas by immersion in acetic acid for 10 min. Samples were annealed at 100 °C for 1 h after the wet etching process.

Field-effect transistor device fabrication. Interdigitated Au source and drain electrodes (45 μm length, 1300 μm width) were patterned on top of the In_2O_3 nanoribbons to obtain uniform current distributions. Electrodes were patterned by standard photolithography. The 10 nm Ti and 30 nm Au films were deposited *via* a CHA solution e-beam evaporator at high vacuum (10^{-8} Torr) at an evaporation rate of 0.1 nm/s.

Substrate characterization. Scanning electron microscope (SEM) images were obtained using a Zeiss Supra 40VP scanning electron microscope with an Inlens SE Detector (Inlens secondary electron detector). Atomic force microscope (AFM) imaging was performed on a Bruker FastScan system (Bruker, Billerica, MA) under PeakForce tapping mode with a ScanAsyst-Air cantilevers (Bruker, spring constant = 0.4 ± 0.1 N/m). Electronic performance measurements were carried out on a manual analytical probe station (Signatone, Gilroy, CA) equipped with a Keithley 4200A (Tektronix, Beaverton, OR) semiconductor parameter analyzer. Optical images were taken with a digital camera attached to a Zeiss Axiotech optical microscope.

5.4. Results and Discussions

Most commonly used thin-film metal oxide deposition strategies rely on physical/chemical vapor deposition methods, such as pulsed-laser deposition,[62] sputtering,[63] and atomic-layer deposition,[64] requiring complex processes, extreme conditions (*e.g.*, high

temperature, vacuum), and costly equipment. Recently, simple, scalable sol-gel-based processes have emerged as alternatives for preparing high quality semiconducting metal-oxide films.[65-68] Here, thin films of In_2O_3 were prepared *via* a sol-gel process. Aqueous solutions (0.1 M) of $In(NO_3)_3$ were spin-coated onto SiO_2/Si substrates (100 nm, thermally grown SiO_2 dielectric on heavily doped, *p*-type Si substrates with resistivities of 1–5 mΩ·cm). Following deposition, substrates were heated to 100 °C for 5 min and annealed at 350 °C for 3 h. The thicknesses of the resulting In_2O_3 films were ~3 nm with typical average surface roughnesses of ~0.06 nm determined *via* atomic force microscopy (AFM) (**Figure S5.1**). Note that the In_2O_3 films fabricated via the sol-gel process are amorphous.[45]

Commercially available optical storage media, such as compact discs (CDs) and DVDs are patterned with sub-micron periodic gratings that can be used directly as economical templates for soft lithography. We employed HD-DVDs as masters for CLL PDMS stamps. The HD-DVDs have quasi-1D feature widths of ~200 nm, spaced at a pitch of 400 nm. As shown in **Figure 5.1a**, each HD-DVD is composed of a protection layer (I), a reflective layer (II), a recording layer (III), and a polycarbonate layer (IV) composed of embossed concentric rings that form the basis of the patterns used herein. Layer IV was exposed simply by removing layers I and II with a razor blade and dissolving layer III with ethanol (**Figure 5.1c**). Atomic force microscopy confirmed the expected, grooved pattern on the surface of layer IV, as seen in **Figure 5.1e**. To replicate layer IV features precisely, hard PDMS (*h*-PDMS) was used as the stamp material due to its stiffness compared to regular (soft) Sylgard 184 PDMS.[69] Unpolymerized *h*-PDMS was spin-coated onto masters (2 cm × 2 cm, 40 s at 1000 rpm) and cured at 65 °C for 10 min to form thin and robust films. A layer of soft PDMS (~5 mm) was then applied and cured at 65 °C overnight to form a support for the pattern-containing *h*-PDMS film

and to prevent cracking, prior to demolding stamps from masters. These stamps (**Figure 5.1d**) are reusable and can be employed for repeated, wafer-scale CLL patterning. Atomic-force micrographs of patterned PDMS surfaces (**Figure 5.1f**) confirmed precise replication of HD-DVD features with depths of ~60 nm.

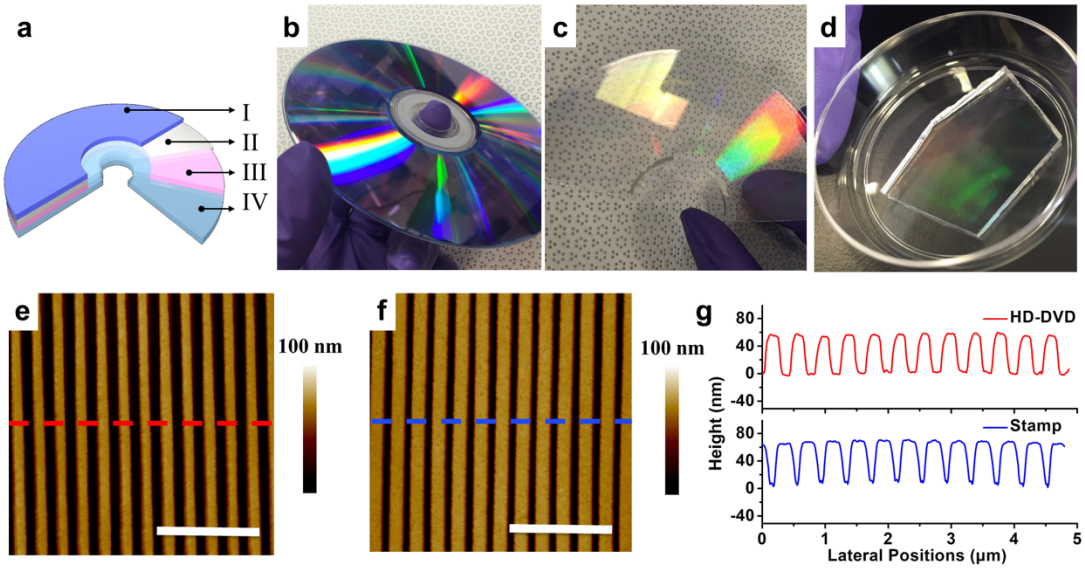

Figure 5.1. (a) Schematic architecture of a high-definition digital-versatile disc (HD-DVD): layer I, polycarbonate protective layer; layer II, mirror-like metal film; layer III, data recording film; layer IV, polycarbonate layer containing concentric rings with typical widths of 250 nm and periodicities of 400 nm. (b-d) Photographs of an HD-DVD, an HD-DVD master (layer IV), and a patterned polydimethylsiloxane (PDMS) stamp, respectively. Atomic force micrographs of (e) a representative HD-DVD master and (f) a patterned PDMS stamp. Scale bars are 2 μm. (g) Topographic profiles across the corrugated features in (e) and (f).

The scheme used to fabricate In_2O_3 nanoribbons is illustrated in **Figure 5.2**. *Step 1:* layers of Ti (10 nm) and Au (30 nm) were deposited on previously prepared In_2O_3 films. The $Au/Ti/In_2O_3/SiO_2/Si$ stacks were then incubated in 1 mM ethanolic solutions of 11-mercapto-1-undecanol ($HSCH_2(CH_2)_9CH_2OH$) to form SAMs terminated with –OH moieties, enabling CLL patterning. *Step 2:* oxygen plasma was used to "activate" PDMS stamp surfaces, generating siloxyl groups (SiOH). Stamps were then brought into conformal contact with SAMs. Condensation reactions occur between the hydroxyl- (–OH) terminated SAMs and the SiOH groups of the activated *h*-PDMS, forming covalent linkages (Si–O–SAM). *Step 3:* Upon removal of the stamps, molecules within the contracted regions of the SAMs were selectively removed transferring the stamp pattern to the monolayer. Notably, in the lift-off process, monolayers of Au atoms are also removed as Au–S bonds (between SAM molecules and the underlying Au substrate atoms) are stronger than Au–Au bonds in the substrates.

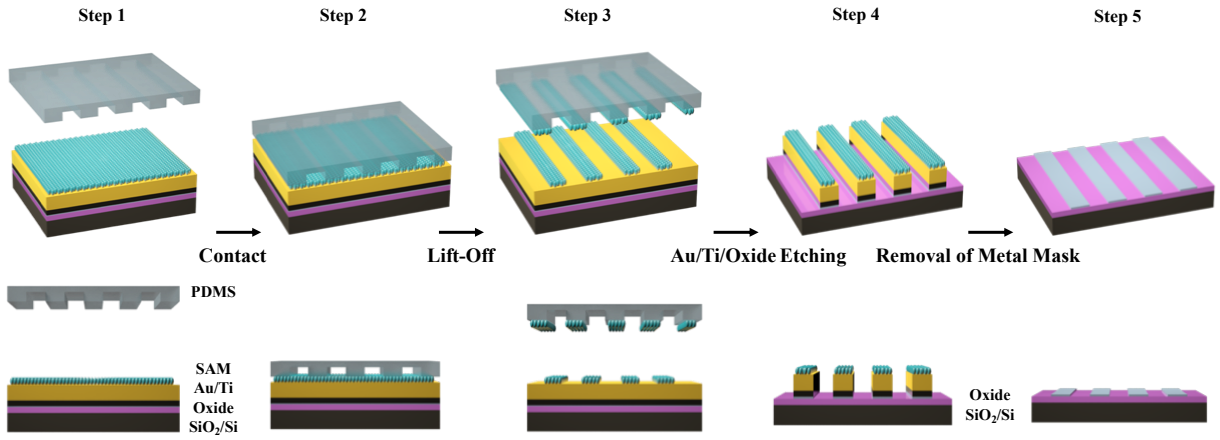

Figure 5.2. Fabrication scheme of In_2O_3 nanoribbons. Step 1: a thin film of 3-nm In_2O_3 is deposited on a SiO_2/Si substrate *via* a sol-gel process followed by Au (30 nm)/Ti (10 nm) deposition and functionalization with a self-assembled monolayer (SAM). Step 2: a polydimethylsiloxane (PDMS) stamp, activated by an oxygen plasma, is brought into

conformal contact with the substrate. Step 3: Upon lifting the stamp from the surface, SAM molecules in the contacted areas are removed, transferring the pattern (periodic lines and spaces) into the SAM. Step 4: Successive selective etch processes remove Au/Ti and In_2O_3 layers from unprotected regions on the surface. Step 5: Remaining SAM, Au, and Ti are removed to produce In_2O_3 nanoribbon arrays.

Scanning electron microscopy of CLL-patterned SAMs (**Figure 5.3a)** confirmed the presence of 1D features (200 nm linewidths) over large areas, matching those on the stamps (**Figure 5.1f**). *Step 4:* Intact monolayers in the non-contacted regions acted as resists for successive etching by solutions of $Fe(NO_3)_3$ and thiourea (removing exposed Au) and EDTA disodium salt, NH_4OH, and H_2O_2 (removing Ti), thereby transferring the SAM patterns through the metal layers. The metal layers acted as etch masks protecting the underlying In_2O_3 films from removal by glacial acetic acid. The resulting Au/Ti/In_2O_3 nanoribbons were investigated by AFM (**Figure 5.3b**) and found to have heights of ~45 nm, corresponding to the sum of the expected heights of the constituent layers above the surrounding Si/SiO_2 surfaces exposed by previous etch processes. *Step 5*: metal layers were completely removed to expose arrays of In_2O_3 nanoribbons extending over centimeter length scales (**Figure 5.3c)**. The widths (~200 nm) and heights (~3 nm) of the metal oxide nanoribbons are the smallest, to our knowledge, fabricated *via* top-down approaches.

To demonstrate the versatility of CLL patterning for additional feature sizes, In_2O_3 nanoribbons of different linewidths (350 nm and 1500 nm) were fabricated using alternate master patterns (**Figure 5.3d and 5.3e**, respectively). The Au nanoribbons produced as an

intermediate product of this process (*Step 4*) can also be used for a variety of applications, such as surface plasmon resonance biosensors. Note that In_2O_3 nanoribbon edges are rougher than those of similarly produced Au nanoribbons and the feature sizes are reduced; this is a common phenomenon associated with isotropic etch processes, which can undercut regions below the protective masks.

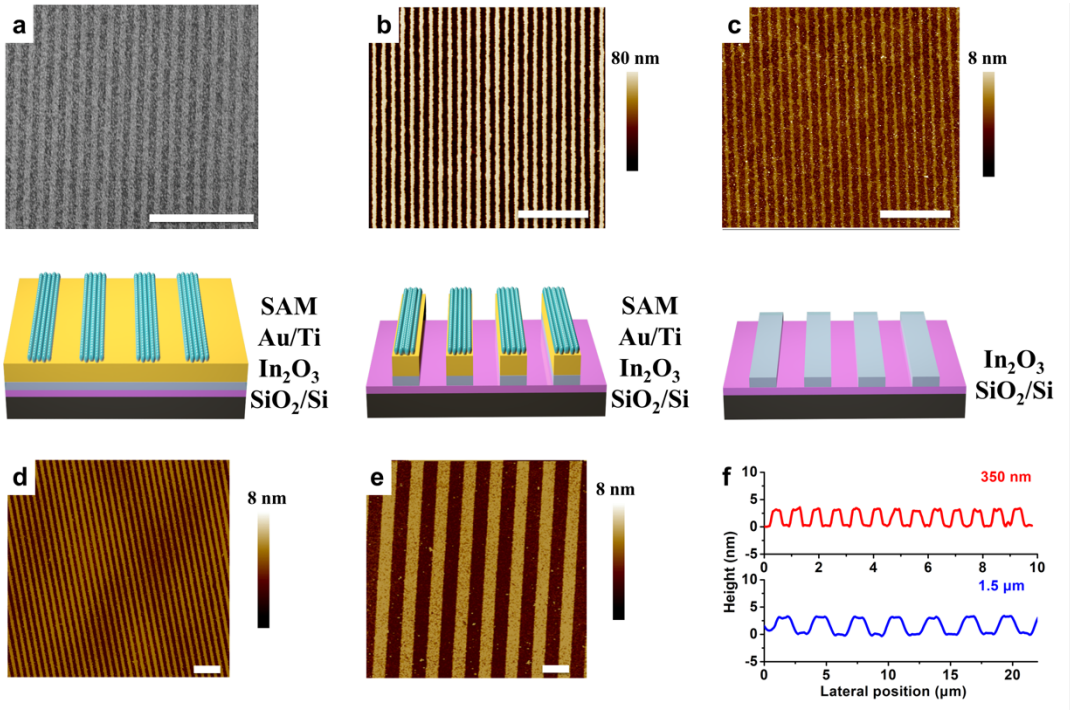

Figure 5.3. (a) (top) Scanning electron microscope image and (bottom) schematic of a self-assembled monolayer (SAM) patterned *via* chemical lift-off lithography. (b,c) (top) Topographic images measured using atomic force microscopy (AFM) and (bottom) schematic illustrations of SAM/Au/Ti/In_2O_3 and bare In_2O_3 nanoribbons, respectively, with line widths of ~200 nm. Atomic force topographs of In_2O_3 nanoribbons with line widths of (d) 350 nm and (e) 1.5 µm. Thicknesses of each set of In_2O_3 nanoribbons (c-e) were

measured to be ~3 nm by AFM. (f) Height profiles of (top) 500-nm-wide In_2O_3 nanoribbons and (bottom) 1.5-µm-wide nanoribbons. Scale bars in all images are 3 µm.

Field-effect transistors have key advantages over optical or electrochemical platforms for biosensing applications, including low detection limits, real-time and label-free measurements, and simple integration with standard semiconductor-device processing.[45] To evaluate the performance of In_2O_3 nanoribbons in devices, we constructed FETs in a bottom-gate, top-contact configuration as shown in **Figure 5.4**. Gold electrodes were deposited atop arrays of as-prepared In_2O_3 nanoribbons *via* electron-beam evaporation through conventional photolithography. The device measurement setup is shown in **Figure S5.2**. As shown in **Figure S5.3**, interdigitated electrodes with widths of 1300 µm and lengths of 45 µm were used.

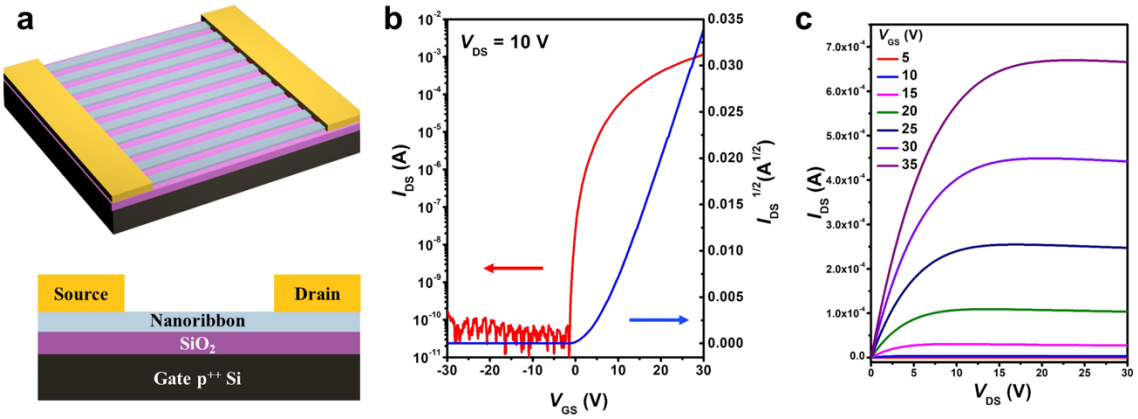

Figure 5.4. (a) Schematic illustrations of an In_2O_3 field-effect transistor (FET) in a bottom-gate-top-contact configuration. Gate: Si (p^{++}); Source/Drain: Au; semiconducting channel: In_2O_3 nanoribbons. The widths and lengths of the inter-digital electrodes are 1300 and 45 µm, respectively. The widths and pitches of the nanoribbons are 200 and 400 nm, respectively. (b) Transfer and (c) output characteristics of an ultrathin In_2O_3 nanoribbon

FET, showing the measured current between the drain and source (I_{DS}) in response to varying gate to source voltages (V_{GS}) and source to drain (V_{DS}) potentials, relative to the source. Devices displayed *n*-type pinch-off behavior with carrier motilities of 10.0 ± 2.6 cm^2 V^{-1} s^{-1}, averaged over 10 devices with a peak value of 13.7 cm^2 V^{-1} s^{-1}, and a current on/off ratio >10^7.

The spatially ordered arrangement of In_2O_3 nanoribbons on surfaces facilitated straightforward fabrication of FETs with consistent numbers of channels per device, controlled by the widths of the contact electrodes. Here, ~3000 200-nm-wide In_2O_3 nanoribbons were incorporated into each FET device. These FETs had high field-effect mobilities (μ_{sat}=10.0 ± 2.6 cm^2 V^{-1} s^{-1}), averaged over 10 devices with a peak value of 13.7 cm^2 V^{-1} s^{-1} and a current on/off ratio >10^7. We attribute the variations in mobilities to imperfections of the sol-gel-processed thin-film material itself (such as defects), as we have observed similar variations in analogous thin film FETs.[45] These nanoribbon FETs have similar electronic properties to In_2O_3 thin-film transistors,[45] but have higher surface-to-volume ratios. The performance of these devices, such as current on/off ratio, exceeded those previously reported for 1D nanowire-based devices fabricated *via* bottom-up approaches.[15,16] High-performance In_2O_3 nanoribbon FETs can be used in a variety of applications, such as electronic devices and ultrasensitive FET-based pH, gas, chemical, and biological sensors, where the surface of In_2O_3 can be functionalized with a variety of molecules including antibodies and aptamers using linkers such as (3-aminopropyl)trimethoxysilane.[45,57,59,65]

5.5 Conclusions and Prospects

In summary, we report a high-throughput, large-scale strategy enabling fabrication of ultrathin, metal oxide nanoribbons that are readily integrated into devices. We leverage and extend the capabilities of CLL, in combination with selective etching processes, to pattern, successively, SAMs, metal films, and ultrathin layers of In_2O_3 to create arrays of periodic, 1D nanostructures. Nanoribbons fabricated by this approach are uniform and continuous over centimeter scales. We demonstrate high-performance FETs fabricated using In_2O_3 nanoribbons having carrier mobilities up to 13.7 $cm^2 V^{-1} s^{-1}$ and on/off current ratios $>10^7$. By employing widely available low-cost HD-DVDs as nanostructured master patterns, in conjunction with CLL, a scalable and high-fidelity chemical patterning technique that does not require sophisticated equipment and facilities, we lower barriers to nanostructure and device fabrication. The advances demonstrated here serve to extend large-area nanofabrication and to broaden application and user bases by providing alternative patterning strategies to photo- and electron-beam lithographies. This work provides a general approach for the facile and large-scale patterning of semiconductor 1D nanostructure arrays with high-surface-to-volume ratios, which have a broad range of applications in electronic devices, optical devices, displays, and biochemical sensors.

5.6 Supplementary Materials

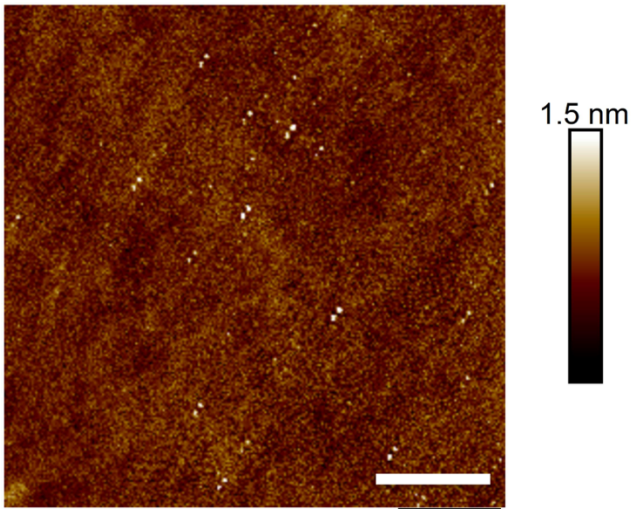

Figure S5.1. Atomic force microscope image of In_2O_3 films. The average roughness (Ra) is ~0.06 nm. The scale bar is 1 µm.

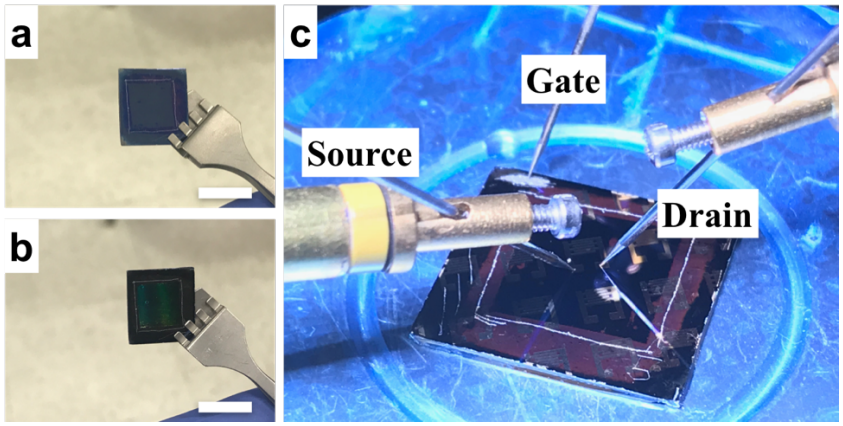

Figure S5.2. Images of the fabricated devices and test configuration. (a,b) In_2O_3 nanoribbons on a 1.5 cm × 1.5 cm Si wafer. The 1 cm × 1 cm square region in the center contains the nanoribbons. The rainbow colors in the central region of the bottom image (b)

indicate light interference from the periodic nanoribbon pattern. (c) Device test configuration using a probe station with bottom gate and top source/drain electrodes.

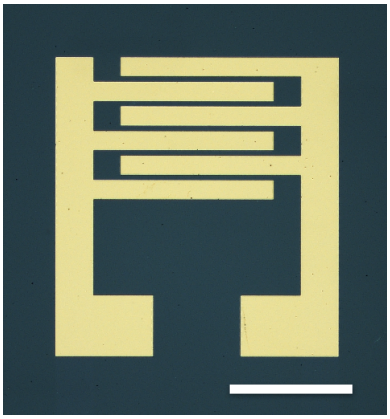

Figure S5.3. Photograph of a representative device with the interdigitated electrode configuration. The widths and lengths of the inter-digital electrodes are 1300 and 45 µm, respectively. The scale bar is 1000 µm.

5.7 References

(1) Cui, Y.; Lieber, C. M. Functional Nanoscale Electronic Devices Assembled Using Silicon Nanowire Building Blocks. *Science* **2001,** *291*, 851–853.

(2) Xu, X.; Liu, C.; Kim, K.; Fan, D. L. Electric-Driven Rotation of Silicon Nanowires and Silicon Nanowire Motors. *Adv. Funct. Mater.* **2014,** *24*, 4843–4850.

(3) Memisevic, E.; Hellenbrand, M.; Lind, E.; Persson, A. R.; Sant, S.; Schenk, A.; Svensson, J.; Wallenberg, R.; Wernersson, L. E. Individual Defects in InAs/InGaAsSb/Gasb

Nanowire Tunnel Field-Effect Transistors Operating Below 60 mV/Decade. *Nano Lett*. **2017,** *17*, 4373–4380.

(4) Lee, H.; Manorotkul, W.; Lee, J.; Kwon, J.; Suh, Y. D.; Paeng, D.; Grigoropoulos, C. P.; Han, S.; Hong, S.; Yeo, J.; Ko, S. H. Nanowire-on-Nanowire: All-Nanowire Electronics by On-Demand Selective Integration of Hierarchical Heterogeneous Nanowires. *ACS Nano* **2017,** *11*, 12311–12317.

(5) Qiu, C.; Zhang, Z.; Xiao, M.; Yang, Y.; Zhong, D.; Peng, L. M. Scaling Carbon Nanotube Complementary Transistors to 5-nm Gate Lengths. *Science* **2017,** *355*, 271–276.

(6) Huang, M. H.; Mao, S.; Feick, H.; Yan, H.; Wu, Y.; Kind, H.; Weber, E.; Russo, R.; Yang, P. Room-Temperature Ultraviolet Nanowire Nanolasers. *Science* **2001,** *292*, 1897–1899.

(7) Law, M.; Sirbuly, D. J.; Johnson, J. C.; Goldberger, J.; Saykally, R. J.; Yang, P. Nanoribbon Waveguides for Subwavelength Photonics Integration. *Science* **2004,** *305*, 1269–1273.

(8) Xu, X.; Kim, K.; Fan, D. Tunable Release of Multiplex Biochemicals by Plasmonically Active Rotary Nanomotors. *Angew. Chem., Int. Ed.* **2015,** *54*, 2525–2529.

(9) Liu, P.; He, X.; Ren, J.; Liao, Q.; Yao, J.; Fu, H. Organic-Inorganic Hybrid Perovskite Nanowire Laser Arrays. *ACS Nano* **2017,** *11*, 5766–5773.

(10) Xu, X.; Yang, Q.; Wattanatorn, N.; Zhao, C.; Chiang, N.; Jonas, S. J.; Weiss, P. S. Multiple-Patterning Nanosphere Lithography for Fabricating Periodic Three-Dimensional Hierarchical Nanostructures. *ACS Nano* **2017,** *11*, 10384–10391.

(11) Law, M.; Greene, L. E.; Johnson, J. C.; Saykally, R.; Yang, P. Nanowire Dye-Sensitized Solar Cells. *Nat. Mater.* **2005,** *4*, 455–459.

(12) Zhang, L.; Jia, Y.; Wang, S.; Li, Z.; Ji, C.; Wei, J.; Zhu, H.; Wang, K.; Wu, D.; Shi, E.; Fang, Y.; Cao, A. Carbon Nanotube and Cdse Nanobelt Schottky Junction Solar Cells. *Nano Lett.* **2010,** *10*, 3583–3589.

(13) Kong, J. Nanotube Molecular Wires as Chemical Sensors. *Science* **2000,** *287*, 622–625.

(14) Cui, Y.; Wei, Q.; Park, H.; Lieber, C. M. Nanowire Nanosensors for Highly Sensitive and Selective Detection of Biological and Chemical Species. *Science* **2001,** *293*, 1289–1292.

(15) Li, C.; Zhang, D.; Liu, X.; Han, S.; Tang, T.; Han, J.; Zhou, C. In2O3 Nanowires as Chemical Sensors. *Appl. Phys. Lett.* **2003,** *82*, 1613–1615.

(16) Zhang, D.; Liu, Z.; Li, C.; Tang, T.; Liu, X.; Han, S.; Lei, B.; Zhou, C. Detection of No2down to ppb Levels Using Individual and Multiple In2o3nanowire Devices. *Nano Lett.* **2004,** *4*, 1919–1924.

(17) Cheng, Y.; Xiong, P.; Yun, C. S.; Strouse, G. F.; Zheng, J. P.; Yang, R. S.; Wang, Z. L. Mechanism and Optimization of Ph Sensing Using Sno2nanobelt Field Effect Transistors. *Nano Lett.* **2008,** *8*, 4179–4184.

(18) Xu, X.; Li, H.; Hasan, D.; Ruoff, R. S.; Wang, A. X.; Fan, D. L. Near-Field Enhanced Plasmonic-Magnetic Bifunctional Nanotubes for Single Cell Bioanalysis. *Adv. Funct. Mater.* **2013,** *23*, 4332–4338.

(19) Kim, K.; Xu, X.; Guo, J.; Fan, D. L. Ultrahigh-Speed Rotating Nanoelectromechanical System Devices Assembled from Nanoscale Building Blocks. *Nat. Commun.* **2014,** *5*, 3632.

(20) Xu, X.; Hou, S.; Wattanatorn, N.; Wang, F.; Yang, Q.; Zhao, C.; Yu, X.; Tseng, H.-R.; Jonas, S. J.; Weiss, P. S. Precision-Guided Nanospears for Targeted and High-Throughput Intracellular Gene Delivery. *ACS Nano* **2018,** *12*, 4503–4511.

(21) Kim, J.; Lee, M.; Shim, H. J.; Ghaffari, R.; Cho, H. R.; Son, D.; Jung, Y. H.; Soh, M.; Choi, C.; Jung, S.; Chu, K.; Jeon, D.; Lee, S. T.; Kim, J. H.; Choi, S. H.; Hyeon, T.; Kim, D. H. Stretchable Silicon Nanoribbon Electronics for Skin Prosthesis. *Nat. Commun.* **2014,** *5*, 5747.

(22) Liu, R.; Chen, R.; Elthakeb, A. T.; Lee, S. H.; Hinckley, S.; Khraiche, M. L.; Scott, J.; Pre, D.; Hwang, Y.; Tanaka, A.; Ro, Y. G.; Matsushita, A. K.; Dai, X.; Soci, C.; Biesmans, S.; James, A.; Nogan, J.; Jungjohann, K. L.; Pete, D. V.; Webb, D. B.; et al. High Density Individually Addressable Nanowire Arrays Record Intracellular Activity from Primary Rodent and Human Stem Cell Derived Neurons. *Nano Lett.* **2017,** *17*, 2757–2764.

(23) So, H. M.; Won, K.; Kim, Y. H.; Kim, B. K.; Ryu, B. H.; Na, P. S.; Kim, H.; Lee, J. O. Single-Walled Carbon Nanotube Biosensors Using Aptamers as Molecular Recognition Elements. *J. Am. Chem. Soc.* **2005,** *127*, 11906–11907.

(24) Stern, E.; Vacic, A.; Rajan, N. K.; Criscione, J. M.; Park, J.; Ilic, B. R.; Mooney, D. J.; Reed, M. A.; Fahmy, T. M. Label-Free Biomarker Detection from Whole Blood. *Nat. Nanotechnol.* **2010,** *5*, 138–142.

(25) Hahm, J.-i.; Lieber, C. M. Direct Ultrasensitive Electrical Detection of DNA and DNA Sequence Variations Using Nanowire Nanosensors. *Nano Lett.* **2004,** *4*, 51–54.

(26) Sorgenfrei, S.; Chiu, C. Y.; Gonzalez, R. L., Jr.; Yu, Y. J.; Kim, P.; Nuckolls, C.; Shepard, K. L. Label-Free Single-Molecule Detection of DNA-Hybridization Kinetics with a Carbon Nanotube Field-Effect Transistor. *Nat. Nanotechnol.* **2011,** *6*, 126–132.

(27) Patolsky, F.; Zheng, G.; Hayden, O.; Lakadamyali, M.; Zhuang, X.; Lieber, C. M. Electrical Detection of Single Viruses. *Proc. Natl. Acad. Sci. U. S. A.* **2004,** *101*, 14017–14022.

(28) Li, B. R.; Hsieh, Y. J.; Chen, Y. X.; Chung, Y. T.; Pan, C. Y.; Chen, Y. T. An Ultrasensitive Nanowire-Transistor Biosensor for Detecting Dopamine Release from Living Pc12 Cells under Hypoxic Stimulation. *J. Am. Chem. Soc.* **2013,** *135*, 16034–16037.

(29) Patolsky, F.; Zheng, G.; Lieber, C. M. Fabrication of Silicon Nanowire Devices for Ultrasensitive, Label-Free, Real-Time Detection of Biological and Chemical Species. *Nat. Protoc.* **2006,** *1*, 1711–1724.

(30) Wang, Z. L. Piezoelectric Nanogenerators Based on Zinc Oxide Nanowire Arrays. *Science* **2006,** *312*, 242–246.

(31) Liu, C.; Xu, X.; Rettie, A. J. E.; Mullins, C. B.; Fan, D. L. One-Step Waferscale Synthesis of 3-D ZnO Nanosuperstructures by Designed Catalysts for Substantial Improvement of Solar Water Oxidation Efficiency. *J. Mater. Chem. A* **2013,** *1*, 8111.

(32) Gao, N.; Zhou, W.; Jiang, X.; Hong, G.; Fu, T. M.; Lieber, C. M. General Strategy for Biodetection in High Ionic Strength Solutions Using Transistor-Based Nanoelectronic Sensors. *Nano Lett.* **2015,** *15*, 2143–2148.

(33) Constantinou, M.; Rigas, G. P.; Castro, F. A.; Stolojan, V.; Hoettges, K. F.; Hughes, M. P.; Adkins, E.; Korgel, B. A.; Shkunov, M. Simultaneous Tunable Selection and Self-Assembly of Si Nanowires from Heterogeneous Feedstock. *ACS Nano* **2016,** *10*, 4384–4394.

(34) Xu, F.; Durham, J. W.; Wiley, B. J.; Zhu, Y. Strain-Release Assembly of Nanowires on Stretchable Substrates. *ACS Nano* **2011,** *5*, 1556–1563.

(35) Yao, J.; Yan, H.; Lieber, C. M. A Nanoscale Combing Technique for the Large-Scale Assembly of Highly Aligned Nanowires. *Nat. Nanotechnol.* **2013,** *8*, 329–335.

(36) Alam, S. B.; Panciera, F.; Hansen, O.; Molhave, K.; Ross, F. M. Creating New Vls Silicon Nanowire Contact Geometries by Controlling Catalyst Migration. *Nano Lett.* **2015,** *15*, 6535–6541.

(37) Ishikawa, F. N.; Curreli, M.; Chang, H. K.; Chen, P. C.; Zhang, R.; Cote, R. J.; Thompson, M. E.; Zhou, C. A Calibration Method for Nanowire Biosensors to Suppress Device-to-Device Variation. *ACS Nano* **2009,** *3*, 3969–3976.

(38) Li, J.; Zhang, Y.; To, S.; You, L.; Sun, Y. Effect of Nanowire Number, Diameter, and Doping Density on nano-FET Biosensor Sensitivity. *ACS Nano* **2011,** *5*, 6661–6668.

(39) Lee, B. Y.; Sung, M. G.; Lee, J.; Baik, K. Y.; Kwon, Y. K.; Lee, M. S.; Hong, S. Universal Parameters for Carbon Nanotube Network-Based Sensors: Can Nanotube Sensors Be Reproducible? *ACS Nano* **2011,** *5*, 4373–4379.

(40) Stern, E.; Klemic, J. F.; Routenberg, D. A.; Wyrembak, P. N.; Turner-Evans, D. B.; Hamilton, A. D.; LaVan, D. A.; Fahmy, T. M.; Reed, M. A. Label-Free Immunodetection with CMOS-Compatible Semiconducting Nanowires. *Nature* **2007,** *445*, 519–522.

(41) Knopfmacher, O.; Tarasov, A.; Fu, W.; Wipf, M.; Niesen, B.; Calame, M.; Schonenberger, C. Nernst Limit in Dual-Gated Si-Nanowire FET Sensors. *Nano Lett*. **2010,** *10*, 2268–2274.

(42) Tong, H. D.; Chen, S.; van der Wiel, W. G.; Carlen, E. T.; van den Berg, A. Novel Top-Down Wafer-Scale Fabrication of Single Crystal Silicon Nanowires. *Nano Lett*. **2009,** *9*, 1015–1022.

(43) Hwang, S. W.; Lee, C. H.; Cheng, H.; Jeong, J. W.; Kang, S. K.; Kim, J. H.; Shin, J.; Yang, J.; Liu, Z.; Ameer, G. A.; Huang, Y.; Rogers, J. A. Biodegradable Elastomers and Silicon Nanomembranes/Nanoribbons for Stretchable, Transient Electronics, and Biosensors. *Nano Lett*. **2015,** *15*, 2801–2808.

(44) Liao, W. S.; Cheunkar, S.; Cao, H. H.; Bednar, H. R.; Weiss, P. S.; Andrews, A. M. Subtractive Patterning via Chemical Lift-Off Lithography. *Science* **2012,** *337*, 1517-1521.

(45) Kim, J.; Rim, Y. S.; Chen, H.; Cao, H. H.; Nakatsuka, N.; Hinton, H. L.; Zhao, C.; Andrews, A. M.; Yang, Y.; Weiss, P. S. Fabrication of High-Performance Ultrathin In_2O_3 Film Field-Effect Transistors and Biosensors Using Chemical Lift-Off Lithography. *ACS Nano* **2015,** *9*, 4572–4582.

(46) Andrews, A. M.; Liao, W. S.; Weiss, P. S. Double-Sided Opportunities Using Chemical Lift-Off Lithography. *Acc. Chem. Res*. **2016,** *49*, 1449–1457.

(47) Xu, X.; Yang, Q.; Cheung, K. M.; Zhao, C.; Wattanatorn, N.; Belling, J. N.; Abendroth, J. M.; Slaughter, L. S.; Mirkin, C. A.; Andrews, A. M.; Weiss, P. S. Polymer-Pen Chemical Lift-Off Lithography. *Nano Lett*. **2017,** *17*, 3302–3311.

(48) Zhao, C.; Xu, X.; Yang, Q.; Man, T.; Jonas, S. J.; Schwartz, J. J.; Andrews, A. M.; Weiss, P. S. Self-Collapse Lithography. *Nano Lett*. **2017,** *17*, 5035–5042.

(49) Slaughter, L. S.; Cheung, K. M.; Kaappa, S.; Cao, H. H.; Yang, Q.; Young, T. D.; Serino, A. C.; Malola, S.; Olson, J. M.; Link, S.; Hakkinen, H.; Andrews, A. M.; Weiss, P. S. Patterning of Supported Gold Monolayers via Chemical Lift-Off Lithography. *Beilstein J. Nanotech*. **2017,** *8*, 2648–2661.

(50) Cao, H. H.; Nakatsuka, N.; Serino, A. C.; Liao, W. S.; Cheunkar, S.; Yang, H.; Weiss, P. S.; Andrews, A. M. Controlled DNA Patterning by Chemical Lift-Off Lithography: Matrix Matters. *ACS Nano* **2015,** *9*, 11439–11454.

(51) Abendroth, J. M.; Nakatsuka, N.; Ye, M.; Kim, D.; Fullerton, E. E.; Andrews, A. M.; Weiss, P. S. Analyzing Spin Selectivity in DNA-Mediated Charge Transfer via Fluorescence Microscopy. *ACS Nano* **2017,** *11*, 7516–7526.

(52) Cao, H. H.; Nakatsuka, N.; Liao, W.-S.; Serino, A. C.; Cheunkar, S.; Yang, H.; Weiss, P. S.; Andrews, A. M. Advancing Biocapture Substrates via Chemical Lift-Off Lithography. *Chem. Mater*. **2017,** *29*, 6829–6839.

(53) Chen, C. Y.; Wang, C. M.; Chen, P. S.; Liao, W. S. Surface Functional DNA Density Control by Programmable Molecular Defects. *Chem. Comm*. **2018,** *54*, 4100–4103.

(54) Chen, C. Y.; Wang, C. M.; Chen, P. S.; Liao, W. S. Self-Standing Aptamers by an Artificial Defect-Rich Matrix. *Nanoscale* **2018,** *10*, 3191–3197.

(55) Ko, H.; Takei, K.; Kapadia, R.; Chuang, S.; Fang, H.; Leu, P. W.; Ganapathi, K.; Plis, E.; Kim, H. S.; Chen, S. Y.; Madsen, M.; Ford, A. C.; Chueh, Y. L.; Krishna, S.; Salahuddin, S.;

Javey, A. Ultrathin Compound Semiconductor on Insulator Layers for High-Performance Nanoscale Transistors. *Nature* **2010,** *468*, 286–289.

(56) Rim, Y. S.; Bae, S. H.; Chen, H.; Yang, J. L.; Kim, J.; Andrews, A. M.; Weiss, P. S.; Yang, Y.; Tseng, H. R. Printable Ultrathin Metal Oxide Semiconductor-Based Conformal Biosensors. *ACS Nano* **2015,** *9*, 12174–12181.

(57) Chen, H.; Rim, Y. S.; Wang, I. C.; Li, C.; Zhu, B.; Sun, M.; Goorsky, M. S.; He, X.; Yang, Y. Quasi-Two-Dimensional Metal Oxide Semiconductors Based Ultrasensitive Potentiometric Biosensors. *ACS Nano* **2017,** *11*, 4710–4718.

(58) Rim, Y. S.; Chen, H.; Zhu, B.; Bae, S.-H.; Zhu, S.; Li, P. J.; Wang, I. C.; Yang, Y. Interface Engineering of Metal Oxide Semiconductors for Biosensing Applications. *Adv. Mater. Inter.* **2017,** *4*, 1700020.

(59) Aroonyadet, N.; Wang, X.; Song, Y.; Chen, H.; Cote, R. J.; Thompson, M. E.; Datar, R. H.; Zhou, C. Highly Scalable, Uniform, and Sensitive Biosensors Based on Top-Down Indium Oxide Nanoribbons and Electronic Enzyme-Linked Immunosorbent Assay. *Nano Lett.* **2015,** *15*, 1943-1951.

(60) Liu, Q.; Aroonyadet, N.; Song, Y.; Wang, X.; Cao, X.; Liu, Y.; Cong, S.; Wu, F.; Thompson, M. E.; Zhou, C. Highly Sensitive and Quick Detection of Acute Myocardial Infarction Biomarkers Using In2O3 Nanoribbon Biosensors Fabricated Using Shadow Masks. *ACS Nano* **2016,** *10*, 10117–10125.

(61) Liu, Q.; Liu, Y.; Wu, F.; Cao, X.; Li, Z.; Alharbi, M.; Abbas, A. N.; Amer, M. R.; Zhou, C. Highly Sensitive and Wearable In2O3 Nanoribbon Transistor Biosensors with Integrated On-Chip Gate for Glucose Monitoring in Body Fluids. *ACS Nano* **2018,** *12*, 1170–1178.

(62) Nomura, K.; Ohta, H.; Takagi, A.; Kamiya, T.; Hirano, M.; Hosono, H. Room-Temperature Fabrication of Transparent Flexible Thin-Film Transistors Using Amorphous Oxide Semiconductors. *Nature* **2004,** *432*, 488–492.

(63) Martins, R. F. P.; Ahnood, A.; Correia, N.; Pereira, L. M. N. P.; Barros, R.; Barquinha, P. M. C. B.; Costa, R.; Ferreira, I. M. M.; Nathan, A.; Fortunato, E. E. M. C. Recyclable, Flexible, Low-Power Oxide Electronics. *Adv. Funct. Mater.* **2013,** *23*, 2153–2161.

(64) Lin, Y. Y.; Hsu, C. C.; Tseng, M. H.; Shyue, J. J.; Tsai, F. Y. Stable and High-Performance Flexible ZnO Thin-Film Transistors by Atomic Layer Deposition. *ACS Appl. Mater. Inter.* **2015,** *7*, 22610–22617.

(65) Kim, H. S.; Byrne, P. D.; Facchetti, A.; Marks, T. J. High Performance Solution-Processed Indium Oxide Thin-Film Transistors. *J. Am. Chem. Soc.* **2008,** *130*, 12580–12581.

(66) Banger, K. K.; Yamashita, Y.; Mori, K.; Peterson, R. L.; Leedham, T.; Rickard, J.; Sirringhaus, H. Low-Temperature, High-Performance Solution-Processed Metal Oxide Thin-Film Transistors Formed by a 'Sol-Gel on Chip' Process. *Nat. Mater.* **2011,** *10*, 45–50.

(67) Hwan Hwang, Y.; Seo, J.-S.; Moon Yun, J.; Park, H.; Yang, S.; Ko Park, S.-H.; Bae, B.-S. An 'Aqueous Route' for the Fabrication of Low-Temperature-Processable Oxide Flexible Transparent Thin-Film Transistors on Plastic Substrates. *NPG Asia Mater.* **2013,** *5*, e45.

(68) Rim, Y. S.; Chen, H.; Song, T.-B.; Bae, S.-H.; Yang, Y. Hexaaqua Metal Complexes for Low-Temperature Formation of Fully Metal Oxide Thin-Film Transistors. *Chem. Mater.* **2015,** *27*, 5808–5812.

(69) Qin, D.; Xia, Y.; Whitesides, G. M. Soft Lithography for Micro- and Nanoscale Patterning. *Nat. Protoc.* **2010,** *5*, 491–502.

Chapter 6

Narrower Nanoribbon Biosensors Fabricated by Chemical Lift-Off Lithography Show Higher Sensitivity

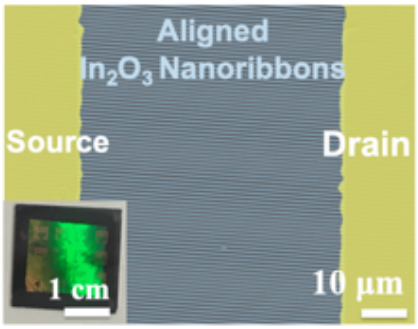

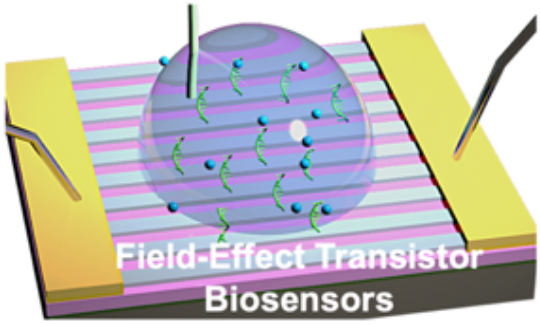

The information in this chapter is in revision for *ACS Nano* and is reprinted here

Authors: **Zhao, C.**; Liu, Q.; Cheung, K. M.; Liu, W.; Yang, Q.; Xu, X.; Man, T.; Weiss, P. S.; Zhou, C.; Andrews, A. M.

6.1 Abstract

Wafer-scale nanoribbon field-effect transistor (FET) biosensors fabricated by straightforward top-down processes are demonstrated as sensing platforms with high sensitivity to a broad range of biological targets. Nanoribbons with 350-nm widths (700-nm pitch) were patterned by chemical lift-off lithography using high throughput, low-cost commercial digital versatile disks as masters. Lift-off lithography was also used to pattern ribbons with 2-μm or 20-μm widths (4-μm or 40-μm pitches, respectively) using masters fabricated by photolithography. For all widths, highly aligned, quasi-one-dimensional ribbon arrays were produced over centimeter length scales by sputtering to deposit 20-nm-thin-film In_2O_3 as the semiconductor. Compared to 20-μm-wide microribbons, FET sensors with 350-nm wide nanoribbons showed higher sensitivity to pH over a broad range (pH 5 to 10). Nanoribbon FETs functionalized with a serotonin-specific aptamer demonstrated serotonin detection down to femtomolar concentrations in high ionic strength buffer. Field-effect transistors with 350-nm-wide nanoribbons functionalized with single-stranded DNA showed greater sensitivity to detecting complementary DNA hybridization *vs* 20-μm microribbon FETs. In all, we illustrate facile fabrication and use of large-area, uniform In_2O_3 nanoribbon FETs for ion, small molecule, and oligonucleotide detection where higher surface-to-volume ratios translate to better detection sensitivities.

6.2 Introduction

One-dimensional (1D) Label-free, ultra-sensitive chemical and biological sensors that monitor biomarkers in body fluids and tissues have broad applications in healthcare and biomedical research, including cancer diagnostics,[1,2] DNA detection,[3-6] bacteria and virus detection,[7-9] and metabolite monitoring.[10-14] One-dimensional (1D) nanomaterials, such as Si

nanowires (SiNWs), are common channel materials in FETs due to their ultra-high surface-to-volume ratios, which increase device sensitivities.[15-17] Developing sensors that provide accurate, real-time information regarding multiple analytes with high sensitivity and selectivity is at the heart of next-generation personalized medical devices, *e.g.*, point-of-care measurements, and implantable and wearable sensors.[18-28] Nanoelectronic field-effect transistor (FET) biosensors have been explored as platforms having unique properties and advantages towards the realization of these applications.

Metal oxide semiconductors have been used to fabricate FET sensors having higher sensitivity and more straightforward surface functionalization over other materials, including graphene and MoS_2 based FETs.[29-31] Bottom-up strategies were used to prepare In_2O_3 nanowires for use as gas sensors, chemical sensors, biosensors, and optical detectors.[32-35] However, like bottom-up fabricated FETs, *e.g.*, Si nanowires or carbon nanotubes, bottom-up fabricated In_2O_3 nanowire sensors suffer from poor device-to-device reproducibility due to random orientations and variable numbers of nanowires between electrodes.[36,37]

In contrast, top-down fabrication strategies, *e.g.,* soft lithography, soft-lithographic molecular printing,[38-40] nanoimprint lithography,[41,42] and nanotransfer printing[43-46] provide precise control over the morphology and shape of nanomaterials. Top-down In_2O_3 nanoribbons fabricated by straightforward photolithographic processes and low-temperature sputtering methods show high device uniformity and reproducibility.[47] We previously developed a lithography-free process involving sputtering In_2O_3 through shadow masks to fabricate ribbons of 25-μm width, ~16-nm thickness, and 500-μm length over cm scales.[47-49] These devices (previously referred to as nanoribbons due to the nanoscale height of the sputtered In_2O_3) had

high field-effect mobilities (>13 cm^2 V^{-1} s^{-1}), large current on/off ratios (>10^7),[47,48] and were functioned as sensors in a variety of applications including pH sensing, cardiac biomarker detection, and wearable sensors for glucose monitoring.[47-49] Flexible multifunctional sensor arrays incorporating these 25-μm-wide ribbons have also been developed to measure temperature, pH, and the neurotransmitters serotonin and dopamine, simultaneously.[50] Nonetheless, ribbons fabricated *via* shadow masks are limited in lateral resolution to tens of microns.

Surface-to-volume ratio is a critical parameter impacting nanobiosensor sensitivity, where higher ratios result in greater target sensitivities.[33,37,51-57] Here, we advance a generalizable, facile, top-down strategy for fabricating highly aligned In_2O_3 nanoribbons.[58,59] We employ chemical lift-off lithography (CLL), which is a soft lithography patterning approach that is cleanroom-free, high throughput, and high-fidelity, and enables micro- and nano-patterning to produce features as small as 15 nm.[60-67] In CLL, polydimethylsiloxane (PDMS) stamps with the desired patterns are used to remove molecules self-assembled on Au surfaces selectively in the stamp contact areas. The remaining molecules in the noncontacted regions act as resists during wet etching to form three-dimensional features. We have used CLL to pattern Au micro- and nanostructures, including Au nanoribbon, disk, square, and circle arrays, and to pattern other metal and semiconductor surfaces.[29,58,64,68]

By combining sputtering with CLL, 20-nm thin-film In_2O_3 ribbons at 350-nm, 2-μm, or 20-μm widths were produced at wafer scales. As-fabricated ribbons were aligned between source and drain electrodes with controllable orientations, numbers, and sizes. Micro- and nanoribbon FET biosensors with different aspect ratios were characterized and compared. The 350-nm-wide nanoribbon FETs showed greater sensitivities for target detection compared to 20-μm-wide

microribbon FETs providing further evidence for the concept that higher surface-to-volume ratios confer greater sensitivities in nanobiosensing applications.

6.3 Materials and Methods

Materials. Prime quality 4″ Si wafers (P/B, 0.001-0.005 Ω-cm, thickness 500 μm) were purchased from Silicon Valley Microelectronics, Inc. (Santa Clara, CA). Sylgard 184® silicone elastomer kits (lot #0008823745) were purchased from Ellsworth Adhesives (Germantown, WI). Indium(III) nitrate hydrate (99.999%), iron nitrate, thiourea, ammonium hydroxide (30% w/v in H_2O), hydrogen peroxide (30% v/v in H_2O), ethylenediaminetetraacetic acid disodium salt dihydrate (EDTA), 3-phosphonopropioninc acid, (3-aminopropyl)trimethoxysilane (APTMS), trimethoxy(propyl)silane, and 3-maleimidobenzoic acid *N*-hydroxysuccinimide (MBS) were purchased from Sigma-Aldrich (St. Louis, MO) and used as received. UltraPure™ nuclease-free distilled water was purchased from Thermo Fisher Scientific (Waltham, MA) and used as received. The masters templated for lift-off lithography were commercially available DVD-R recordable 16× speed 4.7 GB blank discs (Memorex).

Water was deionized before use (18.2 MΩ-cm) using a Milli-Q system (Millipore, Billerica, MA). The serotonin aptamer (/5ThioMC6-D/CG ACT GGT AGG CAG ATA GGG GAA GCT GAT TCG ATG CGT GGG TCG), thiolated ssDNA (/5ThioMC6-D/GG TTC TTG GAT ATA G), and complementary ssDNA (CTA TAT CCA AGA ACC) were synthesized by Integrated DNA Technologies, Inc. (Coralville, IA). The Ag/AgCl reference electrodes were purchased from World Precision Instruments, Inc. (Sarasota, FL).

Buffer solutions. Phosphate-buffered saline solution was purchased from Thermo Fisher Scientific (Waltham, MA, #10010023) and used as received. Artificial cerebrospinal fluid solution was NaCl (14.7 mM), KCl (0.35 mM), $CaCl_2$ (0.1 mM), NaH_2PO_4 (0.1 mM), $NaHCO_3$ (0.25 mM), and $MgCl_2$ (0.12 mM). A detailed procedure for preparations appears in **6.6 Supplementary Materials**.

Fabrication of masters. Photomasks for 2-μm-wide and 4-μm-pitch lines or 20-μm-wide and 40-μm-pitch lines were designed using the AutoCAD software suite (Autodesk, Inc.). Positive photoresist SPR700-1.2 (Rohm & Haas Co., Philadelphia, PA) was used for patterning Si by photolithography. The exposed Si was selectively etched using deep reactive ion etching (Plasma-Therm, LLC, Petersburg, FL). The resulting masters were then coated with trichloro(1H,1H,2H,2H-perfluorooctyl) silane as a release layer. The DVD-R masters for 350-nm-wide nanoribbons were prepared by a separation and rinsing process as previously described.[58,59]

Fabrication of In_2O_3 micro- and nanoribbon FETs. The general fabrication process is illustrated in **Figure 6.1**. The Si substrates with 100 nm SiO_2 were coated with 30-nm Ti followed by 30-nm Au using a CHA solution electron-beam evaporator (CHA Industries, Inc., Fremont, CA) under high vacuum (10^{-8} Torr) at an evaporation rate of 0.1 nm/s. Preparation of *h*-PDMS stamps, CLL patterning, and wet etching processes for nanoribbon fabrication were carried out as previously reported.[58,59] Briefly, an ethanolic 1 mM solution of 11-mercapto-1-undecanol was used to form SAMs on Au surfaces by incubation with substrates for 12 h. Oxygen-plasma-activated DVD-templated *h*-PDMS stamps were brought into contact with SAMs. The soft PDMS stamps for CLL patterning of 2-μm and 20-μm ribbons were made from

Si masters fabricated by conventional photolithography, as described above. The CLL was carried out similar to patterning for 350-nm nanoribbons.

For all formats, upon stamp removal, SAM molecules in the stamp-contacted areas were selectively removed, along with monolayers of Au atoms.[60,66] After the CLL process, Au etchant composed of 20 mM iron nitrate and 30 mM thiourea was used to etch the Au films (~30 min). A Ti etchant (113 mM EDTA, 3% hydrogen peroxide (v/v in H_2O), and 1.26% ammonia hydroxide solution (w/v in H_2O)) was used to etch to Ti for ~9 min. Wet etching transferred the patterns through the metal layers. After wet etching, substrates were oxygen-plasma treated to remove remaining SAM molecules in the non-contact areas prior to In_2O_3 sputtering.

The In_2O_3 (~20 nm) was deposited onto the patterned substrates using a radio frequency (RF) sputtering process (Denton Discovery 550 Sputtering System, Nanoelectronics Research Facility (NRF), University of California, Los Angeles (UCLA)). Sputtering is a room-temperature process, which is compatible with a variety of substrates including Si, glass, polyesters, and polyimide.[47-49] Metal removal was then performed by immersing substrates into Ti etchant for ~9 min under ultrasonication (Branson Ultrasonics, Danbury, CT), leaving In_2O_3 micro- or nanoribbons on Si/SiO_2 substrates. Devices were cleaned with water and dried under N_2 before measurements or further functionalization. Source/drain electrodes of 10-nm thick Ti and 50-nm-thick Au were defined by conventional photolithography and deposited using a solution electron-beam evaporator (CHA Industries, Inc., Fremont, CA) under high vacuum (10^{-8} Torr) with an evaporation rate of 0.1 nm/s. An optical microscope image of the electrode configuration with respect to In_2O_3 nanoribbons is shown in **Figure S6.2**.

Characterization. Scanning electron microscope images were obtained using a Supra 40VP scanning electron microscope with an Inlens SE Detector (Carl Zeiss Microscopy, LLC, White Plains, NY). Atomic force microscope imaging was performed using a FastScan AFM with ScanAsyst-Air tips (Bruker, Billerica, MA). Electronic FET measurements were carried out on a manual analytical probe station (Signatone, Gilroy, CA) equipped with a Keithley 4200A SCS (Tektronix, Beaverton, OR) or an Agilent 4156B semiconductor parameter analyzer (Santa Clara, CA). Optical images were recorded with a digital camera attached to a Zeiss Axiotech optical microscope.

Biosensing. For pH sensing, real-time source-drain current measurements were performed (*i*-t), where the gate voltage (V_{GS}) was held at 300 mV and the drain voltage (V_D) was held at 100 mV throughout. Buffer solutions of pH 7.4 were used to obtain stable baselines. Buffer solutions from pH 10 to 5 were sequentially added and removed using pipettes.

Thiolated serotonin aptamer or thiolated ssDNA (1 μM in nuclease-free water) were immobilized onto the oxide surfaces of FETs using APTMS and MBS ester as linkers. Serotonin (final concentration 10 fM-1 μM) or complementary ssDNA (final concentration 1 fM-1 μM) in 1 μL aliquots were added into the buffer solutions (39 μL) over FETs and mixed with a pipette. Source-drain current (I_{DS}) transfer curves were obtained, wherein gate voltages (V_{GS}) were applied from -200 to 400 mV with a step voltage of 5 mV, while the drain voltage (V_D) was held at 10 mV throughout. Five gate-voltage sweeps were repeated (five sweeps at 0, 5, and 10 min). The sweeps at each time point were averaged to determine each transfer curve. Calibrated responses were calculated by dividing the absolute sensor response (ΔI), which takes into

account baseline subtraction, by the change in source-drain current with voltage sweep ($\Delta I_{DS}/\Delta V_G$).[14]

Statistics. Data for pH, serotonin, and ssDNA sensing were analyzed by two-way analysis of variance with ribbon width and target concentration as the independent variables (GraphPad Prism 7.04, San Diego, CA). Data for 10 nM, 100 nM, and 1 μM serotonin were excluded from the statistical analysis because sensor responses were saturated (**Figure 6.5c**). Two data points from the 20-μm-wide nanoribbon DNA sensing data were excluded from plotting and analysis due to external disturbance of the Ag/AgCl reference electrode noted during experiments (**Figure 6.5f**).

Numerical simulations. COMSOL Multiphysics 5.2 was used to simulate the sensitivities with different nanowire widths. Details of model used in this work can be found from previous report.[69] Here, In_2O_3 nanoribbons were designed to be 2 μm long and 20 nm thick, with varying widths from 5 nm to 20 μm. In_2O_3 is intrinsically doped by oxygen vacancies with a concentration of 2.48 x 10^{16} cm^{-3} *n*-type doping.[47] The substrate was 200-nm silicon dioxide. Surface charge density of 1.6 x 10^{-3} C/m^{-2} was added to model the biomolecules induced charge change on the channel and SiO_2 surface. Semiconductor physics was applied to compute the source-drain electric current when sweeping gate voltage. The sensitivity was then calculated based on previous work.[14] Results are shown in **Figure S6.7**.

6.4. Results and Discussions

The general In_2O_3 micro- and nanoribbon fabrication process is shown in **Figure 6.1** and described in detail in section **6.3 Materials and Methods**. We fabricated ribbon features for subsequent In_2O_3 sputtering followed by a process to remove Au/Ti features leaving behind

In_2O_3 micro-or nanoribbons. We used commercial digital versatile disks-recordable (DVD-R) as templates to fabricate 350-nm-wide nanoribbons. These disks are economical, easily accessible masters (<$0.5/disc). Blank DVD-R disks contain sub-μm grating features.[58,59] The DVD-R masters were prepared by a straightforward separation and rinsing process as previously described.[58,59] Hard PDMS (*h*-PDMS) was used to replicate the high-aspect ratio DVD-R features.[58,59]

The DVD-R nanoribbon features, transfer of these features to *h*-PDMS, and further transfer to alkanethiol monolayers on Au has been characterized.[58,59] Previously, we deposited In_2O_3 *via* a sol-gel process with the Au/Ti layers deposited on top.[58] The SAMs on Au were then patterned. The Au/Ti areas that were not contacted by activated *h*-PDMS served as wet etching masks. The stamp-contacted/exposed Au/Ti features were etched to expose the underlying In_2O_3. Our previous patterning approach resulted in overetching into and sometimes through the underlying 4-nm In_2O_3 layer, which turned out to be critical for precise patterning.[58] Even when overetching was avoided, etching undercut the protected Au/Ti features to produce In_2O_3 nanoribbons that were wider than the features of the masters.[58,59] Further, nanoribbons patterned in this manner had a high degree of line-edge roughness. Here, we solved this important problem, by combining wet etching and sputtering, resulting in high fidelity In_2O_3 nanoribbons fabricated over large areas.

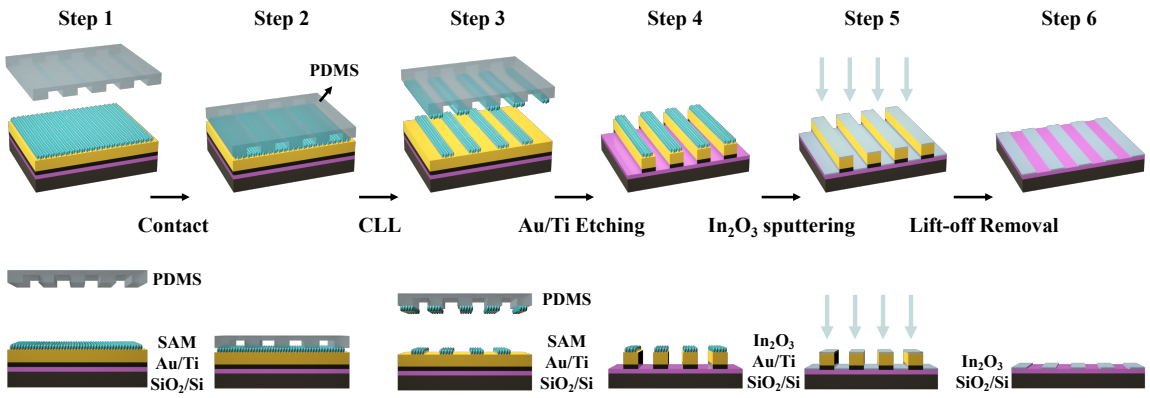

Figure 6.1. Schematic illustration of the fabrication process for In_2O_3 nanoribbons. Step 1: A Au layer (30 nm) was deposited over Ti (30 nm) on Si/SiO_2 (100 nm). A monolayer of 11-mercapto-1-undecanol was then self-assembled on the Au surface. Step 2: An oxygen plasma "activated" polydimethylsiloxane (PDMS) stamp with micro- or nanoribbon features was brought into conformal contact with the substrate. Step 3: Stamp removal from the surface (chemical lift-off lithography, CLL), lifted off self-assembled molecules in the contacted areas. Step 4: Selective etching processes removed Au and Ti in the unprotected (contacted) regions on the surface. Step 5: Sputtering was used to deposit In_2O_3 (20 nm) over the entire substrate. Step 6: The remaining Au/Ti structures were removed to obtain In_2O_3 nanoribbon arrays.

Here, In_2O_3 was deposited using sputtering *after* Au/Ti etching. Sputtering was carried out normal to the substrate surface such that undercut of the Au/Ti structures did not influence the widths of the resulting In_2O_3 nanoribbons. Nanoribbons (350-nm) were imaged before and after the lift-off process using atomic force microscopy (AFM), as shown in **Figure 6.2**. Using the present fabrication process, In_2O_3 nanoribbons had heights of ~60 nm after In_2O_3 sputtering (**Figure 6.2a**), corresponding to the sum of the heights of the underlying Au and Ti layers.

Sputtered does not add to the apparent height difference as In_2O_3 was sputtered atop both the patterned Au and the interleaved Si areas.

After removing the Au nanoribbon structures (and the overlying In_2O_3), uniform and continuous In_2O_3 nanoribbons with 350-nm widths and 20-nm heights remained, as shown *via* AFM (**Figure 6.2b**). To compare the widths and heights of the ribbons before and after removal of the Au templates, height profiles along the nanoribbons were analyzed (**Figure 6.2c)**. The widths of In_2O_3 nanoribbons matched with the spacing between the Au nanoribbons demonstrating high-fidelity patterning and features characterized by sharp edges and high continuity.

Nanoribbons were fabricated on 1.5 cm × 1.5 cm Si wafers. The light blue In_2O_3 nanoribbon patterned region in the center of a representative wafer showed a strong iridescence when viewed at non-perpendicular angles under white light indicative of periodic (diffraction) grating patterns on the surface (**Figure 6.2d**). Scanning electron microscopy (SEM) indicated that nanoribbons were continuous over tens of microns and highly defined at the single nanoribbon scale (**Figure 6.2e,f**). Energy-dispersive X-ray (EDX) mapping was performed (**Figure 6.2g**), where the indium $L_{\alpha 1}$ energy of 3.286 keV (**Figure S6.1**) was mapped and calculated (**Table S6.1**). The EDX images showed In_2O_3 nanoribbons of ~350 nm widths, consistent with the results from AFM and SEM imaging.

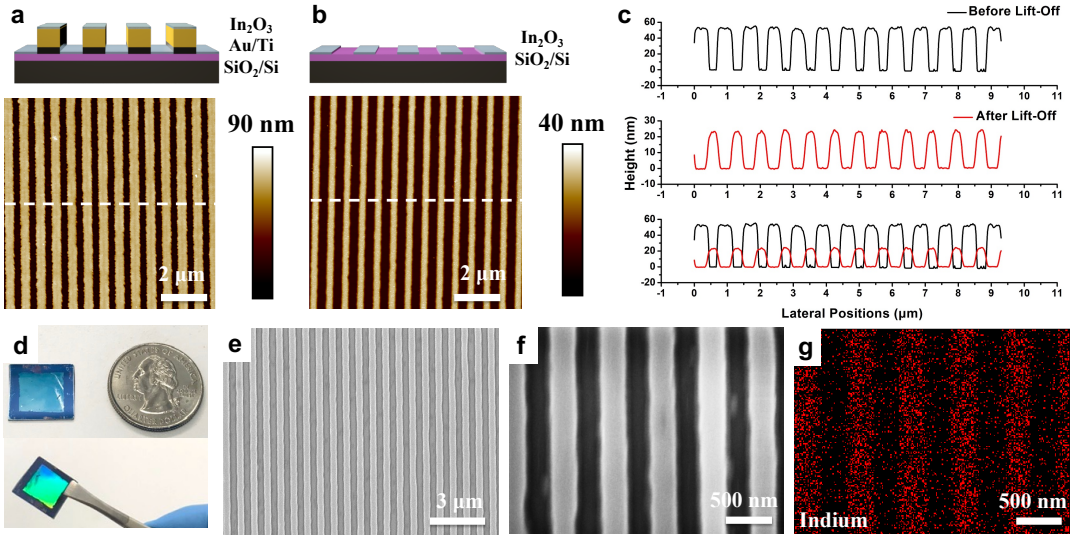

Figure 6.2. Atomic force microscope (AFM) images of 350-nm nanoribbon substrates (a) before (Step 5, Figure 6.1) and (b) after removing underlying Au structures (Step 6, Figure 6.1). (c) Height profiles from the AFM images in (a) and (b) across the nanoribbons. (d) Photographs of In_2O_3 nanoribbons at different viewing angles. (e,f) Scanning electron microscope (SEM) images of 350-nm-wide In_2O_3 nanoribbons. (g) Energy-dispersive X-ray mapping of indium from the SEM image in (f).

To construct micro- and nanoribbon FETs, the orientations of well-aligned In_2O_3 structures were identified by AFM or SEM. Source and drain electrodes were then fabricated perpendicular to the nanoribbons (**Figure 6.3a**) or microribbons. The Au/Ti source and drain electrodes were deposited on top of as-prepared In_2O_3 ribbons *via* electron-beam evaporation. Interdigitated electrodes with lengths of 1300 μm and widths of 45 μm were prepared (**Figure S6.2**). Electrodes aligned well with as-fabricated 350-nm wide In_2O_3 nanoribbons, as shown in the SEM images in **Figure 6.3b** and **3c**. Substrates with 2-μm- or 20-μm-wide In_2O_3 microribbons

similarly demonstrated well-aligned configurations between the ribbons and electrodes (**Figure 6.3d**,**3e, and S3**).

As discussed above and previously reported,[36,37] the orientations and numbers of nanowires or nanoribbons are challenging to control using bottom-up approaches. By contrast, using a top-down CLL patterning approach, orientations and numbers of ribbons were straightforwardly controllable based on the widths and pitches of the ribbons and the widths of the electrodes. For example, ~1850 350-nm-wide In_2O_3 nanoribbons were incorporated and aligned with each pair of electrodes. Transistor performances were tested using a bottom-gate top-contact configuration, where p^{++} Si served as the bottom gate and SiO_2 as the gate dielectric (**Figure 6.3f**). Transfer and output curves for 350-nm wide In_2O_3 nanoribbon FETs are shown in **Figure 6.3g** and **3h**, respectively, demonstrating current on/off ratios $>10^6$. The FETs with 2-μm- or 20-μm-wide ribbons, or continuous thin-film In_2O_3 FETs showed similar characteristics in solid state measurements (**Figure S6.4**).

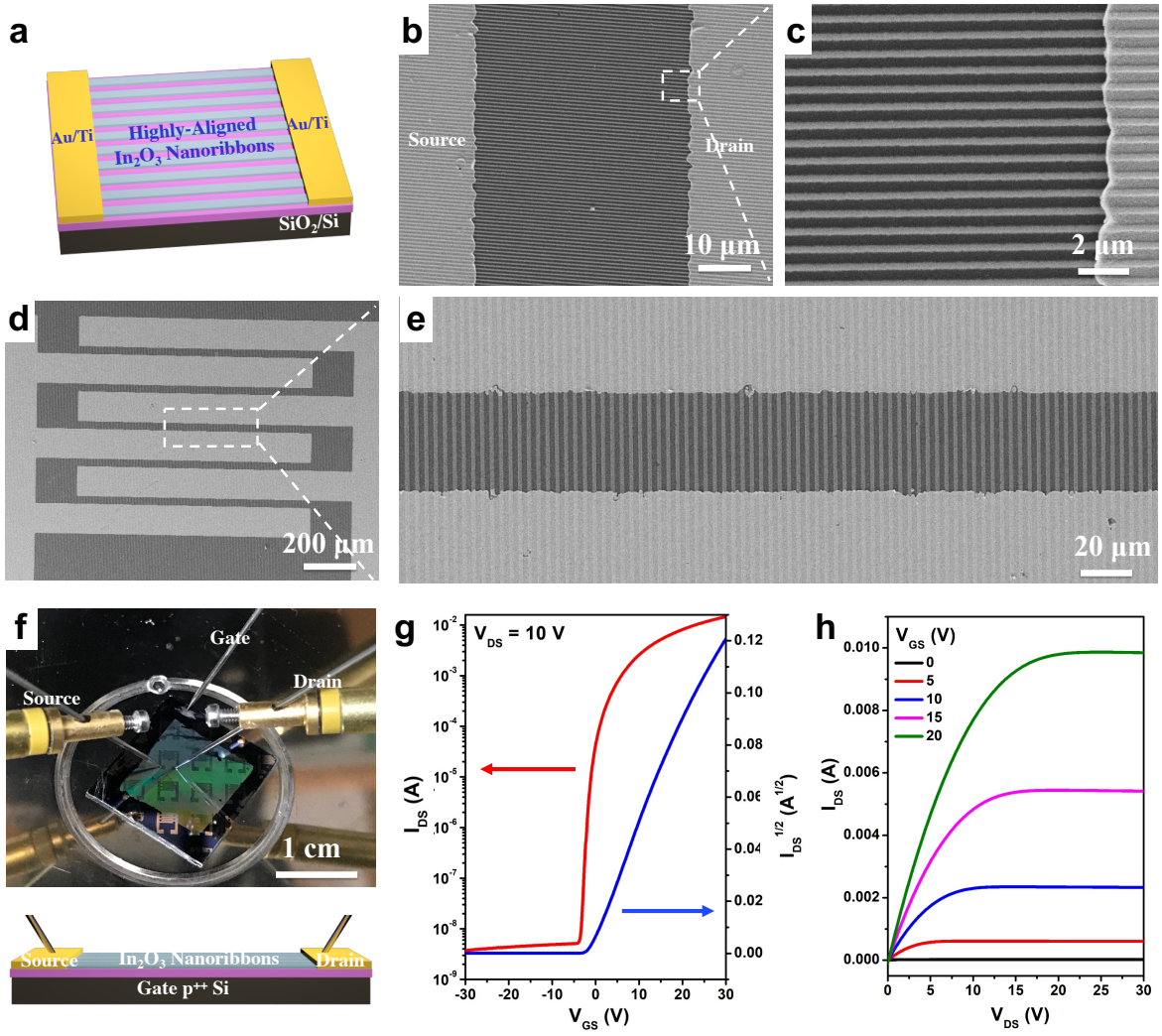

Figure 6.3. Field-effect transistor (FET) configuration using In_2O_3 nanoribbons. (a) Schematic illustration of the field-effect transistor (FET) configuration using In_2O_3 nanoribbons (or microribbons) as the channel material aligned perpendicular to source and drain electrodes. (b,c) Scanning electron microscope images of 350-nm-wide In_2O_3 nanoribbons with source and drain electrodes. (d,e) Scanning electron microscope images of 2-μm-wide In_2O_3 nanoribbons with source and drain electrodes. (f) Photograph (top) and schematic illustration (bottom) of the solid-state measurement set-up for In_2O_3

nanoribbon (and microribbon) FETs, where p^{++} Si serves as the bottom gate. The lavender layer is SiO_2. Transfer (g) and output (h) characteristics of representative 350-nm In_2O_3 nanoribbon FETs.

The electrical performances of 350-nm-wide nanoribbon FET devices in a liquid environment were tested using solution gating, which corresponds to how devices were used for biosensing (*vide infra*). Each device was covered with a PDMS well filled with an electrolyte solution (**Figure 6.4a**). A Ag/AgCl reference electrode was used to apply a bias voltage through the electrolyte solution to gate each FET. Transfer and output curves for liquid-gated 350-nm-wide In_2O_3 nanoribbon FETs in phosphate-buffered saline (PBS) are shown in **Figure 6.4b** and **4c**, respectively. The nanoribbon FETs fabricated here operate in a liquid environment with current on/off ratios of 10^3, transfer curve saturation behavior, low gate leakage current (**Figure 6.4d, Figure S6.5**), and low driving voltages. Microribbon FETs with different widths or continuous thin-film FETs showed similar liquid-state performance characteristics (**Figure S6.6**).

Ion-sensitive FETs (ISFETs), where FETs respond to changes in environmental ion concentrations, are used for a majority of FET chemical and biological sensing applications.[70-74] To investigate the performance of In_2O_3 nanoribbon ISFETs, we conducted pH sensing by systematically increasing the hydrogen ion concentrations of the solutions contacting FETs. We previously compared the pH sensitivities of 25-μm wide In_2O_3 ribbon FET sensors having different ribbon heights.[47] Microribbons having thinner 10- or 20-nm In_2O_3 films showed higher sensitivities to pH compared to thicker microribbons, *e.g.*, 50-nm In_2O_3 films. Here, micro- and nanoribbons with constant 20-nm heights were used to compare the effects of changing ribbon widths.

Threshold voltage changes of ISFETs were determined for 350-nm-wide nanoribbons from pH 5 to 10. Representative transfer curves (drain current to gate voltage) are shown in **Figure 6.4d**. Time-related increases in drain current were observed with decreasing pH values (**Figure 6.4e**), which is typical for *n*-type semiconductor gate-voltage modulation behavior.[30,48,49] At lower pH values, there are greater numbers of positively charged hydrogen ions in solution, leading to higher currents as more negative charge carriers are generated in *n*-type channels. The In_2O_3 surface is functionalized with (3-aminopropyl)triethoxysilane, where the terminal amine undergoes protonation and deprotonation with changes in pH. Note that the In_2O_3-based FETs are less stable at lower pH due to the chemical nature of metal oxides in acids.[58]

Relative pH sensing responses for 350-nm- *vs* 20-μm-wide In_2O_3 nanoribbon FETs were compared (**Figure 6.4f**). Device currents for both configurations increased as the $[H^+]$ increased (*i.e.*, pH decreased). Surface-to-volume ratios for FETs with different ribbon widths were calculated (see **6.6 Supplementary Materials, Figure S6.8**). Ribbons with 350-nm widths had a modest 10% increase in surface-to-volume ratio compared to ribbons with 20-μm-widths (**Table S6.2**). Yet, this increase in surface-to-volume ratio was sufficient to produce increased pH sensitivity, particularly at lower pH ($P<0.01$) (see **Table S6.3** for full statistics). These findings provide evidence that FETs with nanoscale features having higher surface-to-volumes are associated with higher ion sensitivities.

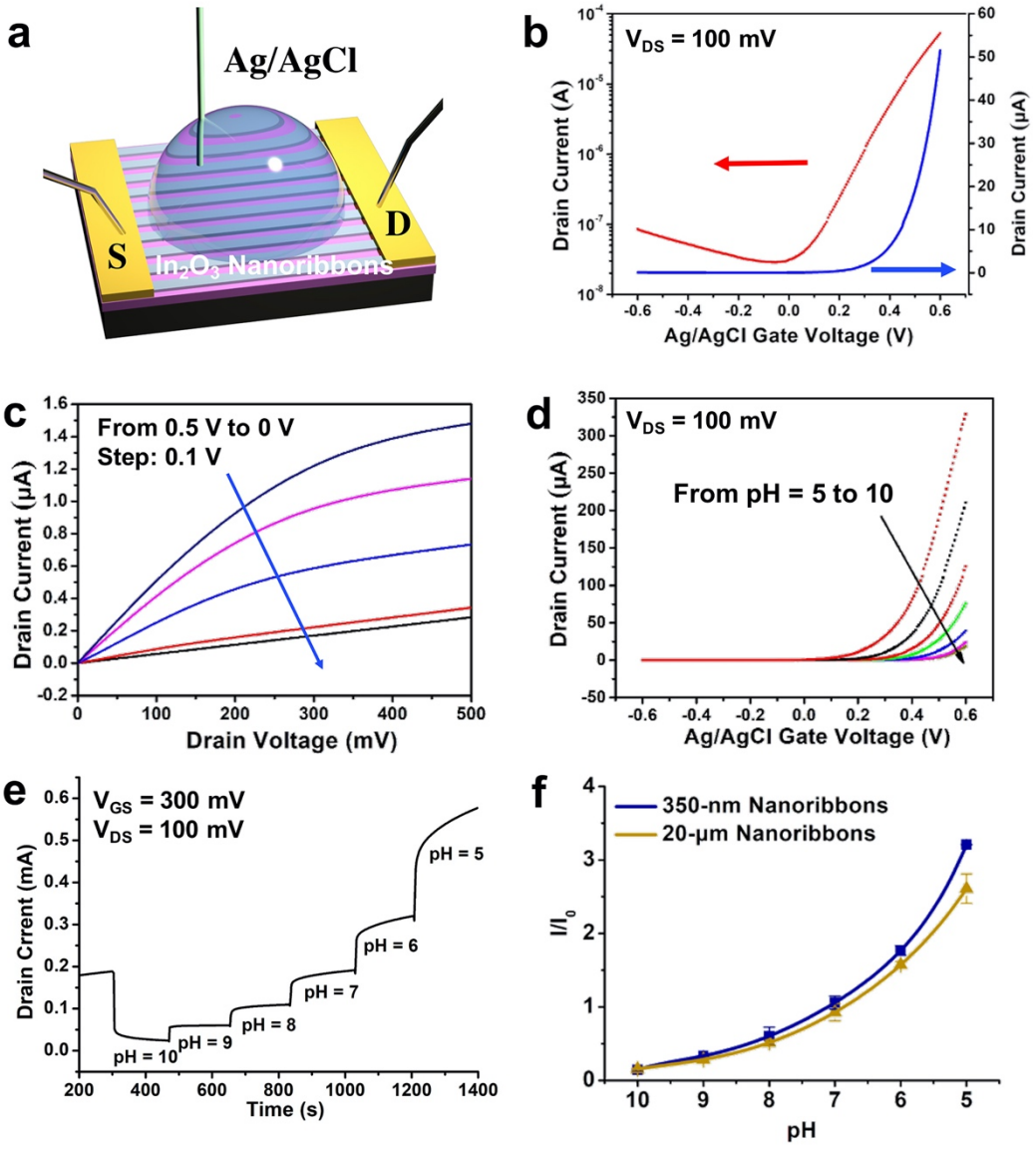

Figure 6.4. Liquid state measurements of In_2O_3 nanoribbon FETs. (a) Schematic illustration of a liquid state measurement where a Ag/AgCl electrode serves as the top-gate. Transfer (b) and output (c) characteristics of 350-nm-wide In_2O_3 nanoribbon field-effect transistors (FETs) in the liquid-gate setup shown in (a). (d) Transfer curves of 350-nm-wide In_2O_3 nanoribbon FETs in solutions of pH 10 to 5. (e) Real-time current responses from a representative 350-nm-wide In_2O_3 nanoribbon FET exposed to commercial buffer solutions

of pH 10 to 5. (f) Current responses relative to baseline for solutions of pH 10 to 5 using 350-nm- or 20-μm-wide ribbon In_2O_3 FETs. Error bars are standard errors of the means with *N*=3 FETs for each configuration. I/I_0 was defined as normalized current to the baseline pH before the experiments (I_0, pH = 7.4).

Debye screening in high-ionic strength solutions presents challenges for FET biosensing in physiological environments.[51,75,76] Overcoming Debye-length limitations enables the detection of biological targets *ex vivo* and *in vivo* to extend potential uses of FET biosensors for medical and biological applications, *e.g.*, sensing in body fluids for point-of-care or at-home monitoring. We developed aptamer-based FET biosensors for small-molecule detection under high ionic-strength conditions.[14,23,29] Aptamers, which are single-stranded oligonucleotides isolated specifically for adaptive target recognition, are functionalized on semiconductor surfaces. Upon target binding, aptamers undergo conformational rearrangements involving their negatively charged backbones (and associated solution ions) resulting in charge redistribution near semiconductor surfaces. Signal transduction arising from aptamer charge redistribution has enabled direct detection of charged, as well as neutral small-molecule targets under physiological conditions.[14]

Aptamers that selectively recognize serotonin were covalently immobilized on In_2O_3 (and SiO_2) ribbons (**Figure 6.5a**). Aptamers immobilized on the SiO_2 dielectric contribute minimally to target-induced currents. We conducted neurotransmitter sensing by adding different concentrations of serotonin into the PBS solutions above FETs. Representative transfer curves for 350-nm-wide In_2O_3 nanoribbon FETs at different serotonin concentrations are shown in **Figure 6.5b**. Calibrated response curves comparing the performance of 350-nm- *vs* 20-μm-wide

ribbons both having 20-nm thin-film In_2O_3 are shown in **Figure 6.5c**. Nanoribbons with 350-nm widths showed a trend toward higher sensitivity to serotonin compared to 20-μm-wide nanoribbons, where the responses from 20-μm-wide nanoribbons shifted to higher concentrations ($0.1<P<0.05$). Tuning nanoribbon sizes provides another strategy for shifting overall device sensitivities, in addition to truncating or destabilizing aptamer stems and/or changing aptamer surface densities.[14,23] These strategies will be important for translation to *in vivo* sensing applications where target concentrations vary widely, *e.g.*, serotonin concentrations in the gut (micromolar range)[77] *vs* the brain extracellular space (nanomolar range).[78] We previously reported that changing the solution pH values affects the aptamer sensor signals.[50] This signal is attributed to H+-associated changes in charge redistribution around aptamers and near FET surfaces. For *in vivo* applications where the environmental pH varies, a separate pH sensor can be incorporated as part of a multiplexed device to measure changes in environmental pH simulataneously.[50] Note that we have carried out experiments for the serotonin aptamer systems with unfunctionalized FETs, FETs functionalized with scrambled aptamer sequences, and experiments in the presence of structurally similar interferants, which showed that the aptamer FETs showed high selectivity.[14,50] We have also investigated real-time serotonin sensing and showed detection from fM to μM with a temporal resolution of ~5 s, which was limited by the measurement system response time.[50]

Oligonucleotide sensing is important for clinical diagnostics, such as genotyping for cancer immunotherapy and for diagnosing infectious diseases.[5,6,79-82] Here, label-free DNA detection was performed on micro- and nanoribbon FET biosensors. Thiolated single-stranded DNA (ssDNA) was covalently immobilized onto In_2O_3 (and SiO_2). Solutions containing 10^6 to 10^{15} copies of complementary oligonucleotide (~1 fM to ~1 μM) were added to the sensing

environment in artificial cerebrospinal fluid (aCSF) (**Figure 6.5d**). The aCSF was diluted 10-fold to increase the Debye length and thereby, to maximize low copy-number detection.

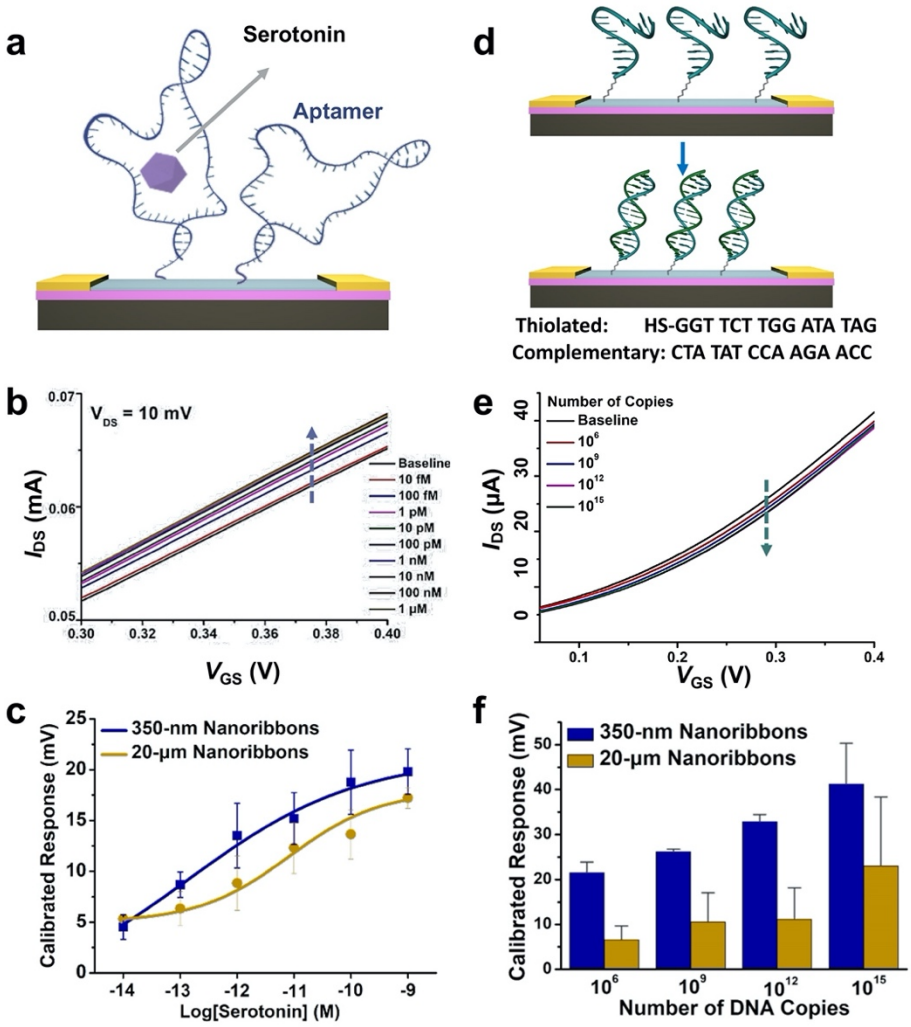

Figure 6.5 Sensing results of In_2O_3 field-effect transistor (FET) biosensors. (a) Schematic illustration of serotonin detection using aptamer-functionalized In_2O_3 field-effect transistor (FET) biosensors. (b) Representative transfer curves for serotonin responses from 10 fM to 1 μM for 350-nm In_2O_3 nanoribbon FET biosensors. (c) Calibrated response curves for serotonin (10 fM to 1 μM) from 350-nm- ***vs*** **20-μm-wide In_2O_3 nanoribbon FET biosensors.**

Error bars are standard errors of the means for *N*=3 350-nm-wide nanoribbon and *N*=2 20-µm-wide nanoribbon devices. (d) Schematic illustration of DNA hybridization detection. (e) Representative transfer curves for responses for complementary DNA hybridization (10^6 to 10^{15} copies) for 350-nm In_2O_3 nanoribbon FET biosensors. (f) Calibrated responses for complementary DNA hybridization for 350-nm- *vs* 20-µm-wide In_2O_3 nanoribbon FET biosensors. Error bars are standard errors of the means for *N*=2 350-nm-wide nanoribbon and *N*=3 20-µm-wide microribbon devices.

Representative transfer curves for 350-nm-wide In_2O_3 nanoribbon FETs at different target DNA copy numbers are shown in **Figure 6.5e**. Calibrated responses are compared in **Figure 6.5f** for the performance of 350-nm-nanoribbon *vs* 20-µm-microribbon In_2O_3 FETs. Nanoribbons with 350-nm widths showed higher sensitivity to DNA hybridization than 20-µm-wide microribbons ($P<0.05$). The direction of change for *n*-type In_2O_3 FET transfer characteristics is due to gating effects associated with negatively charged oligonucleotides.[14,23] For aptamer-based sensing, the serotonin aptamers used here reorient away from FET surfaces upon target binding resulting in increases in concentration-related currents in *i*-V sweeps due to increased transconductance.[14] For DNA hybridization, decreases in currents in the *i*-V sweeps with increasing DNA concentrations are due to the accumulation of net negative surface charge, which occurs upon DNA hybridization.[79] Note that we have carried out control experiments with noncomplementary sequences, as well as sequences that contain single base mismatches, and both experiments indicate high selectivity.[79] The highly sensitive platform developed here and our recent work[79] provide a lable-free strategy for oligonucleotide (DNA, RNA) sensing, which can be applied for a wide variety of infectious agents, including the severe acute respiratory-related coronavirus 2 (SARS-CoV-2).[82,83]

Relationships between FET sensitivity and surface-to-volume ratio have been investigated using different types of channel materials.[33,37,51-57] Silicon nanowires with dimensions ≥50 nm have been most often investigated.[37,52,56] Silicon nanowires with higher surface-to-volume ratios have higher sensitivities towards pH, protein, and DNA detection.[37,52,56] For example, Linnros and colleagues studied silicon-on-insulator (SOI) nanowires with widths of 50-170 nm fabricated by electron-beam lithography having a 100-nm semiconductor layer.[56] For their smallest, 50-nm, nanowires, the surface-to-volume ratio was only 2/100 nm^{-1} (*i.e.*, 0.4/20 nm^{-1}), which is 60% lower than the surface-to-volume ratio of our 20-nm-thin-film In_2O_3 FETs (*i.e.*, 1/20 nm^{-1}; see section **6.6 Supplementary Materials** for calculations and **Table S6.2**).

For bottom-up fabricated cylindrical nanowires, the surface-volume-ratio is related to 2/r, where r is the nanowire radius. In principle, Si nanowires with diameters larger than 80 nm (*i.e.*, surface-to-volume ratio 1/20 nm^{-1}) have surface-to-volume ratios lower than the microribbon, nanoribbon, and thin-film FETs investigated here. For instance, Sun and coworkers produced Si nanowire devices for sensing protein adsorption.[37] Fabrication involved nanowire contract printing and SEM to select and to remove nanowires individually to produce device with specific numbers and diameters of nanowire. Single nanowire devices were grouped by diameter ranges (*i.e.*, 60-80 nm, 81-100 nm, and 101-120 nm). The smallest 60-nm nanowires had surface-to-volume ratios of 2/30 nm^{-1} (*i.e.*, 1.3/20 nm^{-1})—a 17% increase over the surface-to-volume ratio of the 350-nm nanoribbons investigated here (**Table S6.2**).

Williams and co-authors explored the effects of surface-to-volume ratio in the context of ssDNA hybridization with single-stranded peptide nucleic acids functionalized on Si nanowire

FETs having widths of 50, 100, 200 nm, 400, and 800 nm.[52] The Si semiconductor layer was 50 nm. For these sensors, the signal-to-volume ratios were 3/50, 2/50, 1.5/50, 1.25/50, and 1.125/50, respectively (*i.e.*, 1.2/20, 0.8/20. 0.6/20, 0.5/20, and 0.45/20, respectively). Hybridization sensitivity was linear for nanowires with widths between 800 and 100 nm. A sharp increase in sensitivity to DNA hybridization for the 50-nm wide Si nanowires was attributed to nonlinear increases in conductance at small nanowire diameters, which was determined experimentally and *via* simulation. For In_2O_3 nanoribbon FETs, sensor sensitivity could be increased by reducing nanoribbon dimensions using In_2O_3 sol-gel processing to produce thinner semiconductor layers[29,30,58] and/or *via* CLL with masters fabricated by e-beam lithography to pattern features as small as 15 nm.[60-67] To expand our findings beyond two feature sizes tested, we performed finite element analysis simulations (COMSOL, Multiphysics 5.2) to study the sensitivities in relation to different feature sizes. As shown in Figure 6.S7, enhanced sensitivity was observed in FETs with smaller widths at the same thickness (20 nm), which is attributed to higher surface-to-volume ratios.

In this work, we focused on top-down approaches using soft lithography. Traditional top-down approaches, such as electron beam lithography (EBL), also offer precise control over the orientations, sizes, and numbers of 1D nanostructures, thereby enabling fabrication of biosensors with high reproducibility.[84] Nonetheless, top-down fabrication of sub-micron features needed to achieve high surface-to-volume ratios requires techniques that are challenging to translate for broad applications. For example, commonly used EBL methods are low throughput and suffer from high equipment and usage costs. Moreover, fabrication of Si-based nanomaterials, *e.g.*, SiNWs, often relies on silicon-on-insulator wafers, which are considerably more expensive (>$500 per 4" wafer) than standard Si wafers (<$50 per 4" wafer).[85] Together, these drawbacks

present significant barriers to the use of top-down fabricated nanomaterials in actual biomedical applications, and necessitate the development of high throughput, cost-effective, and precise fabrication strategies for biosensors.

6.5 Conclusions and Prospects

Highly aligned In_2O_3 nanoribbon FETs were fabricated by chemical lift-off lithography using commercially available DVD-R disks as nanostructured templates and low temperature sputtering to produce 20-nm In_2O_3 thin-films. These nanoribbon FET sensors have high surface-to-volume ratios that impart greater sensitivity for ion, small-molecule, and oligonucleotide detection, all other factors being equal. The fabrication and sensing approaches reported herein represent generalizable strategies for improving electronic biosensing by fabricating high surface-to-volume ratio nanoscale features for applications where high and/or tunable sensitivities are critical. This top-down, large-scale nanolithography strategy to fabricate metal-oxide nanoribbons can be implemented as a high-throughput, cost-effective, cleanroom-free means of production. Even so, nanostructure surface-to-volume ratio is only one of many parameters that impacts nanobiosensor sensitivity. Other factors include semiconductor material, doping, and nanowire/nanostructure densities. If surface receptors are employed for selective biosensing, receptor type (*e.g.*, protein, nucleic acid), density, and target affinity, as well as the ionic strength of the sensing environment and biofouling will influence performance.

6.6 Supplementary Materials

Artificial cerebrospinal fluid (aCSF) was prepared from stock solutions. The 10× base stock combines NaCl (1470 mM), KCl (35 mM), NaH_2PO_4 (10 mM), and $NaHCO_3$ (25 mM) in deionized distilled water. The base stock is aliquoted and stored at room temperature. It is stable

for at least one year. **Preparation note:** Neither $CaCl_2$ nor $MgCl_2$ should be added directly to the 10× base stock solution due to their low solubility in aqueous solution at pH >7.5. The Mg and Ca precipitate as $Mg(OH)_2$ and $Ca(OH)_2$ causing the stock solution to appear cloudy and/or for a visible precipitate to form. Stock solutions of $CaCl_2$ (901 mM) and $MgCl_2$ (1050 mM) in deionized distilled water are each prepared separately. **Safety note:** The addition of $CaCl_2$ or $MgCl_2$ to water is exothermic. Use caution, cold water, and slow stirring when preparing thes solutions. The $CaCl_2$ and $MgCl_2$ stocks are aliquoted into 1-mL Eppendorf tubes and stored at -80 °C indefinitely.

Before experiments, the working aCSF solution (physiological concentration, "1×") was prepared. One aliquot each of the $CaCl_2$ and $MgCl_2$ stocks was thawed. Deionized distilled water was added to a beaker at ~80% of the final volume of the working solution. The 10× base stock was added, *e.g.*, 50 mL 10× base stock was added to ~400 mL water for 500 mL final volume of working solution. The pH was initially adjusted to 7.4-7.5 with ~1% HCl. The $CaCl_2$ stock was then added dropwise slowly using a pipette. The working solution was constantly stirred to avoid precipitation for a final concentration of 1.0 mM $CaCl_2$, *e.g.*, 555 µL for a final volume of 500 mL working solution. Next, the $MgCl_2$ stock solution was added dropwise slowly while stirring, for a final concentration of 1.2 mM, *e.g.*, 571 µL for a final volume of 500 mL working solution. The pH of the working solution was adjusted to 7.30 ± 0.03 using ~1% HCl. Finally, the solution was to the final volume with deionized distilled water, *e.g.*, final volume 500 mL. The final concentrations of the working aCSF solution (1×) were NaCl (147 mM), KCl (3.5 mM), NaH_2PO_4 (1.0 mM), $NaHCO_3$ (2.5 mM), $CaCl_2$ (1.0 mM), and $MgCl_2$ (1.2 mM). The working solution was stored at 4 °C for ≤2 weeks. this work, we focused on top-down approaches using soft lithography.

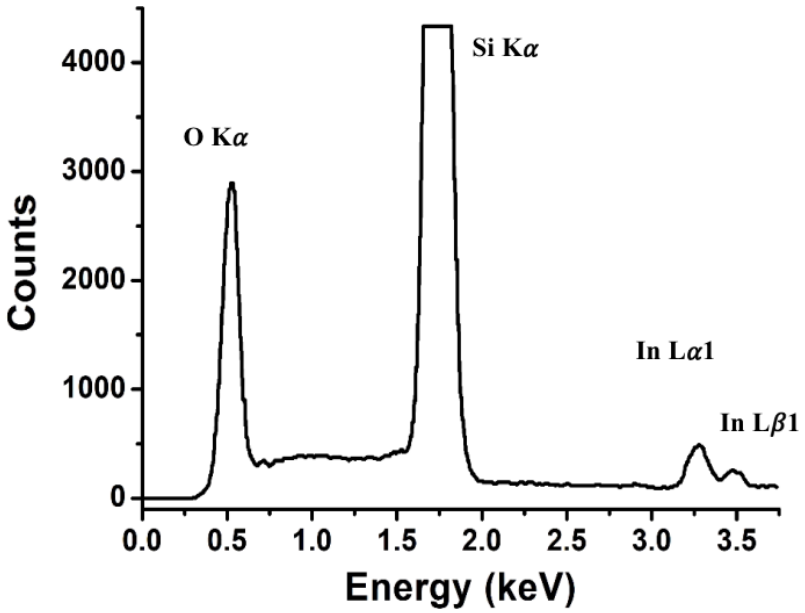

Figure S6.1. Elemental energy spectrum for In_2O_3 nanoribbons from energy-dispersive X-ray mapping.

Table S6.1. Elemental quantification analysis of In_2O_3 nanoribbons by energy-dispersive X-ray mapping.

Element Line	Net Counts	Element wt.%	Element wt.% Error	Atom%	Atom% Error
O K	26915	50.60	---	66.48	±0.51
Si L	0	---	---	---	---
Si K	213374	43.30	±0.14	32.40	±0.11
In M	0	---	---	---	---
In L	10378	6.10	±0.26	1.12	±0.05
Total		100.0		100.0	

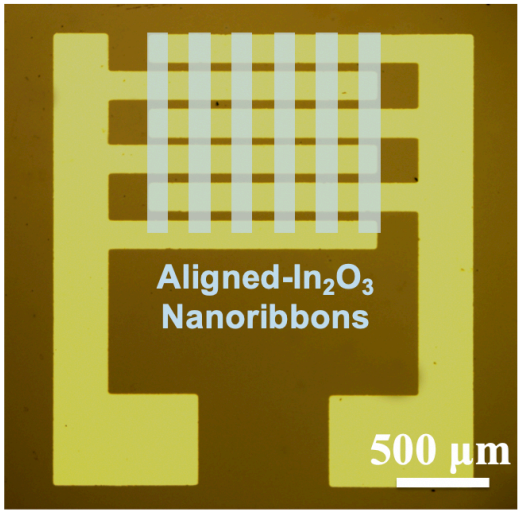

Figure S6.2. Optical microscope image of interdigitated electrodes (yellow). Orientations of In_2O_3 nanoribbons are depicted in overlay (light blue).

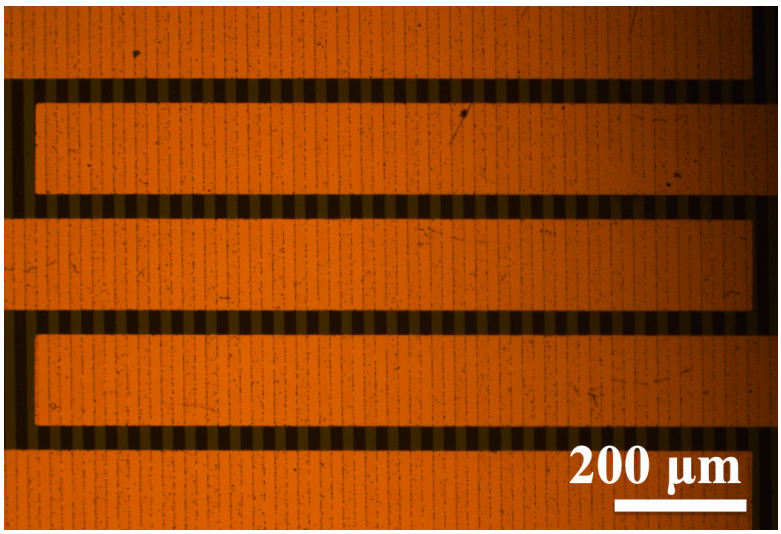

Figure S6.3. Optical microscope images of 20-µm-wide In_2O_3 nanoribbons with source and drain electrodes.

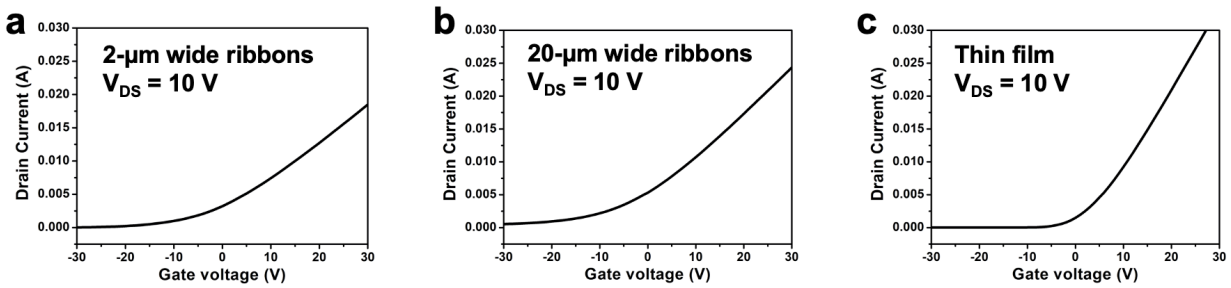

Figure S6.4. Solid-state transfer characteristics of In_2O_3 FETs with different nanoribbon widths, (a) 2 μm, (b) 20 μm, and (c) thin film.

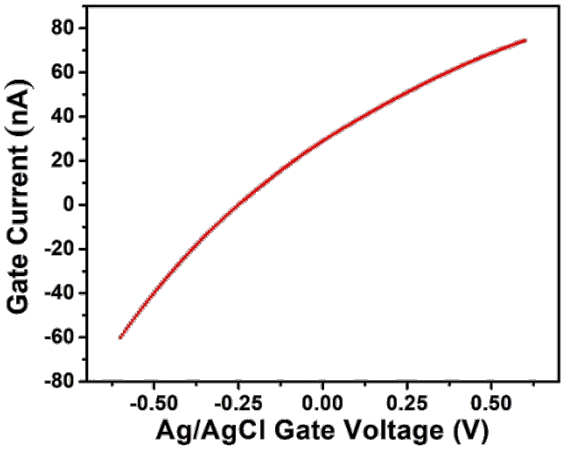

Figure S6.5. Gate leakage current (gate current to gate voltage) in buffer solution (pH = 7.4) at V_{DS} = 100 mV.

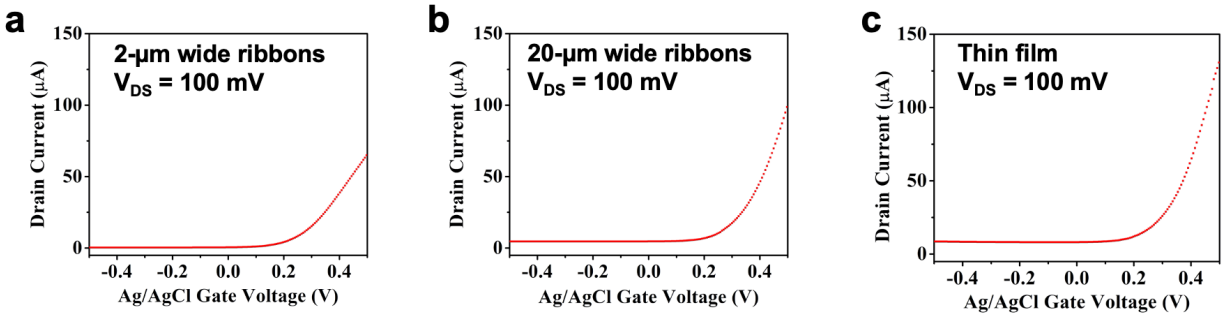

Figure S6.6. Liquid-state transfer characteristics of In_2O_3 FETs with nanoribbon different widths, (a) 2 µm, (b) 20 µm, or (c) thin film.

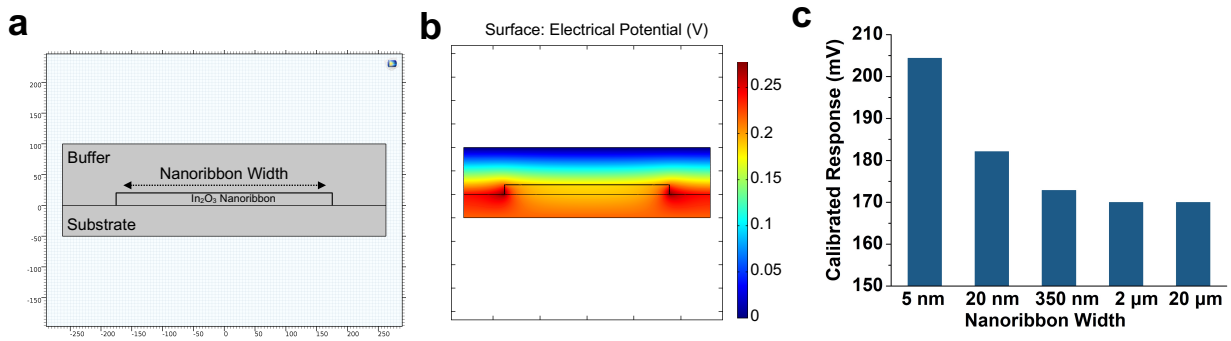

Figure S6.7. Numerical simulation results. (a) Model used in simulation, where nanoribbons are 20 nm thick with widths vary from 5 nm to 20 µm. (b) Simulation results of the change in electrostatic potential due to the charge of the biomolecules. (c) Calibrated responses at different widths showing the sensitivity of In_2O_3 nanoribbon FETs increased at smaller widths. Note the number of calibrated response is not comparable with experimental results in main text as a nature of simulation complexity in semiconductor system.

Calculation of surface-to-volume ratios

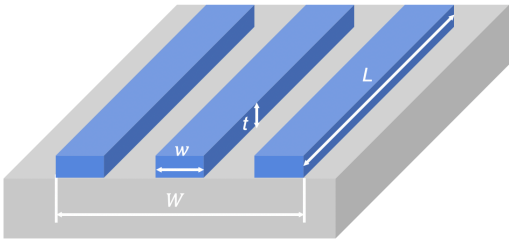

Figure S6.8. Schematic of nanoribbons for calculation of surface-to-volume ratio.

Consider a nanoribbon array, where the surface-to-volume ratio of an arbitrary area with width W is calculated. For each In_2O_3 nanoribbon, the length is denoted as L, width as w, and thickness as t. The pitch of the nanoribbons is $2w$ for different widths of nanoribbons. For nanoribbon surface area calculations, only the top surface and the two side surfaces are included. Results are summarized in **Table S6.2**.

Number of ribbons (per arbitrary area): $N = \frac{W}{2w}$ Eq. 1

Surface area: $S = (w * L) + (2 * L * t)$ Eq. 2

Volume: $V = w * L * t$ Eq. 3

Surface-to-volume ratio (per nanoribbon): $\frac{S}{V} = \frac{w*L+2*L*t}{w*L*t} = \frac{w+2*t}{w*t} = \frac{1+2*\frac{t}{w}}{t}$ Eq. 4

Surface-to-volume ratio (per arbitrary area): $\frac{S}{V} = \frac{(w*L+2*L*t)*N}{(w*L*t)*N} = \frac{(w*L+2*L*t)}{(w*L*t)} = \frac{1+2*\frac{t}{w}}{t}$ Eq. 5

For w_1 = 350 nm:

$$\frac{S}{V} = \frac{1+2*\frac{t}{w}}{t} = \frac{1+2*\frac{20\ nm}{350\ nm}}{20\ nm} = \frac{1+0.11}{20} nm^{-1} = \frac{1.11}{20} nm^{-1}$$

For w_2 = 2 μm:

$$\frac{S}{V} = \frac{1+2*\frac{t}{w}}{t} = \frac{1+2*\frac{20\ nm}{2000\ nm}}{20\ nm} = \frac{1+0.02}{20} nm^{-1} = \frac{1.02}{20} nm^{-1}$$

For w_3 = 20 μm:

$$\frac{S}{V} = \frac{1+2*\frac{t}{w}}{t} = \frac{1+2*\frac{20\ nm}{20000\ nm}}{20\ nm} = \frac{1+0.002}{20} nm^{-1} = \frac{1.002}{20} nm^{-1}$$

For thin-films:

$$\frac{t}{w} \to 0, \frac{S}{V} = \frac{1+2*\frac{t}{w}}{t} = \frac{1}{20} nm^{-1}$$

Table S6.2. Surface-to-volume ratios for different configurations of In_2O_3 FETs

Width	Pitch	Thickness	Surface-to-Volume Ratio	Surface-to-Volume Ratio Increase *vs* Thin Film
350 nm	700 nm	20 nm	$\frac{1.11}{20}\ nm^{-1}$	11%
2 μm	4 μm	20 nm	$\frac{1.02}{20}\ nm^{-1}$	2%
20 μm	40 μm	20 nm	$\frac{1.002}{20}\ nm^{-1}$	0.2%
Thin Film	—	20 nm	$\frac{1}{20}\ nm^{-1}$	—

Table S6.3. Concentration-dependent field-effect transistor data were analyzed by two-way analysis of variance with nanoribbon sizes and target concentration as the independent variables.

Type	Figure	Interaction Term	Nanoribbon Width	Concentration
pH	Fig. 4f	F (5,24) = 3.395 $P = 0.019$	F (1,24) = 13.09 $P = 0.001$	F (5,24) = 307.0 $P < 0.0001$
Serotonin	Fig. 5c	F (5,18) = 0.375 $P = 0.859$	F (1,18) = 4.010 $P = 0.061$	F (5,18) = 9.107 $P = 0.0002$
DNA	Fig. 5f	F (3,10) = 0.054 $P = 0.982$	F (1,10) = 7.293 $P = 0.022$	F (3,10) = 1.518 $P = 0.269$

6.7 References

(1) Arya, S. K.; Bhansali, S. Lung Cancer and Its Early Detection Using Biomarker-Based Biosensors. *Chem. Rev.* **2011,** *111*, 6783–6809.

(2) Huang, X.; Liu, Y.; Yung, B.; Xiong, Y.; Chen, X. Nanotechnology-Enhanced No-Wash Biosensors for *in Vitro* Diagnostics of Cancer. *ACS Nano* **2017,** *11*, 5238–5292.

(3) Hahm, J.-i.; Lieber, C. M. Direct Ultrasensitive Electrical Detection of DNA and DNA Sequence Variations Using Nanowire Nanosensors. *Nano Lett.* **2004,** *4*, 51–54.

(4) Sorgenfrei, S.; Chiu, C. Y.; Gonzalez, R. L., Jr.; Yu, Y. J.; Kim, P.; Nuckolls, C.; Shepard, K. L. Label-Free Single-Molecule Detection of DNA-Hybridization Kinetics with a Carbon Nanotube Field-Effect Transistor. *Nat. Nanotechnol.* **2011,** *6*, 126–132.

(5) Ping, J.; Vishnubhotla, R.; Vrudhula, A.; Johnson, A. T. Scalable Production of High-Sensitivity, Label-Free DNA Biosensors Based on Back-Gated Graphene Field Effect Transistors. *ACS Nano* **2016,** *10*, 8700–8704.

(6) Blair, E. O.; Corrigan, D. K. A Review of Microfabricated Electrochemical Biosensors for DNA Detection. *Biosens. Bioelectron.* **2019,** *134*, 57–67.

(7) Patolsky, F.; Zheng, G.; Hayden, O.; Lakadamyali, M.; Zhuang, X.; Lieber, C. M. Electrical Detection of Single Viruses. *Proc. Natl. Acad. Sci. U. S. A.* **2004,** *101*, 14017–14022.

(8) Miranda, O. R.; Li, X.; Garcia-Gonzalez, L.; Zhu, Z. J.; Yan, B.; Bunz, U. H.; Rotello, V. M. Colorimetric Bacteria Sensing Using a Supramolecular Enzyme-Nanoparticle Biosensor. *J. Am. Chem. Soc.* **2011,** *133*, 9650–9653.

(9) Seo, G.; Lee, G.; Kim, M. J.; Baek, S. H.; Choi, M.; Ku, K. B.; Lee, C. S.; Jun, S.; Park, D.; Kim, H. G.; Kim, S. J.; Lee, J. O.; Kim, B. T.; Park, E. C.; Kim, S. I. Rapid Detection of COVID-19 Causative Virus (SARS-CoV-2) in Human Nasopharyngeal Swab Specimens Using Field-Effect Transistor-Based Biosensor. *ACS Nano* **2020,** *14*, 5135–5142.

(10) Gao, W.; Emaminejad, S.; Nyein, H. Y. Y.; Challa, S.; Chen, K.; Peck, A.; Fahad, H. M.; Ota, H.; Shiraki, H.; Kiriya, D.; Lien, D. H.; Brooks, G. A.; Davis, R. W.; Javey, A. Fully Integrated Wearable Sensor Arrays for Multiplexed *in Situ* Perspiration Analysis. *Nature* **2016,** *529*, 509–514.

(11) Koh, A.; Kang, D.; Xue, Y.; Lee, S.; Pielak, R. M.; Kim, J.; Hwang, T.; Min, S.; Banks, A.; Bastien, P.; Manco, M. C.; Wang, L.; Ammann, K. R.; Jang, K. I.; Won, P.; Han, S.; Ghaffari, R.; Paik, U.; Slepian, M. J.; Balooch, G.; et al. A Soft, Wearable Microfluidic Device for the Capture, Storage, and Colorimetric Sensing of Sweat. *Sci. Transl. Med.* **2016,** *8*, 366ra165.

(12) Zhang, Y.; Clausmeyer, J.; Babakinejad, B.; Cordoba, A. L.; Ali, T.; Shevchuk, A.; Takahashi, Y.; Novak, P.; Edwards, C.; Lab, M.; Gopal, S.; Chiappini, C.; Anand, U.; Magnani, L.; Coombes, R. C.; Gorelik, J.; Matsue, T.; Schuhmann, W.; Klenerman, D.; Sviderskaya, E. V.; et al. Spearhead Nanometric Field-Effect Transistor Sensors for Single-Cell Analysis. *ACS Nano* **2016,** *10*, 3214–3221.

(13) Emaminejad, S.; Gao, W.; Wu, E.; Davies, Z. A.; Yin Yin Nyein, H.; Challa, S.; Ryan, S. P.; Fahad, H. M.; Chen, K.; Shahpar, Z.; Talebi, S.; Milla, C.; Javey, A.; Davis, R. W. Autonomous Sweat Extraction and Analysis Applied to Cystic Fibrosis and Glucose Monitoring

Using a Fully Integrated Wearable Platform. *Proc. Natl. Acad. Sci. U. S. A.* **2017,** *114*, 4625–4630.

(14) Nakatsuka, N.; Yang, K. A.; Abendroth, J. M.; Cheung, K. M.; Xu, X.; Yang, H.; Zhao, C.; Zhu, B.; Rim, Y. S.; Yang, Y.; Weiss, P. S.; Stojanovic, M. N.; Andrews, A. M. Aptamer-Field-Effect Transistors Overcome Debye Length Limitations for Small-Molecule Sensing. *Science* **2018,** *362*, 319–324.

(15) Cui, Y.; Wei, Q.; Park, H.; Lieber, C. M. Nanowire Nanosensors for Highly Sensitive and Selective Detection of Biological and Chemical Species. *Science* **2001,** *293*, 1289–1292.

(16) Patolsky, F.; Zheng, G.; Lieber, C. M. Fabrication of Silicon Nanowire Devices for Ultrasensitive, Label-Free, Real-Time Detection of Biological and Chemical Species. *Nat Protoc* **2006,** *1*, 1711–1724.

(17) Hu, P.; Yan, M.; Wang, X.; Han, C.; He, L.; Wei, X.; Niu, C.; Zhao, K.; Tian, X.; Wei, Q.; Li, Z.; Mai, L. Single-Nanowire Electrochemical Probe Detection for Internally Optimized Mechanism of Porous Graphene in Electrochemical Devices. *Nano Lett.* **2016,** *16*, 1523–1529.

(18) Pollock, N. R.; Rolland, J. P.; Kumar, S.; Beattie, P. D.; Jain, S.; Noubary, F.; Wong, V. L.; Pohlmann, R. A.; Ryan, U. S.; Whitesides, G. M. A Paper-Based Multiplexed Transaminase Test for Low-Cost, Point-of-Care Liver Function Testing. *Sci. Transl. Med.* **2012,** *4*, 152ra129.

(19) Kim, J.; Lee, M.; Shim, H. J.; Ghaffari, R.; Cho, H. R.; Son, D.; Jung, Y. H.; Soh, M.; Choi, C.; Jung, S.; Chu, K.; Jeon, D.; Lee, S. T.; Kim, J. H.; Choi, S. H.; Hyeon, T.; Kim, D. H. Stretchable Silicon Nanoribbon Electronics for Skin Prosthesis. *Nat. Commun.* **2014,** *5*, 5747.

(20) Liu, R.; Chen, R.; Elthakeb, A. T.; Lee, S. H.; Hinckley, S.; Khraiche, M. L.; Scott, J.; Pre, D.; Hwang, Y.; Tanaka, A.; Ro, Y. G.; Matsushita, A. K.; Dai, X.; Soci, C.; Biesmans, S.; James, A.; Nogan, J.; Jungjohann, K. L.; Pete, D. V.; Webb, D. B.; et al. High Density Individually Addressable Nanowire Arrays Record Intracellular Activity from Primary Rodent and Human Stem Cell Derived Neurons. *Nano Lett*. **2017,** *17*, 2757–2764.

(21) Taylor, I. M.; Du, Z.; Bigelow, E. T.; Eles, J. R.; Horner, A. R.; Catt, K. A.; Weber, S. G.; Jamieson, B. G.; Cui, X. T. Aptamer-Functionalized Neural Recording Electrodes for the Direct Measurement of Cocaine *in Vivo*. *J. Mater. Chem. B* **2017,** *5*, 2445–2458.

(22) Bariya, M.; Nyein, H. Y. Y.; Javey, A. Wearable Sweat Sensors. *Nat. Electron*. **2018,** *1*, 160–171.

(23) Cheung, K. M.; Yang, K. A.; Nakatsuka, N.; Zhao, C.; Ye, M.; Jung, M. E.; Yang, H.; Weiss, P. S.; Stojanovic, M. N.; Andrews, A. M. Phenylalanine Monitoring *via* Aptamer-Field-Effect Transistor Sensors. *ACS Sens*. **2019,** *4*, 3308–3317.

(24) Kim, J.; Campbell, A. S.; de Avila, B. E.; Wang, J. Wearable Biosensors for Healthcare Monitoring. *Nat. Biotechnol*. **2019,** *37*, 389–406.

(25) Gao, W.; Ota, H.; Kiriya, D.; Takei, K.; Javey, A. Flexible Electronics toward Wearable Sensing. *Acc. Chem. Res*. **2019,** *52*, 523–533.

(26) Wen, X.; Wang, B.; Huang, S.; Liu, T. L.; Lee, M. S.; Chung, P. S.; Chow, Y. T.; Huang, I. W.; Monbouquette, H. G.; Maidment, N. T.; Chiou, P. Y. Flexible, Multifunctional Neural Probe with Liquid Metal Enabled, Ultra-Large Tunable Stiffness for Deep-Brain Chemical Sensing and Agent Delivery. *Biosens. Bioelectron*. **2019,** *131*, 37–45.

(27) Scida, K.; Plaxco, K. W.; Jamieson, B. G. High Frequency, Real-Time Neurochemical and Neuropharmacological Measurements *in Situ* in the Living Body. *Transl. Res.* **2019,** *213*, 50–66.

(28) He, X.; Yang, S.; Pei, Q.; Song, Y.; Liu, C.; Xu, T.; Zhang, X. Integrated Smart Janus Textile Bands for Self-Pumping Sweat Sampling and Analysis. *ACS Sens.* **2020,** *5*, 1548–1554.

(29) Kim, J.; Rim, Y. S.; Chen, H.; Cao, H. H.; Nakatsuka, N.; Hinton, H. L.; Zhao, C.; Andrews, A. M.; Yang, Y.; Weiss, P. S. Fabrication of High-Performance Ultrathin In_2O_3 Film Field-Effect Transistors and Biosensors Using Chemical Lift-Off Lithography. *ACS Nano* **2015,** *9*, 4572–4582.

(30) Rim, Y. S.; Bae, S. H.; Chen, H.; Yang, J. L.; Kim, J.; Andrews, A. M.; Weiss, P. S.; Yang, Y.; Tseng, H. R. Printable Ultrathin Metal Oxide Semiconductor-Based Conformal Biosensors. *ACS Nano* **2015,** *9*, 12174–12181.

(31) Chen, H.; Rim, Y. S.; Wang, I. C.; Li, C.; Zhu, B.; Sun, M.; Goorsky, M. S.; He, X.; Yang, Y. Quasi-Two-Dimensional Metal Oxide Semiconductors Based Ultrasensitive Potentiometric Biosensors. *ACS Nano* **2017,** *11*, 4710–4718.

(32) Li, C.; Zhang, D.; Liu, X.; Han, S.; Tang, T.; Han, J.; Zhou, C. In_2O_3 Nanowires as Chemical Sensors. *Appl. Phys. Lett.* **2003,** *82*, 1613–1615.

(33) Zhang, D.; Liu, Z.; Li, C.; Tang, T.; Liu, X.; Han, S.; Lei, B.; Zhou, C. Detection of NO_2 Down to ppb Levels Using Individual and Multiple In_2O_3 Nanowire Devices. *Nano Lett.* **2004,** *4*, 1919–1924.

(34) Tang, T.; Liu, X.; Li, C.; Lei, B.; Zhang, D.; Rouhanizadeh, M.; Hsiai, T.; Zhou, C. Complementary Response of In_2O_3 Nanowires and Carbon Nanotubes to Low-Density Lipoprotein Chemical Gating. *Appl. Phys. Lett.* **2005,** *86*, 103903.

(35) Curreli, M.; Li, C.; Sun, Y.; Lei, B.; Gundersen, M. A.; Thompson, M. E.; Zhou, C. Selective Functionalization of In_2O_3 Nanowire Mat Devices for Biosensing Applications. *J. Am. Chem. Soc.* **2005,** *127*, 6922–6923.

(36) Lee, B. Y.; Sung, M. G.; Lee, J.; Baik, K. Y.; Kwon, Y. K.; Lee, M. S.; Hong, S. Universal Parameters for Carbon Nanotube Network-Based Sensors: Can Nanotube Sensors Be Reproducible? *ACS Nano* **2011,** *5*, 4373–4379.

(37) Li, J.; Zhang, Y.; To, S.; You, L.; Sun, Y. Effect of Nanowire Number, Diameter, and Doping Density on nano-FET Biosensor Sensitivity. *ACS Nano* **2011,** *5*, 6661–6668.

(38) Xia, Y.; Rogers, J. A.; Paul, K. E.; Whitesides, G. M. Unconventional Methods for Fabricating and Patterning Nanostructures. *Chem. Rev.* **1999,** *99*, 1823–1848.

(39) Mizuno, H.; Buriak, J. M. Catalytic Stamp Lithography for Sub-100 nm Patterning of Organic Monolayers. *J. Am. Chem. Soc.* **2008,** *130*, 17656–17657.

(40) Braunschweig, A. B.; Huo, F.; Mirkin, C. A. Molecular Printing. *Nat. Chem.* **2009,** *1*, 353–358.

(41) Wang, H.; Haroldson, R.; Balachandran, B.; Zakhidov, A.; Sohal, S.; Chan, J. Y.; Zakhidov, A.; Hu, W. Nanoimprinted Perovskite Nanograting Photodetector with Improved Efficiency. *ACS Nano* **2016,** *10*, 10921–10928.

(42) Wang, C.; Shao, J.; Lai, D.; Tian, H.; Li, X. Suspended-Template Electric-Assisted Nanoimprinting for Hierarchical Micro-Nanostructures on a Fragile Substrate. *ACS Nano* **2019,** *13*, 10333–10342.

(43) Meitl, M. A.; Zhu, Z.-T.; Kumar, V.; Lee, K. J.; Feng, X.; Huang, Y. Y.; Adesida, I.; Nuzzo, R. G.; Rogers, J. A. Transfer Printing by Kinetic Control of Adhesion to an Elastomeric Stamp. *Nat. Mater.* **2005,** *5*, 33–38.

(44) Seo, M. H.; Yoo, J. Y.; Choi, S. Y.; Lee, J. S.; Choi, K. W.; Jeong, C. K.; Lee, K. J.; Yoon, J. B. Versatile Transfer of an Ultralong and Seamless Nanowire Array Crystallized at High Temperature for Use in High-Performance Flexible Devices. *ACS Nano* **2017,** *11*, 1520–1529.

(45) Han, H. J.; Jeong, J. W.; Yang, S. R.; Kim, C.; Yoo, H. G.; Yoon, J. B.; Park, J. H.; Lee, K. J.; Kim, T. S.; Kim, S. W.; Jung, Y. S. Nanotransplantation Printing of Crystallographic-Orientation-Controlled Single-Crystalline Nanowire Arrays on Diverse Surfaces. *ACS Nano* **2017,** *11*, 11642–11652.

(46) Lee, S. H.; Shin, S. H.; Madsen, M.; Takei, K.; Nah, J.; Lee, M. H. A Soft Lithographic Approach to Fabricate InAs Nanowire Field-Effect Transistors. *Sci. Rep.* **2018,** *8*, 3204.

(47) Aroonyadet, N.; Wang, X.; Song, Y.; Chen, H.; Cote, R. J.; Thompson, M. E.; Datar, R. H.; Zhou, C. Highly Scalable, Uniform, and Sensitive Biosensors Based on Top-Down Indium Oxide Nanoribbons and Electronic Enzyme-Linked Immunosorbent Assay. *Nano Lett.* **2015,** *15*, 1943-1951.

(48) Liu, Q.; Aroonyadet, N.; Song, Y.; Wang, X.; Cao, X.; Liu, Y.; Cong, S.; Wu, F.; Thompson, M. E.; Zhou, C. Highly Sensitive and Quick Detection of Acute Myocardial Infarction Biomarkers Using In_2O_3 Nanoribbon Biosensors Fabricated Using Shadow Masks. *ACS Nano* **2016,** *10*, 10117–10125.

(49) Liu, Q.; Liu, Y.; Wu, F.; Cao, X.; Li, Z.; Alharbi, M.; Abbas, A. N.; Amer, M. R.; Zhou, C. Highly Sensitive and Wearable In_2O_3 Nanoribbon Transistor Biosensors with Integrated On-Chip Gate for Glucose Monitoring in Body Fluids. *ACS Nano* **2018,** *12*, 1170–1178.

(50) Liu, Q.; Zhao, C.; Chen, M.; Liu, Y.; Zhao, Z.; Wu, F.; Li, Z.; Weiss, P. S.; Andrews, A. M.; Zhou, C. Flexible Multifunctional In_2O_3 Nanoribbon Aptamer-Field-Effect Transistor Biosensing. *iScience* **2020**, in press.

(51) Nair, P. R.; Alam, M. A. Screening-Limited Response of Nanobiosensors. *Nano Lett.* **2008,** *8*, 1281-1285.

(52) Li, Z.; Rajendran, B.; Kamins, T. I.; Li, X.; Chen, Y.; Williams, R. S. Silicon Nanowires for Sequence-Specific DNA Sensing: Device Fabrication and Simulation. *Appl. Phys. A* **2005,** *80*, 1257–1263.

(53) Sheehan, P. E.; Whitman, L. J. Detection Limits for Nanoscale Biosensors. *Nano Lett.* **2005,** *5*, 803-807.

(54) Zhiyong, F.; Lu, J. G. Chemical Sensing with ZnO Nanowire Field-Effect Transistor. *IEEE Trans. Nanotechnol.* **2006,** *5*, 393–396.

(55) Stern, E.; Klemic, J. F.; Routenberg, D. A.; Wyrembak, P. N.; Turner-Evans, D. B.; Hamilton, A. D.; LaVan, D. A.; Fahmy, T. M.; Reed, M. A. Label-Free Immunodetection with CMOS-Compatible Semiconducting Nanowires. *Nature* **2007,** *445*, 519–522.

(56) Elfstrom, N.; Juhasz, R.; Sychugov, I.; Engfeldt, T.; Karlstrom, A. E.; Linnros, J. Surface Charge Sensitivity of Silicon Nanowires: Size Dependence. *Nano Lett*. **2007,** *7*, 2608–2612.

(57) Elfstrom, N.; Karlstrom, A. E.; Linnros, J. Silicon Nanoribbons for Electrical Detection of Biomolecules. *Nano Lett*. **2008,** *8*, 945–949.

(58) Zhao, C.; Xu, X.; Bae, S. H.; Yang, Q.; Liu, W.; Belling, J. N.; Cheung, K. M.; Rim, Y. S.; Yang, Y.; Andrews, A. M.; Weiss, P. S. Large-Area, Ultrathin Metal-Oxide Semiconductor Nanoribbon Arrays Fabricated by Chemical Lift-Off Lithography. *Nano Lett*. **2018,** *18*, 5590–5595.

(59) Zhao, C.; Xu, X.; Ferhan, A. R.; Chiang, N.; Jackman, J. A.; Yang, Q.; Liu, W.; Andrews, A. M.; Cho, N. J.; Weiss, P. S. Scalable Fabrication of Quasi-One-Dimensional Gold Nanoribbons for Plasmonic Sensing. *Nano Lett*. **2020,** *20*, 1747–1754.

(60) Liao, W. S.; Cheunkar, S.; Cao, H. H.; Bednar, H. R.; Weiss, P. S.; Andrews, A. M. Subtractive Patterning *via* Chemical Lift-Off Lithography. *Science* **2012,** *337*, 1517–1521.

(61) Cao, H. H.; Nakatsuka, N.; Serino, A. C.; Liao, W.-S.; Cheunkar, S.; Yang, H.; Weiss, P. S.; Andrews, A. M. Controlled DNA Patterning by Chemical Lift-Off Lithography: Matrix Matters. *ACS Nano* **2015,** *9*, 11439–11454.

(62) Andrews, A. M.; Liao, W. S.; Weiss, P. S. Double-Sided Opportunities Using Chemical Lift-Off Lithography. *Acc. Chem. Res*. **2016,** *49*, 1449–1457.

(63) Xu, X.; Yang, Q.; Cheung, K. M.; Zhao, C.; Wattanatorn, N.; Belling, J. N.; Abendroth, J. M.; Slaughter, L. S.; Mirkin, C. A.; Andrews, A. M.; Weiss, P. S. Polymer-Pen Chemical Lift-Off Lithography. *Nano Lett*. **2017,** *17*, 3302–3311.

(64) Zhao, C.; Xu, X.; Yang, Q.; Man, T.; Jonas, S. J.; Schwartz, J. J.; Andrews, A. M.; Weiss, P. S. Self-Collapse Lithography. *Nano Lett*. **2017,** *17*, 5035–5042.

(65) Cao, H. H.; Nakatsuka, N.; Liao, W.-S.; Serino, A. C.; Cheunkar, S.; Yang, H.; Weiss, P. S.; Andrews, A. M. Advancing Biocapture Substrates *via* Chemical Lift-Off Lithography. *Chem. Mater*. **2017,** *29*, 6829–6839.

(66) Slaughter, L. S.; Cheung, K. M.; Kaappa, S.; Cao, H. H.; Yang, Q.; Young, T. D.; Serino, A. C.; Malola, S.; Olson, J. M.; Link, S.; Hakkinen, H.; Andrews, A. M.; Weiss, P. S. Patterning of Supported Gold Monolayers *via* Chemical Lift-Off Lithography. *Beilstein J. Nanotechnol*. **2017,** *8*, 2648–2661.

(67) Cao, H. H.; Nakatsuka, N.; Serino, A. C.; Liao, W.-S.; Cheunkar, S.; Yang, H.; Weiss, P. S.; Andrews, A. M. Small-Molecule Patterning *via* Prefunctionalized Alkanethiols. *Chem. Mater*. **2018,** *30*, 4017–4030.

(68) Cheung, K. M.; Stemer, D. M.; Zhao, C.; Young, T. D.; Belling, J. N.; Andrews, A. M.; Weiss, P. S. Chemical Lift-Off Lithography of Metal and Semiconductor Surfaces. *ACS Mater. Lett*. **2019,** *2*, 76–83.

(69) Shoorideh, K.; Chui, C. O. On the Origin of Enhanced Sensitivity in Nanoscale FET-Based Biosensors. *Proc. Natl. Acad. Sci. U. S. A*. **2014,** *111*, 5111–5116.

(70) Zayats, M.; Huang, Y.; Gill, R.; Ma, C. A.; Willner, I. Label-Free and Reagentless Aptamer-Based Sensors for Small Molecules. *J. Am. Chem. Soc.* **2006,** *128*, 13666–13667.

(71) Lee, C. S.; Kim, S. K.; Kim, M. Ion-Sensitive Field-Effect Transistor for Biological Sensing. *Sensors (Basel)* **2009,** *9*, 7111–7131.

(72) Zhang, J.; Rupakula, M.; Bellando, F.; Garcia Cordero, E.; Longo, J.; Wildhaber, F.; Herment, G.; Guerin, H.; Ionescu, A. M. Sweat Biomarker Sensor Incorporating Picowatt, Three-Dimensional Extended Metal Gate Ion Sensitive Field Effect Transistors. *ACS Sens.* **2019,** *4*, 2039–2047.

(73) Keeble, L.; Moser, N.; Rodriguez-Manzano, J.; Georgiou, P. ISFET-Based Sensing and Electric Field Actuation of DNA for On-Chip Detection: A Review. *IEEE Sens. J.* **2020**.

(74) Jeon, J. H.; Cho, W. J. Ultrasensitive Coplanar Dual-Gate ISFETs for Point-of-Care Biomedical Applications. *ACS Omega* **2020,** *5*, 12809–12815.

(75) Stern, E.; Wagner, R.; Sigworth, F. J.; Breaker, R.; Fahmy, T. M.; Reed, M. A. Importance of the Debye Screening Length on Nanowire Field Effect Transistor Sensors. *Nano Lett.* **2007,** *7*, 3405–3409.

(76) Lee, K.; Nair, P. R.; Scott, A.; Alam, M. A.; Janes, D. B. Device Considerations for Development of Conductance-Based Biosensors. *J. Appl. Phys.* **2009,** *105*, 102046.

(77) Patel, B. A. Continuous Amperometric Detection of Co-Released Serotonin and Melatonin from the Mucosa in the Ileum. *Analyst* **2008,** *133*, 516–524.

(78) Yang, H.; Thompson, A. B.; McIntosh, B. J.; Altieri, S. C.; Andrews, A. M. Physiologically Relevant Changes in Serotonin Resolved by Fast Microdialysis. *ACS Chem. Neurosci*. **2013,** *4*, 790–798.

(79) Cheung, K. M.; Abendroth, J. M.; Nakatsuka, N.; Zhu, B.; Yang, Y.; Andrews, A. M.; Weiss, P. S. Detecting DNA and RNA and Differentiating Single-Nucleotide Variations *via* Field-Effect Transistors. *Nano Lett*. **2020**, DOI: 10.1021/acs.nanolett.1020c01971.

(80) Xiao, Y.; Qu, X.; Plaxco, K. W.; Heeger, A. J. Label-Free Electrochemical Detection of DNA in Blood Serum *via* Target-Induced Resolution of an Electrode-Bound DNA Pseudoknot. *J. Am. Chem. Soc*. **2007,** *129*, 11896–11897.

(81) Sassolas, A.; Leca-Bouvier, B. D.; Blum, L. J. DNA Biosensors and Microarrays. *Chem. Rev*. **2008,** *108*, 109–139.

(82) Chu, D. K. W.; Pan, Y.; Cheng, S. M. S.; Hui, K. P. Y.; Krishnan, P.; Liu, Y.; Ng, D. Y. M.; Wan, C. K. C.; Yang, P.; Wang, Q.; Peiris, M.; Poon, L. L. M. Molecular Diagnosis of a Novel Coronavirus (2019-nCoV) Causing an Outbreak of Pneumonia. *Clin. Chem*. **2020,** *66*, 549–555.

(83) Fauci, A. S.; Lane, H. C.; Redfield, R. R. Covid-19–Navigating the Uncharted. *N. Engl. J. Med*. **2020,** *382*, 1268–1269.

(84) Behzadirad, M.; Nami, M.; Wostbrock, N.; Zamani Kouhpanji, M. R.; Feezell, D. F.; Brueck, S. R. J.; Busani, T. Scalable Top-Down Approach Tailored by Interferometric Lithography to Achieve Large-Area Single-Mode Gan Nanowire Laser Arrays on Sapphire Substrate. *ACS Nano* **2018**.

(85) Knopfmacher, O.; Tarasov, A.; Fu, W.; Wipf, M.; Niesen, B.; Calame, M.; Schonenberger, C. Nernst Limit in Dual-Gated Si-Nanowire FET Sensors. *Nano Lett*. **2010,** *10*, 2268–2274.

Chapter 7

Flexible Multiplexed In_2O_3 Nanoribbon Aptamer-Field-Effect Transistors for Biosensing

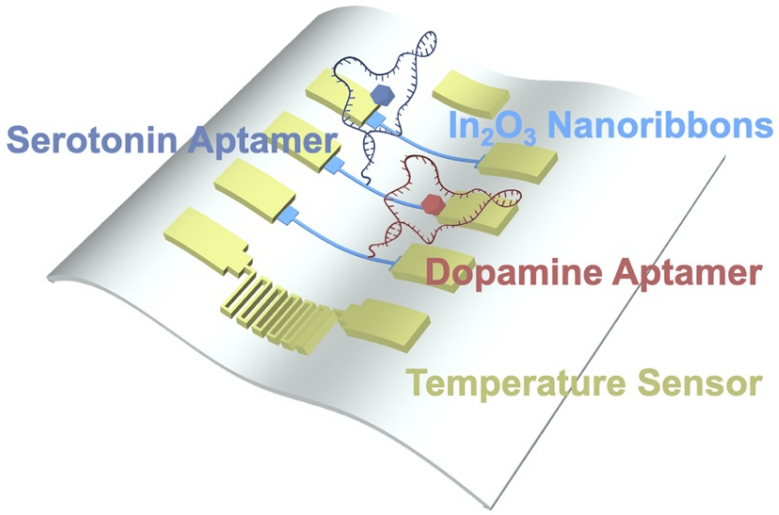

The information in this chapter is reprinted with permission from

iScience. **2020**, *23*, 101469 Copyright (2020) Elsevier

Authors: Liu, Q.; **Zhao, C.**; Chen, M.; Liu, Y.; Zhao, Z.; Wu, F.; Li, Z.; Weiss, P.S.; Andrews, A. M.; Zhou, C.

7.1 Abstract

Flexible sensors are essential for advancing implantable and wearable bioelectronics for monitoring chemical signals within and on the body. Developing biosensors for monitoring multiple neurotransmitters in real time represents a key *in vivo* application that will increase understanding of information encoded in brain neurochemical fluxes. Here, arrays of devices having multiple In_2O_3 nanoribbon field-effect transistors (FETs) were fabricated on 1.4-μm-thick polyethylene terephthalate (PET) substrates using shadow mask patterning techniques. Thin PET-FET devices withstood crumpling and bending such that stable transistor performance with high mobility was maintained over >100 bending cycles. Real-time detection of the small-molecule neurotransmitters serotonin and dopamine was achieved by immobilizing recently identified high-affinity nucleic-acid aptamers on individual In_2O_3 nanoribbon devices. Limits of detection were 10 fM for serotonin and dopamine with detection ranges spanning eight orders of magnitude. Simultaneous sensing of temperature, pH, serotonin, and dopamine enabled integration of physiological and neurochemical data from individual bioelectronic devices.

7.2 Introduction

Electronic devices that extend or create new capabilities for elucidating complex functions in brains,[1-3] skin,[4-7] and other biological systems[8] are of substantial interest. Advances have been made in the areas of soft[9-11] and minimally invasive bioelectronics.[12-14] Wearable electronics enable sensor systems for monitoring vital signs from skin and biomarkers in sweat, such as ions, glucose, lactase, and cortisol.[15-24] Efforts have been made towards bioelectronics for implantable devices, including liquid-metal- and hydrogel-based systems.[25-28] Soft materials yield readily to pressure and thus, more closely comply with the pliable and in some cases, stretchable nature of biological tissues. Fabrication of electronic devices on substrates having low Young's moduli, *i.e.*, greater elasticity, compared with rigid substrates reduces immunological responses after brain implantation.[29,30] Soft bioelectronics with capabilities to detect multiple neurotransmitters simultaneously and in real time are needed to investigate chemical information processing in brains,[31] particularly in the context of chronic neural recordings.[32]

We have developed aptamer-field-effect transistor (FET) biosensors that detect small molecules, including serotonin, dopamine, glucose, and phenylalanine under high-ionic strength conditions.[33,34] Aptamers are rare, single-stranded nucleic acid sequences isolated from oligonucleotide combinatorial libraries that recognize specific targets.[35-37] Aptamers can be functionalized to semiconducting materials used in FETs, *e.g.*, organic,[38] carbon-based,[39,40] and metal oxides.[41] Target-induced rearrangement of negatively charged DNA aptamer backbones results in changes in surface potentials near semiconductor channels to gate FET transconductance.[33] This sensing mechanism is label-free, and highly sensitive in physiological environments, *e.g.*, brain tissue, dilute serum.

Metal oxides, such as In_2O_3, have several advantages over other channel materials for FET-based sensors. Similar to Si devices, which can be fabricated with high scalability and uniformity, metal-oxide thin-film transistors have been widely used in industry, *e.g.,* touch screens, displays, solar cells, due to their electronic performance and large-area uniformity. The main advantages of metal oxides over silicon in wearable sensor applications are the ease of fabrication and compatibility with flexible substrates.[12,33,34,41-43]

Recently, a number of types of flexible electronics, including displays,[44,45] photovoltaics,[46] and wearable biosensors[12,42] have been fabricated using metal oxides in their structures. The In_2O_3 FETs are well suited to wearable or implantable sensing applications *vs.* a variety of other metal oxides, such as indium-gallium-zinc oxide (IGZO) and ZnO, as the latter are unstable under physiological conditions.[47,48] For example, ZnO nanoribbon FETs dissolve completely after 14 h of exposure to phosphate buffer saline (PBS). Top-down-fabricated In_2O_3 nanoribbon biosensors, in addition to being stable in physiological solutions, have fast response times, wide detection ranges, low limits of detection, high uniformity, and the capability to be integrated with microfluidics and microprocessors.[47,49]

Given the needs for implantable and wearable bioelectronics and the advantageous sensing capabilities of aptamer-FET biosensors under biologically relevant conditions, we aim to advance aptamer-functionalized In_2O_3 FETs in soft, flexible formats. Previously, we fabricated sol-gel processed thin-film In_2O_3 FETs on flexible polyimide for pH and glucose sensing.[12] The fabrication process involved spin-coating and high-temperature annealing (>350 °C). We have also fabricated In_2O_3 nanoribbon FETs *via* sputtering at room temperature on thick (~5 μm) polyethylene terephthalate (PET) for wearable applications in enzymatic glucose sensing.[42] Here,

we advance flexible substrates by fabricating arrays of In_2O_3 nanoribbon FETs on thin (1.4 μm) PET. These new devices exhibited uniform transistor performance, small batch-to-batch variation, and stable performance in high ionic strength solutions, *i.e.*, undiluted physiological buffered saline (PBS) and artificial cerebrospinal fluid (aCSF), in a format with robust mechanical flexibility. Thin-film PET-FETs were used to detect serotonin and dopamine over wide concentration ranges, including those occurring in the brain extracellular space,[50-52] in real time, and in a multiplexed format that included temperature and pH sensing.

7.3 Materials and Methods

Materials. All chemicals were purchased from Sigma-Aldrich Co. (St. Louis, MO), unless otherwise noted below. The SYLGARD 184 for fabricating PDMS wells and brain mimics was from Dow Corning Corporation (Midland, MI). Brain mimics were produced using silicone brain molds (Amazon #B003AQB2XK). The PDMS wells were made by cutting holes (~5 mm) in 3-mm PDMS sheets. The 1.4-μm-thick PET substrates were purchased from DuPont Teijin Films (Chester, VA) and used as received. Film thicknesses were measured and determined by the vendor using dielectric strength.

Physiological phosphate-buffered saline contained 137 mM NaCl, 2.7 mM KCl, 10 mM Na_2HPO_4, 1.8 mM KH_2PO_4. Artificial cerebrospinal fluid contained 147 mM NaCl, 3.5 mM KCl, 1 mM NaH_2PO_4, 2.5 mM $NaHCO_3$, 1 mM $CaCl_2$, and 1.2 mM $MgCl_2$. Oligonucleotides were obtained from Integrated DNA Technologies (Coralville, IA). Serotonin aptamer: 5'-/5ThioMC6-D/CGACTGGTAGGCAGATAGGGGAA GCTGATTCGATGCGTGGGTCG-3'. Serotonin scrambled aptamer: 5'-/5ThioMC6-

D/CCCGGGAATTCCGGAATTGGGGCAATTGATGA GGGGGTCATGGG-3'. Dopamine aptamer: 5'-/5ThioMC6-D/CGACGCCAGTTTGA AGGTTCGTTCGCAGGTGTGGAGTGACGTCG-3'.

Device fabrication. Each 1.4-μm-thick PET film was attached to a rigid carrier wafer *via* a PDMS adhesion layer. The lamination was performed by attaching a corner of each PET film to a sacrificial PDMS layer, then aligning the edges. A soft scraper was used to smooth the attached film and to remove any bubbles. After immersing in consecutive acetone and isopropanol rinses for 15 min each, the first shadow mask was attached to each substrate to define the In_2O_3 nanoribbons. The In_2O_3 was deposited by RF sputtering (Denton Discovery 550 sputtering system). The nanoribbon thickness was controlled by the sputtering time. An In_2O_3 thickness of 16 nm was selected for all devices because this was the thinnest In_2O_3 layer that could be sputtered to give consistent device performance and high sensitivities to ion concentrations, *e.g.*, pH.[47] Nanoribbon FETs with the same width and different thicknesses have been compared, where thinner nanoribbon FETs with higher surface-to-volume ratios showed the highest sensitivity to pH.[47]

The source, drain, and common gate electrodes, and temperature sensors were patterned using a second shadow mask. The bottom 1-nm Ti and top 50-nm Au layers were deposited *via* electron-beam (e-beam) evaporation. Device arrays were then peeled from their carrier wafers. Metal films deposited by e-beam evaporation were patterned using shadow masks, which is a cost-effective, cleanroom-free, and high-throughput process.[42,47] Moreover, this process does not result in In_2O_3 photoresist contamination or chemical exposure.[47] The thickness of the electrode metal layers impacts their performance. Previous studies indicated that the use of Au at 10-50 nm

with a Ti adhesion layer of <5 nm provides robust flexibility with minimal cracking.[53-55] Graphene is another electrode candidate for flexible electronics. Graphene has been deposited as a liquid-based mat and patterned by ink-jet printing or photolithography, the latter of which requires cleanroom processing and chemical exposure associated with the use of photoresist.[56-59] Other conductive metal oxides that have been used for electrodes, such as indium-tin-oxide or fluorine-doped tin-oxide,[57,60] have similar chemical properties as the channel material used here, *i.e.*, In_2O_3, which makes it challenging to functionalize channel regions separately from the electrodes.

Surface functionalization. (3-Aminopropyl)trimethoxysilane and trimethoxy(propyl)silane 1:9 (v/v) were thermally evaporated using vapor-phase deposition onto In_2O_3 surfaces at 40 °C for 1 h followed by incubation in 1 mM ethanolic 1-dodecanethiol for 1 h to passivate Au electrodes. Substrates were rinsed in ethanol and immersed in 1 mM solutions of 3-maleimidobenzoic acid *N*-hydroxysuccinimide ester (MBS) dissolved in a 1:9 (v/v) mixture of dimethyl sulfoxide and PBS for 30 min. The MBS crosslinks amine-terminated silanes with thiolated DNA aptamers.[33]

Aptamers (1 mM in nuclease-free water) were stored at -20 °C and diluted to 1 μM in nuclease-free water. Aptamers were heated for 5 min at 95 °C and cooled in an ice bath to room temperature. Substrates were rinsed with deionized water and immersed in 1 μM solutions of thiolated DNA aptamers overnight (~18 h), rinsed again with deionized water, and blown dry with N_2 gas before measurements. For multiplexed measurements, serotonin and dopamine aptamers (50 μL each) were added using a pipette onto two different adjacent devices. One FET

on the serotonin device was covered by a PDMS mask before adding the aptamer solution. The mask was then removed to expose an unfunctionalized FET, which served as a pH sensor.

Measurements. Each FET was connected with indium wires for electronic measurements. For the crumpling test, device arrays were crumpled tightly and held crumpled using tweezers for each crumpling cycle as shown in Fig. 3b. After ~5 s of crumpling, each array was then flattened. The crumpling and flattening cycles were repeated 100 times. Data were collected after 5, 10, 50, and 100 crumpling cycles. The concentrations of serotonin and dopamine tested were selected based on estimates of *in vivo* extracellular concentrations from our previous *in vivo* microdialysis measurements.[50-52] For multiplexed sensing, after using indium wires to connect the bonding pads of each FET, pH, serotonin, dopamine, and temperature sensors were covered with aCSF or different neurotransmitter solutions. Electrical characteristics under ambient conditions for the In_2O_3 FET devices were measured using an Agilent 4156B precision semiconductor parameter analyzer. Electrical characteristics in buffer and sensing results were measured with an Agilent B1500 semiconductor analyzer with capability to measure eight FETs at the same time.[61,62] Testing solutions of 300 μL were added to the PDMS wells. After each measurement, solutions were quickly removed using one pipette and the next testing solution was added immediately using a second pipette.

Mobility calculation. The charge-carrier mobility of the In_2O_3 nanoribbon FETs is estimated using the following equation:

$$g_m = \frac{dI_D}{dV_{GS}} = \frac{W}{L} \cdot C_{DL} \cdot \mu_{FE} \cdot V_{DS}$$

where W is the channel width, L is the channel length, and C_{DL} is the electrical double layer capacitance per unit area in 0.1 M ionic strength aqueous solution (phosphate-buffered saline), reported previously as 25.5 μF cm^{-2}.[63] The maximum transconductance of 4.77 μS was obtained at a drain voltage of 0.2 V and a gate voltage of 0.43 V. The corresponding mobility is 18.7 cm^2 V^{-1} s^{-1}.

Tensile strain calculation. To calculate the tensile strain when In_2O_3 nanoribbon FETs were wrapped tightly around a copper wire with a radius ~ 0.1 mm, we used the following formula:

$$\varepsilon = \frac{1}{R} \times \frac{d_s + d_f}{2} \times \frac{\chi \cdot \gamma^2 + 2 \cdot \chi \cdot \gamma + 1}{\chi \cdot \gamma^2 + \chi \cdot \gamma + \gamma + 1}$$

Here, R is the bending radius, d_s is the thickness of the substrate, d_f is the thickness of the In_2O_3 nanoribbon, $\gamma = d_f / d_s$ and $\chi = Y_f / Y_s$, where Y_f and Y_s are the Young's moduli of the In_2O_3 FET and substrate, respectively. If we assume $Y_f = Y_s$, the above equation can be simplified to:

$$\varepsilon = \frac{1}{R} \times \frac{d_s + d_f}{2}$$

The thickness of the polyethylene terephthalate (PET) substrate is 1.4 μm and the total thickness of the FET is less than 100 nm. With a bending radius of 0.1 mm, the tensile strain is calculated to be ~ 0.75 %.

7.4. Results and Discussions

The fabrication process for device arrays on flexible thin-film PET substrates is illustrated in **Figure 7.1a** and described in detail in Methods. Briefly, each 3-inch Si/SiO_2 substrate was spin-coated with a 20-μm polydimethylsiloxane (PDMS) adhesion layer. Next, 1.4-μm PET films were adhered to PDMS *via* van der Waals interactions. Polyethylene terephthalate is a common thermoplastic polymer resin used to make single-use food and liquid containers, and polyester clothing fiber. Here, PET films were used as-received at room temperature. The current approach has potential for highly scalable and uniform roll-to-roll fabrication.

A shadow mask was used to pattern 16-nm thick In_2O_3 nanoribbons on PET layers using radio frequency (RF) sputtering. A different shadow mask was then aligned to pattern source, drain, and gate electrodes and temperature sensors each composed of underlying 1-nm Ti layers and overlaying 50-nm Au films. The use of two aligned shadow mask steps eliminated the need for photolithography. The entire fabrication process was completed without the need for a cleanroom. Moreover, this fabrication strategy eliminated photoresist contamination and chemical exposure.[42,47,49] We have used thin metal films on PET for flexible electronics; these films showed high stability and reproducibility.[42,64] Each patterned PET biosensor film was delaminated from its sacrificial PDMS layer and the FET arrays were used for measurements.

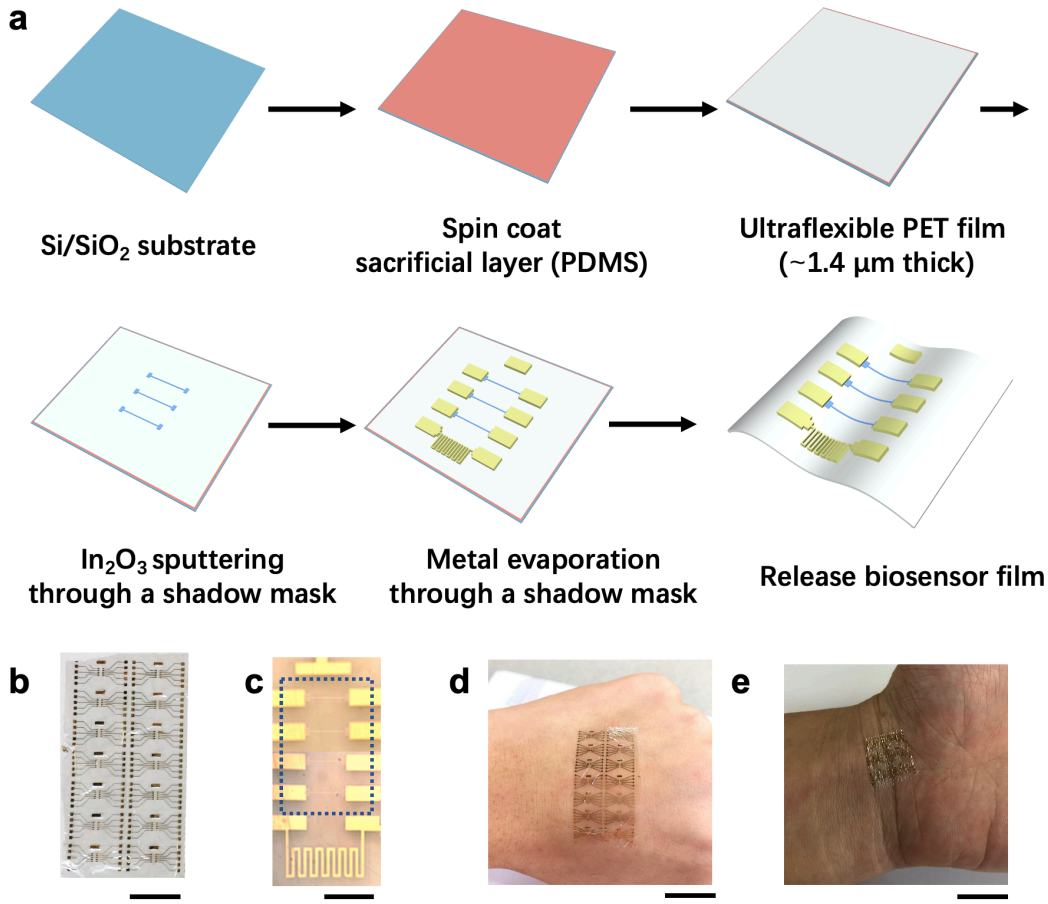

Figure 7.1 Fabrication of flexible In_2O_3 nanoribbon biosensors. (a) Schematic of the fabrication process. Each Si/SiO_2 substrate was coated with a polydimethylsiloxane (PDMS) adhesion layer. Next, a 1.4-µm polyethylene terephthalate (PET) film was laminated over the PDMS. The In_2O_3 nanoribbons were patterned by sputtering on the PET layer through a shadow mask. A 1-nm Ti adhesion layer followed by a 50-nm Au layer were deposited through a different shadow mask to pattern source, drain, gate, and temperature sensor electrodes. The biosensor film was then delaminated from the rigid carrier wafer. (b) Photograph of as-fabricated device array. Scale bar is 1 cm. Each array has 14 devices with four field-effect transistors (FETs) per device. (c) Optical microscope image of a single device showing the Au common-gate electrode, four In_2O_3 nanoribbon

FETs (dotted blue box), and a Au resistive temperature sensor (from top to bottom). The low contrast of the In_2O_3 nanoribbons is due to their transparency. Scale bar is 500 μm. (d) Flexibility of a sensor array is illustrated by conformal attachment to human skin. Scale bar is 2 cm. (e) Biosensor film wrinkled during human body movement. Scale bar is 1 cm.

Multiple transistor devices in arrays were fabricated on each 5 cm × 5 cm PET film. Each array consisted of 14 devices (**Figure 7.1b**). The total thickness of each array was ~1.5 μm and the total weight was ~2.5 mg. **Figure 7.1c** shows an individual device containing a Au common gate electrode, four In_2O_3 nanoribbon FETs, and a temperature sensor. Each In_2O_3 nanoribbon was16 nm thick, 25 μm wide, and 500 μm long (**Figure S7.1**). Device arrays were conformally applied to human skin (**Figure 7.1d**), illustrating the potential for wearable electronics for healthcare and personal monitoring applications. Devices could be bent and wrinkled when worn on skin (**Figure 7.1e**) When used as implantable devices, biosensors may be wrinkled or bent during the insertion process.

The flexible In_2O_3 nanoribbon FET devices exhibited uniform and stable electronic properties under high ionic-strength conditions. **Figure 7.2a** shows the transfer characteristics of a representative In_2O_3 nanoribbon transistor controlled using a common Au gate electrode. Black and blue curves represent drain current-gate voltage (I_{DS}-V_{GS}) characteristics in logarithmic and linear scales, respectively, and indicate gate modulation of drain current in phosphate buffered saline (PBS) with a current on/off ratio of ~10^3. The corresponding output characteristics demonstrated that the devices exhibited FET behavior typically associated with drain voltage modulation (**Figure 7.2b**). The gate leakage current was negligible compared with the drain-source current. As an example, the gate leakage current was less than 2 nA at V_{DS}=0.2 V

(**Figure S7.2**). All transistors in a representative array were characterized. Nearly 100% were functional (55/56) with only one transistor showing significantly lower mobility compared to the other transistors.

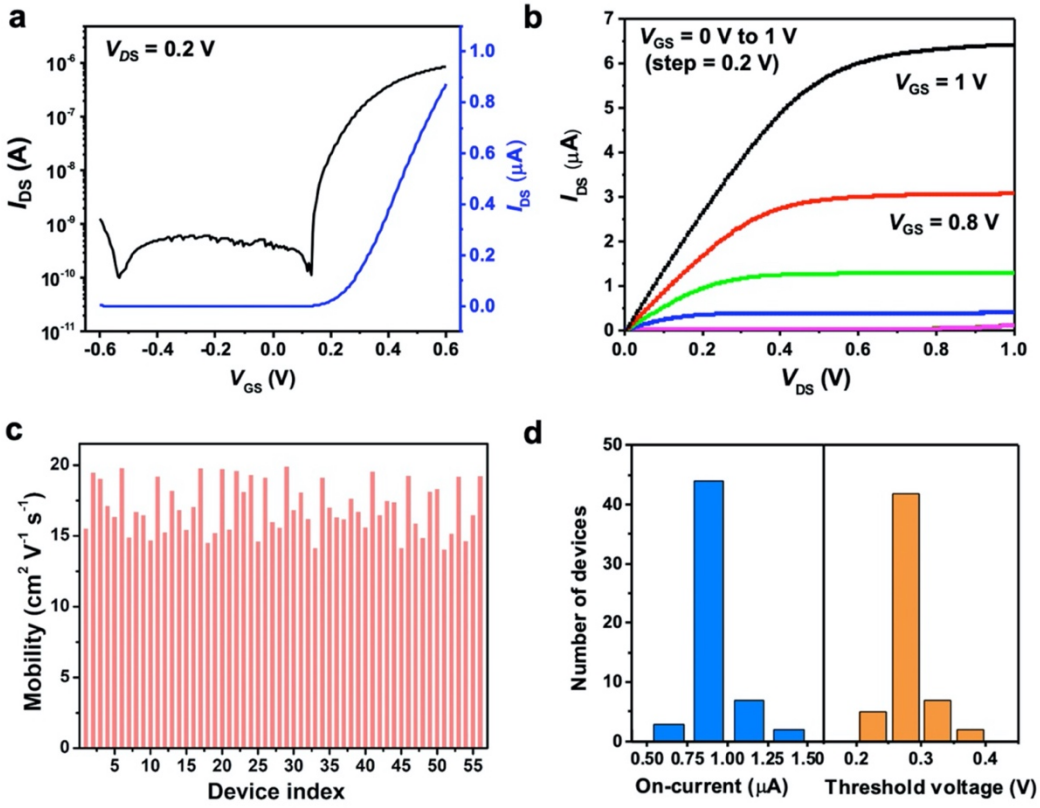

Figure 7.2: Electronic performance of flexible In_2O_3 nanoribbon field-effect transistors. (a) Representative transfer characteristics of an In_2O_3 nanoribbon transistor with L=500 μm, W=25 μm, and H=16 μm in phosphate buffered saline. The I_D (drain current) is shown in a logarithmic scale (left, black trace) and a linear scale (right, blue trace); V_{GS} is the gate-source voltage. The applied drain-source voltage V_{DS} was 0.2 V. (b) Output curves in the linear and saturation regimes. In this plot, I_{DS} is a function of V_{DS} with V_{GS} from 0 to 1 V in 0.2 V steps. (c) Plot of the charge-carrier mobilities of 56 transistors in an array. (d) Histograms showing on-currents and threshold voltages from the same 56 transistors. The average mobility was 17.8 ± 1.8 cm^2 V^{-1} s^{-1}. The average on-current was 0.86 ± 0.1 μA. The average threshold voltage was 0.27 ± 0.02 V.

The charge-carrier mobilities of 56 transistors in a single array were measured and calculated and showed ~10% variability (**Figure 7.2c**), with an average mobility of 17.8±1.8 cm^2 V^{-1} s^{-1}. Figure 2d shows a histogram of the on-state currents and threshold voltages of the 56 devices. Both showed narrow distributions. Notably, In_2O_3 nanoribbon transistors exhibited uniform and stable electronic performance in a physiological environment (all data in **Figure 7.2** were collected in undiluted PBS) at relatively low voltages (<1 V). These characteristics are favorable for implantable neural recording devices and on-skin electronics.

Mechanical flexibility of In_2O_3 nanoribbon FETs was evaluated in experiments that involved bending and crumpling. Figure 3a shows a photograph of a PET sheet patterned with In_2O_3 FETs tightly wrapped around a copper wire having a radius of 100 μm. Under these conditions, a tensile strain of ~0.75% (calculations in 7.6) was applied to the In_2O_3 nanoribbons with the direction of strain parallel to the current flow. In another test, a 5 cm × 5 cm PET sheet of In_2O_3 FET devices was tightly crumpled for ~5 s (**Figure 7.3b**), then flattened for electronic measurements.

The electronic performance of In_2O_3 FETs while bent and after crumpling was measured in PBS. Typical transfer curves of representative devices in the relaxed state, bent with a radius curvature of ~0.1 mm, and after 100 crumpling cycles are shown in **Figure 7.3c**, **3d** and **3e** show mobilities and threshold voltages averaged over 15 devices after 5, 10, 50, and 100 bending or crumpling cycles, respectively. After 100 bending cycles, the change in average mobility was 5.6% (from 18.4 cm^2 V^{-1} s^{-1} to 17.3 cm^2 V^{-1} s^{-1}); the threshold voltage showed only a small variation from 0.23 V to 0.27 V. Similar results were observed in repeated crumpling tests. The change in mobility was 6.1% after 100 crumpling cycles and the threshold voltage remained

around 0.26 V. Together, these findings illustrate that the In_2O_3 nanoribbon FET devices fabricated on thin-film PET are suitable for flexible electronics with reliable performance even under extreme bending and crumpling cycles. Bending events are common for both wearable bioelectronics and implantable devices. For example, bending occurs in and on soft tissue where devices need to adapt to movement.

Figure 7.3f shows transfer curves for FET devices before and after immersion in PBS for 1, 2, 3, 5, or 7 day(s). Based on data in linear and logarithmic scales, there were no significant changes in FET performance. These findings substantiate the long-term stability of In_2O_3 transistors in high ionic strength solutions and indicate that these sensors are robust for at least one week when exposed to physiological fluids.

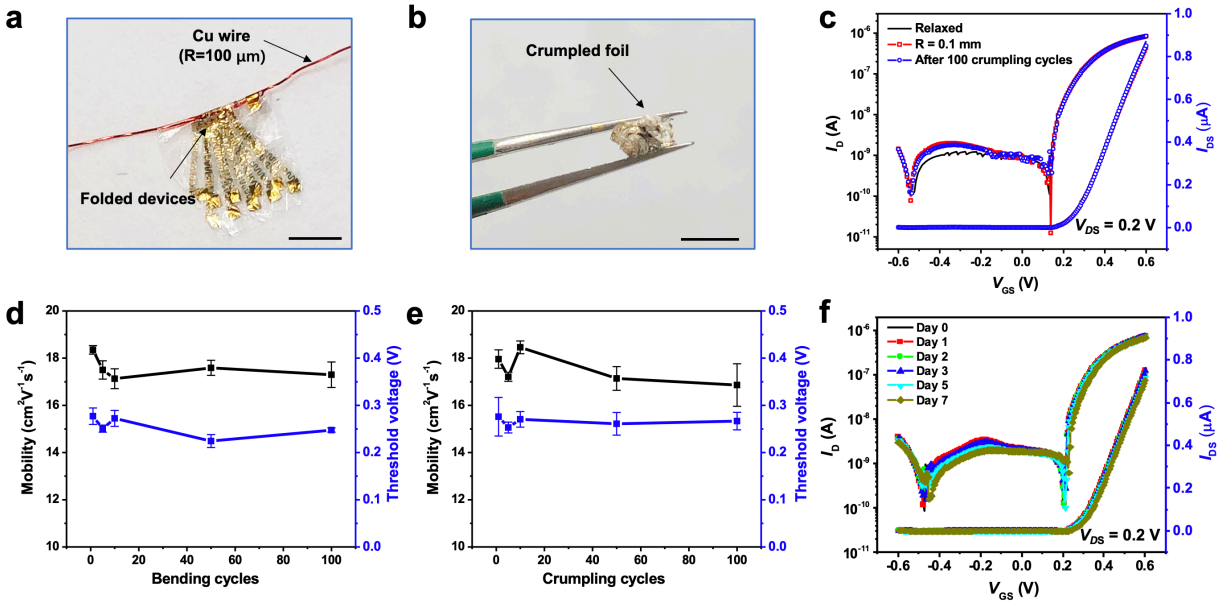

Figure 7.3. Stability of flexible In_2O_3 nanoribbon sensors. (a) Photograph of flexible thin-film (1.4 μm) PET In_2O_3 sensor arrays wrapped around a copper wire with a radius of 100 μm. Scale bar is 5 mm. (b) Photograph of a crumpled In_2O_3 biosensor film (original size: 5 cm × 5 cm). Scale bar is 0.5 cm. (c) Transfer characteristics of a representative In_2O_3 transistor in a relaxed state, bent around a copper wire with a radius of ~0.2 mm, and after crumpling, respectively. Mobilities (left) and threshold voltages (right) obtained in a relaxed state (d) after different numbers of bending cycles and (e) after various numbers of crumpling cycles. (f) Transfer characteristics of an In_2O_3 transistor measured immediately after fabrication (Day 0) and after immersion in undiluted PBS for 1, 2, 3, 5, and 7 day(s). Error bars in (d) and (e) are standard deviations of *N*=15 devices.

A portion of the negatively charged backbone of the serotonin aptamer used herein is hypothesized to move away from In_2O_3 channel surfaces upon target capture (**Figure 7.4a**).[20] Thus, the electrostatic repulsion between the electrons in an *n*-type semiconductor channel and negatively charged aptamers decreases, and channel conductance increases in response to aptamer-target association. Results for serotonin detection using In_2O_3 nanoribbon FETs functionalized with serotonin aptamers are shown in **Figure 7.4b**. Details of the surface functionalization and aptamer sequences are in Methods.

To evaluate sensor reliability in a high ionic strength buffer that approximates the brain extracellular fluid, serotonin was dissolved in artificial cerebrospinal fluid (aCSF). Devices were operated at a 0.25 V gate bias applied using the Au common gate electrode. Entire devices, including the channels, were submerged in aCSF to obtain baseline currents. After changing the solution to 10 fM serotonin in aCSF, the sensing signal increased by ~1% after stabilization (~150 s). As the solutions over the FETs were changed to include higher serotonin concentrations ranging from 0.1 pM to 1 μM sequentially, stepwise I_{DS} increases in currents were observed (**Figure 7.4b**).

To test reproducibility of detection, we conducted sensing with nine different devices. The relationship between serotonin concentration and saturated current response is shown in Figure 4c. We performed the same sensing procedure on control devices, *i.e.*, those with surface functionalization *sans* aptamers (**Figure S7.3**). The latter results are plotted in **Figure 7.4c** for comparison and showed minimal signal compared to that of FETs functionalized with aptamers. A device functionalized with a scrambled serotonin aptamer sequence also showed minimal response to serotonin indicating target selectivity (**Figure S7.4**).

In contrast to the serotonin aptamer, a portion of the negatively charged backbone of the dopamine aptamer used here is hypothesized to move closer to *n*-type semiconductor channels upon dopamine binding, thus increasing electrostatic repulsion and decreasing the In_2O_3 transconductance (**Figure 7.4d**).[20] The results of real-time dopamine sensing are shown in **Figure 7.4e**, and a summary of the relationship between dopamine concentrations and the corresponding FET responses from nine different devices is plotted in **Figure 7.4f**. The limit of detection for dopamine sensing was also on the order of 10 fM. Data were collected every 2 s and indicated that aptamer-FETs have ~5-s response times (**Figure S7.5**). Our determination of response time was limited by the semiconductor analyzer and software, thus measured response times are an upper limit.

We fabricated flexible sensing devices with the capability to monitor temperature, pH, serotonin, and dopamine simultaneously in real time. We performed sensing while devices were conformally applied to the surface of an "artificial brain", a brain replica made from PDMS, as a demonstration of working on/in irregular tissue surfaces (**Figure 7.5a**). The sensors developed here could be used as implanted or surface brain sensors or as wearable biosensors on the skin.

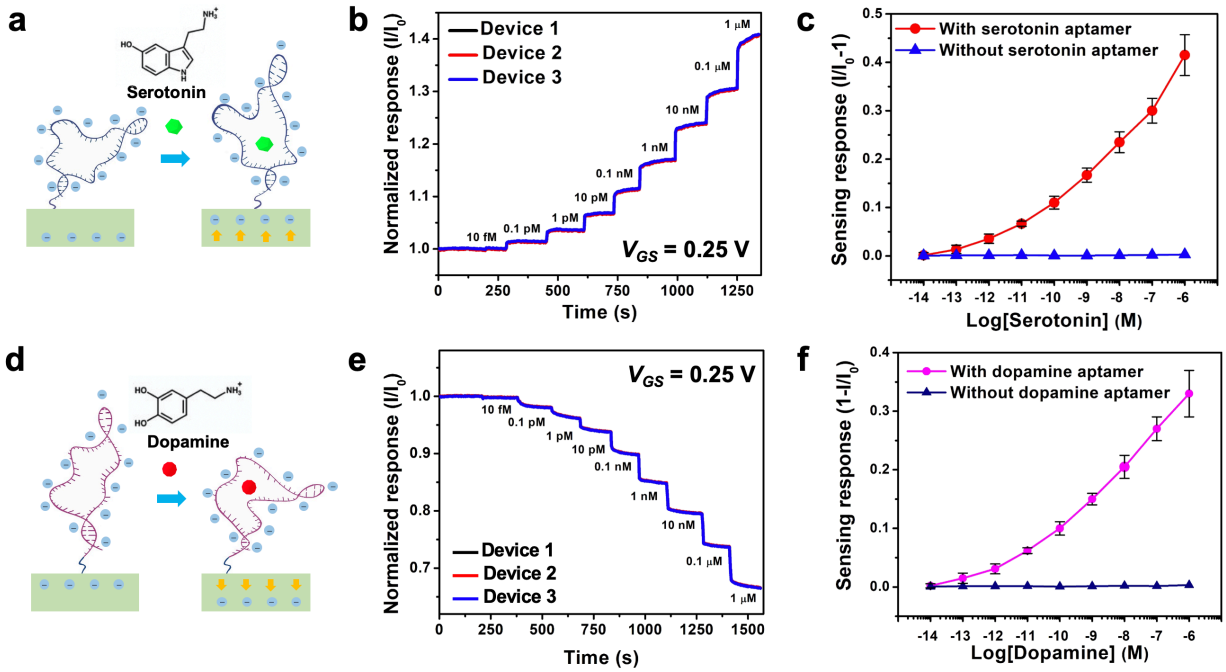

Figure 7.4: Characterization of serotonin- and dopamine-aptamer-functionalized sensors. **(a) Some aptamers, such as the aptamer used here to recognize serotonin, reorient a portion of their backbones away from semiconductor channels upon target binding, thereby increasing transconductance for *n*-type semiconductors. (b) Normalized (I/I_0; unitless) real-time sensing results from three In_2O_3 nanoribbon biosensors functionalized with the serotonin aptamer. Devices showed responses to serotonin (in undiluted artificial cerebrospinal fluid) at concentrations ranging from 10 fM to 1 μM. (c) Relationship between serotonin concentration and current responses from nine different devices. Results from unfunctionalized devices lacking aptamers are plotted for comparison. (d) Other aptamers, such as the dopamine aptamer used here, reorient a portion of their negatively charged oligonucleotide backbones closer to field-effect transistors upon target recognition to deplete channels electrostatically. (e) Normalized (I/I_0; unitless) real-time sensing results from three In_2O_3 nanoribbon biosensors functionalized with the dopamine aptamer. Devices showed responses to dopamine (in undiluted artificial cerebrospinal fluid) at**

concentrations ranging from 10 fM to 1 μM. (f) Relationship between dopamine concentration and current responses from nine different devices. Results from devices lacking the dopamine aptamer are also plotted. All devices were operated with V_{DS}=0.2 V and V_{GS}=0.25 V. Errors bars in (c) and (f) are standard deviations for N=9 devices (from three separate substrates where each substrate had three devices) and are too small to be visualized in some cases.

Local temperature change monitoring provides useful intraparenchymal and superficial information. For example, internal brain temperature is an indicator of neural functional activity.[65] Brain temperature is regionally specific and fluctuates by as much at 4 °C under normal activation states. Clinical studies indicate a relationship between brain temperature changes and cerebral injury.[66] Moreover, therapeutics, *e.g.*, anesthesia, drugs of abuse, cause large and sometimes devastating changes in brain temperature, in the case of the latter.[67] Skin temperature is also considered clinically informative, where it has been linked to a variety of diseases and skin injuries.[68,69] Therefore, sensing devices with integrated temperature sensors provide information to supplement target molecule monitoring.

Thermistors fabricated from Au wires have been used as temperature indicators in wearable sensor systems.[5] Here, we adapted a similar design and integrated fabrication within the shadow mask designs. **Figure 7.5b** shows the resistance of a representative Au thermistor in PBS ranging from 20 to 50 °C with 5 °C increments. The measured resistances were highly correlated with changes in temperature at a sensitivity of ~4 Ω/°C.

Field-effect transistor sensors are sensitive to pH changes, *i.e.*, $[H^+]$, because sensing mechanisms involves detecting changes in charge close to semiconductor surfaces.[12,47,49]

Fluctuations in brain pH occur as a result of changes in CO_2 levels, *i.e.*, carbonic acid, which increase in conjunction with neural activity, neurotransmitter release, and oxygen consumption.[70] Sensing pH is useful in wearable bioelectronics as sweat pH values also vary due to changes in carbonic acid levels.[5] Monitoring pH in sweat can be indicative of variations in electrolyte concentrations, which are biomarkers of disease and metabolic activity.[71-74] Here, unfunctionalized In_2O_3 nanoribbons responded to pH in buffer solutions ranging from pH 10 to pH 4 (**Figure 7.5c**). Devices showed increases in conductance when the pH of solutions decreased, corresponding to a positive gating effect at *n*-type In_2O_3 transistors.[12,47,49] We note that in addition to unfunctionalized FETs, devices functionalized with aptamers can be pH sensitive.[75-77] As pH decreases, negatively charged oligonucleotide backbones become associated with larger numbers of protons changing local charge near semiconductor surfaces.

Including pH sensors in our devices enables discriminating target-specific changes in transconductance at aptamer-functionalized sensors from those associated with local pH changes. Three devices from adjacent groups on the same substrate array were used for multiplexed sensing. One device was functionalized with the serotonin aptamer to work as a serotonin sensor. Another device next to the serotonin sensor was protected by a PDMS mask during the aptamer functionalization. After that, the PDMS mask was removed, and this device consisting of an unfunctionalized FET was used as a pH sensor. A third device from an adjacent group of devices was functionalized with the dopamine aptamer and was used as a dopamine sensor. Lastly, a patterned gold wire thermistor on the same substrate was used as a temperature sensor.

After obtaining a stable baseline current in aCSF (pH 7.4), solutions above FETs were sequentially replaced with aCSF containing 1 pM serotonin, 1 pM dopamine, 1 nM serotonin, or

1 nM dopamine. The two aptamer-functionalized devices detected and differentiated physiologically relevant concentrations of serotonin and dopamine, simultaneously (**Figure 7.5d**). No current changes occurred at the pH sensing FET in response to the addition of serotonin or dopamine. In contrast, when aCSF (pH 7.3) *sans* neurotransmitters was introduced at t=1100 s, all three FETs showed responses to a 0.1 pH unit change. For physiological sensing applications where pH and neurotransmitter concentrations change simultaneously, neurotransmitter-specific FET responses can be distinguished by subtracting responses occurring at pH sensors.

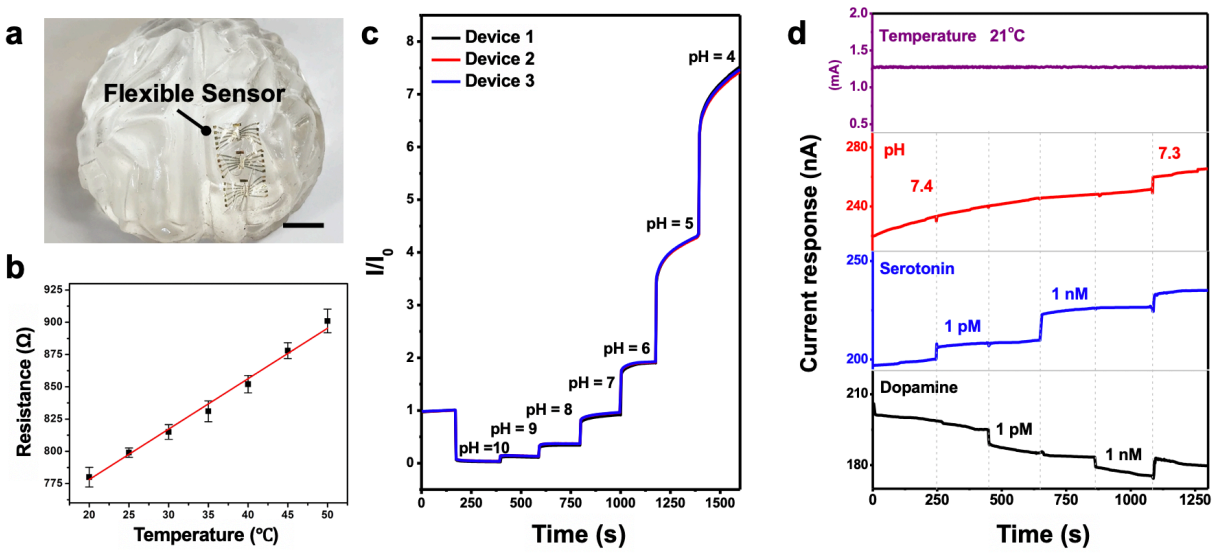

Figure 7.5. Multiplexed biosensing. (a) Photograph of three sensor devices attached conformally to a polydimethylsiloxane brain mimic. Scale bar is 1 cm. (b) Changes in resistance with respect to temperature in artificial cerebrospinal fluid (aCSF). Error bars are standard deviations for *N*=5 devices. For linear regression (y=ax+b), resistance=(3.9×temperature)+700, where temperature is in °Celsius; R^2=0.99 (c) Real-time pH sensing at unfunctionalized In_2O_3 nanoribbons in three different devices exposed to buffer solutions with pH values from 10 to 4. (d) Simultaneous sensing of temperature, pH, serotonin, and dopamine in aCSF (pH=7.4). Two adjacent devices were simultaneously exposed to solutions of 1 pM serotonin, 1 pM dopamine, 1 nM serotonin, and 1 nM dopamine, sequentially. Only transistors functionalized with the respective target-specific aptamers responded to the corresponding targets. All sensors responded to a pH change in aCSF (7.4 to 7.3). The devices were operated at V_{DS}=0.2 V and V_{GS}=0.25 V.

7.5 Conclusions and Prospects

We have demonstrated flexible conformal sensor devices for multiplexed and selective detection of neurotransmitters and other key physiological parameters. Devices displayed excellent flexibility when mechanically deformed and long-term stability in high ionic strength solutions. Real-time sensing of neurotransmitters at low, physiologically relevant concentrations was achieved. These sensors can be combined with integrated circuits for device operation and signal processing for wearable or implantable applications. To overcome spatial limitations for functionalization with different aptamers, an electrochemical approach to addressing different FETs in the same device can be applied for future studies. In sum, the current findings illustrate multiplexed, temporally resolved FET sensing of targets over large physiologically relevant concentration ranges, under high ionic strength conditions, and in a robust, flexible format. In conjunction with previous demonstrations of selectivity and sensing in biological tissues, small-molecule physiological sensors are expected to advance our understanding of the brain and other biological systems.

7.6 Supplementary Materials

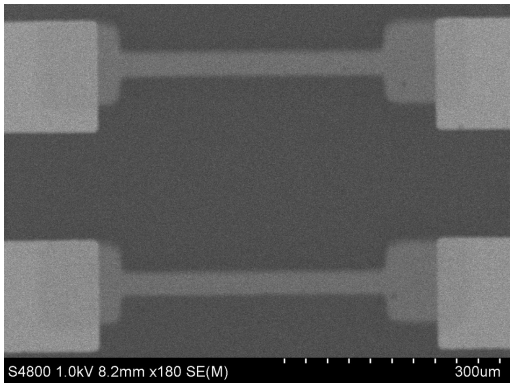

Figure S7.1. Scanning electron microscope image of two In_2O_3 nanoribbon field-effect transistors on a polyethylene terephthalate substrate. Each nanoribbon has a length of 500 µm and a width of 25 µm.

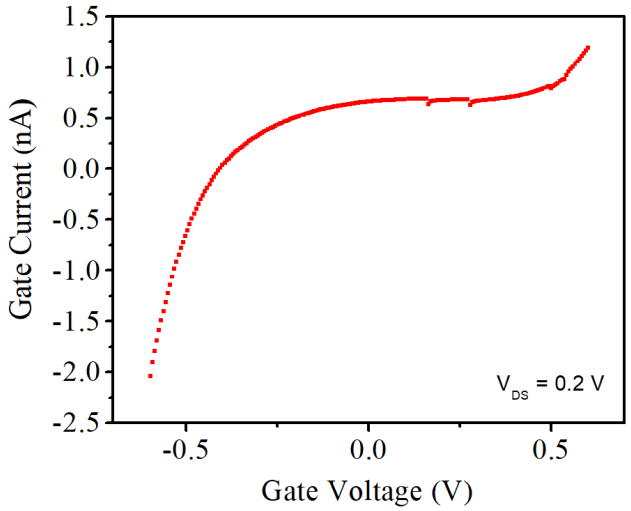

Figure S7.2. Gate leakage current *vs.* gate voltage from a representative In_2O_3 FET using a Au common gate. The gate leakage was negligible, and as shown, was smaller than 2 nA at V_{DS}=0.2 V.

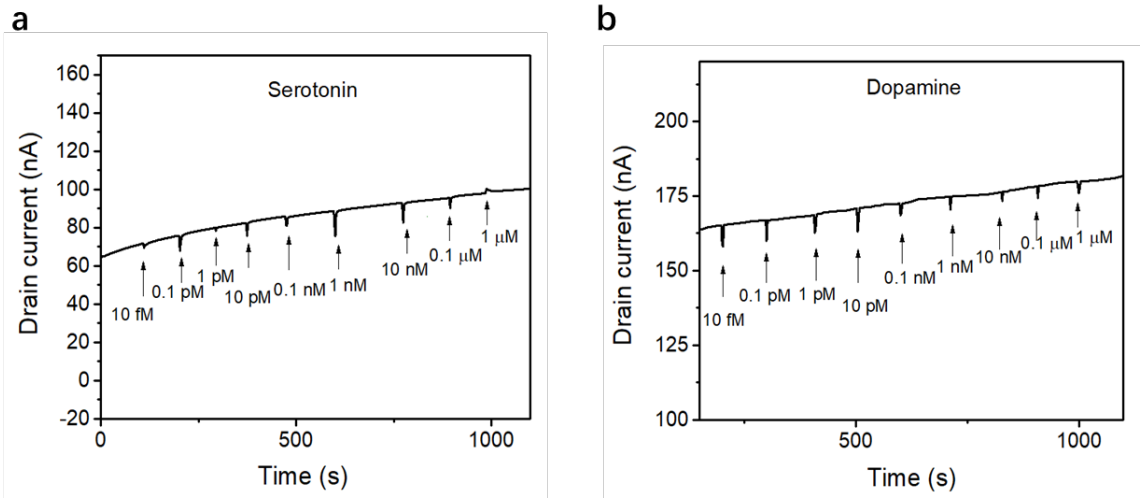

Figure S7.3. Control experiments for serotonin and dopamine sensing. The same sensing procedure was used at that in Figure 4 in the main text except sensors lacked (a) serotonin aptamers and (b) dopamine aptamers.

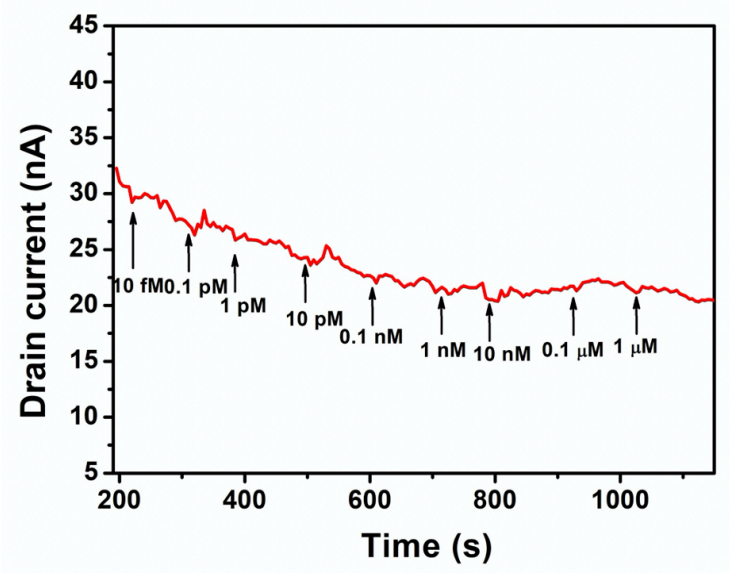

Figure S7.4. Control experiment with scrambled serotonin aptamer sequence for serotonin sensing.

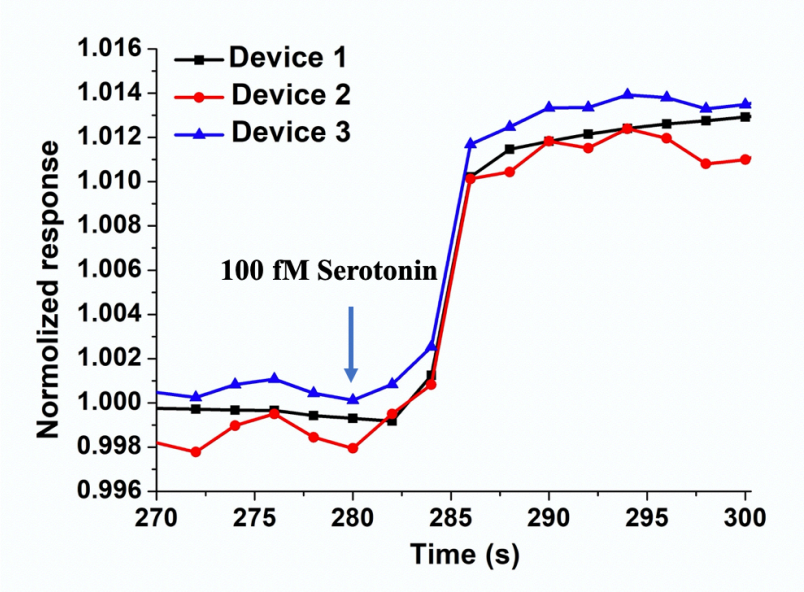

Figure S7.5. Temporal responses of In_2O_3 nanoribbon FETs to addition of 100 fM serotonin. Data are the same as those shown in Figure 7.4b in main text but are graphed to focus on temporal resolution for target sensing.

7.7 References

(1) Alivisatos, A. P.; Andrews, A. M.; Boyden, E. S.; Chun, M.; Church, G. M.; Deisseroth, K.; Donoghue, J. P.; Fraser, S. E.; Lippincott-Schwartz, J.; Looger, L. L.; Masmanidis, S.; McEuen, P. L.; Nurmikko, A. V.; Park, H.; Peterka, D. S.; Reid, C.; Roukes, M. L.; Scherer, A.; Schnitzer, M.; Sejnowski, T. J.; et al. Nanotools for Neuroscience and Brain Activity Mapping. *ACS Nano* **2013,** *7*, 1850–1866.

(2) Alivisatos, A. P.; Chun, M.; Church, G. M.; Deisseroth, K.; Donoghue, J. P.; Greenspan, R. J.; McEuen, P. L.; Roukes, M. L.; Sejnowski, T. J.; Weiss, P. S.; Yuste, R. The Brain Activity Map. *Science* **2013,** *339*, 1284–1285.

(3) Weiss, P. S. President Obama Announces the Brain Initiative. *ACS Nano* **2013,** *7*, 2873–2874.

(4) Liu, Z.; Qi, D.; Leow, W. R.; Yu, J.; Xiloyannnis, M.; Cappello, L.; Liu, Y.; Zhu, B.; Jiang, Y.; Chen, G.; Masia, L.; Liedberg, B.; Chen, X. 3D-Structured Stretchable Strain Sensors for out-of-Plane Force Detection. *Adv. Mater.* **2018,** *30*, e1707285.

(5) Gao, W.; Emaminejad, S.; Nyein, H. Y. Y.; Challa, S.; Chen, K.; Peck, A.; Fahad, H. M.; Ota, H.; Shiraki, H.; Kiriya, D.; Lien, D. H.; Brooks, G. A.; Davis, R. W.; Javey, A. Fully Integrated Wearable Sensor Arrays for Multiplexed *in Situ* Perspiration Analysis. *Nature* **2016,** *529*, 509–514.

(6) Kim, J.; Campbell, A. S.; de Avila, B. E.; Wang, J. Wearable Biosensors for Healthcare Monitoring. *Nat. Biotechnol.* **2019,** *37*, 389–406.

(7) Rogers, J.; Bao, Z.; Lee, T. W. Wearable Bioelectronics: Opportunities for Chemistry. *Acc. Chem. Res.* **2019,** *52*, 521–522.

(8) Biteen, J. S.; Blainey, P. C.; Cardon, Z. G.; Chun, M.; Church, G. M.; Dorrestein, P. C.; Fraser, S. E.; Gilbert, J. A.; Jansson, J. K.; Knight, R.; Miller, J. F.; Ozcan, A.; Prather, K. A.; Quake, S. R.; Ruby, E. G.; Silver, P. A.; Taha, S.; van den Engh, G.; Weiss, P. S.; Wong, G. C.; et al. Tools for the Microbiome: Nano and Beyond. *ACS Nano* **2016,** *10*, 6–37.

(9) Kim, D. H.; Viventi, J.; Amsden, J. J.; Xiao, J.; Vigeland, L.; Kim, Y. S.; Blanco, J. A.; Panilaitis, B.; Frechette, E. S.; Contreras, D.; Kaplan, D. L.; Omenetto, F. G.; Huang, Y.; Hwang, K. C.; Zakin, M. R.; Litt, B.; Rogers, J. A. Dissolvable Films of Silk Fibroin for Ultrathin Conformal Bio-Integrated Electronics. *Nat. Mater.* **2010,** *9*, 511–517.

(10) Minev, I. R.; Musienko, P.; Hirsch, A.; Barraud, Q.; Wenger, N.; Moraud, E. M.; Gandar, J.; Capogrosso, M.; Milekovic, T.; Asboth, L.; Torres, R. F.; Vachicouras, N.; Liu, Q.; Pavlova, N.; Duis, S.; Larmagnac, A.; Voros, J.; Micera, S.; Suo, Z.; Courtine, G.; et al. Electronic Dura Mater for Long-Term Multimodal Neural Interfaces. *Science* **2015,** *347*, 159–163.

(11) Wang, S.; Xu, J.; Wang, W.; Wang, G. N.; Rastak, R.; Molina-Lopez, F.; Chung, J. W.; Niu, S.; Feig, V. R.; Lopez, J.; Lei, T.; Kwon, S. K.; Kim, Y.; Foudeh, A. M.; Ehrlich, A.; Gasperini, A.; Yun, Y.; Murmann, B.; Tok, J. B.; Bao, Z. Skin Electronics from Scalable Fabrication of an Intrinsically Stretchable Transistor Array. *Nature* **2018,** *555*, 83–88.

(12) Rim, Y. S.; Bae, S. H.; Chen, H.; Yang, J. L.; Kim, J.; Andrews, A. M.; Weiss, P. S.; Yang, Y.; Tseng, H. R. Printable Ultrathin Metal Oxide Semiconductor-Based Conformal Biosensors. *ACS Nano* **2015,** *9*, 12174–12181.

(13) Luan, L.; Wei, X. L.; Zhao, Z. T.; Siegel, J. J.; Potnis, O.; Tuppen, C. A.; Lin, S. Q.; Kazmi, S.; Fowler, R. A.; Holloway, S.; Dunn, A. K.; Chitwood, R. A.; Xie, C. Ultraflexible Nanoelectronic Probes Form Reliable, Glial Scar-Free Neural Integration. *Sci. Adv.* **2017,** *3*, e1601966.

(14) Zhou, T.; Hong, G.; Fu, T. M.; Yang, X.; Schuhmann, T. G.; Viveros, R. D.; Lieber, C. M. Syringe-Injectable Mesh Electronics Integrate Seamlessly with Minimal Chronic Immune Response in the Brain. *Proc. Natl. Acad. Sci. U. S. A.* **2017,** *114*, 5894–5899.

(15) Heo, S. Y.; Kim, J.; Gutruf, P.; Banks, A.; Wei, P.; Pielak, R.; Balooch, G.; Shi, Y.; Araki, H.; Rollo, D.; Gaede, C.; Patel, M.; Kwak, J. W.; Pena-Alcantara, A. E.; Lee, K. T.; Yun, Y.; Robinson, J. K.; Xu, S.; Rogers, J. A. Wireless, Battery-Free, Flexible, Miniaturized Dosimeters Monitor Exposure to Solar Radiation and to Light for Phototherapy. *Sci. Transl. Med.* **2018,** *10*, eaau1643.

(16) Zhao, Y.; Wang, B.; Hojaiji, H.; Wang, Z.; Lin, S.; Yeung, C.; Lin, H.; Nguyen, P.; Chiu, K.; Salahi, K.; Cheng, X.; Tan, J.; Cerrillos, B. A.; Emaminejad, S. A Wearable Freestanding Electrochemical Sensing System. *Sci. Adv.* **2020,** *6*, eaaz0007.

(17) Kim, J.; Jeerapan, I.; Imani, S.; Cho, T. N.; Bandodkar, A.; Cinti, S.; Mercier, P. P.; Wang, J. Noninvasive Alcohol Monitoring Using a Wearable Tattoo-Based Iontophoretic-Biosensing System. *ACS Sens.* **2016,** *1*, 1011–1019.

(18) Nyein, H. Y. Y.; Tai, L. C.; Ngo, Q. P.; Chao, M.; Zhang, G. B.; Gao, W.; Bariya, M.; Bullock, J.; Kim, H.; Fahad, H. M.; Javey, A. A Wearable Microfluidic Sensing Patch for Dynamic Sweat Secretion Analysis. *ACS Sens.* **2018,** *3*, 944–952.

(19) Chung, H. U.; Kim, B. H.; Lee, J. Y.; Lee, J.; Xie, Z.; Ibler, E. M.; Lee, K.; Banks, A.; Jeong, J. Y.; Kim, J.; Ogle, C.; Grande, D.; Yu, Y.; Jang, H.; Assem, P.; Ryu, D.; Kwak, J. W.; Namkoong, M.; Park, J. B.; Lee, Y.; et al. Binodal, Wireless Epidermal Electronic Systems with in-Sensor Analytics for Neonatal Intensive Care. *Science* **2019,** *363*, eaau0780.

(20) Torrente-Rodriguez, R. M.; Tu, J.; Yang, Y.; Min, J.; Wang, M.; Song, Y.; Yu, Y.; Xu, C.; Ye, C.; IsHak, W. W.; Gao, W. Investigation of Cortisol Dynamics in Human Sweat Using a Graphene-Based Wireless Mhealth System. *Matter* **2020,** *2*, 921–937.

(21) Yang, Y.; Song, Y.; Bo, X.; Min, J.; Pak, O. S.; Zhu, L.; Wang, M.; Tu, J.; Kogan, A.; Zhang, H.; Hsiai, T. K.; Li, Z.; Gao, W. A Laser-Engraved Wearable Sensor for Sensitive Detection of Uric Acid and Tyrosine in Sweat. *Nat. Biotechnol.* **2020,** *38*, 217–224.

(22) He, X.; Xu, T.; Gu, Z.; Gao, W.; Xu, L. P.; Pan, T.; Zhang, X. Flexible and Superwettable Bands as a Platform toward Sweat Sampling and Sensing. *Anal. Chem.* **2019,** *91*, 4296–4300.

(23) He, X.; Yang, S.; Pei, Q.; Song, Y.; Liu, C.; Xu, T.; Zhang, X. Integrated Smart Janus Textile Bands for Self-Pumping Sweat Sampling and Analysis. *ACS Sens.* **2020,** *5*, 1548–1554.

(24) Liu, C.; Xu, T.; Wang, D.; Zhang, X. The Role of Sampling in Wearable Sweat Sensors. *Talanta* **2020,** *212*, 120801.

(25) Yu, K. J.; Kuzum, D.; Hwang, S. W.; Kim, B. H.; Juul, H.; Kim, N. H.; Won, S. M.; Chiang, K.; Trumpis, M.; Richardson, A. G.; Cheng, H.; Fang, H.; Thomson, M.; Bink, H.; Talos, D.; Seo, K. J.; Lee, H. N.; Kang, S. K.; Kim, J. H.; Lee, J. Y.; et al. Bioresorbable Silicon Electronics for Transient Spatiotemporal Mapping of Electrical Activity from the Cerebral Cortex. *Nat. Mater.* **2016,** *15*, 782–791.

(26) Fang, H.; Yu, K. J.; Gloschat, C.; Yang, Z.; Chiang, C. H.; Zhao, J.; Won, S. M.; Xu, S.; Trumpis, M.; Zhong, Y.; Song, E.; Han, S. W.; Xue, Y.; Xu, D.; Cauwenberghs, G.; Kay, M.; Huang, Y.; Viventi, J.; Efimov, I. R.; Rogers, J. A. Capacitively Coupled Arrays of Multiplexed

Flexible Silicon Transistors for Long-Term Cardiac Electrophysiology. *Nat. Biomed. Eng.* **2017,** *1*, 0038.

(27) Liu, Y.; Liu, J.; Chen, S.; Lei, T.; Kim, Y.; Niu, S.; Wang, H.; Wang, X.; Foudeh, A. M.; Tok, J. B.; Bao, Z. Soft and Elastic Hydrogel-Based Microelectronics for Localized Low-Voltage Neuromodulation. *Nat. Biomed. Eng.* **2019,** *3*, 58–68.

(28) Wen, X.; Wang, B.; Huang, S.; Liu, T. L.; Lee, M. S.; Chung, P. S.; Chow, Y. T.; Huang, I. W.; Monbouquette, H. G.; Maidment, N. T.; Chiou, P. Y. Flexible, Multifunctional Neural Probe with Liquid Metal Enabled, Ultra-Large Tunable Stiffness for Deep-Brain Chemical Sensing and Agent Delivery. *Biosens. Bioelectron.* **2019,** *131*, 37–45.

(29) Kozai, T. D.; Jaquins-Gerstl, A. S.; Vazquez, A. L.; Michael, A. C.; Cui, X. T. Brain Tissue Responses to Neural Implants Impact Signal Sensitivity and Intervention Strategies. *ACS Chem. Neurosci.* **2015,** *6*, 48–67.

(30) Gunasekera, B.; Saxena, T.; Bellamkonda, R.; Karumbaiah, L. Intracortical Recording Interfaces: Current Challenges to Chronic Recording Function. *ACS Chem. Neurosci.* **2015,** *6*, 68–83.

(31) Andrews, A. M. The Brain Initiative: Toward a Chemical Connectome. *ACS Chem. Neurosci.* **2013,** *4*, 645.

(32) Du, Z. J.; Kolarcik, C. L.; Kozai, T. D. Y.; Luebben, S. D.; Sapp, S. A.; Zheng, X. S.; Nabity, J. A.; Cui, X. T. Ultrasoft Microwire Neural Electrodes Improve Chronic Tissue Integration. *Acta Biomater.* **2017,** *53*, 46–58.

(33) Nakatsuka, N.; Yang, K. A.; Abendroth, J. M.; Cheung, K. M.; Xu, X.; Yang, H.; Zhao, C.; Zhu, B.; Rim, Y. S.; Yang, Y.; Weiss, P. S.; Stojanovic, M. N.; Andrews, A. M. Aptamer-Field-Effect Transistors Overcome Debye Length Limitations for Small-Molecule Sensing. *Science* **2018,** *362*, 319–324.

(34) Cheung, K. M.; Yang, K. A.; Nakatsuka, N.; Zhao, C.; Ye, M.; Jung, M. E.; Yang, H.; Weiss, P. S.; Stojanovic, M. N.; Andrews, A. M. Phenylalanine Monitoring *via* Aptamer-Field-Effect Transistor Sensors. *ACS Sens*. **2019,** *4*, 3308–3317.

(35) Hamaguchi, N.; Ellington, A.; Stanton, M. Aptamer Beacons for the Direct Detection of Proteins. *Anal. Biochem*. **2001,** *294*, 126–131.

(36) Willner, I.; Zayats, M. Electronic Aptamer-Based Sensors. *Angew. Chem. Int. Ed*. **2007,** *46*, 6408–6418.

(37) Nakatsuka, N.; Cao, H. H.; Deshayes, S.; Melkonian, A. L.; Kasko, A. M.; Weiss, P. S.; Andrews, A. M. Aptamer Recognition of Multiplexed Small-Molecule-Functionalized Substrates. *ACS Appl. Mater. Interfaces* **2018,** *10*, 23490–23500.

(38) Hammock, M. L.; Knopfmacher, O.; Naab, B. D.; Tok, J. B. H.; Bao, Z. A. Investigation of Protein Detection Parameters Using Nanofunctionalized Organic Field-Effect Transistors. *ACS Nano* **2013,** *7*, 3970–3980.

(39) So, H. M.; Park, D. W.; Jeon, E. K.; Kim, Y. H.; Kim, B. S.; Lee, C. K.; Choi, S. Y.; Kim, S. C.; Chang, H.; Lee, J. O. Detection and Titer Estimation of *Escherichia Coli* Using Aptamer-Functionalized Single-Walled Carbon-Nanotube Field-Effect Transistors. *Small* **2008,** *4*, 197–201.

(40) Sorgenfrei, S.; Chiu, C. Y.; Gonzalez, R. L., Jr.; Yu, Y. J.; Kim, P.; Nuckolls, C.; Shepard, K. L. Label-Free Single-Molecule Detection of DNA-Hybridization Kinetics with a Carbon Nanotube Field-Effect Transistor. *Nat. Nanotechnol.* **2011,** *6*, 126–132.

(41) Kim, J.; Rim, Y. S.; Chen, H. J.; Cao, H. H.; Nakatsuka, N.; Hinton, H. L.; Zhao, C. Z.; Andrews, A. M.; Yang, Y.; Weiss, P. S. Fabrication of High-Performance Ultrathin In_2O_3 Film Field-Effect Transistors and Biosensors Using Chemical Lift-Off Lithography. *ACS Nano* **2015,** *9*, 4572–4582.

(42) Liu, Q.; Liu, Y.; Wu, F.; Cao, X.; Li, Z.; Alharbi, M.; Abbas, A. N.; Amer, M. R.; Zhou, C. Highly Sensitive and Wearable In_2O_3 Nanoribbon Transistor Biosensors with Integrated On-Chip Gate for Glucose Monitoring in Body Fluids. *ACS Nano* **2018,** *12*, 1170–1178.

(43) Zhao, C.; Xu, X.; Bae, S. H.; Yang, Q.; Liu, W.; Belling, J. N.; Cheung, K. M.; Rim, Y. S.; Yang, Y.; Andrews, A. M.; Weiss, P. S. Large-Area, Ultrathin Metal-Oxide Semiconductor Nanoribbon Arrays Fabricated by Chemical Lift-Off Lithography. *Nano Lett.* **2018,** *18*, 5590–5595.

(44) Lewis, J.; Grego, S.; Chalamala, B.; Vick, E.; Temple, D. Highly Flexible Transparent Electrodes for Organic Light-Emitting Diode-Based Displays. *Appl. Phys. Lett.* **2004,** *85*, 3450–3452.

(45) Park, J. S.; Kim, T. W.; Stryakhilev, D.; Lee, J. S.; An, S. G.; Pyo, Y. S.; Lee, D. B.; Mo, Y. G.; Jin, D. U.; Chung, H. K. Flexible Full Color Organic Light-Emitting Diode Display on Polyimide Plastic Substrate Driven by Amorphous Indium Gallium Zinc Oxide Thin-Film Transistors. *Appl. Phys. Lett.* **2009,** *95*, 013503.

(46) Fan, Z.; Razavi, H.; Do, J. W.; Moriwaki, A.; Ergen, O.; Chueh, Y. L.; Leu, P. W.; Ho, J. C.; Takahashi, T.; Reichertz, L. A.; Neale, S.; Yu, K.; Wu, M.; Ager, J. W.; Javey, A. Three-Dimensional Nanopillar-Array Photovoltaics on Low-Cost and Flexible Substrates. *Nat. Mater.* **2009,** *8*, 648–653.

(47) Aroonyadet, N.; Wang, X.; Song, Y.; Chen, H.; Cote, R. J.; Thompson, M. E.; Datar, R. H.; Zhou, C. Highly Scalable, Uniform, and Sensitive Biosensors Based on Top-Down Indium Oxide Nanoribbons and Electronic Enzyme-Linked Immunosorbent Assay. *Nano Lett.* **2015,** *15*, 1943–1951.

(48) Jin, S. H.; Kang, S. K.; Cho, I. T.; Han, S. Y.; Chung, H. U.; Lee, D. J.; Shin, J.; Baek, G. W.; Kim, T. I.; Lee, J. H.; Rogers, J. A. Water-Soluble Thin Film Transistors and Circuits Based on Amorphous Indium-Gallium-Zinc Oxide. *ACS Appl. Mater. Interfaces* **2015,** *7*, 8268–8274.

(49) Liu, Q.; Aroonyadet, N.; Song, Y.; Wang, X.; Cao, X.; Liu, Y.; Cong, S.; Wu, F.; Thompson, M. E.; Zhou, C. Highly Sensitive and Quick Detection of Acute Myocardial Infarction Biomarkers Using In_2O_3 Nanoribbon Biosensors Fabricated Using Shadow Masks. *ACS Nano* **2016,** *10*, 10117–10125.

(50) Yang, H.; Thompson, A. B.; McIntosh, B. J.; Altieri, S. C.; Andrews, A. M. Physiologically Relevant Changes in Serotonin Resolved by Fast Microdialysis. *ACS Chem. Neurosci.* **2013,** *4*, 790–798.

(51) Yang, H.; Sampson, M. M.; Senturk, D.; Andrews, A. M. Sex- and SERT-Mediated Differences in Stimulated Serotonin Revealed by Fast Microdialysis. *ACS Chem. Neurosci.* **2015,** *6*, 1487–1501.

(52) Mathews, T. A.; Fedele, D. E.; Coppelli, F. M.; Avila, A. M.; Murphy, D. L.; Andrews, A. M. Gene Dose-Dependent Alterations in Extraneuronal Serotonin but Not Dopamine in Mice with Reduced Serotonin Transporter Expression. *J. Neurosci. Methods* **2004,** *140*, 169–181.

(53) Adrega, T.; Lacour, S. P. Stretchable Gold Conductors Embedded in Pdms and Patterned by Photolithography: Fabrication and Electromechanical Characterization. *J. Micromech. Microeng.* **2010,** *20*, 055025.

(54) Seghir, R.; Arscott, S. Controlled Mud-Crack Patterning and Self-Organized Cracking of Polydimethylsiloxane Elastomer Surfaces. *Sci. Rep.* **2015,** *5*, 14787.

(55) Baetens, T.; Pallecchi, E.; Thomy, V.; Arscott, S. Cracking Effects in Squashable and Stretchable Thin Metal Films on Pdms for Flexible Microsystems and Electronics. *Sci. Rep.* **2018,** *8*, 9492.

(56) Liu, Y.; Zhou, H.; Cheng, R.; Yu, W.; Huang, Y.; Duan, X. Highly Flexible Electronics from Scalable Vertical Thin Film Transistors. *Nano Lett.* **2014,** *14*, 1413–1418.

(57) Yang, W.; Wang, C. Graphene and the Related Conductive Inks for Flexible Electronics. *J. Mater. Chem. C* **2016,** *4*, 7193–7207.

(58) Han, T.-H.; Kim, H.; Kwon, S.-J.; Lee, T.-W. Graphene-Based Flexible Electronic Devices. *Mater. Sci. Eng. R Rep.* **2017,** *118*, 1–43.

(59) Song, D.; Mahajan, A.; Secor, E. B.; Hersam, M. C.; Francis, L. F.; Frisbie, C. D. High-Resolution Transfer Printing of Graphene Lines for Fully Printed, Flexible Electronics. *ACS Nano* **2017,** *11*, 7431–7439.

(60) Spechler, J. A.; Koh, T.-W.; Herb, J. T.; Rand, B. P.; Arnold, C. B. A Transparent, Smooth, Thermally Robust, Conductive Polyimide for Flexible Electronics. *Adv. Funct. Mater.* **2015,** *25*, 7428–7434.

(61) Ishikawa, F. N.; Curreli, M.; Chang, H. K.; Chen, P. C.; Zhang, R.; Cote, R. J.; Thompson, M. E.; Zhou, C. A Calibration Method for Nanowire Biosensors to Suppress Device-to-Device Variation. *ACS Nano* **2009,** *3*, 3969–3976.

(62) Chang, H. K.; Ishikawa, F. N.; Zhang, R.; Datar, R.; Cote, R. J.; Thompson, M. E.; Zhou, C. Rapid, Label-Free, Electrical Whole Blood Bioassay Based on Nanobiosensor Systems. *ACS Nano* **2011,** *5*, 9883–9891.

(63) Park, S.; Lee, S.; Kim, C.-H.; Lee, I.; Lee, W.-J.; Kim, S.; Lee, B.-G.; Jang, J.-H.; Yoon, M. H. Sub-0.5 V Highly Stable Aqueous Salt Gated Metal Oxide Electronics. *Sci. Rep.* **2015,** *5*, 13088.

(64) Cao, X.; Cao, Y.; Zhou, C. Imperceptible and Ultraflexible p-Type Transistors and Macroelectronics Based on Carbon Nanotubes. *ACS Nano* **2016,** *10*, 199–206.

(65) Wang, H.; Wang, B.; Normoyle, K. P.; Jackson, K.; Spitler, K.; Sharrock, M. F.; Miller, C. M.; Best, C.; Llano, D.; Du, R. Brain Temperature and Its Fundamental Properties: A Review for Clinical Neuroscientists. *Front. Neurosci.* **2014,** *8*, 307.

(66) Nielsen, N.; Wetterslev, J.; Cronberg, T.; Erlinge, D.; Gasche, Y.; Hassager, C.; Horn, J.; Hovdenes, J.; Kjaergaard, J.; Kuiper, M.; Pellis, T.; Stammet, P.; Wanscher, M.; Wise, M. P.; Aneman, A.; Al-Subaie, N.; Boesgaard, S.; Bro-Jeppesen, J.; Brunetti, I.; Bugge, J. F.; et al.

Targeted Temperature Management at 33℃ Versus 36℃ after Cardiac Arrest. *N. Engl. J. Med.* **2013,** *369*, 2197 – 2206.

(67) Kiyatkin, E. A. Brain Temperature: From Physiology and Pharmacology to Neuropathology. *Handb. Clin. Neurol.* **2018,** *157*, 483–504.

(68) Sprigle, S.; Linden, M.; McKenna, D.; Davis, K.; Riordan, B. Clinical Skin Temperature Measurement to Predict Incipient Pressure Ulcers. *Adv. Skin. Wound Care* **2001,** *14*, 133–137.

(69) Webb, R. C.; Bonifas, A. P.; Behnaz, A.; Zhang, Y.; Yu, K. J.; Cheng, H.; Shi, M.; Bian, Z.; Liu, Z.; Kim, Y. S.; Yeo, W. H.; Park, J. S.; Song, J.; Li, Y.; Huang, Y.; Gorbach, A. M.; Rogers, J. A. Ultrathin Conformal Devices for Precise and Continuous Thermal Characterization of Human Skin. *Nat. Mater.* **2013,** *12*, 938–944.

(70) Meunier, C. J.; Mitchell, E. C.; Roberts, J. G.; Toups, J. V.; McCarty, G. S.; Sombers, L. A. Electrochemical Selectivity Achieved Using a Double Voltammetric Waveform and Partial Least Squares Regression: Differentiating Endogenous Hydrogen Peroxide Fluctuations from Shifts in Ph. *Anal. Chem.* **2018,** *90*, 1767–1776.

(71) Patterson, M. J.; Galloway, S. D.; Nimmo, M. A. Variations in Regional Sweat Composition in Normal Human Males. *Exp. Physiol.* **2000,** *85*, 869–875.

(72) Burry, J. S.; Coulson, H. F.; Esser, I.; Marti, V.; Melling, S. J.; Rawlings, A. V.; Roberts, G.; Mills, A. K. Erroneous Gender Differences in Axillary Skin Surface/Sweat Ph. *Int. J. Cosmet. Sci.* **2001,** *23*, 99–107.

(73) Sonner, Z.; Wilder, E.; Heikenfeld, J.; Kasting, G.; Beyette, F.; Swaile, D.; Sherman, F.; Joyce, J.; Hagen, J.; Kelley-Loughnane, N.; Naik, R. The Microfluidics of the Eccrine Sweat Gland, Including Biomarker Partitioning, Transport, and Biosensing Implications. *Biomicrofluidics* **2015,** *9*, 031301.

(74) Lee, H.; Song, C.; Hong, Y. S.; Kim, M. S.; Cho, H. R.; Kang, T.; Shin, K.; Choi, S. H.; Hyeon, T.; Kim, D. H. Wearable/Disposable Sweat-Based Glucose Monitoring Device with Multistage Transdermal Drug Delivery Module. *Sci. Adv.* **2017,** *3*, e1601314.

(75) Idili, A.; Vallee-Belisle, A.; Ricci, F. Programmable Ph-Triggered DNA Nanoswitches. *J. Am. Chem. Soc.* **2014,** *136*, 5836–5839.

(76) Porchetta, A.; Idili, A.; Vallee-Belisle, A.; Ricci, F. General Strategy to Introduce Ph-Induced Allostery in DNA-Based Receptors to Achieve Controlled Release of Ligands. *Nano Lett.* **2015,** *15*, 4467–4471.

(77) Gordon, C. K. L.; Eisenstein, M.; Soh, H. T. Direct Selection Strategy for Isolating Aptamers with Ph-Sensitive Binding Activity. *ACS Sens.* **2018,** *3*, 2574–2580.

Chapter 8

Implantable Aptamer-Field-Effect Transistor Neuroprobes towards *in Vivo* Serotonin Monitoring

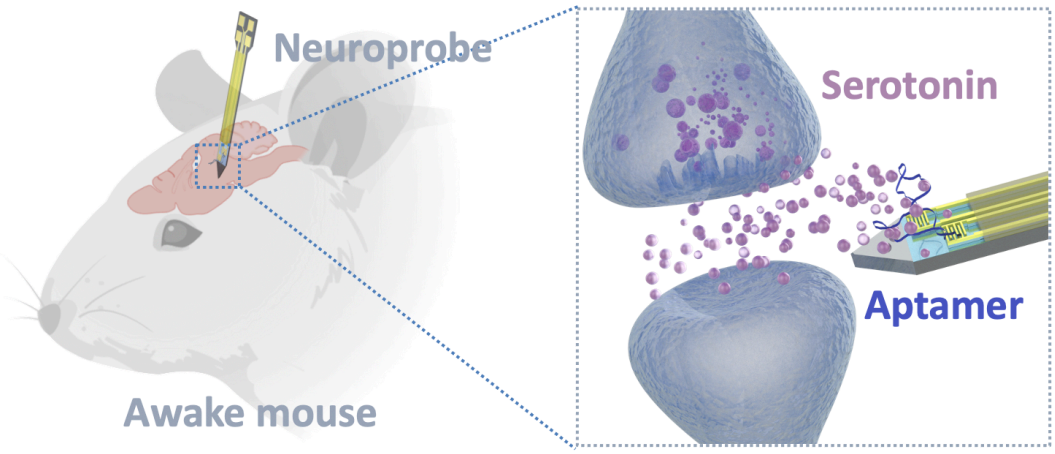

The information in this chapter is in preparation for submission and has been adapted here.

Authors: **Zhao, C.**; Huang, I. W.; Cheung, K. M.; Nakatsuka, N.; Yang, H.; Liu, W.; Cao, Y.; Man. T.; Weiss, P. S.; Monbouquette, H. G.; Andrews, A. M.

8.1 Abstract

In combination with electrophysiological signaling, chemical communication *via* neurotransmitters plays central roles in brain information processing. While tools for electrophysiological monitoring *in vivo* have been developed extensively, technologies for neurochemical recording are more limited. To address challenges associated with high resolution neurotransmitter monitoring, implantable aptamer field-effect transistor (FET) neuroprobes have been developed. Silicon-based implantable neuroprobes were fabricated using high-throughput micro-electro-mechanical-system technologies, where 150 probes with shanks of *ca.* 150 μm widths and thicknesses were fabricated on each 4-inch Si wafer. Nanoscale FETs with ultrathin In_2O_3 (~3 nm) semiconductor films were prepared using a scalable sol-gel process. The In_2O_3 surface was coupled with synthetic oligonucleotide receptors (*i.e.*, aptamers) that recognize neurotransmitters such as serotonin to achieve selective and sensitive detection of neurotransmission *in vivo*. Aptamer neuroprobes showed femtomolar serotonin detection limits in brain tissue homogenates without significant biofouling. *In vivo* measurements were conducted using head-fixed, awake, behaving mice. This study opens opportunities for neurochemical recordings with high spatiotemporal resolution to advance our understanding of brain activity.

8.2 Introduction

For example, understanding how information is encoded in brain function is at the heart of neuroscience. New discoveries in brain information processing have led to improvements in the treatment of neurological diseases, such as Parkinson's disease, Alzheimer's disease, and epilepsy.[1-3] Understanding neural function requires advanced technologies that approach the spatial and temporal resolution of neurotransmission. Implantable and genetically encoded neural recording strategies have emerged as powerful tools to monitor brain activity directly with high spatiotemporal resolution.[4,5] Efforts for implantable electrodes have focused on monitoring electrical signals, such as action potentials, which travel along axons and are one major form of information processing in the nervous system.[6] With recent innovations in micro- and nanofabrication, materials science, and electrical engineering, implantable neural devices have become more sophisticated with increased densities of electrodes of decreased sizes. In recent reports, up to 1,024 recording units have been integrated onto a single neuroprobe of <100 μm width.[7-13]

In addition to electrical signaling, chemical neurotransmission plays an equally important role in brain information processing.[14-17] However, far fewer tools are available for investigating neurochemical transmission directly by monitoring rapid changes in neurotransmitter concentration *in vivo*.[18] A well-established technique is *in vivo* microdialysis coupled with high performance liquid chromatography (HPLC), which can monitor neurotransmission in near real-time by sampling molecules through a semi-permeable membrane (typically 200-300 μm diameter with 1-4 mm length) at the tip of an implanted microdialysis probe.[19-23] Recent advances in fast microdialysis have shown improved sampling with the employment of capillary electrophoresis, microfluidic chips, and miniaturized devices.[19] Others and we have developed

fast microdialysis and achieved ~1 min sampling resolution for real-time monitoring of serotonin and dopamine *in vivo*.[20,22,24] However, the temporal resolution of this technique is limited by multiple factors, especially to meet the required sensitivity of the HPLC component (>10 pM in dialysate samples).

Fast-scan cyclic voltammetry (FSCV) is another *in vivo* real-time neurotransmitter monitoring method with relatively high temporal (subsecond) and spatial (2-5 μm) resolution using implantable carbon-fiber microelectrodes (CFMs).[13,25-31] However, FSCV has low selectivity for neurochemicals with similar oxidation/reduction potentials. In addition, many neurotransmitters, such as gamma-aminobutyric acid, are not electrochemically active.[32-35] Enzyme-based biosensors have also been developed for *in vivo* neurotransmitter monitoring, which has enabled the detection of electrochemically inactive targets, such as glutamate.[36-39] However, this approach is limited to targets that have suitable redox enzymes (*e.g.*, glutamate oxidase for glutamate sensors). Some important neurotransmitters, such as gamma-aminobutyric acid, are neither electrochemically active nor do they have a suitable redox enzyme.[18,40]

Therefore, it is of importance to develop sensing platforms that do not rely on the electrochemical properties of neurotransmitters or their enzymes. To measure and to understand complex neurochemical fluxes in the brain, recording devices must be able to monitor neurotransmitters with high selectivity and sensitivity in the appropriate physiological ranges, and with the potential to measure and to discriminate multiple neurotransmitters concurrently.

Recently, we developed aptamer field-effect transistor (FET) biosensors for small-molecule detection under high-ionic strength conditions.[41-45] We used nanoscale In_2O_3 semiconducting films (~3 nm thick) as an ultrasensitive platform for biosensing. Aptamers

previously selected for specific target binding were coupled onto the semiconductor surface of FETs.[44] Conformational changes of the charged aptamer backbones occurred upon target capture, and the subsequent surface charge redistribution was detected by FET sensors.[44] This sensing mechanism was independent of the charge or electrochemical properties of the analytes, and thus presents a promising approach for universal neurotransmitter and signaling molecule monitoring.

We demonstrated detection of a variety of biomarkers in complex physiological environments using aptamer-FETs, including serotonin, glucose, and phenylalanine.[41-44] Due to the high selectivity of our aptamers, aptamer-FET biosensors showed high selectivity against structurally similar molecules. We have also reported the real-time and simultaneous detection of serotonin and dopamine using aptamer-FET biosensors, which lays the foundation for the multiplexed monitoring of neurotransmitters in the brain.[41]

Here, we report on the design, fabrication, and testing of implantable aptamer-FET neuroprobes to monitor the small molecule neurotransmitter serotonin. We validated device functionality *in vitro*, *ex vivo*, and *in vivo* in awake, behaving mice (scheme shown in **Figure 8.1**). We designed Si-based neuroprobes with In_2O_3 FETs on the shank tips (**Figure 8.1B**). Serotonin aptamers were functionalized onto the In_2O_3 surfaces of the FETs to detect serotonin in the extracellular space *in vivo*. The shanks were coated with a parylene insulation layer (**Figure 8.1C**)

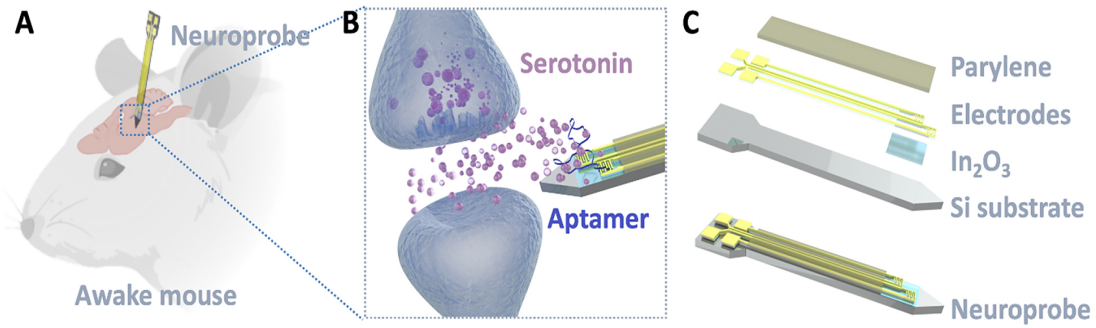

Figure 8.1. Schematic illustration of implantable aptamer biosensor neuroprobe design and application. (A) Illustration showing a neurochemical probe implanted in the brain of a mouse for neurotransmitter monitoring. (B) Illustration showing released serotonin in the extracellular space monitored by an aptamer-based neuroprobe. (C) An exploded view of the layer-by-layer design of a neuroprobe. Top to bottom: parylene, Au electrodes, In_2O_3, and the Si substrate.

8.3 Materials and Methods

Materials. Prime quality 4" Si wafers (P/B, 0.001-0.005 Ω cm, thickness 150 μm) were purchased from Silicon Valley Microelectronics, Inc. (Santa Clara, CA, USA). All chemicals were purchased from Sigma-Aldrich Co. (St. Louis, MO), unless otherwise noted below. Oligonucleotides were obtained from Integrated DNA Technologies (Coralville, IA). The SYLGARD 184 for fabricating polydimethylsiloxane (PDMS) wells was from Dow Corning Corporation (Midland, MI). Water was deionized before use (18.2 MΩ) *via* a Milli-Q system (Millipore, Billerica, MA).

Fabrication of neuroprobes: Aqueous solutions of 0.1 M indium(III) nitrate hydrate (99.999%) were spin-coated onto the 4" Si substrates at 3000 rpm for 30 s. The wafers were

annealed at 100 ℃ for 10 min and then 350 ℃ for 4 h to form the In_2O_3 film. A photolithography process was then applied to define the source and drain electrodes. Electrodes of 10 nm Ti and 30 nm Au films were deposited using CHA solution electron-beam evaporator (CHA Industries, Inc., Fremont, CA) under high vacuum (10^{-8} Torr) at an evaporation rate of 0.1 nm/s. A thin layer of parylene (~1 μm) was coated on the surface using a SCS Parylene C coating system (Specialty Coating System Inc., Indianapolis, IN), and then defined by photolithography and etched by oxygen plasma. Another photolithographic treatment was performed to define the outline of the probes. Deep reactive ion etching with the Bosch process was used to etch through the silicon substrate (~150 μm) using a Deep Silicon Etcher III (Plasma-Therm, Fremont, CA).

Surface modification of neuroprobes: Released probes were rinsed in ethanol and dried with N_2 to clean the surface. After thorough cleaning, (3-aminopropyl)triethoxysilane (APTES) and trimethoxy(propyl)silane (PTMS) (1:9, v/v) were thermally deposited on the In_2O_3 surface at 40 ℃ for 1 h, and then annealed at 80 ℃ for 10 min. The probes were immersed in a 1 mM solution of 3-maleimidobenzoic acid *N*-hydroxysuccinimide ester dissolved in a 1:9 (v/v) mixture of dimethyl sulfoxide and phosphate-buffered saline (PBS, Gibco, Fisher Scientific, Waltham, MA) for 30 min. To immobilize aptamers, each substrate was immersed in a 1 μM solution of thiolated DNA in 1× PBS overnight. Probes were again rinsed with deionized water and dried with N_2 before measurements.

***In vitro and ex vivo* experiments:** A mixture of 10-15% gelatin (Lot #H219, Mallinckrodt, St. Louis, MO) in artificial cerebrospinal fluid (aCSF)[22] was prepared first. The mixture was microwaved for ~1 min until the gelatin was dissolved completely. The clear

solution was cast in a 48-well plate (Lot #CLS3548, Sigma-Aldrich Co., St. Louis, MO) where each well is roughly the size of a mouse brain (~1 cm in diameter). A mold for holes was templated into the gelatin (*e.g.*, 0.125" diameter metal wiring, Lot#7667A12， McMaster-Carr Supply Co., Atlanta, GA) for the addition of neurotransmitter solutions to simulate neurotransmitter release in the brain. The gelatin solution was kept at 4 ℃ for ~12 h. Afterwards, the metal mold was taken out carefully by hand using tweezers. Neuroprobe and Ag/AgCl reference electrodes were implanted by hand using tweezers before measurements.

Polydimethylsiloxane (PDMS) wells were sealed on top of individual probes to hold physiological buffers and targets. Phosphate-buffered saline and aCSF were used for *in vitro* and *ex vivo* experiments. For *ex vivo* experiments, brain tissue lacking serotonin was obtained from *Tph2* knockout mice. The brains were shipped to UCLA on dry ice from the laboratory of Dr. Donald Kuhn (Wayne State University, Detroit, MI). Brain tissue was stored at -80 ℃, until use. Brain tissue collection procedures were approved by the Wayne State University Institutional Animal Care and Use Committee.

Tissues were homogenized in 1× aCSF (1:1 volume ratio) on ice using a VirTis Virsonic600 ultrasonic cell disruptor (Gardiner, NY) with the microtip set at 4 with 50% duty for 30-40 1-sec pulses. Commercially available Ag/AgCl reference electrodes (Super Dri-Ref, World Precision Instruments, Inc., Sarasota, FL) were placed in the tissue homogenates above the FETs. All FET measurements were performed using a Keithley 4200A (Tektronix, Beaverton, OR) semiconductor analyzer. Source-drain current (I_{DS}) transfer curves were obtained by sweeping the gate voltage (V_{GS}) from 0 to 400 mV while maintaining the drain

voltage (V_{DS}) at 10 mV. Calibrated responses were calculated at 300 mV to minimize device-to-device variation as previously reported.[44]

***In vivo* experiments:** The Association for Assessment and Accreditation of Laboratory Animal Care International has fully accredited UCLA. All animal care and use met the requirements of the NIH Guide for the Care and Use of Laboratory Animals, revised 2011. The UCLA Chancellor's Animal Research Committee (Institutional Animal Care and Use Committee) preapproved all procedures. Food and water were available *ad libitum* throughout the experiment, with the exception of testing days. Surgeries were carried out under aseptic conditions with isoflurane anesthesia on a KOPF Model 1900 Stereotaxic Alignment System (KOPF, Tujunga, CA).

Beginning the day of each surgery, 5 mg/kg Caprofen was injected (subcutaneously) daily for 3 days and 1 mg/mL ibuprofen (analgesics) and 0.5 mg/mL amoxicillin (antibiotic) were administered in drinking water for 14 days. The light−dark cycle was set to 12/12; all testing was carried out during the light phase. The light was set on at 0600 h (ZT0). Mice were generated at the University of California, Los Angeles (UCLA) from a SERT-deficient lineage on a mixed CD1 × 129S6/SvEv background *via* SERT heterozygous (SERT+/-) pairings. Female SERT-knockout (SERT-/-) mice were studied at 4-6 months of age. Mice were housed in groups of 4 to 5 same-sex siblings per cage until head-bar implantation surgery, after which mice were individually housed. Animals first underwent a surgical procedure to receive head-bar implantation. In brief, a pair of rectangular head-bars (9 mm × 7 mm × 0.76 mm, 0.6 g each, laser cut from stainless steel at Fab2Order) for head fixation were attached on each side of the

skull by C&B-METABOND (Parkell, Edgewood, NY).[7] After surgery, animals were single housed and allowed to recover for 1-3 weeks.

The subjects were trained to acclimate to the head-fixed stage for 15-30 min/session × 1-2 session/day for a total 6-10 sessions. Then, a second surgery to make three craniotomies was carried out 24-48 h ahead of the *in vivo* recording. A 2.5 mm width (ML) × 1.0 mm length (AP) piece of skull was surgically removed over the brain stem serotonin cell body region (centered at AP -4.48 mm, ML ±0.00 mm from Bregma) for the insertion of a stimulation electrode. A 1.5 mm width × 1.5 mm length craniotomy aimed at the right striatum area (centered at AP +0.80 mm, ML +0.80 mm from Bregma) was carried out for the insertion of the aptamer-FET neuroprobe. An additional 0.4 mm diameter hole (centered at AP +2.80 mm, ML -2.00 mm from Bregma) was made on the left side of the skull for Ag/AgCl gate electrode implantation.

The dura remained intact for all the surgery areas. All craniotomy areas were then sealed with a thin layer of Kwik-Cast & Kwik-Sil (World Precision Instruments, Sarasota, FL) and the whole surgery area was secured with a top thin layer of C&B-METABOND. Animals were allowed to recover from the surgery for 24-48 h before entering *in vivo* testing. On the testing day, mice were transferred from their home cages and mounted to the head-fixed stage *via* their head-bars. Each subject was supported on a Styrofoam ball that served as treadmill for the subject to engage freely in locomotor behavior.

After a 10-min brief habituation period, the top layer of C&B-METABOND was removed carefully. Then, the thin layer of Kwik-Cast & Kwik-Sil seal and the dura above the brain in the craniotomy areas were also carefully removed using a ceramic coated Dumont #5 forceps (Roboz Surgical Instrument Co., Gaithersburg, MD). A Ag/AgCl reference electrode was

constructed of a 0.010” diameter Ag wire freshly coated with AgCl (A-M Systems, Sequim, WA) by immersing into bleach solution for 15 min and manually lowered into the designated craniotomy site at 1.5-2 mm in depth. An untwisted 2-channel tungsten stimulation electrode (PlasticsOne, Roanoke, VA) was lowered 3.5 mm from skull level aimed at the raphe serotonin cell body region using a 10-μm-presision manual micromanipulator (Narishige International, Amityville, NY). The stimulation electrode tips were 2.0 mm apart.

After another 10-min brief habituation period, a train of electrical stimulation (biphasic pulses of 300 μA × 4 ms at 30 Hz for 5 s) was delivered, which evoked behavioral responses such as freezing, running, shaking, and significant change in breathing rate. If no behavioral responses were observed, the stimulation electrode was lowered an additional 50 μm per step. Another train of stimulation was delivered with an >5 min interval. This process of locating the stimulating electrode continued until strong stimulation-induced behavioral responses were observed. After positioning, the stimulation electrode (DV -3.5 to -4.5 mm) remained constant throughout the experiment.

Finally, the aptamer-FET neuroprobe was lowered 1.0 mm from the brain surface to penetrate the striatum using a 1-μm precision motorized digital micromanipulator (MP-225, Sutter Instrument, Novato, CA). A biphasic, 300 μA, 4 ms, and 30 Hz waveform was applied for 5 s to evoke serotonin release. At each recording depth, 2-4 stimulation trains were delivered at 5-10 min intervals. Each biosensor was lowered 50-150μm per step for additional testing. Throughout the experiment, sterile saline was used to clean the exposed skull and brain areas and to keep them moist. Water and milk were delivered to the subject every 2-3 h by hand using a dropper. The overall health condition and behavioral responses to stimulation were closely

monitored throughout the experiment. At the end of the experiment, both electrodes and the biosensor were removed. The subject was prepared for histology verification of the positions of stimulation and recording paths/sites. No subject failed histology verification.

Statistics. Data for selectivity and sensing in gelatin were analyzed by one-way analysis of variance (GraphPad Prism 7.04, San Diego, CA).

8.4. Results and Discussions

A schematic illustration of the neuroprobe fabrication process is shown in **Figure 8.2A**. Micro-electro-mechanical-system (MEMS) technologies were used to produce neuroprobes in a high-throughput manner, where 150 probes were fabricated on each wafer. This fabrication process is compatible with conventional microfabrication processes, which is advantageous for translational neuroscience.

Briefly, thin films of In_2O_3 were formed *via* sol-gel chemistry by spin-coating an aqueous solution of indium(III) nitrate hydrate onto heavily doped 4-inch Si wafers (150-μm thick p^{++} Si with 100-nm thick SiO_2 on top) (step 1 in **Figure 8.2A**). The Au and Ti electrodes (30 nm and 10 nm thick, respectively) were then patterned on top of the In_2O_3 (step 2 in **Figure 8.2A**). To provide an insulating layer for *in vivo* environments, a thin layer of parylene (~1 μm) was coated on the probe surfaces (step 3 in **Figure 8.2A**). Parylene is a biocompatible and biostable material with excellent dielectric properties that is widely used in implanted medical devices, such as cardiac assist devices and mandrel catheters.[46,47] The parylene layer at the tip of each probe shank were removed to expose the transistor area for sensing. Finally, outlines of individual

probes were defined using another photolithography step. Wafer were then etched through to release individual probes (step 4 in **Figure 8.2A**). The fabrication process is described in greater detail in **6.3 Materials and Methods**.

A 4" wafer with 150 probes is shown before the probe release step in **Figure 8.2B** (step 4 in **Figure 8.2A**). The entire wafer was semi-transparent after the etching process, where the outline of each probe was defined. A released single probe is shown in **Figure 8.2C**. The neuroprobe shanks were characterized using scanning electron microscopy (SEM), as shown in **Figure 8.2D**. Pseudo colors were assigned to different components of the probe, where parylene (dark yellow) shows the insulating layer. The Au and Ti source and drain electrodes (yellow) were constructed in an interdigitated design. The In_2O_3 (light blue) was coated onto a150-μm thick Si wafer (grey).

Solid state measurements were first conducted to test FET performance in a bottom-gate top-contact structure (**Figure 8.2E**). Representative transfer and output characteristics are shown in **Figure 8.2F** and **8.2G**, respectively. The FET neuroprobes showed high current on/off ratios (I_{on}/I_{off}) of ~10^8, comparable to our devices with centimeter dimensions.[44]

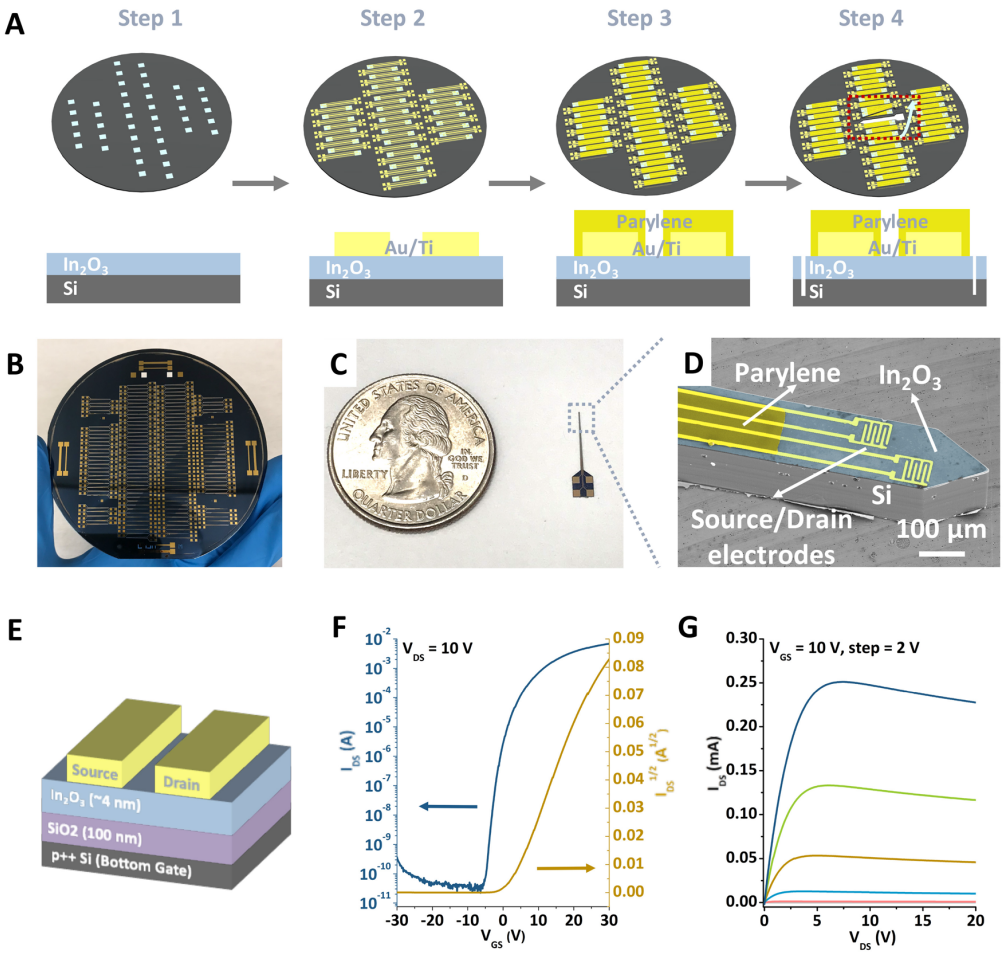

Figure 8.2. Neuroprobe fabrication and device characterization. (A) A schematic illustration showing the neuroprobe fabrication process. (B) A photograph of a 4" Si wafer with 150 neuroprobes after deep reactive-ion etching. (C) A photograph showing a released neuroprobe next to a quarter dollar coin to illustrate size. (D) Scanning electron microscope image of the shank and tip of a neuroprobe with false colors showing parylene, Au electrodes, In_2O_3, and the Si substrate. (E) A schematic illustration of the solid-state measurement setup. (F,G) Representative transfer and output characteristics, respectively.

For biosensing experiments, FET-based neuroprobes were operated in electrolyte solutions through liquid gating. On the shank of each neuroprobe, two devices were fabricated side by side and were gated by a Ag/AgCl reference electrode (**Figure 8.3A**). A schematic of the liquid-gated transistor operation set-up is shown in **Figure 8.3B**. Here, the electrical double layers formed in the electrolyte solution serve as the gate dielectric. Representative transfer and output characteristics are shown in **Figure 8.3C** and **8.3D**, respectively. As shown in **Figure 8.3C**, the transfer curves of two different devices overlapped with minimal contribution from gate leakage currents.

To construct aptamer biosensors, thiol-terminated DNA aptamers were immobilized onto In_2O_3 surfaces using APTES and 3-maleimidobenzoic acid *N*-hydroxysuccinimide ester as a linker (**Figure 8.3E**).[44] *In vitro* serotonin detection was performed in aCSF, which is a buffer solution that mimics the ionic strength and composition of the brain extracellular space.[44] Aptamer-FET neuroprobes detected serotonin over a large concentration range (fM to nM, **Figure 8.3F**). Neuroprobes were selective against similarly structured serotonin precursors and metabolites, along with other monoamine neurotransmitters and molecules that co-exist in extracellular fluid, such as L-5-hydroxytryptophan, 5-hydroxyindoleacetic acid, dopamine, norepinephrine, uric acid, and ascorbic acid (**Figure 8.3G,** see **Table S8.1** for full statistics). These molecules are present at recording sites at 1000× greater concentrations than that of serotonin and thus, are potential interferents during sensing.[30,31,44] It is important to note that the selectivity of aptamer-FET neuroprobes is intrinsic to the aptamers themselves, while for other platforms such as FSCV or enzyme-based *in vivo* neural probes, target-specific signals may be convoluted with nonspecific signals from oxidation peaks of other electroactive species present

or the generation of H_2O_2 respectively, which is challenging for simultaneous multiplexed neurotransmitter detection.

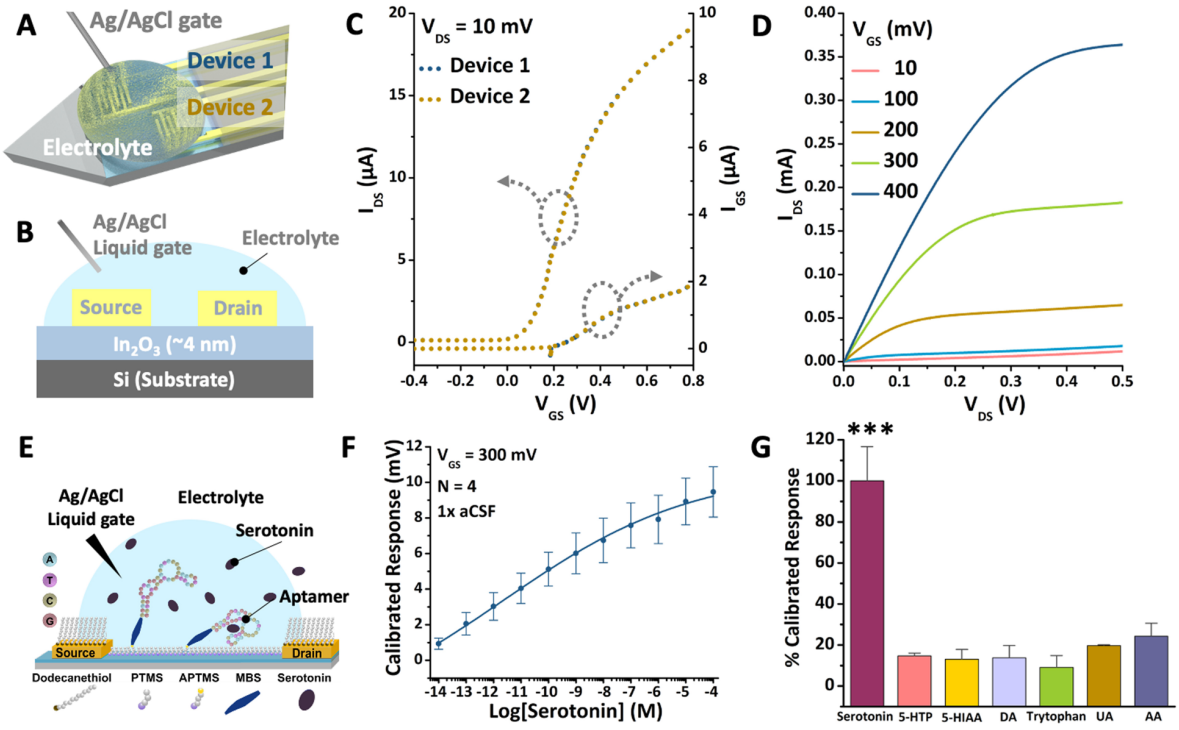

Figure 8.3. (A,B) Schematic illustrations of the liquid-gate measurement setup. (C) Representative transfer characteristics (I_{DS}-V_{GS}) and leakage current (I_{GS}-V_{GS}) of two transistors on a single probe in phosphate-buffered saline. (D) Representative transfer characteristics (I_{DS}-V_{DS}) at different gate voltages showing typical transistor behavior with saturation. (E) Schematic illustration showing the surface functionalization strategy for In_2O_3 transistor channels. (F) Serotonin aptamer-field-effect transistor (FET) response curve in 1× artificial cerebrospinal fluid (aCSF). Error bars are standard errors of the means with *N*=4 individual FETs. (G) Serotonin aptamer-functionalized neuroprobe responses to 100 μM dopamine, L-5-hydroxytryptophan (L-5-HTP), 5-hydroxyindoleacetic

acid (5-HIAA), dopamine, L-tryptophan, 200 µM ascorbic acid, and 50 µM uric acid were negligible relative to serotonin (100 nM). Error bars are standard errors of the means for *N*=4 individual FETs for serotonin and *N*=3 individual FETs for the other molecules. ******P*<0.005 *vs.* nontargets.

To evaluate the *in vivo* capability of the neuroprobes further, additional sensing experiments were performed in the presence of an electrical stimulator. Electrical stimulation is a well established and widely applied *in vivo* approach to induce neurotransmitter release in the central nervous system (CNS).[43] However, as the detection mechanism of FET-based biosensors relies on charge redistribution near the semiconductor surface, external electrical stimulation could potentially convolute FET signals associated with target capture. To test for electrical interference, neuroprobes were placed in PBS with stimulating electrodes, as shown in **Figures S8.1A**,**B**. Representative I_{DS}-V_{GS} sweeps were collected before and after electrical stimulation (biphasic pulses of 300 µA 4 ms at 30 Hz for 5 s, **Figure S8.1C)**. The FET measurement after stimulation showed negligible differences when compared to the measurement before the stimulation, suggesting negligible influence of the electronic stimulation upon signals measured from the FET neuroprobes.

Furthermore, brain tissue is a complicated biological matrix. Applying potentials to the source, drain, and gate electrodes required for the operation of FETs while in the brain could be challenging. Moreover, neurotransmitters are expected to diffuse from releasing axons to probe surfaces over at least couple hundred micrometers through brain tissue. Therefore, it is important to test the function of neuroprobes in solid matrices that mimic brain tissue. A brain tissue mimic based on 10-15% gelatin in aCSF was designed to represent the Young's modulus and

stiffness,[48] along with the physiological ionic environment of the brain. The gelatin was cast in the wells of a 48-well plate to mimic the size of a mouse brain (~1 cm in diameter). As shown in **Figure S8.2**, a hole was templated into the gelatin for the addition of neurotransmitter solutions to simulate neurotransmitter release and diffusion in the brain (**Figure 8.4A**).

To test the function of the neuroprobes in a solid gelatin matrix, a 1 mL 1 μM serotonin solution was introduced into the 10 mL gelatin (**Figure 8.4A**). This concentration was chosen to represent a physiologically relevant serotonin concentration in the brain.[20,22] Data were collected immediately after, and 3 and 12 min after serotonin addition (**Figure 8.4B**). There was a significant increase in the FET response 12 min after serotonin addition (see **Table S8.1** for full statistics), demonstrating the capability of the neuroprobes to function in the solid gelatin matrix. We have previously reported response times of our aptamer-FET sensors on the order of seconds,[44] and the 12 min response time is likely based on the target diffusion time across the gelatin/aCSF matrix from the addition location to the device surface (~0.25 cm).

We tested neuroprobes in *ex vivo* brain tissue homogenates to assess their capability to operate in a complex biological matrix. Brain tissue from *Tph2* null mice lacking serotonin in the CNS[49] was homogenized in aCSF to test neuroprobe performance *ex vivo* (**Figure 8.4C**). As shown in **Figure 8.4D**, serotonin aptamer neuroprobes retained detection limits down to fM serotonin concentrations with minimal biofouling during the measurement periods. The concentration of extracellular serotonin has been determined to be in the nM range (highlighted in yellow in **Figure 8.4D**).[20,22] The detection range of the aptamer neuroprobes in brain tissue covered this estimated extracellular serotonin concentration range (**Figure 8.4D**). Thus, the

sensitivity and selectivity of the aptamer neuroprobes in addition to the results from the gelatin and brain tissue homogenate experiments demonstrated the potential for further *in vivo* studies.

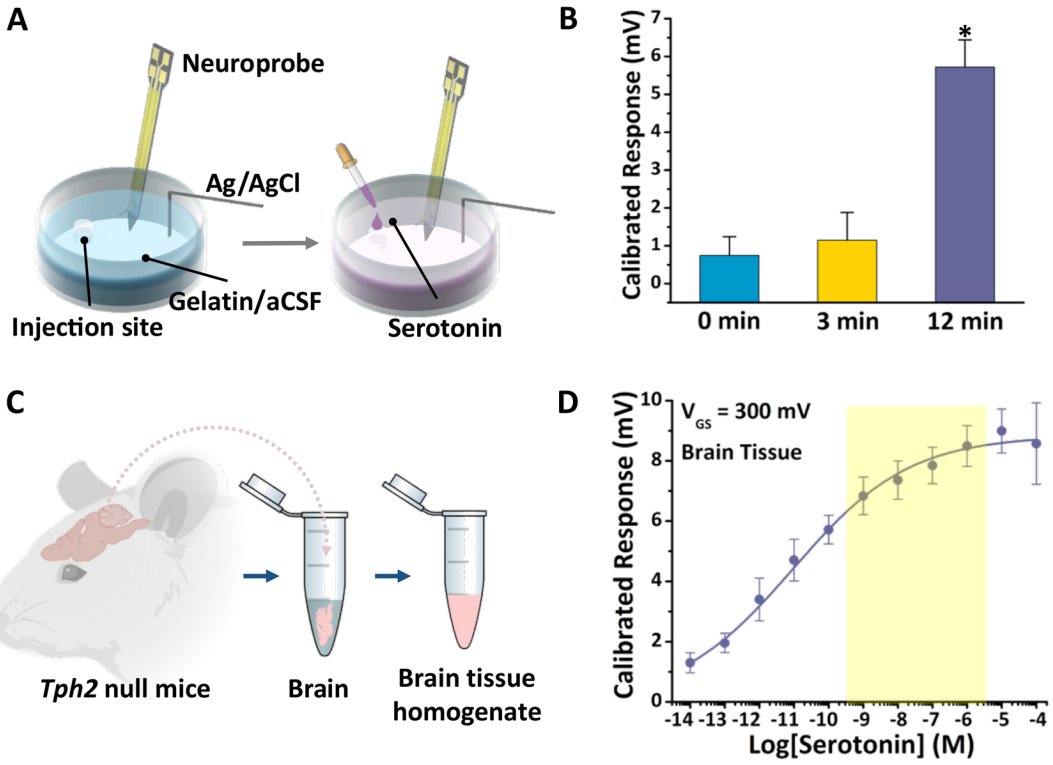

Figure 8.4. (A) Schematic illustrations showing *in vitro* experiments in a brain-mimicking solid matrix composed of gelatin with artificial cerebrospinal fluid. (B) Calibrated responses after addition of 100 nM serotonin over time. Error bars are standard errors of the mean with *N*=2 individual probes, **P*<0.05 versus responses in the first three min. (C) Schematic illustration of the preparation of brain tissue homogenates. Brains from *Tph2* null mice were removed and homogenized with artificial cerebrospinal fluid. (D) Serotonin aptamer-field-effect transistor response curve in brain tissue homogenates. Highlighted yellow ranges are physiological ranges. Error bars are standard errors of the means with *N*=3 individual FETs.

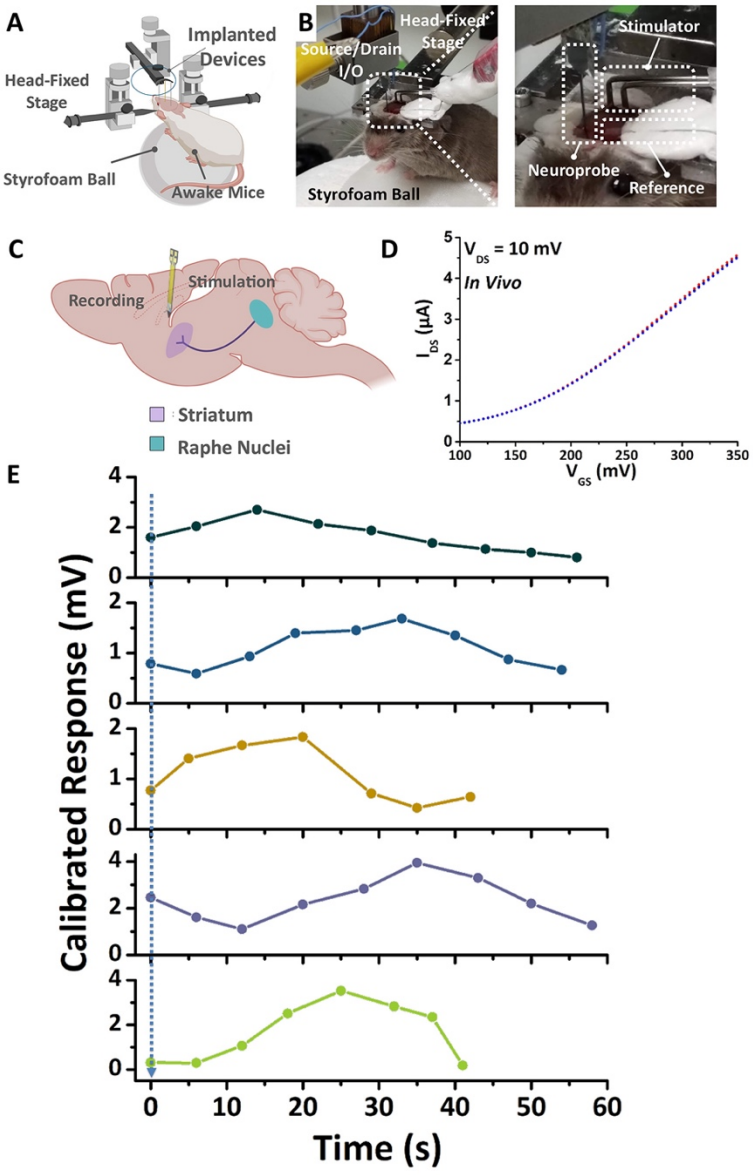

Figure 8.5. ***In vivo*** **serotonin monitoring using aptamer field-effect transistor neuroprobes. (A) Schematic illustration and (B) photographs of an** ***in vivo*** **experiment, where the neuroprobe, Ag/AgCl reference electrode, and stimulator were implanted into the brain of a mouse on a head-fixed stage. (C) Schematic illustration of stimulation and recording sites. The stimulating electrode was implanted into the serotonin cell body raphe region and the**

neuroprobe was implanted into the striatum. (D) Three consecutive overlapping output characteristic sweeps (I_{DS}-V_{GS}) *in vivo*, where V_{GS} was swept from 100 to 350 mV, while V_{DS} was set at constant 10 mV. (E) Five *in vivo* serotonin response curves collected after electrical stimulation (biphasic, 300 µA, 4 ms, and 30 Hz for 5 s) over a period of *ca.* 60 s from the same awake mouse. Dot line indicated the end of electrical stimulation.

An *in vivo* experiment was conducted for proof-of-concept in a female SERT deficient mouse. Mice can be fully acclimated to being head-fixed and trained to perform behavioral tasks. A schematic of the experiment for the *in vivo* measurements is shown in **Figure 8.5A**. Photographs of the actual experiment are shown in **Figure 8.5B**, where a neuroprobe, Ag/AgCl reference electrode, and electrical stimulation electrode are shown implanted into the brain of an awake and behaving mouse. The stimulation electrode was implanted into the raphe nuclei just above the serotonin neuron cell bodies. The neuroprobe was implanted into the striatum where serotonin axons are known to project. Electrical stimulation of the raphe nuclei result in the release of serotonin in the striatum (**Figure 8.5C**), which is known to be one of the serotonin pathways in the brain.[50,51] Detailed information of the implantation surgery is included in the **8.3 Materials and Methods** section.

After implantation, we first tested device functionality by collecting transfer (I_{DS}-V_{GS}) curves of the FETs. As shown in **Figure 8.5D**, the transfer curves showed typical FET characteristics. Three overlapping transfer curves were collected immediately before electrical stimulation, showing that the biosensors were relatively stable while implanted in the brain without observable drift. For *in vivo* serotonin measurements, electrical stimulation (biphasic, 300 µA, 4 ms, and 30 Hz for 5 s) was applied and serotonin release was measured *via* the

aptamer neuroprobe immediately after the electrical stimulation. Five representative responses over time after five stimulations from the same mouse are shown in **Figure 8.5E.** Increases in response after electrical stimulation were observed, suggesting that the neuroprobe having FETs functionalized with a serotonin-specific aptamer detect the release of serotonin after stimulation (**Figure 8.5E)**. Through this acute *in vivo* experiment, we demonstrated that the aptamer neuroprobes were functional *in vivo,* with the ability to monitor serotonin in the extracellular space in real time.

8.5 Conclusions and Prospects

We have developed an implantable aptamer-FET neuroprobe towards *in vivo* neurotransmitter detection. Ultrathin In_2O_3 (~3 nm) with a high surface-to-volume ratio was prepared using a sol-gel process and employed as the channel material in FETs. High-throughput MEMS technologies were used to fabricate 150 neuroprobes per 4-inch Si wafer, where each probe was *ca.* 150 μm wide and thick at the shank. Aptamers were coupled on In_2O_3 surfaces to achieve selective detection of serotonin with detection in the nanomolar to femtomolar range in physiological environments (*i.e.*, aCSF and brain tissue homogenates). We showed that neuroprobes were stable under electrical stimulation conditions and *in vitro* in gelatin/aCSF, a material that mimics the solid matrix and physiological environment of the brain. *In vivo* measurements were conducted using a head-fixed awake mouse. An implanted aptamer FET neuroprobe was able to monitor stimulated serotonin efflux *in vivo*.

The neuroprobes described here represent a generic strategy to monitor neurochemicals in the brain. Previously, we showed that in addition to serotonin, aptamer FET biosensors can be used to detect dopamine, glucose, and phenylalanine, with more aptamers under development.[41-

[44] As we continue to identify and characterize additional neurotransmitter aptamers, we envision that our approach will enable monitoring of multiple neurotransmitters in the brain with high sensitivity and selectivity, regardless of their electrochemical properties. Moreover, aptamer biosensors can be multiplexed in a straightforward manner due to the high selectivity of our aptamers. We previously developed multiplexed sensor arrays to monitor serotonin, dopamine, pH, and temperature simultaneously in real time.[41] The capability to monitor multiple neurotransmitters will provide new insights into the interplay between signaling pathways in the brain.[52] Advances in this direction can provide knowledge about fundamental brain function, the etiologies of neurological and neuropsychiatric disorders, and can accelerate the deployment of new medical inventions for translation into neuroscience and medicine.

Nonetheless, challenges remain with this technology that require further investigation. For example, while we have previously achieved temporal resolution on the order of seconds using aptamer-FET sensors,[41,44] subsecond temporal resolution will further improve understanding of the dynamic flux of neurochemical transmission and the information encoded therein. This advance requires additional investigation and development of both sensors and instrumentation. For multiplexed neurotransmitter detection, it will be necessary to functionalize the shank with two or more different aptamers. Although we have demonstrated multiplexing of two aptamers, it is challenging to functionalize microscale devices that are spatially close to one another. “Addressable” functionalization strategies using electroactive linkers have been shown,[53] and are under development for the specific functionalization of small devices (~10 μm apart). Moreover, while Si neuroprobes are generally applicable for acute measurements (hours), for chronic recording other challenges arise from immunological responses after longer implantation times. It has been shown that the Young’s modulus mismatch between implanted

devices and brain tissue causes immunological responses, which can interfere with biosensing.[54,55] Developing neuroprobes based on biocompatible and soft materials is an important ongoing direction. Nonetheless, we have developed and demonstrated an implantable aptamer-FET neuroprobe platform towards the real-time measurements of chemical neurotransmission *in vivo*.

8.6 Supplementary Materials

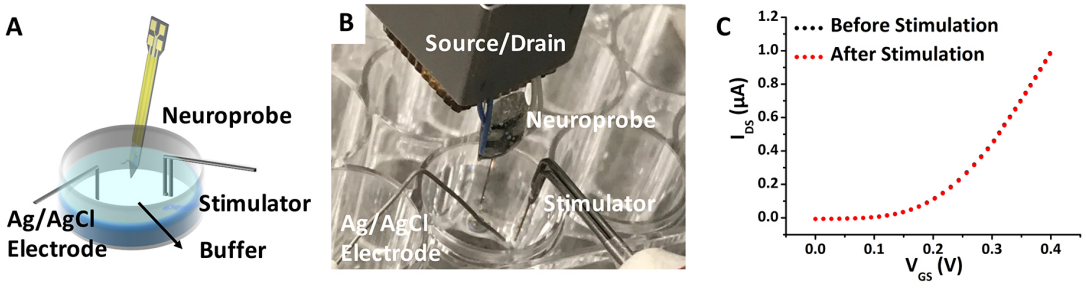

Figure S8.1. Electrical stimulation stability test. (A) Schematic (B) and photograph of the experimental setup, where neuroprobes were placed into phosphate-buffered saline with stimulating electrodes. (C) Representative I_{DS}-V_{GS} sweeps immediately before and after electrical stimulation (biphasic pulses of 300 µA, 4 ms at 30 Hz for 5 s), showing overlapping curves.

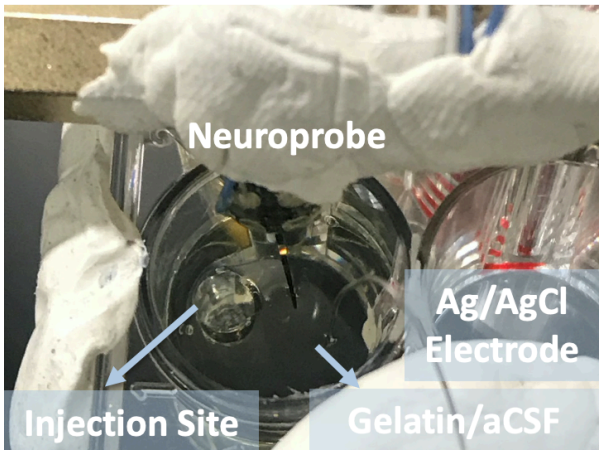

Figure S8.2. Gelatin brain mimic experiment. Photograph of the experimental setup where a 48-well plate was used to mimic the size of a mouse brain (~1 cm in diameter). A hole was

templated for the addition of the neurotransmitter during the experimenbt, simulating neurotransmitter release upon electrical stimulation.

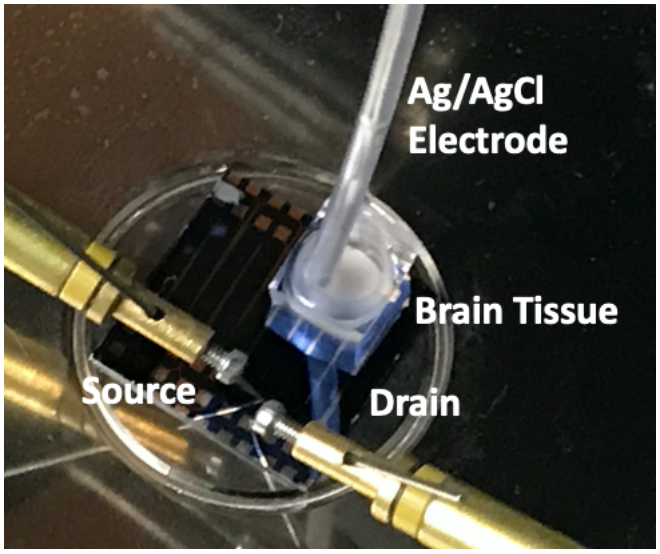

Figure S8.3. Photograph of the *ex vivo* setup. Brain tissue homogenates were added to a polydimethylsiloxane well with a Ag/AgCl electrode.

Table S8.1. Summary of statistics. Reponses from biosensors were analyzed by one-way analysis of variance (ANOVA).

Type	Figure	ANOVA	Multiple Comparisons
Selectivity	Fig. 3G	F (6,15) = 3.395 *P* < 0.0001	Serotonin *vs.* Uric acid, P = 0.0002 Serotonin *vs.* Others, P <0.0001
Gelatin	Fig. 4B	F (2,3) = 17.76 *P* = 0.0217	0 min *vs.* 3 min, Not signficant 0 min *vs.* 12 min, P = 0.0257 3 min *vs.* 12 min, P = 0.0323

8.7 References

(1) Rivnay, J.; Wang, H.; Fenno, L.; Deisseroth, K.; Malliaras, G. G. Next-Generation Probes, Particles, and Proteins for Neural Interfacing. *Sci. Adv.* **2017,** *3*, e1601649.

(2) Chen, R.; Canales, A.; Anikeeva, P. Neural Recording and Modulation Technologies. *Nat. Rev. Mater.* **2017,** *2*, 16093.

(3) Chapman, C. A. R.; Goshi, N.; Seker, E. Multifunctional Neural Interfaces for Closed-Loop Control of Neural Activity. *Adv. Funct. Mater.* **2018,** *28*, 1703523.

(4) Seymour, J. P.; Wu, F.; Wise, K. D.; Yoon, E. State-of-the-Art MEMS and Microsystem Tools for Brain Research. *Microsyst. Nanoeng.* **2017,** *3*, 16066.

(5) Won, S. M.; Song, E.; Zhao, J.; Li, J.; Rivnay, J.; Rogers, J. A. Recent Advances in Materials, Devices, and Systems for Neural Interfaces. *Adv. Mater.* **2018,** *30*, e1800534.

(6) Scanziani, M.; Hausser, M. Electrophysiology in the Age of Light. *Nature* **2009,** *461*, 930–939.

(7) Du, J.; Blanche, T. J.; Harrison, R. R.; Lester, H. A.; Masmanidis, S. C. Multiplexed, High Density Electrophysiology with Nanofabricated Neural Probes. *PLoS One* **2011,** *6*, e26204.

(8) Rios, G.; Lubenov, E. V.; Chi, D.; Roukes, M. L.; Siapas, A. G. Nanofabricated Neural Probes for Dense 3-D Recordings of Brain Activity. *Nano Lett.* **2016,** *16*, 6857–6862.

(9) Jun, J. J.; Steinmetz, N. A.; Siegle, J. H.; Denman, D. J.; Bauza, M.; Barbarits, B.; Lee, A. K.; Anastassiou, C. A.; Andrei, A.; Aydin, C.; Barbic, M.; Blanche, T. J.; Bonin, V.; Couto, J.; Dutta, B.; Gratiy, S. L.; Gutnisky, D. A.; Hausser, M.; Karsh, B.; Ledochowitsch, P.; et al.

Fully Integrated Silicon Probes for High-Density Recording of Neural Activity. *Nature* **2017,** *551*, 232–236.

(10) Driscoll, N.; Richardson, A. G.; Maleski, K.; Anasori, B.; Adewole, O.; Lelyukh, P.; Escobedo, L.; Cullen, D. K.; Lucas, T. H.; Gogotsi, Y.; Vitale, F. Two-Dimensional Ti_3C_2 Mxene for High-Resolution Neural Interfaces. *ACS Nano* **2018,** *12*, 10419–10429.

(11) Jiang, Y.; Li, X.; Liu, B.; Yi, J.; Fang, Y.; Shi, F.; Gao, X.; Sudzilovsky, E.; Parameswaran, R.; Koehler, K.; Nair, V.; Yue, J.; Guo, K.; Tsai, H.-M.; Freyermuth, G.; Wong, R. C. S.; Kao, C.-M.; Chen, C.-T.; Nicholls, A. W.; Wu, X.; et al. Rational Design of Silicon Structures for Optically Controlled Multiscale Biointerfaces. *Nat. Biomed. Eng.* **2018,** *2*, 508–521.

(12) Hong, G.; Fu, T. M.; Qiao, M.; Viveros, R. D.; Yang, X.; Zhou, T.; Lee, J. M.; Park, H. G.; Sanes, J. R.; Lieber, C. M. A Method for Single-Neuron Chronic Recording from the Retina in Awake Mice. *Science* **2018,** *360*, 1447–1451.

(13) Venton, B. J.; Cao, Q. Fundamentals of Fast-Scan Cyclic Voltammetry for Dopamine Detection. *Analyst* **2020,** *145*, 1158–1168.

(14) Andrews, A. M. The Brain Initiative: Toward a Chemical Connectome. *ACS Chem. Neurosci.* **2013,** *4*, 645.

(15) Alivisatos, A. P.; Chun, M.; Church, G. M.; Deisseroth, K.; Donoghue, J. P.; Greenspan, R. J.; McEuen, P. L.; Roukes, M. L.; Sejnowski, T. J.; Weiss, P. S.; Yuste, R. The Brain Activity Map. *Science* **2013,** *339*, 1284–1285.

(16) Alivisatos, A. P.; Andrews, A. M.; Boyden, E. S.; Chun, M.; Church, G. M.; Deisseroth, K.; Donoghue, J. P.; Fraser, S. E.; Lippincott-Schwartz, J.; Looger, L. L.; Masmanidis, S.; McEuen, P. L.; Nurmikko, A. V.; Park, H.; Peterka, D. S.; Reid, C.; Roukes, M. L.; Scherer, A.; Schnitzer, M.; Sejnowski, T. J.; et al. Nanotools for Neuroscience and Brain Activity Mapping. *ACS Nano* **2013,** *7*, 1850–1866.

(17) Andrews, A. M.; Schepartz, A.; Sweedler, J. V.; Weiss, P. S. Chemistry and the Brain Initiative. *J. Am. Chem. Soc.* **2014,** *136*, 1–2.

(18) Scida, K.; Plaxco, K. W.; Jamieson, B. G. High Frequency, Real-Time Neurochemical and Neuropharmacological Measurements *in Situ* in the Living Body. *Transl. Res.* **2019,** *213*, 50–66.

(19) Sandlin, Z. D.; Shou, M.; Shackman, J. G.; Kennedy, R. T. Microfluidic Electrophoresis Chip Coupled to Microdialysis for *in vivo* Monitoring of Amino Acid Neurotransmitters. *Anal. Chem.* **2005,** *77*, 7702–7708.

(20) Yang, H.; Thompson, A. B.; McIntosh, B. J.; Altieri, S. C.; Andrews, A. M. Physiologically Relevant Changes in Serotonin Resolved by Fast Microdialysis. *ACS Chem. Neurosci.* **2013,** *4*, 790–798.

(21) Jaquins-Gerstl, A.; Michael, A. C. A Review of the Effects of FSCV and Microdialysis Measurements on Dopamine Release in the Surrounding Tissue. *Analyst* **2015,** *140*, 3696–3708.

(22) Yang, H.; Sampson, M. M.; Senturk, D.; Andrews, A. M. Sex- and SERT-Mediated Differences in Stimulated Serotonin Revealed by Fast Microdialysis. *ACS Chem. Neurosci.* **2015,** *6*, 1487–1501.

(23) Altieri, S. C.; Yang, H.; O'Brien, H. J.; Redwine, H. M.; Senturk, D.; Hensler, J. G.; Andrews, A. M. Perinatal Vs Genetic Programming of Serotonin States Associated with Anxiety. *Neuropsychopharmacology* **2015,** *40*, 1456–1470.

(24) Ngo, K. T.; Varner, E. L.; Michael, A. C.; Weber, S. G. Monitoring Dopamine Responses to Potassium Ion and Nomifensine by *in Vivo* Microdialysis with Online Liquid Chromatography at One-Minute Resolution. *ACS Chem. Neurosci.* **2017,** *8*, 329–338.

(25) Heien, M. L.; Johnson, M. A.; Wightman, R. M. Resolving Neurotransmitters Detected by Fast-Scan Cyclic Voltammetry. *Anal. Chem.* **2004,** *76*, 5697–5704.

(26) Zachek, M. K.; Park, J.; Takmakov, P.; Wightman, R. M.; McCarty, G. S. Microfabricated FSCV-Compatible Microelectrode Array for Real-Time Monitoring of Heterogeneous Dopamine Release. *Analyst* **2010,** *135*, 1556–1563.

(27) Flagel, S. B.; Clark, J. J.; Robinson, T. E.; Mayo, L.; Czuj, A.; Willuhn, I.; Akers, C. A.; Clinton, S. M.; Phillips, P. E.; Akil, H. A Selective Role for Dopamine in Stimulus-Reward Learning. *Nature* **2011,** *469*, 53–57.

(28) Singh, Y. S.; Sawarynski, L. E.; Dabiri, P. D.; Choi, W. R.; Andrews, A. M. Head-to-Head Comparisons of Carbon Fiber Microelectrode Coatings for Sensitive and Selective Neurotransmitter Detection by Voltammetry. *Anal. Chem.* **2011,** *83*, 6658–6666.

(29) Park, C.; Oh, Y.; Shin, H.; Kim, J.; Kang, Y.; Sim, J.; Cho, H. U.; Lee, H. K.; Jung, S. J.; Blaha, C. D.; Bennet, K. E.; Heien, M. L.; Lee, K. H.; Kim, I. Y.; Jang, D. P. Fast Cyclic Square-Wave Voltammetry to Enhance Neurotransmitter Selectivity and Sensitivity. *Anal. Chem.* **2018,** *90*, 13348–13355.

(30) Shin, H.; Oh, Y.; Park, C.; Kang, Y.; Cho, H. U.; Blaha, C. D.; Bennet, K. E.; Heien, M. L.; Kim, I. Y.; Lee, K. H.; Jang, D. P. Sensitive and Selective Measurement of Serotonin in Vivo Using Fast Cyclic Square-Wave Voltammetry. *Anal. Chem.* **2020,** *92*, 774–781.

(31) Oh, Y.; Heien, M. L.; Park, C.; Kang, Y. M.; Kim, J.; Boschen, S. L.; Shin, H.; Cho, H. U.; Blaha, C. D.; Bennet, K. E.; Lee, H. K.; Jung, S. J.; Kim, I. Y.; Lee, K. H.; Jang, D. P. Tracking Tonic Dopamine Levels in vivo Using Multiple Cyclic Square Wave Voltammetry. *Biosens. Bioelectron.* **2018,** *121*, 174–182.

(32) Pyakurel, P.; Privman Champaloux, E.; Venton, B. J. Fast-Scan Cyclic Voltammetry (FSCV) Detection of Endogenous Octopamine in Drosophila Melanogaster Ventral Nerve Cord. *ACS Chem. Neurosci.* **2016,** *7*, 1112–1119.

(33) Borman, R. P.; Wang, Y.; Nguyen, M. D.; Ganesana, M.; Lee, S. T.; Venton, B. J. Automated Algorithm for Detection of Transient Adenosine Release. *ACS Chem. Neurosci.* **2017,** *8*, 386–393.

(34) Meunier, C. J.; Roberts, J. G.; McCarty, G. S.; Sombers, L. A. Background Signal as an in Situ Predictor of Dopamine Oxidation Potential: Improving Interpretation of Fast-Scan Cyclic Voltammetry Data. *ACS Chem. Neurosci.* **2017,** *8*, 411–419.

(35) Rodeberg, N. T.; Sandberg, S. G.; Johnson, J. A.; Phillips, P. E.; Wightman, R. M. Hitchhiker's Guide to Voltammetry: Acute and Chronic Electrodes for *in Vivo* Fast-Scan Cyclic Voltammetry. *ACS Chem. Neurosci.* **2017,** *8*, 221–234.

(36) Robinson, D. L.; Hermans, A.; Seipel, A. T.; Wightman, R. M. Monitoring Rapid Chemical Communication in the Brain. *Chem. Rev.* **2008,** *108*, 2554–2584.

(37) Wassum, K. M.; Tolosa, V. M.; Wang, J.; Walker, E.; Monbouquette, H. G.; Maidment, N. T. Silicon Wafer-Based Platinum Microelectrode Array Biosensor for C Real-Time Measurement of Glutamate *in Vivo*. *Sensors (Basel)* **2008,** *8*, 5023–5036.

(38) Malvaez, M.; Greenfield, V. Y.; Wang, A. S.; Yorita, A. M.; Feng, L.; Linker, K. E.; Monbouquette, H. G.; Wassum, K. M. Basolateral Amygdala Rapid Glutamate Release Encodes an Outcome-Specific Representation Vital for Reward-Predictive Cues to Selectively Invigorate Reward-Seeking Actions. *Sci. Rep*. **2015,** *5*, 12511.

(39) Wen, X.; Wang, B.; Huang, S.; Liu, T. L.; Lee, M.-S.; Chung, P.-S.; Chow, Y. T.; Huang, I. W.; Monbouquette, H. G.; Maidment, N. T.; Chiou, P.-Y. Flexible, Multifunctional Neural Probe with Liquid Metal Enabled, Ultra-Large Tunable Stiffness for Deep-Brain Chemical Sensing and Agent Delivery. *Biosens. Bioelectron*. **2019,** *131*, 37–45.

(40) Si, B.; Song, E. Recent Advances in the Detection of Neurotransmitters. *Chemosensors* **2018,** *6*, 1.

(41) Liu, Q.; Zhao, C.; Chen, M.; Liu, Y.; Zhao, Z.; Wu, F.; Li, Z.; Weiss, P. S.; Andrews, A. M.; Zhou, C. Flexible Multiplexed In_2O_3 Nanoribbon Aptamer-Field-Effect Transistors for Biosensing. *iScience* **2020,** *23*, 101469.

(42) Cheung, K. M.; Yang, K. A.; Nakatsuka, N.; Zhao, C.; Ye, M.; Jung, M. E.; Yang, H.; Weiss, P. S.; Stojanovic, M. N.; Andrews, A. M. Phenylalanine Monitoring *via* Aptamer-Field-Effect Transistor Sensors. *ACS Sens*. **2019,** *4*, 3308–3317.

(43) Kim, J.; Rim, Y. S.; Chen, H.; Cao, H. H.; Nakatsuka, N.; Hinton, H. L.; Zhao, C.; Andrews, A. M.; Yang, Y.; Weiss, P. S. Fabrication of High-Performance Ultrathin In_2O_3 Film

Field-Effect Transistors and Biosensors Using Chemical Lift-Off Lithography. *ACS Nano* **2015,** *9*, 4572–4582.

(44) Nakatsuka, N.; Yang, K. A.; Abendroth, J. M.; Cheung, K. M.; Xu, X.; Yang, H.; Zhao, C.; Zhu, B.; Rim, Y. S.; Yang, Y.; Weiss, P. S.; Stojanovic, M. N.; Andrews, A. M. Aptamer-Field-Effect Transistors Overcome Debye Length Limitations for Small-Molecule Sensing. *Science* **2018,** *362*, 319–324.

(45) Cheung, K. M.; Abendroth, J. M.; Nakatsuka, N.; Zhu, B.; Yang, Y.; Andrews, A. M.; Weiss, P. S. Detecting DNA and RNA and Differentiating Single-Nucleotide Variations *via* Field-Effect Transistors. *Nano Lett*. **2020,** *20*, 5982–5990.

(46) Kim, B. J.; Kuo, J. T.; Hara, S. A.; Lee, C. D.; Yu, L.; Gutierrez, C. A.; Hoang, T. Q.; Pikov, V.; Meng, E. 3D Parylene Sheath Neural Probe for Chronic Recordings. *J. Neural. Eng*. **2013,** *10*, 045002.

(47) Metallo, C.; White, R. D.; Trimmer, B. A. Flexible Parylene-Based Microelectrode Arrays for High Resolution Emg Recordings in Freely Moving Small Animals. *J. Neurosci. Methods* **2011,** *195*, 176–184.

(48) Kandadai, M. A.; Raymond, J. L.; Shaw, G. J. Comparison of Electrical Conductivities of Various Brain Phantom Gels: Developing a 'Brain Gel Model'. *Mater. Sci. Eng. C* **2012,** *32*, 2664–2667.

(49) Angoa-Perez, M.; Kane, M. J.; Briggs, D. I.; Herrera-Mundo, N.; Sykes, C. E.; Francescutti, D. M.; Kuhn, D. M. Mice Genetically Depleted of Brain Serotonin Do Not Display a Depression-Like Behavioral Phenotype. *ACS Chem. Neurosci*. **2014,** *5*, 908–919.

(50) Ferre, S.; Cortes, R.; Artigas, F. Dopaminergic Regulation of the Serotonergic Raphe-Striatal Pathway: Microdialysis Studies in Freely Moving Rats. *J. Neurosci*. **1994,** *14*, 4839–4846.

(51) Fibiger, H. C.; Miller, J. J. An Anatomical and Electrophysiological Investigation of the Serotonergic Projection from the Dorsal Raphe Nucleus to the *Substantia Nigra* in the Rat. *Neuroscience* **1977,** *2*, 975–987.

(52) Manciu, F. S.; Manciu, M.; Ciubuc, J. D.; Sundin, E. M.; Ochoa, K.; Eastman, M.; Durrer, W. G.; Guerrero, J.; Lopez, B.; Subedi, M.; Bennet, K. E. Simultaneous Detection of Dopamine and Serotonin-A Comparative Experimental and Theoretical Study of Neurotransmitter Interactions. *Biosensors* **2018,** *9*, 3.

(53) Curreli, M.; Li, C.; Sun, Y.; Lei, B.; Gundersen, M. A.; Thompson, M. E.; Zhou, C. Selective Functionalization of In_2O_3 Nanowire Mat Devices for Biosensing Applications. *J. Am. Chem. Soc*. **2005,** *127*, 6922–6923.

(54) Kozai, T. D.; Jaquins-Gerstl, A. S.; Vazquez, A. L.; Michael, A. C.; Cui, X. T. Brain Tissue Responses to Neural Implants Impact Signal Sensitivity and Intervention Strategies. *ACS Chem. Neurosci*. **2015,** *6*, 48–67.

(55) Du, Z. J.; Kolarcik, C. L.; Kozai, T. D. Y.; Luebben, S. D.; Sapp, S. A.; Zheng, X. S.; Nabity, J. A.; Cui, X. T. Ultrasoft Microwire Neural Electrodes Improve Chronic Tissue Integration. *Acta Biomater*. **2017,** *53*, 46–58.

Chapter 9

Research Highlights and Prospects

Part of the information in this chapter is in preparation for submission

and has been adapted here.

Authors: **Zhao, C.**; Huang, I. W.; Cheung, K. M.; Nakatsuka, N.; Yang, H.; Liu, W.; Cao, Y.; Man. T.; Weiss, P. S.; Monbouquette, H. G.; Andrews, A. M.

My graduate research focused on developing scalable and low-cost nanofabrication techniques and multiple sensing platforms towards next-generation, ultrasensitive, nanoscale sensors enabled by these advanced nanofabrication techniques.

We advanced chemical lift-off lithography (CLL), a cleanroom-free, high-throughput, high-fidelity soft-lithographic patterning technique, to fabricate multiple materials on a variety of surfaces with numerous applications in biomedicine.[1-7] To overcome the fundamental limitations of soft lithography, we investigated the mechanical deformation of elastomers. By exploiting the nanoscale deformation of polydimethylsiloxane (PDMS) stamps, we developed self-collapse lithography (SCL), where the nanoscale channels formed from the roof collapse of PDMS stamps were used to produce chemical patterns (**Figure 9.1a**).[7] We further expanded the deformation of polymeric stamps and developed polymer-pen chemical lift-off lithography (PPCLL) using controlled pyramidal and v-shaped polymer-pen arrays to enable large-scale nanoscale patterning with features as small as 50 nm (**Figure 9.1b**).[6] Beyond chemical patterning, the patterned molecular matrix can be used to pattern bioactive molecules with controlled densities, *e.g.*, DNA insertion and patterning.[3,5,8-12]

Previously, CLL has been used primarily to pattern alkanethiols on Au surfaces, including SCL and PPCLL.[6,7] Nonetheless, patterning on other metal and semiconductor surfaces had not yet been explored and was of potential interest for broad applications. We extended the capability of CLL to pattern molecules on different coinage metals (Pt, Pd, Ag, Cu), transition and reactive metals (Ni, Ti, Al), and semiconductor (Ge) surfaces (**Figure 9.1c**).[13]

After CLL, the molecules remaining in the non-contact areas can serve as chemical resists, which enables fabrication of nanostructures by selective wet-etching processes.[7,14-17] We

developed scalable fabrication processes to produce one- and two-dimensional Au micro- and nanostructures, such as Au nanoribbon, nanohole, and nanodisk arrays, using commercially available DVD disks as templates (**Figure 9.1d-h**).[14-17] We had demonstrated previously that CLL can be used to pattern source/drain electrodes for field-effect transistors (FETs).[7] Furthermore, fabricated Au micro- and nanostructures can be used as hard metallic masks for other microfabrication processes, *e.g.*, etching or deposition. We leveraged this approach to produce wafer-scale one-dimensional semiconductor nanoribbons, *e.g.*, In_2O_3 nanoribbons.[15,18]

Another exciting opportunity afforded by CLL is the versatility of substrates used for patterning. Traditional photolithography patterns micro- and nanostructures on rigid, opaque Si wafers, which limits unconventional applications in biomedicine. For example, we demonstrated a high-throughput, cost-effective approach to fabricate Au nanoribbons on transparent glass substrates *via* CLL (**Figure 9.1i**).[16] The capability to fabricate plasmonic nanostructures on transparent substrates enabled plasmonic sensing. We demonstrated real-time tracking of lipid vesicle or protein adsorption using these Au nanoplasmonic sensors.[16]

Chemical lift-off lithography can also be used to fabricate nanostructures on soft substrates, which is promising for developing wearable sensor systems towards biomarkers monitoring in body fluids (**Figure 9.1j**, **9.1k**).[17] As shown in **Figure 9.1j**, two-dimensional Au nanodisk arrays were fabricated on flexible polyimide substrates (~7-μm thick) and were attached onto skin for wearable sensing.[17] The Au nanostructures can also be fabricated on unconventional surfaces depending on the biomedical application. For example, direct patterning of Au plasmonic nanostructures enabled *in situ* drug delivery and molecular screening.[19] We demonstrated photothermal intracellular delivery of biomolecular cargo at high efficiency using

Au nanodisks fabricated directly on the surfaces of petri dishes using CLL (**Figure 9.1l** and **9.1m**).[19]

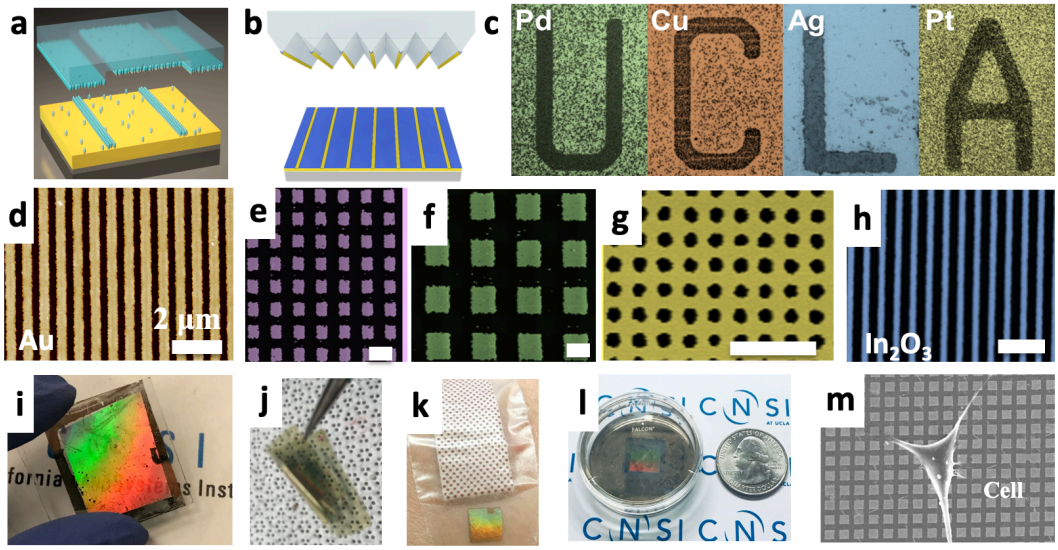

Figure 9.1. Summary of advances in chemical lift-off lithography (CLL) (a) Self-collapse lithography. (b) Polymer-pen CLL. (c) Multi-materials CLL. (d-g) One- and two-dimensional Au micro- and nanostructures fabricated by CLL. (h) In_2O_3 nanoribbons fabricated by CLL. (i) Plasmonic Au nanoribbons fabricated on a glass substrate using CLL. (j,k) Plasmonic Au nanodisk arrays fabricated on flexible polyimide using CLL. (l,m) Au nanodisk arrays fabricated on the surface of a petri dish using CLL for intracellular cargo delivery. Figures reproduced with permission from (a) ref. 7, Copyright 2017, ACS; (b) ref. 6, Copyright 2017, ACS; (c) ref. 13, Copyright 2020, ACS; (d,h) ref. 18; (e-g,j,k) ref. 17; (i) ref. 16, Copyright 2020, ACS; (l,m) ref. 18, Copyright 2020, ACS.

Scalable nanomanufacturing techniques, *e.g.*, CLL, open opportunities to fabricate one-dimensional nanostructures with high surface-to-volume ratios in low cost and high throughput applications, which sets the stage for the development of next-generation sensors. For example,

we have developed nanoscale In_2O_3 field-effect transistor (FET) biosensors to monitor biomarkers in body fluids.[14,18,20-23]

We summarize our discoveries on In_2O_3 FET biosensors since 2015 (**Figure 9.2**). On the top of **Figure 9.2** (in blue), I outline the fabrication advances made leading up to In_2O_3 FET biosensors. A top-down fabrication process was first developed, which combines photolithographic processes and low-temperature sputtering to produce ribbons of 2-μm widths and ~16-nm thickness.[24] A lithography-free process was then developed in 2016, which used two-step sputtering processes and shadow masks.[25] The In_2O_3 ribbons having 25-μm widths, ~16-nm thicknesses, and 500-μm lengths over cm scales were fabricated using this method.[24-26] These devices had high field-effect mobilities (>13 cm^2 V^{-1} s^{-1}) and large current on/off ratios (>10^7).[24,25]

To increase surface-to-volume ratios, we used Au nanoribbons fabricated by CLL as hard masks to produce of In_2O_3 ribbons with smaller features.[27] We deposited In_2O_3 *via* a sol-gel process with the Au/Ti layers deposited on top.[27] Au nanoribbons were patterned using CLL with a subsequent wet-etching process. In_2O_3 nanoribbons were then patterned by wet etching with the Au nanoribbons as masks. Using this approach, I produced In_2O_3 nanoribbons with <200 nm widths and ~3-nm thicknesses. However, this fabrication strategy resulted in overetching into and sometimes through the underlying In_2O_3 layer, which precluded precise patterning.[27] To solve this problem, I developed a fabrication strategy that combined wet etching and sputtering, which resulted in high-fidelity In_2O_3 nanoribbons over large areas.[18] We were able to fabricate and to compare In_2O_3 nanoribbon FET biosensors with different dimensions (350-nm, 2-μm, and 20-μm widths, all thicknesses of ~20 nm). In doing so, we demonstrated that narrower

nanoribbons with higher surface-to-volume ratios showed higher sensitivities in pH and biosensing formats.[18]

In addition to sensor fabrication strategies, we advanced the capabilities of different ultra-sensitive biosensing platforms (bottom of **Figure 9.2,** orange). Nanoscale In_2O_3 FETs have been used for biosensing. We have developed aptamer-based In_2O_3 FETs for small-molecule sensing under high ionic strength concentrations.[28] We demonstrated detection of a variety of biomarkers in complex physiological environments using aptamer-FETs, including serotonin, dopamine, glucose, and phenylalanine.[14,21,22,28] We performed real-time, simultaneous detection of serotonin and dopamine using aptamer-FET biosensors.[22] Apart from aptamer FET biosensors, our collaborators and we developed enzymatic sensors, *e.g.*, glucose oxidase-based glucose-sensing platforms.[25,26,29]

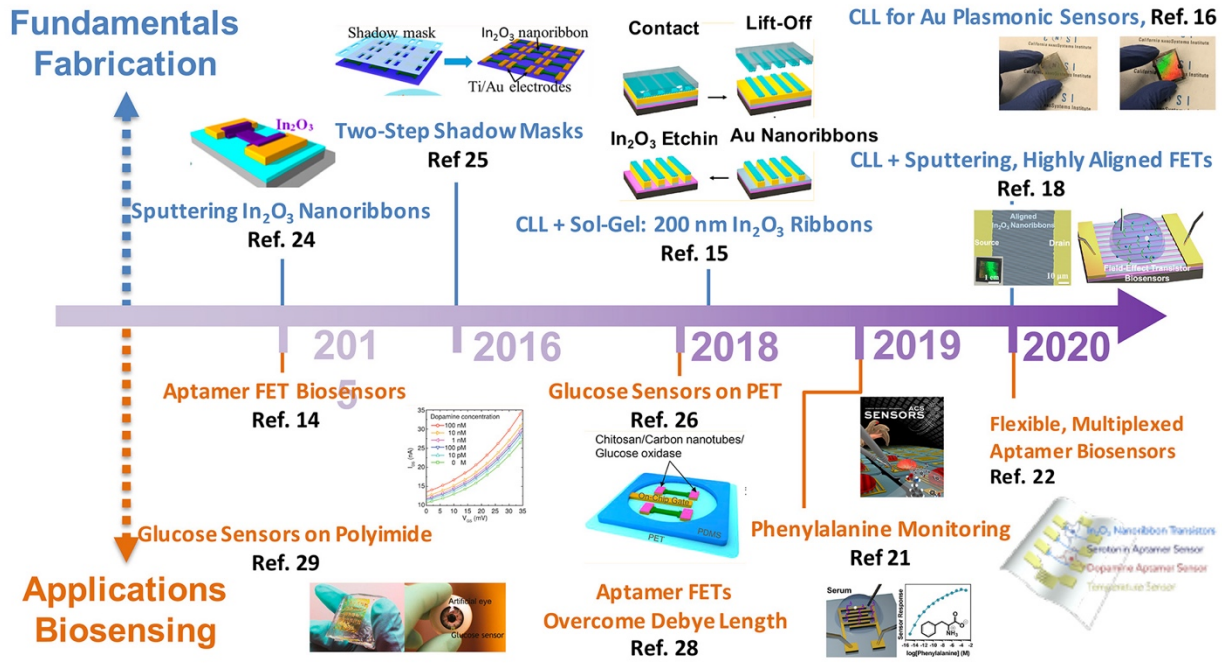

Figure 9.2. Roadmap for In_2O_3 nanoribbon aptamer field-effect transistor biosensors. Top: advances made in fabrication strategies; bottom: advances made in biosensing applications.

Figures reproduced with permission from ref. 24, Copyright 2015, ACS; ref. 25, Copyright 2016, ACS; ref. 15, Copyright 2018, ACS; ref. 16, Copyright 2020, ACS; ref. 14, Copyright 2015, ACS; ref. 29, Copyright 2015, ACS; ref. 26, Copyright 2018, ACS; ref. 28, Copyright 2018, AAAS; ref. 21, copyright 2020, ACS; ref. 22, Copyright 2020, Elsevier.

Conventionally, bioelectronics have been constructed on rigid substrates such as Si. Soft electronics, on the other hand, have elicited substantial interest for their applications in complex biological systems, including brains and skin.[29-38] We demonstrated that In_2O_3 FET biosensors can be fabricated on soft substrates, including polyimide and polyester, with stable and reliable performance for serotonin, dopamine, and glucose sensing.[22,26,29] This work set the foundation for our future efforts in implantable and wearable bioelectronics.

The Andrews' group focuses on developing implantable neuroprobes for monitoring chemical signaling *in vivo*. Understanding how information is encoded in the brain is at the heart of neuroscience. Cracking neural codes will point the way to new treatment and prevention strategies for neuropsychiatric and neurological disorders.[39-41] We demonstrated highly sensitive and selective aptamer-FET biosensors for use in physiological environments.[14,21,22,28] To achieve *in vivo* neurotransmitter detection, we designed, fabricated, and tested implantable aptamer FET Si neuroprobes to monitor small-molecule neurotransmitters (*i.e.*, serotonin) and validated device functionality *in vivo*.[42] We used micro-electro-mechanical-system (MEMS) technologies to fabricate Si-based In_2O_3 FET-based neuroprobes with 150-μm widths and 150-μm thicknesses.[42] We demonstrated the detection of serotonin in behaving mice using these Si aptamer-FET neuroprobes.[42]

The neuroprobe biosensors we developed underlie a general strategy for monitoring neurotransmitter signaling in the brain. Previously, aptamer FET biosensors were shown to detect serotonin, dopamine, glucose, and phenylalanine, with additional aptamers for other neurotransmitters under development.[14,21,22,28] With the isolation of new aptamers, we anticipate that this approach will enable monitoring multiple neurotransmitters in the brain with high sensitivity, selectivity, and high temporal and spatial resolution, regardless of the electrochemical properties of each neurotransmitter. Moreover, aptamer biosensors can be straightforwardly multiplexed due to the high selectivity of the aptamers developed by our Columbia University collaborators. We developed multiplexed sensor arrays to monitor serotonin, dopamine, pH, and temperature simultaneously in real time.[22] The capability to monitor multiple neurotransmitters will provide additional insight into how signaling pathways interact to produce brain function.[43] Advances in this direction will provide knowledge accelerating the development of new medical treatment and improving fundamental neuroscience knowledge.

While our Si neuroprobes are generally applicable for acute measurements over hours, for chronic measurements over days to weeks to months other challenges arise from immunological responses after implantation of hard devices into the brain.[44-46] We envision that next-generation neuroprobes will need to be soft with multi-modal (multiple neurotransmitters, electrophysiology, optical or electrical stimulation, and drug deliver all enabled by the same neuroprobe devices) and with long-term recording capabilities *in vivo*. Soft bioelectronics with capabilities to detect multiple neurotransmitters simultaneously and in real time are needed to investigate chemical information processing in brains,[47] particularly in the context of chronic neural recordings.[45] To achieve this goal, there are challenges and questions that require further investigation.

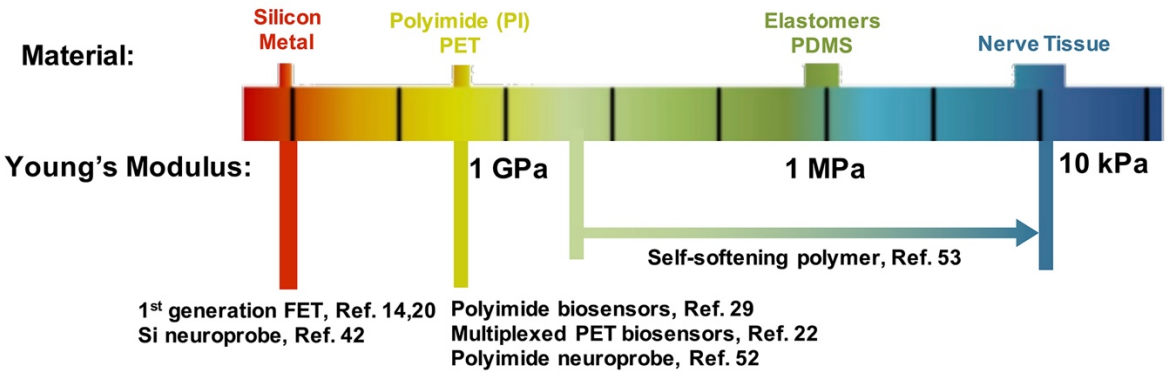

Figure 9.3. Roadmap for neuroprobe development towards tissue-like Young's modulus.

Fabrication of bioelectronics on substrates with lower Young's moduli, *i.e.*, greater elasticity, compared with rigid substrates reduces immunological responses after brain implantation.[44,46] It has been shown that the Young's modulus mismatch between implanted devices and brain tissue causes immunological responses, which can interfere with biosensing.[44,45] Developing neuroprobes with robust, biocompatible, and soft materials is an important direction for next-generation neurochemical probes.[45,48-51] Other aspects, such as fabrication of probes with smaller feature sizes and biomimetic coatings have also been shown to improve the bio-interface after implantation.[45,48-51]

To reduce the Young's moduli of neuroprobes, we developed next-generation neuroprobes on flexible polyimide substrates.[52] However, second generation soft polyimide probes require a rigid carrier device for implantation, which creates extra tissue damage and complicates implantation. Moreover, the Young's modulus of polyimide (~1 GPa) is still five orders higher than nerve tissue (~10 kPa). We are currently working on a third-generation neuroprobe, which utilizes a novel self-softening polymer that is rigid at room temperature and as soft as nerve tissue after implantation into warmer brain tissue.[53] Using this novel temperature

sensitive polymer, we will be able to achieve carrier-free implantation with device's having a Young's modulus close to brain tissue.[53]

While I discussed the importance of developing soft neuroprobes, it remains unclear how soft is "soft enough" such that immunological responses are minimized. This issue is a grand challenge to the minimally invasive and implanted bioelectronics community that needs to be addressed, and requires extensive further study. Another key question involves the impact of device dimensions. It has been shown that smaller implanted devices reduce immune responses.[48-51] However, it is unclear how much miniaturization is needed to minimize immunological responses. Along these lines, I also fabricated Si neuroprobes with 50-µm widths and thicknesses to compare with 150-µm neuroprobes in terms of tissue responses. Further histological studies comparing these device sizes are ongoing.

We have shown that aptamer-FET sensors have temporal resolution on the order of seconds.[22,28] To measure and to understand the dynamic fluxes associated with information encoding in neurochemical transmission, temporal resolutions of tens of milliseconds are necessary. This advance requires further development in term of advances in both sensors and instrumentation.

We have reported the real-time and simultaneous detection of serotonin and dopamine using aptamer-FET biosensors, which lays the foundation for multiplexed monitoring of these neurotransmitters in the brain.[22] For multiplexed neurotransmitter detection *in vivo*, it will be necessary to functionalize the sensor shank with two or more different aptamers. Though we have demonstrated multiplexing of two aptamers on millimeter-scale devices, it is challenging to functionalize micro- or nanoscale devices that are spatially close to one another.

Electrochemically addressable functionalization strategies using electroactive linkers have been demonstrated,[54] and advances and applications in this area are under development for the specific functionalization of small FET devices with different aptamers (~10 μm apart).

Bioelectronics is an exciting field that can revolutionize biomedicine, advancing our understanding of the human body. Better diagnostics and prevention strategies will be available based on discoveries arising from bioelectronics. I spent five years of my graduate career developing bioelectronics to advance our understanding of the brain. The aptamer-FET biosensors foretell a revolution in the biomedicine community with their capabilities to monitor biomarkers inside and on the body. I anticipate that there will be many more exciting discoveries forthcoming in this field.

References

(1) Liao, W.-S.; Cheunkar, S.; Cao, H. H.; Bednar, H. R.; Weiss, P. S.; Andrews, A. M. Subtractive Patterning *via* Chemical Lift-Off Lithography. *Science* 2012, *337*, 1517–1521.

(2) Andrews, A. M.; Liao, W.-S.; Weiss, P. S. Double-Sided Opportunities Using Chemical Lift-Off Lithography. *Acc. Chem. Res.* 2016, *49*, 1449–1457.

(3) Cao, H. H.; Nakatsuka, N.; Liao, W.-S.; Serino, A. C.; Cheunkar, S.; Yang, H.; Weiss, P. S.; Andrews, A. M. Advancing Biocapture Substrates *via* Chemical Lift-Off Lithography. *Chem. Mater.* 2017, *29*, 6829–6839.

(4) Slaughter, L. S.; Cheung, K. M.; Kaappa, S.; Cao, H. H.; Yang, Q.; Young, T. D.; Serino, A. C.; Malola, S.; Olson, J. M.; Link, S.; Häkkinen, H.; Andrews, A. M.; Weiss, P. S. Patterning of Supported Gold Monolayers *via* Chemical Lift-Off Lithography. *Beilstein J. Nanotech.* 2017, *8*, 2648–2661.

(5) Chen, C.-Y.; Wang, C.-M.; Li, H.-H.; Chan, H.-H.; Liao, W.-S. Wafer-Scale Bioactive Substrate Patterning by Chemical Lift-Off Lithography. *Beilstein J. Nanotech.* 2018, *9*, 311–320.

(6) Xu, X.; Yang, Q.; Cheung, K. M.; Zhao, C.; Wattanatorn, N.; Belling, J. N.; Abendroth, J. M.; Slaughter, L. S.; Mirkin, C. A.; Andrews, A. M.; Weiss, P. S. Polymer-Pen Chemical Lift-Off Lithography. *Nano Lett.* 2017, *17*, 3302–3311.

(7) Zhao, C.; Xu, X.; Yang, Q.; Man, T.; Jonas, S. J.; Schwartz, J. J.; Andrews, A. M.; Weiss, P. S. Self-Collapse Lithography. *Nano Lett.* 2017, *17*, 5035–5042.

(8) Cao, H. H.; Nakatsuka, N.; Serino, A. C.; Liao, W.-S.; Cheunkar, S.; Yang, H.; Weiss, P. S.; Andrews, A. M. Controlled DNA Patterning by Chemical Lift-Off Lithography: Matrix Matters. *ACS Nano* 2015, *9*, 11439–11454.

(9) Abendroth, J. M.; Nakatsuka, N.; Ye, M.; Kim, D.; Fullerton, E. E.; Andrews, A. M.; Weiss, P. S. Analyzing Spin Selectivity in DNA-Mediated Charge Transfer *via* Fluorescence Microscopy. *ACS Nano* 2017, *11*, 7516–7526.

(10) Chen, C.-Y.; Wang, C.-M.; Chen, P.-S.; Liao, W.-S. Surface Functional DNA Density Control by Programmable Molecular Defects. *Chem. Commun.* 2018, *54*, 4100–4103.

(11) Chen, C.-Y.; Wang, C.-M.; Chen, P.-S.; Liao, W.-S. Self-Standing Aptamers by an Artificial Defect-Rich Matrix. *Nanoscale* 2018, *10*, 3191–3197.

(12) Cao, H. H.; Nakatsuka, N.; Deshayes, S.; Abendroth, J. M.; Yang, H.; Weiss, P. S.; Kasko, A. M.; Andrews, A. M. Small-Molecule Patterning *via* Prefunctionalized Alkanethiols. *Chem. Mater.* 2018, *30*, 4017-4030.

(13) Cheung, K. M.; Stemer, D. M.; Zhao, C.; Young, T. D.; Belling, J. N.; Andrews, A. M.; Weiss, P. S. Chemical Lift-Off Lithography of Metal and Semiconductor Surfaces. *ACS Mater. Lett.* 2019, *2*, 76–83.

(14) Kim, J.; Rim, Y. S.; Chen, H.; Cao, H. H.; Nakatsuka, N.; Hinton, H. L.; Zhao, C.; Andrews, A. M.; Yang, Y.; Weiss, P. S. Fabrication of High-Performance Ultrathin In_2O_3 Film Field-Effect Transistors and Biosensors Using Chemical Lift-Off Lithography. *ACS Nano* 2015, *9*, 4572–4582.

(15) Zhao, C.; Xu, X.; Bae, S. H.; Yang, Q.; Liu, W.; Belling, J. N.; Cheung, K. M.; Rim, Y. S.; Yang, Y.; Andrews, A. M.; Weiss, P. S. Large-Area, Ultrathin Metal-Oxide Semiconductor Nanoribbon Arrays Fabricated by Chemical Lift-Off Lithography. *Nano Lett.* 2018, *18*, 5590–5595.

(16) Zhao, C.; Xu, X.; Ferhan, A. R.; Chiang, N.; Jackman, J. A.; Yang, Q.; Liu, W.; Andrews, A. M.; Cho, N. J.; Weiss, P. S. Scalable Fabrication of Quasi-One-Dimensional Gold Nanoribbons for Plasmonic Sensing. *Nano Lett.* 2020, *20*, 1747–1754.

(17) Zhao, C.; Xu, X.; Chiang, N.; Yang, Q.; Liu, W.; Schwartz, J. J.; Andrews, A. M.; Weiss, P. S. Double Patterning Chemical Lift-Off Lithography. 2020, *in prep*.

(18) Zhao, C.; Liu, Q.; Cheung, K. M.; Liu, W.; Yang, Q.; Xu, X.; Weiss, P. S.; Zhou, C.; Andrews, A. M. Narrower Nanoribbon Biosensors Fabricated by Chemcial Lift-Off Lithography Show Higher Sensitivity. *ACS Nano* 2020, in revision.

(19) Zhao, C.; Man, T.; Xu, X.; Yang, Q.; Liu, W.; Jonas, S. J.; Teitell, M. A.; Chiou, P.-Y.; Weiss, P. S. Photothermal Intracellular Delivery Using Gold Nanodisk Arrays. *ACS Mater. Lett.* 2020, *2*, 1475–1483.

(20) Nakatsuka, N.; Yang, K. A.; Abendroth, J. M.; Cheung, K. M.; Xu, X.; Yang, H.; Zhao, C.; Zhu, B.; Rim, Y. S.; Yang, Y.; Weiss, P. S.; Stojanovic, M. N.; Andrews, A. M. Aptamer-Field-Effect Transistors Overcome Debye Length Limitations for Small-Molecule Sensing. *Science* 2018, *362*, 319-324.

(21) Cheung, K. M.; Yang, K. A.; Nakatsuka, N.; Zhao, C.; Ye, M.; Jung, M. E.; Yang, H.; Weiss, P. S.; Stojanovic, M. N.; Andrews, A. M. Phenylalanine Monitoring *via* Aptamer-Field-Effect Transistor Sensors. *ACS Sens.* 2019, *4*, 3308–3317.

(22) Liu, Q.; Zhao, C.; Chen, M.; Liu, Y.; Zhao, Z.; Wu, F.; Li, Z.; Weiss, P. S.; Andrews, A. M.; Zhou, C. Flexible Multiplexed In_2O_3 Nanoribbon Aptamer-Field-Effect Transistors for Biosensing. *iScience* 2020, *23*, 101469.

(23) Cheung, K. M.; Abendroth, J. M.; Nakatsuka, N.; Zhu, B.; Yang, Y.; Andrews, A. M.; Weiss, P. S. Detecting DNA and RNA and Differentiating Single-Nucleotide Variations *via* Field-Effect Transistors. *Nano Lett.* 2020, *20*, 5982–5990.

(24) Aroonyadet, N.; Wang, X.; Song, Y.; Chen, H.; Cote, R. J.; Thompson, M. E.; Datar, R. H.; Zhou, C. Highly Scalable, Uniform, and Sensitive Biosensors Based on Top-Down Indium Oxide Nanoribbons and Electronic Enzyme-Linked Immunosorbent Assay. *Nano Lett.* 2015, *15*, 1943-1951.

(25) Liu, Q.; Aroonyadet, N.; Song, Y.; Wang, X.; Cao, X.; Liu, Y.; Cong, S.; Wu, F.; Thompson, M. E.; Zhou, C. Highly Sensitive and Quick Detection of Acute Myocardial Infarction Biomarkers Using In_2O_3 Nanoribbon Biosensors Fabricated Using Shadow Masks. *ACS Nano* 2016, *10*, 10117–10125.

(26) Liu, Q.; Liu, Y.; Wu, F.; Cao, X.; Li, Z.; Alharbi, M.; Abbas, A. N.; Amer, M. R.; Zhou, C. Highly Sensitive and Wearable In_2O_3 Nanoribbon Transistor Biosensors with Integrated On-Chip Gate for Glucose Monitoring in Body Fluids. *ACS Nano* 2018, *12*, 1170–1178.

(27) Zhao, C.; Xu, X.; Bae, S. H.; Yang, Q.; Liu, W.; Belling, J. N.; Cheung, K. M.; Rim, Y. S.; Yang, Y.; Andrews, A. M.; Weiss, P. S. Large-Area, Ultrathin Metal-Oxide Semiconductor Nanoribbon Arrays Fabricated by Chemical Lift-Off Lithography. *Nano Lett.* 2018, *18*, 5590–5595.

(28) Nakatsuka, N.; Yang, K. A.; Abendroth, J. M.; Cheung, K. M.; Xu, X.; Yang, H.; Zhao, C.; Zhu, B.; Rim, Y. S.; Yang, Y.; Weiss, P. S.; Stojanovic, M. N.; Andrews, A. M. Aptamer-Field-Effect Transistors Overcome Debye Length Limitations for Small-Molecule Sensing. *Science* 2018, *362*, 319–324.

(29) Rim, Y. S.; Bae, S. H.; Chen, H.; Yang, J. L.; Kim, J.; Andrews, A. M.; Weiss, P. S.; Yang, Y.; Tseng, H. R. Printable Ultrathin Metal Oxide Semiconductor-Based Conformal Biosensors. *ACS Nano* 2015, *9*, 12174–12181.

(30) Kim, D. H.; Viventi, J.; Amsden, J. J.; Xiao, J.; Vigeland, L.; Kim, Y. S.; Blanco, J. A.; Panilaitis, B.; Frechette, E. S.; Contreras, D.; Kaplan, D. L.; Omenetto, F. G.; Huang, Y.; Hwang, K. C.; Zakin, M. R.; Litt, B.; Rogers, J. A. Dissolvable Films of Silk Fibroin for Ultrathin Conformal Bio-Integrated Electronics. *Nat. Mater.* 2010, *9*, 511–517.

(31) Minev, I. R.; Musienko, P.; Hirsch, A.; Barraud, Q.; Wenger, N.; Moraud, E. M.; Gandar, J.; Capogrosso, M.; Milekovic, T.; Asboth, L.; Torres, R. F.; Vachicouras, N.; Liu, Q.; Pavlova, N.; Duis, S.; Larmagnac, A.; Voros, J.; Micera, S.; Suo, Z.; Courtine, G.; et al. Electronic Dura Mater for Long-Term Multimodal Neural Interfaces. *Science* 2015, *347*, 159–163.

(32) Wang, S.; Xu, J.; Wang, W.; Wang, G. N.; Rastak, R.; Molina-Lopez, F.; Chung, J. W.; Niu, S.; Feig, V. R.; Lopez, J.; Lei, T.; Kwon, S. K.; Kim, Y.; Foudeh, A. M.; Ehrlich, A.;

Gasperini, A.; Yun, Y.; Murmann, B.; Tok, J. B.; Bao, Z. Skin Electronics from Scalable Fabrication of an Intrinsically Stretchable Transistor Array. *Nature* 2018, *555*, 83–88.

(33) Luan, L.; Wei, X. L.; Zhao, Z. T.; Siegel, J. J.; Potnis, O.; Tuppen, C. A.; Lin, S. Q.; Kazmi, S.; Fowler, R. A.; Holloway, S.; Dunn, A. K.; Chitwood, R. A.; Xie, C. Ultraflexible Nanoelectronic Probes Form Reliable, Glial Scar-Free Neural Integration. *Sci. Adv.* 2017, *3*, e1601966.

(34) Zhou, T.; Hong, G.; Fu, T. M.; Yang, X.; Schuhmann, T. G.; Viveros, R. D.; Lieber, C. M. Syringe-Injectable Mesh Electronics Integrate Seamlessly with Minimal Chronic Immune Response in the Brain. *Proc. Natl. Acad. Sci. U. S. A.* 2017, *114*, 5894–5899.

(35) Liu, Z.; Qi, D.; Leow, W. R.; Yu, J.; Xiloyannnis, M.; Cappello, L.; Liu, Y.; Zhu, B.; Jiang, Y.; Chen, G.; Masia, L.; Liedberg, B.; Chen, X. 3D-Structured Stretchable Strain Sensors for Out-of-Plane Force Detection. *Adv. Mater.* 2018, *30*, e1707285.

(36) Gao, W.; Emaminejad, S.; Nyein, H. Y. Y.; Challa, S.; Chen, K.; Peck, A.; Fahad, H. M.; Ota, H.; Shiraki, H.; Kiriya, D.; Lien, D. H.; Brooks, G. A.; Davis, R. W.; Javey, A. Fully Integrated Wearable Sensor Arrays for Multiplexed in Situ Perspiration Analysis. *Nature* 2016, *529*, 509–514.

(37) Kim, J.; Campbell, A. S.; de Avila, B. E.; Wang, J. Wearable Biosensors for Healthcare Monitoring. *Nat. Biotechnol.* 2019, *37*, 389–406.

(38) Rogers, J.; Bao, Z.; Lee, T. W. Wearable Bioelectronics: Opportunities for Chemistry. *Acc. Chem. Res.* 2019, *52*, 521–522.

(39) Rivnay, J.; Wang, H.; Fenno, L.; Deisseroth, K.; Malliaras, G. G. Next-Generation Probes, Particles, and Proteins for Neural Interfacing. *Sci. Adv.* 2017, *3*, e1601649.

(40) Chen, R.; Canales, A.; Anikeeva, P. Neural Recording and Modulation Technologies. *Nat. Rev. Mater.* 2017, *2,* 16093.

(41) Chapman, C. A. R.; Goshi, N.; Seker, E. Multifunctional Neural Interfaces for Closed-Loop Control of Neural Activity. *Adv. Funct. Mater.* 2018, *28*, 1703523.

(42) Zhao, C.; Huang, I., W.; Cheung, K. M.; Nakatsuka, N.; Yang, H.; Liu, W.; Cao, Y.; Man, T.; Weiss, P. S.; Monbouquette, H. G.; Andrews, A. M. Implantable Aptamer-Field-Effect Transistor Neuroprobes Towards *in Vivo* Monitoring of Serotonin. 2020, *in prep*.

(43) Manciu, F. S.; Manciu, M.; Ciubuc, J. D.; Sundin, E. M.; Ochoa, K.; Eastman, M.; Durrer, W. G.; Guerrero, J.; Lopez, B.; Subedi, M.; Bennet, K. E. Simultaneous Detection of Dopamine and Serotonin-A Comparative Experimental and Theoretical Study of Neurotransmitter Interactions. *Biosensors* 2018, *9*, 3.

(44) Kozai, T. D.; Jaquins-Gerstl, A. S.; Vazquez, A. L.; Michael, A. C.; Cui, X. T. Brain Tissue Responses to Neural Implants Impact Signal Sensitivity and Intervention Strategies. *ACS Chem. Neurosci.* 2015, *6*, 48–67.

(45) Du, Z. J.; Kolarcik, C. L.; Kozai, T. D. Y.; Luebben, S. D.; Sapp, S. A.; Zheng, X. S.; Nabity, J. A.; Cui, X. T. Ultrasoft Microwire Neural Electrodes Improve Chronic Tissue Integration. *Acta Biomater.* 2017, *53*, 46–58.

(46) Gunasekera, B.; Saxena, T.; Bellamkonda, R.; Karumbaiah, L. Intracortical Recording Interfaces: Current Challenges to Chronic Recording Function. *ACS Chem. Neurosci.* 2015, *6*, 68–83.

(47) Andrews, A. M. The Brain Initiative: Toward a Chemical Connectome. *ACS Chem. Neurosci.* 2013, *4*, 645.

(48) Szostak, K. M.; Grand, L.; Constandinou, T. G. Neural Interfaces for Intracortical Recording: Requirements, Fabrication Methods, and Characteristics. *Front. Neurosci.* 2017, *11*, 665.

(49) Feiner, R.; Dvir, T. Tissue–Electronics Interfaces: From Implantable Devices to Engineered Tissues. *Nat. Rev. Mater.* 2017, *3*.

(50) Winslow, B. D.; Christensen, M. B.; Yang, W. K.; Solzbacher, F.; Tresco, P. A. A Comparison of the Tissue Response to Chronically Implanted Parylene-C-Coated and Uncoated Planar Silicon Microelectrode Arrays in Rat Cortex. *Biomaterials* 2010, *31*, 9163–9172.

(51) Polikov, V. S.; Tresco, P. A.; Reichert, W. M. Response of Brain Tissue to Chronically Implanted Neural Electrodes. *J. Neurosci. Methods* 2005, *148*, 1–18.

(52) Zhao, C.; Huang, I., W.; Cao, Y.; Liu, W.; Weiss, P. S.; Monbouquette, H. G.; Andrews, A. M. Flexible Polyimide Aptamer Field-Effect Transistor Neuroprobe. *in prep*.

(53) Xie, Z.; Zhao, C.; Wu, H.; Gad, P.; Zhong, H.; Liu, W.; Weiss, P. S.; Edgerton, R.; Andrews, A. M.; Pei, Q. Self-Softening, Multi-Modal Implantable Neuroprobe. 2020, *in prep*.

(54) Curreli, M.; Li, C.; Sun, Y.; Lei, B.; Gundersen, M. A.; Thompson, M. E.; Zhou, C. Selective Functionalization of In_2O_3 Nanowire Mat Devices for Biosensing Applications. *J. Am. Chem. Soc.* 2005, *127*, 6922–6923.